UNIVERZA V LJUBLJANI
FAKULTETA ZA MATEMATIKO IN FIZIKO

Gregor Skačej

Modeliranje močno ograjenih tekočekristalnih sistemov

disertacija

LJUBLJANA 2002

University of Ljubljana
Faculty of Mathematics and Physics

Gregor Skačej

Modeling of strongly confined liquid-crystalline systems

---

thesis

Ljubljana 2002

Za pomoč in številne nasvete na raziskovalni poti ter pri nastajanju tega dela se zahvaljujem svojemu mentorju, Slobodanu Žumru.

⋆ ⋆ ⋆

I am grateful to Paolo Pasini, Claudio Zannoni, and Cesare Chiccoli (all from Bologna), as well as to Nikolai V. Priezjev and Robert A. Pelcovits (Providence, RI), for sharing their experience in Monte Carlo methods and lattice models. I also wish to thank Giovanni Barbero (Torino), Claudio Ferrero, and Thomas Günzel (both from Grenoble) for the joint efforts in the phenomenology work.

Moreover, I wish to acknowledge the support by CINECA through the EC Access to Research Infrastructures action of the Improving Human Potential Programme. Computational work in support of this research was performed also at the Theoretical Physics Computing Facility at Brown University.

⋆ ⋆ ⋆

Za dobro delovno vzdušje in številna razčiščena vprašanja hvala vsem tekočekristalcem iz petega nadstropja, zlasti Andreji, Danielu, Piki in Primožu.

Za vsestransko podporo gre velika zahvala tudi mojim domačim in prijateljem.

Povzetek

To delo se ukvarja z izbranimi problemi modeliranja močno ograjenih tekočekristalnih sistemov: z urejanjem molekul in površinskim sidranjem v plasti nematika, z molekulsko dinamiko in učinki zunanjih polj v nematskih kapljicah, ter z urejanjem, ki ga vsiljujejo v nematiku dispergirane polimerne mreže pravilne ali nepravilne oblike. Modeliranje teh sistemov sloni na fenomenološkem Landau-de Gennesovem opisu in na simulacijah vrste Monte Carlo v okviru mikroskopskih mrežnih modelov. Posebna pozornost je posvečena vzpostavitvi povezave med rezultati simulacij in eksperimentalnimi opazljivkami, kot so spektri ^{2}H NMR, električna kapacitivnost in intenziteta skozi vzorec prepuščene svetlobe. Rezultati študija urejanja v plasti nematika kažejo, da spreminjanje stopnje nematske ureditve ob površini privede do pojava elastične deformacije, ki jo spremlja prispevek k notranjemu sidranju. Pri študiju nematskih kapljic je bila razvita nova metodologija za napoved spektrov ^{2}H NMR iz rezultatov simulacij Monte Carlo, ki pravilno opiše gibanja molekul v vzorcu. Metodologija je bila preizkušena pri obravnavi fluktuacij dolgih osi molekul, translacijske difuzije in učinkov zunanjega električnega ali magnetnega polja. Na koncu so predstavljene simulacije nematikov z dispergiranimi polimernimi mrežami. Te kažejo, da so vlakna mreže sposobna urediti nematik, ki jih obdaja, četudi je njihova površina dokaj groba. Poleg tega lahko zunanje polje povzroči strukturne prehode, prikazane v preprostem faznem diagramu, pri čemer igra pomembno vlogo sama topografija mreže. Nad temperaturo prehoda v izotropno fazo je v sistemu moč opaziti tudi paranematsko urejanje. Rezultati simulacij so omogočili tudi vpogled v notranjo strukturo topoloških defektov v nematski ureditvi, do katerih lahko pride v primerno ograjenih sistemih.

Ključne besede: nematski tekoči kristal, ograditev, polimerne disperzije, elastičnost, sidranje, topološki defekti, zunanje polje, mrežni modeli, simulacije Monte Carlo, ^{2}H NMR, kapacitivnost, prepuščanje svetlobe

PACS: 61.30.Cz, 61.30.Gd

Abstract

This thesis addresses selected topics in the field of strongly confined nematic liquid crystals: molecular ordering and surface anchoring in a nematic slab, dynamical and external field effects in nematic droplets, and the orienting ability of regular or irregular polymer networks dispersed in liquid crystals. The modeling of these composite systems is based both on phenomenological (Landau-de Gennes) and microscopic simulation (lattice model Monte Carlo) approaches. A special attention is paid to establishing a relation between the simulation output and experimental observables, in particular ^{2}H NMR line shapes, electric capacitance, and transmitted light intensity. In the simple nematic slab geometry, a subsurface variation in the degree of nematic order is shown to result in a subsurface elastic deformation, accompanied by an intrinsic contribution to surface anchoring. The section on nematic droplets presents a novel methodology for the calculation of ^{2}H NMR line shapes from the output of Monte Carlo simulations, pointing out the importance of translational diffusion, molecular fluctuations, and external magnetic or electric field effects. Finally, simulations of nematics with dispersed polymer networks indicate that the networks are capable of aligning the surrounding liquid crystal even if their surface is fairly rough. In a regular fiber array external field-induced structural transitions are studied in detail, presenting a stability phase diagram for the observed structures. The topography of the network itself is seen to be intimately related to the characteristics of the external field-driven molecular switching process. Moreover, above the nematic-isotropic transition temperature paranematic ordering is detected in the system. Eventually, suitable topological constraints can lead to the formation of defects in nematic ordering. The inner defect structure could then be resolved from molecular simulations.

Keywords: nematic liquid crystal, confinement, polymer dispersions, elasticity, anchoring, topological defects, external field, lattice models, Monte Carlo simulations, ^{2}H NMR, capacitance, light transmission

PACS: 61.30.Cz, 61.30.Gd

Contents

Razširjeni povzetek

Uvod

Na prvi pogled se morda zdi, da izraz *tekoči kristali* vsebuje neskladje, saj se hkrati sklicuje na tekočnost in kristaliničnost snovi. V resnici gre pri tekočih kristalih za organske snovi, ki jih sestavljajo molekule močno anizotropne oblike, in čeprav so ob primernih pogojih tekoči, oblika molekul botruje anizotropiji njihovih makroskopskih lastnosti: lomnega količnika, dielektrične konstante, magnetne susceptibilnosti in drugih. Prav zato so tekočekristalni materiali danes izjemno razširjeni v industriji optičnih naprav, kot so hitre zaslonke ali tekočekristalni zasloni, pogosto pa jih srečujemo tudi v vsakdanjem življenju. Prve tekočekristalne snovi so bile odkrite že pred več kot sto leti [1,2] in kaj kmalu se je izkazalo, da gre za novo agregatno stanje med navadno (izotropno) tekočino in trdnino. Danes je znanih mnogo tekočekristalnih faz, od katerih se bomo tukaj omejili na najpreprostejšo izmed njih, *nematske* ("nitaste") tekoče kristale [3]. Sestavljajo jih podolgovate molekule, ki se v velikem vzorcu v povprečju uredijo v določeni smeri. To smer označimo z enotskim vektorjem $\mathbf{n}$ in ga imenujemo *direktor* [4]. Pri tem sta smeri $+\mathbf{n}$ in $-\mathbf{n}$ enakovredni, težišča molekul pa so razporejena naključno po prostoru kot pri navadni tekočini (slika 1). Ponavadi je porazdelitev molekul okoli $\mathbf{n}$ osno simetrična: nematik je tedaj *enoosen.* Če to ne drži, govorimo o *dvoosnem* nematiku. Z višanjem temperature stopnja ureditve okoli $\mathbf{n}$ postopoma pojema, končno pa pride do faznega prehoda v navadno (izotropno) tekočinsko fazo, ki je šibko nezvezen.

Obnašanje nematikov postane veliko bolj zanimivo, če jih ogradimo — z njimi zapolnimo drobne (mikroskopske) kapljice ali pore (slika 1) [5]. Pojem *močne ograditve* se pri tem nanaša na sisteme z visokim razmerjem površine in prostornine. Pomemben je pojav *sidranja* tekočekristalnih molekul na ograjujoči površini [6], pri katerem se molekule lahko urejajo vzdolž površine (*planarno* sidranje [7–10]), pravokotno nanjo (*homeotropno* sidranje [11–13]), ali pa poševno [14]. Red, ki ga vsiljuje površina, lahko ob stenah obstaja tudi nad temperaturo faznega prehoda v izotropno fazo (*paranematski red*). Močno ograditev lahko zagotavljajo tudi v tekočem kristalu razpršene (dispergirane) polimerne mreže [15]. Podobno je moč (raz)urejujoče učinke pričakovati tudi na prosti površini nematika [16,17], čemur pravimo *notranje sidranje* (za razliko od *zunanjega*, ki zadeva urejanje ob trdni površini).

V ograjenih sistemih postane direktor krajevno odvisen, $\mathbf{n} = \mathbf{n}(\mathbf{r})$. Vsako odstopanje od *homogenega* direktorskega profila z $\mathbf{n} \neq \mathbf{n}(\mathbf{r})$ predstavlja *elastično deforma-*

cijo, ki jo spremlja prispevek k prosti energiji [18–20]. Tudi vsakršno odstopanje od smeri, ki jo predpisuje sidranje, poviša prosto energijo [21,22]. Zaradi anizotropije v električni in magnetni susceptibilnosti je na orientacijo molekul (in $\mathbf{n}$) mogoče vplivati tudi z zunanjim poljem [4,20]. Ravnovesni $\mathbf{n}(\mathbf{r})$ potem najdemo z minimizacijo celotne proste energije. V določenih primerih ograditve naletimo na mesta v vzorcu, kjer $\mathbf{n}$ iz topoloških razlogov ni definiran. To so lahko točke, črte ali stene, ki jim pravimo *topološki defekti* [4,23,24].

Danes so na voljo najrazličnejše vrste ograditev: nematske plasti (celice), membrane z mikronskimi *valjastimi porami* [27], *nematske kapljice* v polimerni matriki (PDLC) [28], v tekočem kristalu dispergirane *polimerne mreže* nanometrskih vlaken [26,30,31] in podobno. Te in podobne sisteme so v preteklosti raziskovali z različnimi pristopi. S teoretične plati prednjačijo fenomenološki pristopi, temelječi na *teoriji Landaua in de Gennesa* [16,32], ki jim sledijo študije z *gostotnim funkcionalom* [33–35]. Z razvojem hitrih računalnikov je doživelo razcvet področje simulacij *molekularne dinamike* [36] in simulacij vrste *Monte Carlo* [37]). Oba pristopa sta zasnovana na parskih interakcijah med molekulami in omogočata povezavo med mikroskopskimi in makroskopskimi lastnostmi sistema. Izmed eksperimentalnih metod je bila za študij tekočih kristalov prva uporabljena *polarizacijska mikroskopija* [1,2,26,38]. Sledile so ji ostale metode: *meritve električne kapacitivnosti* [39], *devterijeva jedrska magnetna resonanca* (^{2}H NMR) [5,40,41], *podvajanje frekvence svetlobe* (SHG) [42,43], *elipsometrija* [44], *dinamično sipanje svetlobe* [45,46], *kalorimetrija* [47] in še številne druge.

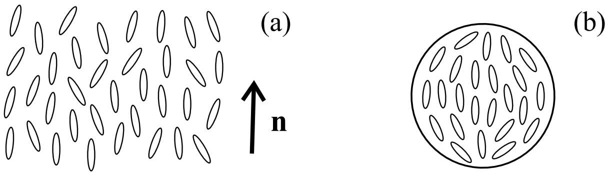

Slika 1 Ureditev molekul v nematski fazi, $\mathbf{n}$ označuje direktor (a). Primer ograjenega nematika v kapljici (b).

V tem doktorskem delu se bomo dotaknili modeliranja izbranih problemov s področja močno ograjenih tekočih kristalov. Pri tem se bomo posvetili dvema ciljema: (i) boljšemu razumevanju urejanja molekul v bližini ograjujočih površin in (ii) opisu nematskega urejanja v primerih kompleksne (tudi nepravilne) ograditve. Temu poglavju bo sledil kratek pregled nekaterih pojmov, potrebnih za opis nematskega urejanja in za razumevanje modeliranja, ki bo predstavljeno v nadaljevanju.

Prvi izmed problemov, ki se ga bomo lotili, bo nematsko urejanje v tanki plasti tekočega kristala. Posebna pozornost bo posvečena spremembam stopnje ureditve ob površini, ki jih spremljajo notranje sidranje in elastične deformacije, opažene tudi eksperimentalno [43,48–51]. Hkrati so bile podobne deformacije napovedane tudi teoretično v okviru fenomenološkega Landau-de Gennesovega opisa z elastično konstanto K_{13} [52,53]. Deformacije, do katerih tak opis privede, so močne [54–58] in zato v neskladju z uporabo kontinuumske teorije [59–61]. Hkrati novejše analize (tudi z uporabo gostotnega funkcionala) kažejo, da za stopničast profil gostote in stopnje ureditve ob ravni površini velja $K_{13} = 0$ [62–65]. To sicer navidez sicer reši omenjeni problem, a kljub temu pušča odprto vprašanje obstoja eksperimentalno opaženih deformacij. Elastične deformacije je možno zaslediti, kadar profil gostote ni stopničast in lahko variira tudi stopnja nematske urejenosti [66,67]. V tem delu se bomo najprej lotili planarne ureditve z namenom podrobno raziskati posledice variacij stopnje reda ob površini [68], pri čemer v deformacijski prosti energiji člena s konstanto K_{13} ne bomo izrecno upoštevali. Študijo bomo na koncu razširili še na neravninske zvojne deformacije [71].

Pojav notranjega sidranja, ki pomembno vpliva na ureditev blizu površine nematskega vzorca [17,72], bomo v plasti nematika obdelali tudi z mikroskopskega stališča. Fenomenološki opis bo nadomestil preprost model s šestkotniško mrežo, temelječ na prostorsko anizotropni interakciji med induciranimi dipoli. Problema se bomo lotili s simulacijami Monte Carlo pri končnih temperaturah. Glavni namen te študije je izmeriti jakost notranjega sidranja in njeno temperaturno odvisnost. V preteklosti je bilo nanizanih že več mikroskopskih študij sidranja ob prostih površinah nematika ali za nematik v stiku s trdno steno: psevdomolekulski kontinuumski pristop z elipsastimi molekulami [73], simulacijske študije v sistemih Gay-Berneovih delcev [74–78] ter študije sistemov trdih elipsoidov [79,80]. Nekatere simulacije molekularne dinamike z Gay-Berneovimi delci kažejo tudi na plastovito urejanje v bližini površine, kar vodi do znatne modulacije v profilu molekulske gostote [84–87] in je bilo opaženo tudi v eksperimentih [88,89]. Ponavadi so v simulacijah določene energije sidranja veliko višje od eksperimentalnih vrednosti [6].

Sledila bo obravnava krogelnih (PDLC) nematskih kapljic premera pod 1μm, ki bo omejena na *radialne* [38,40] in *bipolarne* [38,40,90] kapljice, prve s homeotropnim sidranjem, druge s planarnim (slika 1). V aplikativne namene so posebej zanimivi primeri, ko kapljice postavimo v zunanje polje [40,90]. Eksperimentalno so kapljice preučevali z ^{2}H NMR [40,90] in polarizacijsko mikroskopijo [38], teoretično pa fenomenološko (Landau-de Gennesov opis) [5,25] in s simulacijami Monte Carlo [91,92]. Do sedaj predstavljene simulacije praviloma temeljijo na mrežnem modelu Lebwohla in Lasherja [93] in so se izkazale kot koristne tudi pri napovedovanju eksperimentalnih opazljivk: statičnih spektrov ^{2}H NMR in slik polarizacijske mikroskopije [91,94]. Tukaj se bomo posvetili razvoju nove metodologije za računanje dinamičnih spektrov ^{2}H NMR v prisotnosti molekulskega gibanja — fluktuacij dolgih osi molekul in translacijske difuzije [95] — ter jo preizkusili tudi v primeru nehomogene difuzije [96,97]. Vhodne podatke za izračun spektrov bodo priskrbele simulacije Monte Carlo, izvedene v modelskem sistemu Lebwohla in Lasherja. Obravnavo kapljic bomo zaključili s podrobnim študijem učinkov zunanjega polja [98–100], ki jih bomo spet spremljali predvsem skozi razvoj spektrov ^{2}H NMR.

Naslednje poglavje bo zadevalo nematike z dispergiranimi polimernimi mrežami, kar bo tudi najkompleksnejša od vseh obravnavanih ograditev. Tudi ti sistemi so obetavni za aplikacije, ki v glavnem temeljijo na *preklapljanju* orientacije molekul iz smeri, ki jo določajo polimerna vlakna, v smer zunanjega polja. Nenaden preklop molekulskih orientacij je moč zaznati preko sprememb v kapacitivnosti, optični prepustnosti ali z ^{2}H NMR spektroskopijo [31,39]. Dogajanje v procesu preklapljanja je močno odvisno tako od pogojev sidranja na površini, kot tudi od topografije same mreže, kar lahko oboje reguliramo med njenim nastankom [15,101]. Obstoječe eksperimentalne študije ponavadi spremljajo fenomenološke analize [5,26,31,39], medtem ko je bilo za te sisteme storjenega izjemno malo na področju molekulskih simulacij. Zaradi vsega navedenega bo najprej predstavljena temeljita mikroskopska študija orientacijske sklopitve med polimernimi vlakni in tekočim kristalom, ki jih obdaja. Kot v primeru kapljic bomo uporabili mrežni model Lebwohla in Lasherja, in sicer za vlakna z dobro definirano povprečno smerjo. Obravnavali bomo primere z različno grobostjo površine vlaken [102], pa tudi take, pri katerih pride do tvorbe topoloških defektov [103]. Pri slednjih bomo notranjo zgradbo defektov primerjali s fenomenološkimi napovedmi [104,105]. Simulirali bomo še proces preklapljanja v zunanjem polju, pri tem pa bomo posebej pozorni na vplive nepravilnosti v topografiji polimerne mreže. Stabilnost opaženih direktorskih struktur v primeru pravilne polimerne mreže bo prikazana v preprostem faznem diagramu. Na koncu bo preučena še možnost paranematskega urejanja nad temperaturo prehoda v izotropno fazo. Rezultati simulacij bodo predstavljeni tudi v obliki izbranih eksperimentalnih opazljivk: spektrov ^{2}H NMR, kapacitivnosti in intenzitete skozi vzorec prepuščene svetlobe.

V zaključku bodo predstavljeni glavni dosežki, ki so bili predstavljeni v tem delu, pa tudi še odprta vprašanja in možne usmeritve za prihodnost.

Teoretično ozadje

Fenomenološki opis nematske ureditve

Fenomenološki Landau-de Gennesov opis nematika temelji na uvedbi simetrijskim lastnostim nematika primernega parametra urejenosti, ki ga uporabimo za zapis proste energije sistema. Ravnovesno stanje nato najdemo z iskanjem njenega minimuma.

Orientacijsko urejanje dolgega dosega v enoosnem nematiku opišemo s *tenzorskim parametrom urejenosti* (zaradi enakovrednosti $\pm\mathbf{n}$ vektorski ne bi bil primeren)

$$\mathsf{Q} = \tfrac{1}{2}S\left[3\,\mathbf{n}\otimes\mathbf{n} - \mathsf{I}\right], \tag{1}$$

kjer I pomeni idenititeto [4]. Vpeljali smo $S = \langle\frac{1}{2}(3\cos^2\theta - 1)\rangle$, *skalarni parameter urejenosti*, kjer je $\cos\theta = \mathbf{n}\cdot\mathbf{u}$, enotski vektor $\mathbf{u}$ določa trenutno orientacijo dolge osi posamezne molekule in $\langle ... \rangle$ pomeni ansambelsko povprečje čez več molekul. V primeru idealne nematske ureditve imamo $S = 1$, v neurejeni izotropni fazi pa $S = 0$. Enakovreden opis daje tudi *ureditvena matrika*

$$\underline{Q} = \tfrac{1}{2}\left[3\langle\mathbf{u}\otimes\mathbf{u}\rangle - \mathsf{I}\right]. \tag{2}$$

V njeni lastni vrednosti z največjo absolutno vrednostjo prepoznamo S, v pripadajočem lastnem vektorju pa direktor $\mathbf{n}$. Iz razlike preostalih lastnih vrednosti je mogoče sklepati na stopnjo dvoosnosti orientacijske porazdelitve molekul, P.

Ureditev, ki jo opisuje Q, se odraža tudi na makroskopskih opazljivkah. Tako lahko tenzor magnetne susceptibilnosti $\underline{\chi}$ v enoosnem primeru zapišemo v obliki $\underline{\chi} = \frac{2}{3}\chi_a \mathsf{Q} + \chi_i \mathsf{I}$, kjer pomeni χ_a največjo anizotropijo susceptibilnosti v idealno urejenem nematiku, χ_i pa njeno vrednost v izotropni fazi.

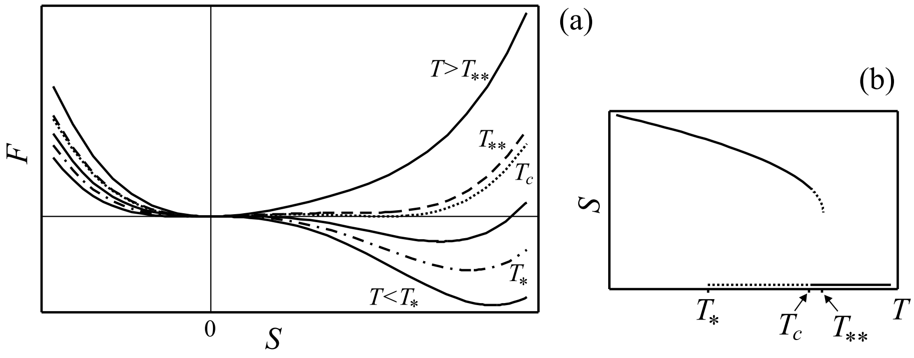

Slika 2 Prehod med nematsko in izotropno fazo: (a) prosta energija F kot funkcija parametra urejenosti S in (b) ravnovesna vrednost S pri različnih temperaturah.

Nezvezni fazni prehod med izotropno ($S = 0$) in nematsko ($S \neq 0$) fazo v okviru Landauove teorije v bližini faznega prehoda opišemo z analitičnim razvojem gostote proste energije f_0 po tistih invariantah parametra urejenosti Q, ki so v soglasju s simetrijo manj urejene faze [32]

$$f_0(S,T) = f_i(T) + \tfrac{1}{2}a(T - T_*)S^2 - \tfrac{1}{3}BS^3 + \tfrac{1}{4}CS^4. \tag{3}$$

Tukaj predstavljajo $a > 0$, $B > 0$ ter $C > 0$ fenomenološke snovne parametre, $f_i(T)$ gostoto proste energije izotropne faze in T_* najnižjo možno temperaturo njene podhladitve. Potek proste energije $F = \int f_0(S,T)dV$ je prikazan na sliki 2, prav tako pa tudi temperaturna odvisnost ravnovesnega parametra urejenosti, ki jo dobimo pri minimizaciji F: $S(T) = \frac{B}{2C}[1 + \sqrt{1 - \frac{4aC}{B^2}(T - T_*)}]$ pri $T < T_c$ (nematska faza) in $S(T) = 0$ pri $T > T_c$ (izotropna faza). Temperaturo faznega prehoda T_c in najnižjo temperaturo podhladitve izotropne faze T_* povezuje zveza $T_c = T_* + 2B^2/9aC$. Možna so tudi metastabilna stanja s pregretim nematikom, vendar le v ozkem območju pod $T_{**} = T_* + B^2/4aC$. Ponavadi velja $T_c - T_* \sim 1$ K in $T_{**} - T_c \sim 0.1$ K. Ker je prehod šibko nezvezen, ga pri T_c spremlja gostota utajene toplote $\mathcal{Q} = \frac{1}{2}aT_cS(T_c)^2$, ki je ponavadi velikostnega reda 10^6 J/m^3.

Kadarkoli se lotimo obravnave ograjenih sistemov, lahko postane stopnja ureditve S krajevno odvisna. V takem *nehomogenem* primeru je potrebno gostoti proste energije (3) dodati člen oblike $\frac{3}{4}L(\nabla S)^2$ (tudi L je snovna konstanta) in variacijsko najti ravnovesni profil $S = S(\mathbf{r})$. Značilno dolžino sprememb S — *korelacijsko dolžino* — določa zveza

$$\xi = \sqrt{\frac{3L}{2a(T - T_*) - 4BS_b + 6CS_b^2}}, \tag{4}$$

kjer pomeni S_b ravnovesno vrednost ureditvenega parametra v velikem homogenem vzorcu, ki jo določimo z minimizacijo izraza (3). Dolžina ξ narašča, ko se približujemo faznemu prehodu, a tam ne divergira: $\xi(T_c) \approx 10$ nm.

V ograjenem sistemu je ponavadi poleg stopnje ureditve $S(\mathbf{r})$ tudi povprečna smer ureditve — direktor $\mathbf{n}(\mathbf{r})$ — od kraja odvisna. V tem primeru je prikladno gostoto proste energije izraziti z od kraja odvisnim tenzorskim parametrom urejenosti $\mathsf{Q}(\mathbf{r})$ (1)

$$\begin{aligned} f(\mathbf{r}) = f_i(T) &+ \tfrac{1}{3}a(T-T_*)\mathrm{tr}\mathsf{Q}^2 - \tfrac{4}{9}B\mathrm{tr}\mathsf{Q}^3 + \tfrac{1}{9}C(\mathrm{tr}\mathsf{Q}^2)^2 + \\ &+ \tfrac{1}{2}L_1\,\mathsf{Q}_{ij,k}\mathsf{Q}_{ij,k} + \tfrac{1}{2}L_2\,\mathsf{Q}_{ij,j}\mathsf{Q}_{ik,k} + \tfrac{1}{2}L_3\,\mathsf{Q}_{ij,k}\mathsf{Q}_{ik,j}, \end{aligned} \tag{5}$$

kjer smo vpeljali krajevne odvode $\mathsf{Q}_{ij,k} = \partial\mathsf{Q}_{ij}/\partial x_k$ [4,107], L_1, L_2 in L_3 pa so elastični snovni parametri. V primeru, ko $S \neq S(\mathbf{r}) = S_b$, lahko prepišemo nehomogeni del izraza (5) v obliki

$$\begin{aligned} f_F(\mathbf{r}) = \tfrac{1}{2}\Big\{K_{11}\,[\nabla\cdot\mathbf{n}]^2 + K_{22}\,[\mathbf{n}\cdot(\nabla\times\mathbf{n})]^2 + K_{33}\,[\mathbf{n}\times(\nabla\times\mathbf{n})]^2\Big\} \\ -K_{24}\,\nabla\cdot[\mathbf{n}\,(\nabla\cdot\mathbf{n}) + \mathbf{n}\times(\nabla\times\mathbf{n})], \end{aligned} \tag{6}$$

imenovan tudi *Frankova* gostota proste energije [18], s tremi elastičnimi konstantami, ki predstavljajo različne deformacijske načine: K_{11} *pahljačno*, K_{22} *zvojno* in K_{33} *upogibno* deformacijo (slika 3). Zadnji, divergenčni člen pripada *sedlasto-pahljačni deformaciji.* Pridemo lahko do naslednjih zvez: $K_{11} = K_{33} = \frac{9}{4}S_b^2(2L_1 + L_2 + L_3)$, $K_{22} = \frac{9}{2}S_b^2 L_1$ in $K_{24} = \frac{9}{4}S_b^2(2L_1 + L_3)$. V primeru, ko je $L_2 + L_3 = 0$, velja $K_{11} = K_{22} = K_{33} = K$, čemur pravimo *približek z eno konstanto.* Ponavadi velja $K \sim 5 \times 10^{-12}$ N, kar je mogoče izmeriti na primer s preučevanjem elastičnih deformacij v zunanjem polju [108,109]. Velja tudi $K_{24} \sim K$ [110].

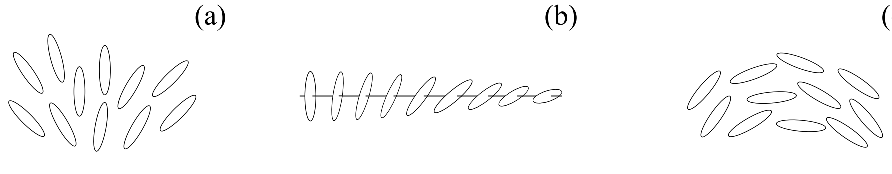

Slika 3 Frankovi načini elastične deformacije: pahljača (a), zvoj (b) in upogib (c).

Divergenčnemu členu s K_{24}, ki pri iskanju ravnovesnega direktorskega profila vpliva le na robne pogoje, je podoben tudi *pahljačno-upogibni* prispevek oblike $K_{13}\nabla\cdot[\mathbf{n}\,(\nabla\cdot\mathbf{n})]$ [52,53]. Od člena s K_{24} se razlikuje po tem, da vsebuje tudi druge odvode $\mathbf{n}$ in kot tak povroča težave pri matematični formulaciji variacijskega problema. Tudi po njihovi odpravi napoveduje (pre)močne elastične deformacije ob površini [55–58], vendar novejše analize kažejo, da je vprašanje pravzaprav brezpredmetno in da za idealno ravno površino velja $K_{13} = 0$ [62,65,111]. Zaradi navedenih nejasnosti se bomo v nadaljevanju členu s konstanto K_{13} izognili.

V okviru fenomenološkega opisa interakcije nematika z ograjujočo trdno površino — imenovane tudi *zunanje sidranje* — površina vsiljuje določeno smer ($\mathbf{n}_0$) in stopnjo ureditve (S_0). Oboje lahko zajamemo v tenzorskem parametru Q_0, površinsko gostoto interakcijske proste energije pa modeliramo z [22]

$$f_a = \tfrac{1}{2} W_e \mathrm{tr}(\mathsf{Q}_s - \mathsf{Q}_0)^2, \tag{7}$$

kjer Q_s opisuje dejansko ureditev ob površini ($\mathbf{n}_s$ in S_s). Kadar vzamemo $S = \mathit{konst.}$, se zgornji izraz poenostavi v *Rapini-Papoularjevo* formulo $f_s^{RP} = -\tfrac{1}{2} W \cos^2\alpha$ [21], ki pogosto predstavlja dovolj dober približek. V njej α pomeni kot odstopanja $\mathbf{n}_s$ od predpisane smeri $\mathbf{n}_0$ ($\cos\alpha = \mathbf{n}_s \cdot \mathbf{n}_0$), energija $W = \tfrac{9}{2} W_e S_b^2$ pa *jakost sidranja*. Značilne vrednosti zanjo so od 10^{-6} J/m^2 do 10^{-4} J/m^2 [6]. Bolj nazorna je izražava s Kléman-de Gennesovo *ekstrapolacijsko dolžino* K/W (slika 4) [4], ki pri navedenih vrednostih K in W niha med 50 nm and 5 μm. Jakost sidranja merijo na mnogo načinov: s povzročitvijo elastične deformacije z zunanjim poljem [6], z analizo direktorskih struktur v kapljicah in porah [112,113], ali pa s študijem fluktuacij direktorja v ograjenih sistemih [45,46].

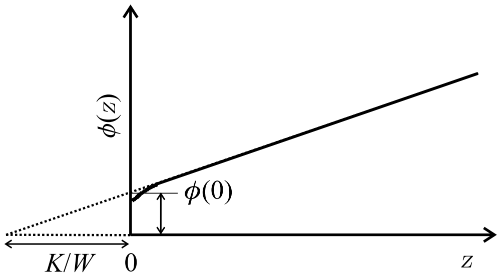

Slika 4 Direktorski profil $\phi(z)$ v deformirani plasti nematika in definicija ekstrapolacijske dolžine K/W [4]. Ograjujoča površina se nahaja pri $z = 0$.

Če nematik izpostavimo zunanjemu polju (na primer magnetnemu jakosti $\mathbf{H}$), to nanj deluje z navorom, do česar pride zaradi anizotropije tenzorja magnetne susceptibilnosti $\underline{\chi}$ (ali dielektrične konstante $\underline{\epsilon}$ v električnem primeru). Pripadajoči prispevek k prosti energiji je

$$f_m = -\tfrac{1}{2} \mu_0 \chi_a S H^2 \cos^2\beta, \tag{8}$$

kjer β pomeni kot med $\mathbf{n}$ in $\mathbf{H}$ ($\cos\beta = \mathbf{n} \cdot \mathbf{H}/H$), χ_a anizotropijo molekulske susceptibilnosti, μ_0 pa indukcijsko konstanto (analogen izraz je moč zapisati tudi za urejanje v električnem polju). V primeru, ko je $\chi_a > 0$, se molekule nematika uredijo v smeri zunanjega polja, ki ga na ta način lahko izkoristimo za krmiljenje povprečne smeri molekul v vzorcu. Ta pojav za svoje delovanje izkorišča velik del tekočekristalnih optičnih naprav.

V ograjenem nematiku neizbežno pride do nesoglasij med ureditvenimi težnjami zunanjega polja in ograjujočih sten. Pričakovati je, da se bodo molekule nematika dovolj daleč od sten usmerile vzdolž smeri polja, blizu sten pa bo nematik zaradi površinskega sidranja deformiran (slika 5). Debelino te deformirane plasti v grobem določa *koherenčna dolžina*, ki jo v primeru magnetnega polja zapišemo takole:

$$\xi_m = \sqrt{\frac{K}{\mu_0 \chi_a S H^2}}. \tag{9}$$

Če imamo potemtakem opravka z ograjenimi sistemi, katerih značilna dimenzija je manjša od ξ_m, zunanje polje na ureditev sploh ne bo vplivalo. Za značilen tekoči kristal v magnetnem polju gostote 1 T znaša $\xi_m \sim 10$ μm. Če zvišamo jakost zunanjega polja tako daleč, da začne veljati $\xi_m < K/W$, se zunanje sidranje ne more več upirati premočnemu zunanjemu polju in dopusti, da se molekule nematika obrnejo v smer polja tudi tik ob steni. Pri tem gre za zvezni strukturni prehod, ki ga imenujemo tudi *saturacijski prehod* (slika 5) [6].

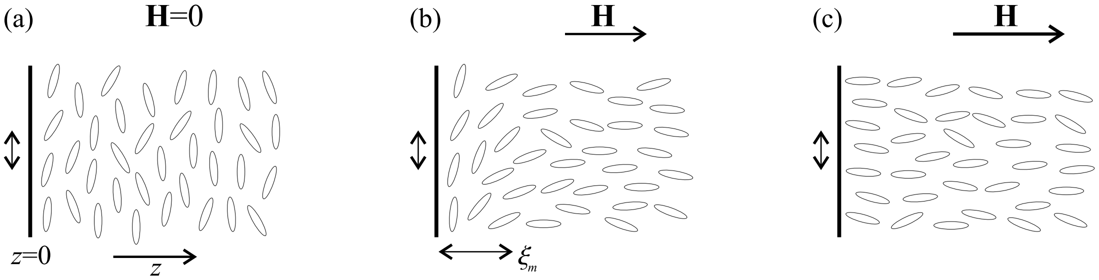

Slika 5 Polneskončni vzorec nematika s planarnim sidranjem v zunanjem polju **H**, usmerjenem pravokotno na steno vzorca: nedeformirana (a), deformirana (b) in zasičena struktura (c).

Nekoliko drugače se obnaša celica debeline d, v kateri je nematik med dvema vzporednima ploščama s planarnim sidranjem in je zunanje polje — kot prej — usmerjeno pravokotno nanju. Za razliko od polneskončnega vzorca dobimo elastično deformiran direktorski profil šele nad določeno vrednostjo poljske jakosti, pod njo pa ureditev določa planarno zunanje sidranje. V primeru neskončno močnega sidranja se ta zvezni prehod — imenovan *Fréederickszov* [108,109] — dogodi, ko $\xi_m = d/\pi$ [4], medtem ko pri šibkem sidranju in $K/W \ll d$ do njega pride že v nekoliko šibkejšem zunanjem polju, ko $\xi_m = (d/\pi)(1 + 2K/Wd)$ [6]. Pri nadaljnjem višanju jakosti polja lahko spet pričakujemo saturacijski prehod. Oba prehoda sta bila podrobno preučevana v preteklosti [115]. Omenimo še to, da omogoča opazovanje Fréederickszovega prehoda meritev elastičnih konstant [116] in jakosti sidranja [6]. Poleg tega lahko dovolj močno zunanje polje vpliva na stopnjo ureditve S in celo premakne prehod med nematsko in izotropno fazo [117,118].

Kadar imamo opravka z makroskopskim vzorcem, izjemno redko naletimo na homogen direktorski profil, ampak na kopico domen, od katerih ima vsaka svojo usmeritev. Na mejah med njimi lahko opazimo topološke defekte, ki jih spremljajo elastične deformacije, zmanjšanje stopnje urejanja S, pa tudi nezanemarljiva dvoosnost. Na defekte naletimo tudi v primerno ograjenih sistemih.

Nekaj primerov defektov je prikazanih na sliki 6. Razlikujejo se po *moči* m, ki jo v dvodimenzijskih primerih (defektne linije) določimo tako, da jedro defekta obkrožimo po zaprti zanki, pri tem pa štejemo obrate direktorja $\mathbf{n}$. Izkaže se, da je prosta energija, ki jo pripišemo defektu moči m, v grobem sorazmerna m^2, kar pomeni, da je tvorba defektov visoke moči malo verjetna [24]. Podobno lahko defekti določene moči razpadejo na več defektov, in sicer tako, da se vsota moči ohrani (defekt moči -1 na primer v par defektov moči $-\frac{1}{2}$). Mogoče je pokazati tudi to, da

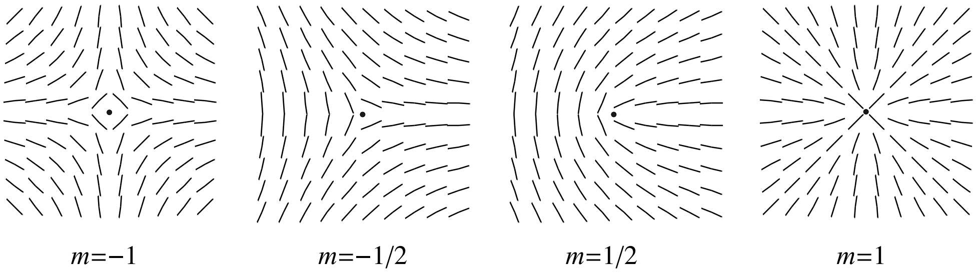

Slika 6 Direktorska polja, ki obdajajo topološke defekte različnih moči m.

se defekti z močmi istega predznaka odbijajo, tisti različnimi pa privlačijo (in celo anihilirajo).

Molekulske simulacije in mrežni modeli

V primerih, ko se v sistemu pojavijo nehomogenosti na razdaljah, ki so primerljive z velikostjo molekul, parametri urejenosti — ti vsebujejo ansambelsko povprečje $\langle ... \rangle$ — več niso dobro definirani. Isto velja v bližini faznih prehodov zaradi nezanemarljivih fluktuacij. Takrat je primerno uporabiti mikroskopske pristope, temelječe na parskih interakcijah med molekulami. Primerni so vedno tudi tedaj, kadar želimo povezati mikroskopske parametre sistema z makroskopskimi opazljivkami.

Na molekulski ravni sta dve skupini interakcij sposobni privesti do tvorbe nematske faze: odbojne sile med podolgovatimi trdimi delci (po Onsagerju) [119] in anizotropne van der Waalsove sile (po Maierju in Saupeju) [120,121]. Narava obojih je takšna, da vzpodbuja vzporedno urejanje dolgih osi molekul, kar posnema tudi preprost mrežni model Lebwohla in Lasherja [93,122]. Prednost mrežnih modelov je zlasti v tem, da pri simulacijah ne zahtevajo previsoke računske moči.

V okviru modela Lebwohla in Lasherja (LL) so enoosni delci (molekule) nematika vrtljivo vpeti na mrežne točke kubične mreže z mrežno konstanto a (slika 7), pri čemer orientacijo $i$tega delca določa tridimenzijski enotski vektor $\mathbf{u}_i$. Delce si je moč predstavljati tudi kot tesno zložene skupke do 10^2 molekul [94,100] (tedaj $a \lesssim$ 5 nm). Kljub mrežni poenostavitvi model dovolj dobro opiše orientacijsko urejanje nematika. Energijo interakcije med sosednjima delcema i in j modeliramo z

$$U_{ij} = -\epsilon \left[\tfrac{3}{2} (\mathbf{u}_i \cdot \mathbf{u}_j)^2 - \tfrac{1}{2} \right] , \tag{10}$$

kjer je ϵ pozitivna konstanta velikostnega reda $\sim$0.02 eV. Pri obravnavi velikih sistemov je potrebno uporabiti periodične robne pogoje [93,122,123] ali njihove izboljšave [124]. Po drugi strani, če želimo simulirati ograjene sisteme, ponavadi izrabimo del nematskih delcev (delce "duhove"), da preko njihovih zamrznjenih orientacij predpišemo robne pogoje — sidranje [91,125]. Konstanta ϵ za interakcije med delci "duhovi" in delci nematika ni nujno enaka tisti za interakcije med delci nematika samimi. Na ta način lahko spreminjamo jakost zunanjega sidranja. Simulacije Monte Carlo so pokazale, da LL model zadovoljivo opiše šibko nezvezen fazni prehod med nematsko in izotropno fazo (v velikem vzorcu pri $T^* = k_B T/\epsilon =$ 1.1232) [93,123], ki je manj izrazit v močno ograjenih vzorcih, na primer nematskih

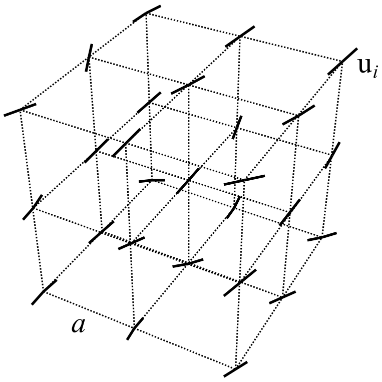

Slika 7 Mrežni model Lebwohla in Lasherja: nematski delci $\mathbf{u}_i$ so pripeti na kubično mrežo.

kapljicah [126,127]. Predstavljena je bila tudi različica modela z dvoosnim potencialom [128]. V model je preprosto vključiti tudi sklopitev delcev $\mathbf{u}_i$ z zunanjim poljem (električnim ali magnetnim)

$$U_i^f = -\epsilon\eta\left[\tfrac{3}{2}(\mathbf{u}_i\cdot\mathbf{f})^2 - \tfrac{1}{2}\right], \tag{11}$$

kjer $\mathbf{f}$ pomeni enotski vektor v smeri zunanjega polja, $\eta = \chi_a V_0 B^2/3\mu_0\epsilon$ pa je konstanta, ki meri moč sklopitve (izpisana za primer magnetnega polja). Tukaj pomeni $B \approx \mu_0 H$ gostoto magnetnega polja, χ_a mikroskopsko anizotropijo magnetne susceptibilnosti in V_0 prostornino, ki jo pripišemo delcu $\mathbf{u}_i$ [99] (podobno storimo v električnem primeru). Poljska jakost je sorazmerna $\sqrt{\eta}$.

Teorija Maierja in Saupeja [120,121] sloni na anizotropnih van der Waalsovih silah in približku povprečnega polja, ki je gotovo upravičen globoko v vzorcu in vodi do vzporednega urejanja delcev (kot tudi model LL). Ob površini vzorca pa tak približek več ni popolnoma neoporečen in lahko pride tudi do bolj zapletenih vzorcev urejanja. V primeru, ko je električna polarizirnost molekul nematika močno anizotropna, lahko energijo interakcije med najbližjima sosedoma $\mathbf{u}_i$ in $\mathbf{u}_j$ zapišemo kot

$$U_{ij} = -\epsilon'\left[\mathbf{u}_i\cdot\mathbf{u}_j - 3\nu(\mathbf{u}_i\cdot\mathbf{r}^*)(\mathbf{u}_j\cdot\mathbf{r}^*)\right]^2, \tag{12}$$

kjer je $\epsilon' > 0$, $\mathbf{r}^*$ pa predstavlja enotski vektor, ki povezuje oba delca. Parameter ν nadzira prostorsko anizotropijo interakcije: za $\nu = 0$ dobimo izotropno interakcijo, ki je neodvisna od $\mathbf{r}^*$ (kot v modelu LL), za $\nu = 1$ pa anizotropno interakcijo med *induciranimi dipoli.* Če je interakcija anizotropna ($\nu \neq 0$), se na površini vzorca pojavijo ureditveni učinki ali *notranje sidranje* [17,81]. Poleg tega za $\nu = 0$ model ustreza približku z eno elastično konstanto, sicer pa ne [129].

Uporaba prostorsko anizotropnih potencialov skupaj s kubično mrežo privede do pojava preferenčnih smeri urejanja tudi globoko v vzorcu, zaradi česar postane model neuporaben za študij sicer tekočinskih nematikov [81]. Izkaže pa se, da šestkotniška mreža (slika 8) te hibe nima, če orientacije delcev $\mathbf{u}_i$ omejimo na ravnino šestkotnikov [17]. Namesto šestih imamo zdaj osem sosedov, enotski vektorji $\mathbf{u}_i$ pa so le dvodimenzijski. Da se v celoti izognemo obstoju periodičnih rešitev, ki so posledica mrežnega približka in anizotropnega potenciala (12), je potrebno zahtevati še

$\nu \lesssim 0.3$ [17]. Ker imamo s tem $\nu \neq 0$, je notranje sidranje ob površini še vedno prisotno, sicer pa se delci najraje urejajo tako, da so njihove dolge osi vzporedne (slednje srečamo tudi v sistemih Gay-Berneovih delcev [130]).

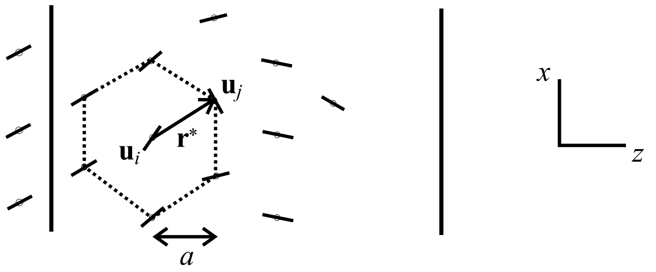

Slika 8 Model s šestkotniško mrežo.

Mrežni modeli so značilni primeri, v katerih je primerno uporabiti simulacije vrste Monte Carlo (MC) za iskanje ravnovesja v sistemu in za izračun termodinamičnih povprečij. Dinamika metode Monte Carlo ne temelji na reševanju enačb gibanja, ampak na Metropolisovem postopku, ki si ga bomo ogledali v nadaljevanju. Naravne dinamike v mrežnih sistemih pravzaprav sploh nima smisla simulirati, saj jim že po definiciji manjka del sicer naravnih prostostnih stopenj.

Termodinamično povprečje spremenljivke $\mathcal{A}$ v sistemu N delcev je definirano z

$$\langle \mathcal{A} \rangle = \frac{\int d\mathbf{u}^N \mathcal{A}(\mathbf{u}^N)\ e^{-\beta \mathcal{H}(\mathbf{u}^N)}}{\int d\mathbf{u}^N\ e^{-\beta \mathcal{H}(\mathbf{u}^N)}} \tag{13}$$

kjer je $\beta^{-1} = k_B T$ (k_B Boltzmannova konstanta, T absolutna temparatura), $\mathbf{u}^N$ pa dolg vektor, ki določa orientacije $\mathbf{u}_i$ vseh N delcev in tako opisuje stanje N-delčnega sistema v faznem prostoru. Poleg tega predstavlja $\mathcal{H}$ hamiltonko sistema, ki je sestavljena iz vsote vseh interakcijskih energij med pari sosedov, pa tudi iz prispevkov njihove sklopitve z zunanjim poljem. Metoda Monte Carlo omogoča izračun ansambelskega povprečja $\langle \mathcal{A} \rangle$, ki je v ergodičnih sistemih enakovredno časovnemu povprečju $\bar{\mathcal{A}}$, dobljenemu iz simulacij molekularne dinamike, kjer sistemu sledimo v času.

Pri metodi Monte Carlo gre za primerno utežen naključni sprehod po faznem prostoru, pri katerem v vsakem koraku vzorčimo količino $\mathcal{A}$. Naključni sprehod sledi *Metropolisovemu postopku* [37], ki ga lahko strnemo v naslednje predpise:

1. Vzemi staro konfiguracijo $\mathbf{u}^N$ (s); izračunaj njeno energijo $\mathcal{H}(\mathbf{u}^N) = \mathcal{H}(s)$.
2. Naključno izberi enega od delcev iz stare konfiguracije s; zasuči ga naključno, da dobiš novo poskusno konfiguracijo $\mathbf{u}'^N$ (n); izračunaj energijo nove konfiguracije $\mathcal{H}(\mathbf{u}'^N) = \mathcal{H}(n)$.
3. Sprejmi premik $\mathbf{u}^N \to \mathbf{u}'^N$ $(s \to n)$ z verjetnostjo $\min\left[1, e^{-\beta[\mathcal{H}(n)-\mathcal{H}(s)]}\right]$.
4. Vrni se k 2. koraku tega postopka.

Mogoče je pokazati, da privede zgornji postopek do kanonične porazdelitve z dobro določeno temperaturo, ki smo jo predpostavili pri definiciji povprečja $\langle \mathcal{A} \rangle$ (13).

Zanesljivost ocene za povprečje $\langle\mathcal{A}\rangle$ je tem večja, čim več delcev sodeluje v simulaciji in čim dlje je simulacija tekla. Če velja $\mathcal{A} \propto N$, se relativna napaka povprečja manjša kot $1/\sqrt{NM}$, kjer M označuje število korakov simulacije.

Naslednje vprašanje zadeva tvorbo poskusnih konfiguracij $\mathbf{u}'^N$. V modelu LL ponavadi uporabljamo tehniko Barkerja in Wattsa [131]: najprej naključno izberemo eno izmed treh kartezičnih osi laboratorijskega koordinatnega sistema in nato okoli nje zavrtimo naključno izbrano molekulo za naključno izbran kot. Največji možni kot zasuka (amplitudo) lahko med simulacijo spreminjamo. Če so namreč zasuki preveliki, je možno, da nova konfiguracija sploh ne bo sprejeta. Če pa so, po drugi strani, zasuki premajhni, Metropolisov postopek obišče premajhen del faznega prostora, da bi ocena za $\langle\mathcal{A}\rangle$ bila količkaj dobra. Ponavadi se amplitudo zasuka prilagaja dinamično, in sicer tako, da je vselej sprejeta okoli polovica vseh nameravanih zasukov. V primeru modela s šestkotniško mrežo, kjer so vektorji $\mathbf{u}_i$ le dvodimenzijski, se zgornji postopek poenostavi v preprosto vrtenje znotraj ravnin šestkotnikov. Včasih je pomembna tudi izbira začetne konfiguracije. V ergodičnih sistemih bi morali rezultati simulacije načeloma biti od nje neodvisni, vendar je treba biti previden zlasti v bližini metastabilnih stanj, še posebej, če simulacija ni tekla dovolj dolgo.

Na koncu je treba določiti še količino $\mathcal{A}$, ki jo želimo povprečiti. To so lahko komponente ureditvene matrike $\underline{Q}$, ureditveni parametri $P_2^v = \frac{1}{2}\langle 3(\mathbf{v}\cdot\mathbf{u}_i)^2 - 1\rangle_i$, kjer predstavlja $\mathbf{v}$ neko fiksno smer, ali pa orientacijske korelacijske funkcije. Še bolj zanimive so eksperimentalne opazljivke, na primer spektri ^{2}H NMR, električna kapacitivnost ali intenziteta prepuščene svetlobe. Tem se bomo posvetili v nadaljevanju.

Eksperimentalne opazljivke

Prva izmed obravnavanih opazljivk bodo spektri devterijeve jedrske magnetne resonance (^{2}H NMR). Ta tehnika je primerna zlasti za raziskave devteriranih nematikov v mikroskopskih votlinah razsežnosti pod 1 μm, ko optične metode odpovedo. ^{2}H NMR daje informacije o orientacijskem urejanju v vzorcu, pa tudi o dinamiki molekul — fluktuacijah dolgih osi in translacijski difuziji [25,40,132,133].

V izotropni fazi v spektru devteriranega nematika vidimo eno samo črto pri Zeemanovi frekvenci ω_Z. Ko vzorec ohladimo v nematsko fazo, se pojavi kvadrupolni razcep ω_Q, zaradi česar vidimo v spektru dve črti. Razcep ω_Q znaša v primeru enoosne ureditve [5,134,135])

$$\omega_Q = \pm\delta\omega_Q\,\tfrac{1}{2}S\,[3\cos^2\theta - 1] \tag{14}$$

ter je odvisen od kota θ med zunanjim magnetnim poljem NMR spektrometra in direktorjem $\mathbf{n}$, pa tudi od stopnje ureditve S. Značilna velikost razcepa je $\delta\omega_Q \sim 2\pi \times 40$ kHz. V ograjenem sistemu sta $\mathbf{n}$ in S od kraja odvisna, posledično pa tudi $\omega_Q = \omega_Q(\mathbf{r})$. Na ta način je mogoče iz spektrov razbrati, za katero izmed možnih direktorskih struktur v vzorcu gre. Razpoznavanje postane težavno zlasti v drobnih votlinah, ko translacijska difuzija obliko spektralnih črt zaznavno popači [136].

Za pravilno obravnavo molekulskih gibanj z značilno časovno skalo krajšo od značilne skale spektroskopije NMR ($t_0 \approx 2\pi/\delta\omega_Q \sim 2.5 \times 10^{-5}$ s) je potrebno uporabiti polklasični pristop s časovno odvisno hamiltonko devterijevih spinov [135]. V okviru tega pristopa je najprej potrebno generirati relaksacijsko funkcijo

$$G(t) = \exp(i\omega_Z t)\Big\langle \exp\,(i\int_0^t \Omega_Q[\mathbf{r}_i(t'),t']\,dt')\Big\rangle_i, \qquad (15)$$

kjer je $\Omega_Q[\mathbf{r}_i(t),t] = \pm\delta\omega_Q\,\frac{1}{2}\,[3(\mathbf{u}_i\cdot\mathbf{B}/B)^2 - 1]$ "trenutni" kvadrupolni razcep (povprečje po fluktuacijah $\mathbf{u}_i$ tu še ni opravljeno), oklepaji $\langle ... \rangle_i$ pa pomenijo ansambelsko povprečje po delcih. Gibanje molekul (fluktuacije ali difuzija) vstopa v $G(t)$ skozi časovno odvisne $\mathbf{u}_i$. Spekter $I(\omega)$ izračunamo potem s Fourierovo transformacijo $I(\omega) = \int e^{i\omega t}\,G(t)\,dt$. Značilna časovna skala fluktuacij molekulskih dolgih osi je okrog $t_F \sim 10^{-8}$ s in je kot taka znatno krajša od t_0 [41]. Tudi značilni čas, ki je potreben za difuzijski premik molekule približno za svojo dolžino (1 nm), je v tem območju: $t_D \sim 10^{-8}$ s [41]. Vsekakor pa je pri difuzijskem procesu bolj merodajen čas t'_D, ki ga molekula potrebuje za premik v področje z znatno drugačnim ω_Q. Spektri so tako vedno izpovprečeni preko fluktuacij dolgih osi $\mathbf{u}_i$, preko difuzijskega gibanja pa le v primeru močne ograditve.

Naslednja izmed eksperimentalnih metod za študij urejanja nematikov je meritev električne kapacitivnosti [39]. Temelji na dejstvu, da je dielektrična konstanta $\underline{\epsilon}$ v nematikih anizotropna. Zamislimo si plast nematika v ploščatem kondenzatorju, čigar normalo označimo za os z (xy potem predstavlja ravnino plošč). V poenostavljeni sliki si plast zamislimo razdrobljeno na množico drobnih kondenzatorjev, katerih kapacitivnosti so sorazmerne z lokalno dielektrično konstanto. Ta je na mestu $i$tega delca z orientacijo $\mathbf{u}_i$ enaka $\epsilon(x,y,z) = \epsilon_\perp + (\epsilon_{||} - \epsilon_\perp)(\mathbf{u}_i \cdot \mathbf{z})^2$, kjer pomeni $\mathbf{z}$ enotski vektor v smeri osi z, $\epsilon_\perp$ in $\epsilon_{||}$ pa lastni vrednosti molekulskega dielektričnega tenzorja. Kondenzatorje si zdaj predstavljamo vezane zaporedno vzdolž osi z, tako nastale verige pa vzporedno po vsej ravnini xy. Celotno kapacitivnost plasti velikosti $a \times b \times d$ potem izračunamo iz zveze

$$C = \epsilon_0 \int_0^a dx \int_0^b dy \left(\int_0^d \frac{dz}{\epsilon(x,y,z)}\right)^{-1}, \qquad (16)$$

kjer pomeni ϵ_0 influenčno konstanto. Kapacitivnost potemtakem predstavlja nazorno merilo za orientacijo molekul nematika in je kot taka uporabna tudi za opazovanje pojava preklapljanja v zunanjem polju [39].

Tretjo in zgodovinsko najstarejšo skupino metod za raziskave nematikov predstavljajo optične metode [1,2]. Podobno kot statična dielektrična konstanta $\underline{\epsilon}$ je tudi visokofrevenčna $\underline{\epsilon}^\infty$ v nematikih anizotropna, z njo pa tudi lomni količnik. Nematiki so optično anizotropna enoosna sredstva, v katerih lokalna smer *optične osi* sovpada z lokalnim direktorjem $\mathbf{n}$. Pri razširjanju elektromagnetnega valovanja skozi nematik imamo tako dva žarka z različnima polarizacijama in hitrostjo razširjanja (lomnim količnikom): *rednega* in *izrednega*. Polarizacija prvega je hkrati pravokotna na optično os in na smer razširjanja valovanja $\mathbf{k}$, lomni količnik pa je enak $n_o = \sqrt{\epsilon_\perp^\infty}$. Polarizacija drugega je pravokotna na $\mathbf{k}$, hkrati pa leži v ravnini, ki jo določata $\mathbf{k}$ in optična os. Ustrezni lomni količnik n_e je odvisen od kota θ med $\mathbf{k}$ in optično osjo, pri čemer velja [137]

$$\frac{1}{n_e^2} = \frac{\cos^2\theta}{\epsilon_\perp^\infty} + \frac{\sin^2\theta}{\epsilon_{||}^\infty}. \tag{17}$$

Povsod v zgornjih izrazih označujeta $\epsilon_\perp^\infty$ in $\epsilon_{||}^\infty$ lastni vrednosti matrike $\underline{\epsilon}^\infty$.

Pri preučevanju razširjanja polarizirane svetlobe skozi nehomogen optično anizotropen nematik si lahko pomagamo s formalizmom Jonesovih vektorjev. Zamislimo si enako geometrijo kot pri meritvah kapacitivnosti, svetlobni žarek pa naj se razširja v smeri osi z. Vzorec najprej razdelimo na majhna območja z dobro določeno lokalno optično osjo — ta naj sovpada kar z orientacijo posameznega delca $\mathbf{u}_i$. Nato razcepimo vpadno polarizacijo na redno in izredno komponento, ki se potem vsaka zase razširjata skozi plast, in ta postopek ponavljamo, dokler ne pridemo skozi ves vzorec. Pri tem zanemarimo lom, uklon in sipanje. Na drugi strani vzorca lahko merimo intenziteto svetlobe, prepuščene skozi analizator, ki ga postavimo pravokotno na smer polarizacije vhodne svetlobe. V primeru, da je kot med optično osjo celotnega vzorca in vhodnega polarizatorja enak φ_0, imamo za intenziteto [138]

$$I = I_0 \sin^2(2\varphi_0)\sin^2(\Delta\Phi/2), \tag{18}$$

kjer je I_0 intenziteta vhodne svetlobe, $\Delta\Phi = (2\pi/\lambda)\int_0^d [n_e(z) - n_o]dz$ pa razlika v fazi med rednim in izrednim žarkom po potovanju skozi vzorec (λ pomeni valovno dolžino svetlobe). Očitno je, da bo I največja za $\varphi_0 = \pi/4$. Takšna eksperimentalna postavitev je bila uporabljena za meritev elastičnih konstant [116], jakosti sidranja [6] in za opazovanje paranematskega urejanja [26].

Do tod smo si ogledali glavna orodja in pristope, potrebne za izpolnitev zadanih si ciljev: preučitve urejanja molekul v bližini površine tanke plasti nematika in nematskega urejanja v zapletenejših ograditvah — kapljicah in sistemih polimernih mrež. V poglavjih, ki sledijo, bodo predstavljeni najpomembnejši rezultati omenjenih študij.

Plast nematika

Fenomenološki opis tanke plasti

V tem poglavju se bomo lotili obravnave plasti nematika, še zlasti v bližini sten. Radi bi raziskali vpliv variacij stopnje nematske ureditve — neizbežnih v bližini vsake ograjujoče površine — na smer nematskega direktorja. Sprva se bomo posvetili ravninskim deformacijam, pri katerih lahko direktor parametriziramo z $\mathbf{n} = \mathbf{n}(z) = (\sin\phi(z), 0, \cos\phi(z))$, stopnjo urejenosti pa opisuje profil $S(z)$ (pri tem os z sovpada s ploskovno normalo sten vzorca). Ko nato tenzorski parameter urejenosti Q (1) izrazimo z $S(z)$ in $\phi(z)$, zapišemo Landau-de Gennesovo gostoto proste energije (5) v obliki $f = f_0(S,T) + f_1(\phi, S') + f_2(\phi', S) + f_3(\phi, \phi', S, S')$, kjer je homogeni člen $f_0(S,T)$ določen z izrazom (3), ostali trije pa z

$$f_1(\phi, S') \;=\; \tfrac{3}{4}L_1\Big\{1 + \tfrac{L_2+L_3}{2L_1}\Big(\cos^2\phi + \tfrac{1}{3}\Big)\Big\}S'^2, \tag{19}$$

$$\begin{aligned} f_2(\phi', S) &= \tfrac{9}{4}L_1 S^2\Big\{1+\tfrac{L_2+L_3}{2L_1}\Big\}\phi'^2 \quad \text{in} &(20)\\ f_3(\phi,\phi',S,S') &= -\tfrac{3}{8}(L_2+L_3)\sin(2\phi)\,\phi' S S'. &(21)\end{aligned}$$

Črtica povsod pomeni odvod glede na z. Prvi člen da pozitivni prispevek, kadar imamo opravka s spremembami stopnje urejenosti ($S' \neq 0$) in je za $L_2 + L_3 \neq 0$ odvisen tudi od kota ϕ. Drugi člen predstavlja Frankov prispevek (6) (prispevek K_{24} je v izbrani geometriji enak nič). Tretji člen je od nič različen le za $L_2+L_3 \neq 0$ — kadar ne upoštevamo približka z eno konstanto — in sklaplja variacije stopnje urejenosti in kota ϕ.

Denimo, da imamo polneskončno plast nematika in da stena predpisuje stopnjo ureditve S_0 ter kot ϕ_0. Dovolj daleč od stene je vrednost S enaka S_b in jo določimo z minimizacijo $f_0(S,T)$ (3). Variacija v profilu $S(z)$ se dogodi na razdalji, ki je blizu korelacijski dolžini ξ (4) in jo moremo tako smatrati za površinski pojav. Izkaže se, da sta prav zato tudi $\mathcal{W} = \int_0^\infty f_1(z)dz$ in $\mathcal{G} = \int_0^\infty f_3(z)dz$ energijska prispevka, ki ju lahko pripišemo površini. Prvi zaradi odvisnosti od kota ϕ predstavlja prispevek k notranjemu sidranju, čigar jakost ocenimo z

$$W_i \approx \tfrac{3}{4}|L_2+L_3|(S_b-S_0)^2(\lambda^*)^{-1} = \tfrac{1}{3}|K_{11}-K_{22}|(\lambda^*)^{-1}\Big(1-\tfrac{S_0}{S_b}\Big)^2, \qquad (22)$$

preferenčna smer urejanja pa je lahko bodisi planarna (za $L_2 + L_3 > 0$) bodisi homeotropna (za $L_2 + L_3 < 0$). Pri tem pomeni λ^* dolžino velikostnega reda ξ. Podobno je moč uvideti, da ima drugi člen ($\mathcal{G}$) enako kotno odvisnost, kot bi jo v obravnavani geometriji imel člen s K_{13} [52,53], ki pa ga v razvoju proste energije (5) nismo izrecno upoštevali, saj smo povsod zapisali le prve krajevne odvode Q. Iz podobnosti lahko sedaj izluščimo *kvazi pahljačno-upogibno elastično konstanto*

$$\tilde{K}_{13} = -\tfrac{3}{8}(L_2+L_3)(S_b^2-S_0^2) = \tfrac{1}{6}(K_{22}-K_{11})\Big[1-\Big(\tfrac{S_0}{S_b}\Big)^2\Big], \qquad (23)$$

ki ima drugačen izvor kot prava K_{13} in kot taka ne povzroča težav pri reševanju variacijskega problema. $\tilde{K}_{13} \neq 0$ dobimo le v primeru, ko $S_b \neq S_0$ in $L_2 + L_3 \neq 0$. Še vedno pa preko sklopitve S' in ϕ' člen f_3 privede do elastične deformacije $\Delta\phi$ ob površini, ki se obnaša podobno kot v primeru prave K_{13}: $\Delta\phi \approx -(\tilde{K}_{13}/2K)\sin 2\phi_0$ [149].

Da bi podrobno preučili pojav notranjega sidranja in deformacij ob površini, si zdaj oglejmo popolno numerično minimizacijo proste energije v končni plasti nematika. Steni vzorca naj bosta vzporedni in naj se nahajata pri $z = \pm\frac{d}{2}$. V prosti energiji upoštevajmo prostorninske člene (5), prispevek zunanjega sidranja pa modelirajmo z izrazom (7). Minimizacija privede do Euler-Lagrangeovih enačb in ustreznih robnih pogojev, njihovo reševanje pa do rešitev $\phi(z)$ in $S(z)$, prikazanih na sliki 9.

Opazimo lahko, da so variacije $S(z)$ dejansko omejene na tanko površinsko plast (debeline okoli 10 nm) in da jih v plasti iste debeline spremlja deformacija v odvisnosti $\phi(z)$. Predznak deformacije $\Delta\phi$ se obnaša skladno z zgornjo napovedjo in je odvisen od predznakov $L_2{+}L_3$ ter $S_0{-}S_b$. Ob primerjavi dejanskih površinskih vrednosti $\phi(\pm\frac{d}{2})$ s ϕ_0, ki ga vsiljuje stena, lahko razberemo tudi učinke že napovedanega

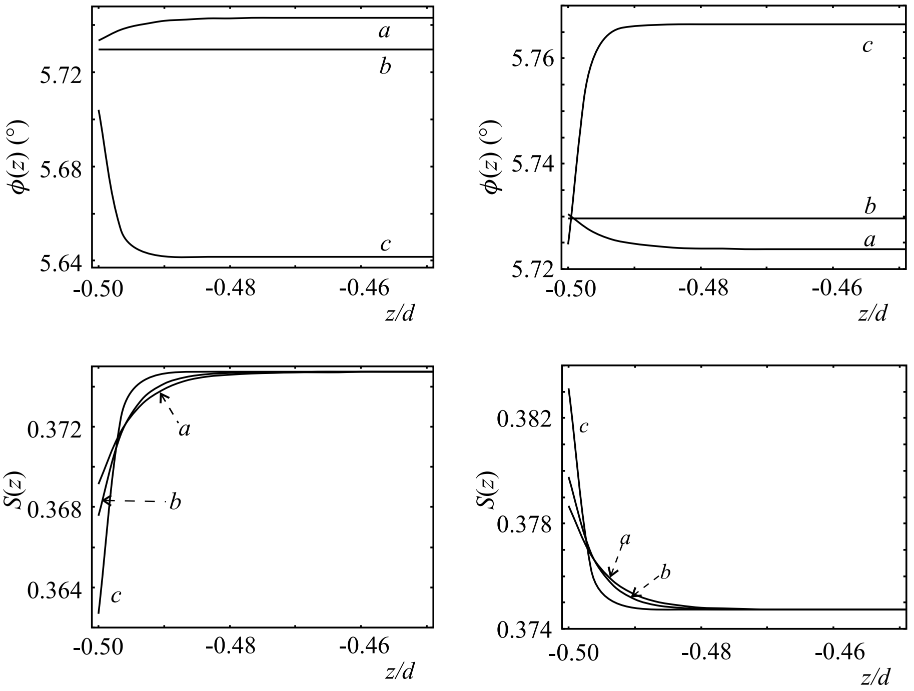

Slika 9 Plast nematika: profili $\phi(z)$ in $S(z)$ za $\phi_0 = 0.1(180^\circ/\pi) \approx 5.73^\circ$ (preferenčna smer zunanjega sidranja), $S_b \approx 0.3747$ in $L_2 + L_3 = +L_1, 0, -L_1$ [primeri (a), (b) in (c)]. Razurejujoča ($S_0 = 0.35$, *levo*) in urejujoča površina ($S_0 = 0.4$, *desno*). Debelina vzorca je enaka $d = 1$ μm, $a = 0.13 \times 10^6$ J/m^{3}K, $B = 1.6 \times 10^6$ J/m^3, $C = 3.9 \times 10^6$ J/m^3 (podatki za 5CB [148]), $T - T_* = 0.4$ K in $L_1 \approx 10^{-11}$ N.

notranjega sidranja. Značilna razdalja vseh variacij je nekoliko odvisna tudi od predznaka $L_2 + L_3$, saj se s tem spreminja tudi vloga stabilizirajočih prispevkov v prosti energiji (5). Jakost celotnega (notranjega in zunanjega) sidranja je mogoče oceniti s poskusom v zunanjem magnetnem polju, kjer molekule v vzorcu poravnamo v smeri polja, hkrati pa opazujemo odstopanja od te smeri v bližini stene zaradi sidranja. Ta so potem merilo za njegovo jakost in s tem za ekstrapolacijsko dolžino K/W (slika 4). Iz tako določenih K/W ter iz analitične ocene (22) lahko sklepamo, da $\lambda^* \approx 6 - 7$ nm, kar je pri izbranih podatkih dejansko blizu korelacijske dolžine ξ. Pri tistih izbirah jakosti sklopitve s površino W_e v enačbi (7), ki še dajo realistične vrednosti za K/W (100 nm in več), so variacije v profilih $S(z)$ in $\phi(z)$ šibke: za $w_e = W_e d/L_1 = 5$, $S_0 = 0.5$, $S_b = 0.3747$ in $\phi_0 = \pi/4$ dobimo $d\phi/dz \approx 3 \times 10^{-4}/\rho_0 \ll 1/\rho_0$ ($\rho_0 \approx 1$ nm pomeni velikost molekule nematika) in $[S(\pm\frac{d}{2}) - S_b]/S_b \sim 0.01$. Oboje pomeni, da so variacije ϕ in S šibke in da je v obravnavanem primeru uporaba kontinuumske teorije upravičena. Hkrati pa to pomeni tudi, da z obstoječim modelom ni moč pojasniti veliko močnejših variacij v nematskem urejanju, ki so bile opažene eksperimentalno [43,48–51]. V ta namen se je površinskega urejanja treba lotiti na molekulski ravni.

Možnost obstoja iz spreminjanja S izvirajoče lokalizirane variacije v direktorskem profilu lahko preučimo tudi v neravninski geometriji za zvojne deformacije. V tem primeru je $\mathbf{n}$ parametriziran z dvema kotoma. Poleg nagiba ϕ imamo zdaj še zvojni kot ω, merjen glede na os x: $\mathbf{n}(z) = (\sin\phi(z)\cos\omega(z), \sin\phi(z)\sin\omega(z), \cos\phi(z))$. V gostoti proste energije edina sprememba nastopi v Frankovem členu

$$f_2(\phi,\phi',\omega',S) = \tfrac{9}{4}L_1S^2\left\{\left(1+\tfrac{L_2'}{2L_1}\right)\phi'^2+\sin^2\phi\left(1+\tfrac{L_2'}{2L_1}\cos^2\phi\right)\omega'^2\right\}, \qquad (24)$$

kjer smo vpeljali $L_2' = L_2 + L_3$. Že njegova zgradba sama napoveduje, da v zvojnem profilu $\omega(z)$ ne smemo pričakovati deformacij, kakršne povzroči prispevek f_3 v odvisnosti $\phi(z)$, saj nikjer ne najdemo členov oblike $S'\omega'$.

Oglejmo si rešitev problema v limiti močnega sidranja za $\phi(\pm\frac{d}{2}) = \pi/2$, ko ni pričakovati nikakršnih deformacij v profilu $\phi(z)$. Hkrati zahtevajmo $\omega(-\frac{d}{2}) = 0$ in $\omega(\frac{d}{2}) = \pi/4$, kar privede do zvojne deformacije, ki se razširja po vsem vzorcu. Če predpostavimo, da $S_0 = S_b$ in tako $S \neq S(z)$, je profil zvojnega kota $\omega(z)$ preprosta linearna funkcija z. V nasprotnem primeru — če imamo variacijo $\Delta S = S_b - S_0 \neq 0$ v plasti debeline λ^* (kot zgoraj za ϕ) — dobimo za $\lambda^* \ll d$ blizu stene $(z \to \pm\frac{d}{2})$ $\omega(z) \approx \omega(-\frac{d}{2}) + \Delta\omega(\frac{z}{d}+\frac{1}{2}) \mp \delta\omega_0\{1-\exp[(\pm z-\frac{d}{2})/\lambda^*]\}$. Iz zapisane zveze lahko izločimo amplitudo dodatne variacije v zvojnem kotu ω, do katere pride zaradi spreminjanja S, $\delta\omega_0 \approx 2(\lambda^*/d)(\Delta S/S_b)\Delta\omega$, kjer smo vpeljali $\Delta\omega = \omega(\frac{d}{2}) - \omega(-\frac{d}{2})$. Dodatna deformacija $\delta\omega_0$ je očitno prisotna samo takrat, ko imamo $\Delta S \neq 0$ in je zvojna deformacija v sistemu že prisotna ($\Delta\omega \neq 0$). Takšno obnašanje napovedujejo tudi numerično izračunane odvisnosti $\omega(z)$, ki so prikazane na sliki 10. Tudi amplituda $\delta\omega_0$ je majhna: za $\Delta\omega = \pi/4$, $\lambda^* \approx 0.01d$ ($d = 1\mu$m), $\Delta S \approx 0.025$ in $S_b \approx 0.375$ ocenimo $\delta\omega_0 \approx 0.06°$, kar se v grobem ujema tudi z numerično rešitvijo (slika 10).

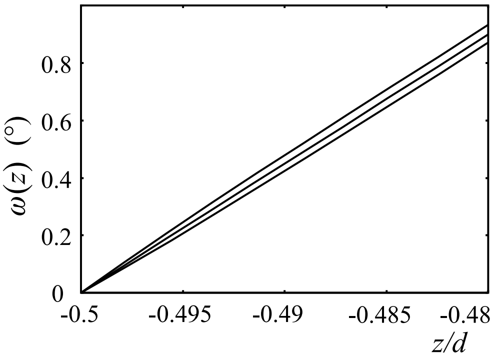

Slika 10 Odvisnosti $\omega(z)$ zvite nematske plasti z lokalizirano variacijo S ob površini. Parametri: $\phi(\pm\frac{d}{2}) = \pi/2$, $S_b \approx 0.375$, $\Delta S \approx 0.025$, 0, -0.025 (zgornja, srednja in spodnja črta), $\omega(-\frac{d}{2}) = 0$, $\omega(\frac{d}{2}) = \pi/4$; $L_2' = 0$. Vrednosti a, B, C, $T - T_*$ in L_1 so enake tistim pri sliki 9.

Na koncu je potrebno povedati, da dodatna zvojna deformacija, ki se pojavi zaradi sprememb S ob površini, nima istega izvora kot tista v kotu ϕ pri planarnih deformacijah: namesto člena f_3 je njen izvor navadni Frankov elastični člen f_2. Deformacijo s tem povzročajo spremembe elastičnih konstant, pa še to le v primeru, ko je zvojna deformacija v vzorcu že prisotna.

Mikroskopski opis tanke plasti

Zdaj želimo obravnavati urejanje v plasti nematika še na molekulski ravni. Posebno pozornost bomo posvetili pojavu notranjega sidranja in ga modelirali v okviru modela s šestkotniško mrežo in anizotropno interakcijo med induciranimi dipoli (12) [17]. Še zlasti se bomo zanimali za temperaturno odvisnost ekstrapolacijske dolžine K/W, ki so jo že poskušali določiti za zunanje sidranje [152]. Eksperimentalna opažanja namreč kažejo, da jakost sidranja W s temperaturo pada, vendar ni videti splošnega pravila za odvisnost $W(S)$ [46,112,143,153,154]. Tako lahko poskusi kažejo celo na $W \propto S^4$ [46], medtem ko nekateri modelski sistemi napovedujejo le $W \propto S$ [157,158]. V prvem primeru ob bližanju faznemu prehodu z upoštevanjem $K \propto S^2$ zaznamo povečanje K/W, v drugem pa zmanjšanje. Še pred samo meritvijo temperaturne odvisnosti K/W bo potrebno preučiti sam fazni prehod med nematsko in izotropno fazo (prehod NI).

Simulacije, predstavljene v tem razdelku, so sledile metodi Monte Carlo (glej prejšnje poglavje). Razdelitev šestkotniške mreže na tri podmreže je omogočila vektorizacijo in s tem pospešitev računalniškega algoritma. Prehod NI je bil preučen v vzorcu velikosti $30 \times 30 \times 30$ delcev s periodičnimi robnimi pogoji v vseh treh smereh, K/W pa je bila merjena v plasti velikosti $48 \times 48 \times 46$ delcev s periodičnimi robnimi pogoji v smereh x in y, prosto površino pri $z = 0$ in trdno steno pri $z = d$. Za uravnovešanje je bilo izvedenih po 2×10^5 MC korakov (v enem koraku pride na vrsto za morebitno reorientacijo vsak izmed delcev), še nadaljnjih 10^5 pa za izračun povprečij. Za začetno konfiguracijo je bila izbrana tista z naključnimi orientacijami delcev $\mathbf{u}_i$, lahko pa tudi že uravnovešena konfiguracija pri temperaturi ne predaleč od obravnavane. Poleg notranje energije predstavlja pomembno opazljivko dvodimenzijska ureditvena matrika, ki jo po analogiji z izrazom (2) lahko vpeljemo kot

ν	T°_{NI}	T°	ℓ (a)
0.05	1.375 ± 0.025	1.3	15.5 ± 1
		1.2	13 ± 1
		1.1	13 ± 1
0.1	1.225 ± 0.025	1.175	4 ± 2
		1.1	5 ± 1
		1.0	5 ± 1
0.2	0.950 ± 0.025	0.9	-1 ± 0.5
		0.8	$+1 \pm 0.5$
		0.7	$+1 \pm 0.5$
0.3	0.675 ± 0.025	0.6	-4 ± 1
		0.5	-4 ± 1
		0.4	-4 ± 1

Tabela 1 Temperaturna odvisnost ekstrapolacijske dolžine notranjega sidranja ℓ (merjena v enotah mreže a) za različne ν in pripadajoče reducirane temperature faznega prehoda T°_{NI}.

$\underline{q} = 2\langle \mathbf{u}_i \otimes \mathbf{u}_i \rangle_i - \mathsf{I}$ in iz nje po diagonalizaciji določimo direktor $\mathbf{n}$ ter dvodimenzijski skalarni parameter urejenosti $s = \langle 2(\mathbf{u}_i \cdot \mathbf{n})^2 - 1 \rangle_i$. Direktor lahko ponovno parametriziramo z $\mathbf{n} = \mathbf{n}(z) = (\sin\phi(z), 0, \cos\phi(z))$.

Temperaturo faznega prehoda T°_{NI} je mogoče določiti iz temperaturnih odvisnosti notranje energije. Rezultati v reducirani skali $T^\circ = k_B T/\epsilon'$ so za različne vrednosti parametra anizotropije ν zbrani v tabeli 1. Opazimo, da T°_{NI} z rastočim ν pada, kar je v skladu z upadanjem Frankove elastične konstante pri povečevanju ν [129].

Meritev ekstrapolacijske dolžine je bila izvedena v plasti, podobni hibridni celici. Na prosti površini ($z = 0$) deluje notranje sidranje, ki je za $\nu \lesssim 0.3$ homeotropno. Pri $z = d$ imamo močno planarno sidranje, ki v vzorcu zadostne debeline privede do elastične deformacije [114]. To lahko vidimo tudi iz odvisnosti $\phi(z)$, prikazanih na sliki 11 za $\nu = 0.05$, razen v primeru, ko se je zaradi bližine prehoda v izotropno fazo nematik v celici stalil — slednje je razvidno tudi iz profilov $s(z)$. Z ekstrapolacijo direktorskega profila, kot je nakazana na sliki 4, dobimo dolžino ℓ, ki je ekvivalentna K/W le v primeru dovolj šibkega sidranja, ko $\ell \gtrsim \xi$ [ξ označuje korelacijsko dolžino (4)]. Iz tabele 1 je razvidno, da je razen za $\nu = 0.05$ ℓ mikroskopska dolžina (reda nekaj a) in da se veča z manjšanjem parametra anizotropije ν. Poleg tega vidimo, da je za $\nu \gtrsim 0.2$ sidranje tako močno, da postane ekstrapolirana ℓ zaradi zanemarjenih sprememb stopnje urejenosti s negativna in zato ne predstavlja K/W [143]. Zdi se tudi, da je temperaturna odvisnost ℓ le šibka in slabo izražena, razen za $\nu = 0.05$, kjer ℓ ob bližanju prehodu v izotropno fazo blago naraste. V grobem torej kaže, da imamo v pričujočem sistemu $W \propto S^\delta$ z $\delta \sim 2$.

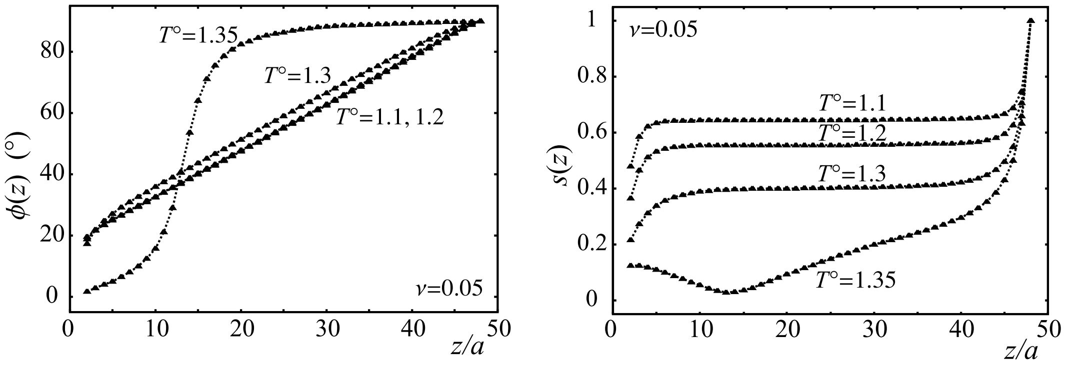

Slika 11 Temperaturni odvisnosti $\phi(z)$ in $s(z)$ za $\nu = 0.05$. Iz ektrapolacije profilov $\phi(z)$ proti levi lahko določimo ℓ notranjega sidranja. Pri temperaturah blizu faznega prehoda se nematik v vzorcu stali, zmanjša stopnjo urejenosti s in se s tem izogne upogibni deformaciji. Hkrati v bližini trdne stene vedno opazimo povišanje s.

Kaže, da je ujemanje ℓ z eksperimentalnimi vrednostmi (100 nm in več) mogoče doseči le za dovolj majhne ν. V takih primerih medmolekulski potencial (12) vzpodbuja pretežno vzporedno ureditev molekul, kot jo, na primer, tudi sterične odbojne interakcije med podolgovatimi delci, ki jih nismo nikjer izrecno upoštevali. Ostali neupoštevani pojavi zajemajo še dipolne in kvadrupolne interakcije, prisotnost nečistoč [161], krajevne spremembe v gostoti nematika [66,67], elektrostatske interakcije zaradi selektivne adsorpcije ionov [160] in grobost trdne površine (zadnja pojava le v primeru sidranja na trdni podlagi).

Nematske kapljice

V tem poglavju se bomo ukvarjali z nematskim urejanjem v nekoliko zapletenejši geometriji: v podmikronskih kapljicah. Najdemo jih v sistemih PDLC, kjer so ujete v polimerno matriko. Obdelali bomo primer s homeotropnim sidranjem — radialno kapljico — ter takšnega s planarnim — bipolarno (slika 12). Številne fenomenološke, simulacijske in eksperimentalne študije so v preteklosti privedle do precej dobrega poznavanja teh sistemov [5,91]. Tukaj se bomo lotili še ne v celoti obdelanega vprašanja razlage rezultatov simulacij Monte Carlo skozi spektre ^{2}H NMR, vključno z dinamiko molekul in urejujočimi učinki zunanjih polj.

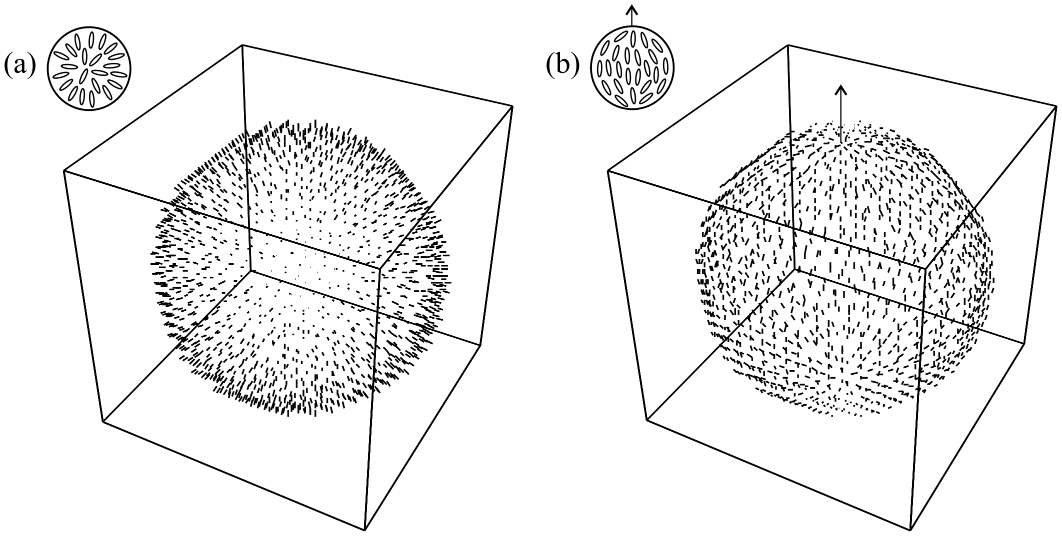

Slika 12 Površinska plast delcev “duhov”, ki pripadajo polimerni matriki in določajo robne pogoje: (a) radialna in (b) bipolarna kapljica (puščica označuje bipolarno simetrijsko os). Ureditev molekul v vsaki izmed kapljic je prikazana tudi shematično.

Simulacije urejanja v kapljicah (vrste Monte Carlo) so bile izvedene v okviru Lebwohl-Lasherjevega modela (glej poglavje o simulacijah). Kapljice s polmerom $R = 12a$ in zahtevanimi robnimi pogoji so bile izžagane iz kubične mreže, kot kaže slika 12. Jakost interakcije ϵ med nematskimi delci — pri izbranem R jih je 5832 — je bila enaka jakosti interakcij delcev nematika z delci, ki pripadajo polimerni matriki (teh je skupaj 1352). Za začetek vsake simulacije je bila privzeta konfiguracija, ki ustreza idealni ureditvi v skladu z izbranimi robnimi pogoji, ali pa že uravnovešena konfiguracija pri bližnji temperaturi, čemur je sledila uporaba Metropolisovega postopka z Barker-Wattsovo tehniko. Sistem delcev je bil uravnovešan skozi vsaj 5×10^4 korakov, potem pa je bilo zajetih 1024 konfiguracij, iz katerih so bila izračunana vsa povprečja in spektri ^{2}H NMR. V nadaljevanju bodo vse temperature izražene v brezdimenzijski skali, določeni s $T^* = k_B T/\epsilon$. Simulacije v nematski fazi so bile tako izvedene pri $T^* = 0.8$, v izotropni pa pri $T^* = 1.2$. Za izračun spektrov ^{2}H NMR je bil uporabljen pristop s časovno odvisno spinsko hamiltonko (glej poglavje o eksperimentalnih opazljivkah), ki omogoča pravilno upoštevanje procesov, kot sta translacijska difuzija in fluktuacije dolgih osi molekul.

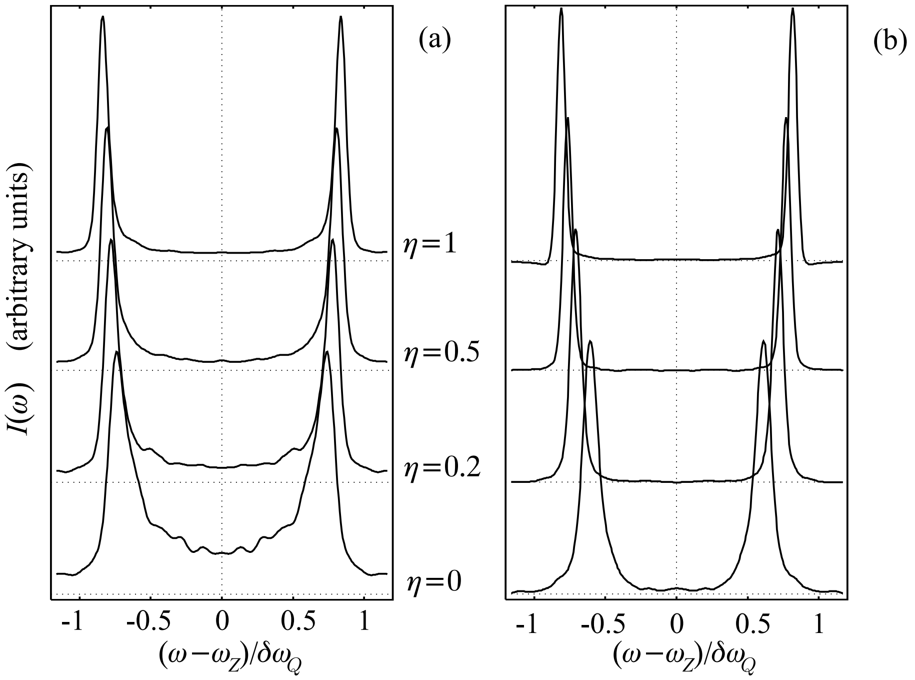

Slika 13 Simulirani spektri ^{2}H NMR za eno bipolarno kapljico v nematski fazi pri $T^* = 0.8$ in za različne jakosti zunanjega polja ($\propto \sqrt{\eta}$); brez difuzije (a), s hitro difuzijo (b). Kvadrupolni razcep narašča z η.

Za začetek si oglejmo kapljice v odsotnosti zunanjih polj ($\eta = 0$), najprej bipolarno. Od zunanjih polj imejmo edino polje NMR spektrometra, potrebno za meritev spektrov, vendar naj bo tako šibko, da ne vpliva na molekulsko ureditev v kapljicah [$R \ll \xi_m$; ξ_m označuje magnetno koherenčno dolžino (9)]. Poleg tega se zaenkrat posvetimo limiti brez translacijske difuzije, katere veljavnosti je zadoščeno za $R \gg \sqrt{6Dt_0}$ (D pomeni efektivno difuzijsko konstanto, t_0 pa značilni čas spektroskopije NMR) — torej v dovolj velikih kapljicah. Edina gibanja, s katerimi imamo zdaj opravka v vzorcu, so fluktuacije dolgih osi molekul $\mathbf{u}_i$, ki določajo S in $\mathbf{n}$. Izkaže se, da tovrstne fluktuacije sicer nenaravna dinamika metode Monte Carlo opiše dovolj dobro. Ureditev v bipolarni kapljici je takšna, da je velik del molekul usmerjen približno v smeri bipolarne osi. Če usmerimo magnetno polje spektrometra vzdolž te smeri (tega se bomo držali do nadaljnjega), naletimo v spektru na dobro izražena vrhova pri približno $\omega_Z \pm S\delta\omega_Q$ (slika 13). Iz njune lege je tako mogoče približno določiti $S \approx 0.73 \pm 0.01$. Do ocene za S lahko pridemo tudi neposredno iz simulacijskih podatkov z diagonalizacijo lokalnih ureditvenih matrik $\underline{Q}$ (2), ki jih potem povprečimo po vsej kaplji: $S \approx 0.76 \pm 0.04$. Pripomniti je treba še, da imamo v realnem vzorcu z mnogo kapljicami porazdelitev po smereh bipolarnih osi. Primer, kot ga obravnavamo tukaj, srečamo le, če že sam proces nastajanja kapljic (na primer fazna separacija [28]) poteka v zunanjem polju, ki usmeri vse bipolarne osi v isto smer [40]. Poleg tega je bilo za glajenje spektrov potrebno izvesti konvolucijo z jedrom širine $0.04\delta\omega_Q$.

Kadar velja $R \ll \sqrt{6Dt_0}$ (na primer v majhnih kapljah), posamezna molekula zaradi difuzije v času t_0 prepotuje dolžino, primerljivo z R. Zato se ω_Q zaradi $S = S(\mathbf{r})$ in $\mathbf{n}{=}\mathbf{n}(\mathbf{r})$ v tem času znatno spremeni. V takih primerih dobimo v spektru dva vrhova pri povprečni frekvenci $\omega_Z + \langle\omega_Q\rangle$, kjer $\langle\omega_Q\rangle = \pm\delta\omega_Q\,\frac{1}{2}\langle S(\mathbf{r})\,[3\cos^2\theta(\mathbf{r}) - 1]\rangle$ in gre povprečje $\langle ... \rangle$ po difuzijskih gibanjih molekul. Pri računanju spektrov je tovrstno gibanje bilo modelirano s preprostim postopkom naključnega sprehoda po kubični mreži, in sicer ob predpostavki, da je difuzijski proces izotropen in prostorsko homogen. Na sliki 13 vidimo, da sta v spektru še vedno prisotna dva vrhova, vendar je razcep manjši kot v primeru brez difuzije: $\langle\omega_Q\rangle = (0.61 \pm 0.02)\,\delta\omega_Q$. Do tega pride, ker direktor v bližini sten odstopa od smeri bipolarne osi (in s tem polja spektrometra). Povprečno frekvenco $\langle\omega_Q\rangle$ se da izračunati tudi iz podatkov simulacije: $0.59\,\delta\omega_Q$.

Urejanje v kapljici lahko preučimo tudi tako, da jo razdelimo na koncentrične lupine in izračunamo primerne parametre urejenosti kot funkcijo razdalje od središča kapljice. Prvi izmed parametrov je lahko že računani S (dobljen iz diagonalizacije $\underline{Q}$), drugi pa $\langle P_2\rangle_B$, ki meri stopnjo ureditve glede na vnaprej določeno smer. Vpeljemo ga kot $\langle P_2\rangle_B = \langle\frac{1}{2}[3(\mathbf{f}\cdot\mathbf{u}_i)^2 - 1]\rangle_i$, kjer je $\mathbf{f}$ enotski vektor v smeri magnetnega polja spektrometra, povprečje $\langle ... \rangle_i$ pa teče preko delcev v določeni plasti. Iz odvisnosti na sliki 14 lahko razberemo, da so v središču kapljice molekule večidel usmerjene vzdolž bipolarne osi in da prihaja do odstopanj od te smeri le v bližini sten. Poleg tega je tam stopnja nematske ureditve povišana.

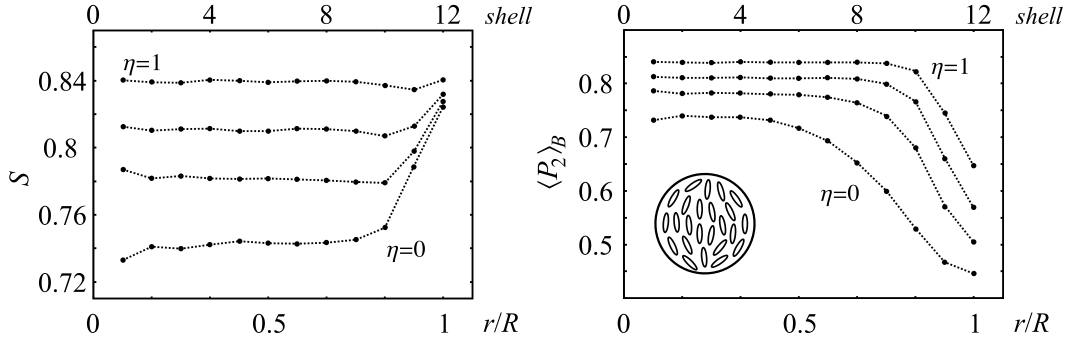

Slika 14 Parametri urejenosti za bipolarno kapljico pri $T^* = 0.8$: (a) S in (b) $\langle P_2\rangle_B$ kot funkcija razdalje od središča kapljice (r). Krivulje so narisane za $\eta = 1$, $\eta = 0.5$, $\eta = 0.2$ in $\eta = 0$ (od zgoraj navzdol). Zunanje polje poviša stopnjo nematske urejenosti (a), pa tudi velikost vzdolž polja urejene sredice (b).

V primeru radialnih kapljic (še vedno brez dodatnega zunanjega polja; $\eta = 0$) je orientacijska porazdelitev skoraj prostorsko izotropna, zato je s stališča NMR enakovredna polikristaliničnemu vzorcu, pri katerem v spektru naletimo na *Pake*ov vzorec: dva nesimetrična vrhova pri $\omega_Z \pm \frac{1}{2}S\delta\omega_Q$ in rameni, ki segata do $\omega_Z \pm S\delta\omega_Q$.

Simulacije v primeru brez translacijske difuzije dejansko dajo opisanemu podoben spekter (slika 15), ki spet omogoča določitev S iz položaja vrhov in ramen ($S \approx 0.72 \pm 0.02$), pa tudi iz podatkov simulacije ($S \approx 0.73 \pm 0.10$). Kadar je difuzija hitra, dobimo v spektru zaradi izotropnosti orientacijske porazdelitve en sam vrh pri $\omega_Q \approx 0$, iz podatkov Monte Carlo pa $\langle \omega_Q \rangle \approx 0.03\,\delta\omega_Q$. Kot kaže, je v obeh limitah (z in brez difuzije) s primerjavo spektrov vedno mogoče razlikovati med radialno in bipolarno kapljico. Razlika v obnašanju spektrov je še posebej nazorna, če vzorec obračamo v polju spektrometra: za razliko od spektrov bipolarne kapljice se spektri radialne pri tem ne spreminjajo.

Slika 16 prikazuje radialno odvisnost parametrov S in $\langle P_2 \rangle_B$. Za $\eta = 0$ opazimo, da je v središču radialne kapljice — kjer pričakujemo topološki defekt — stopnja ureditve S dejansko znatno nižja kot v zunanjih delih kapljice, kjer je radialno

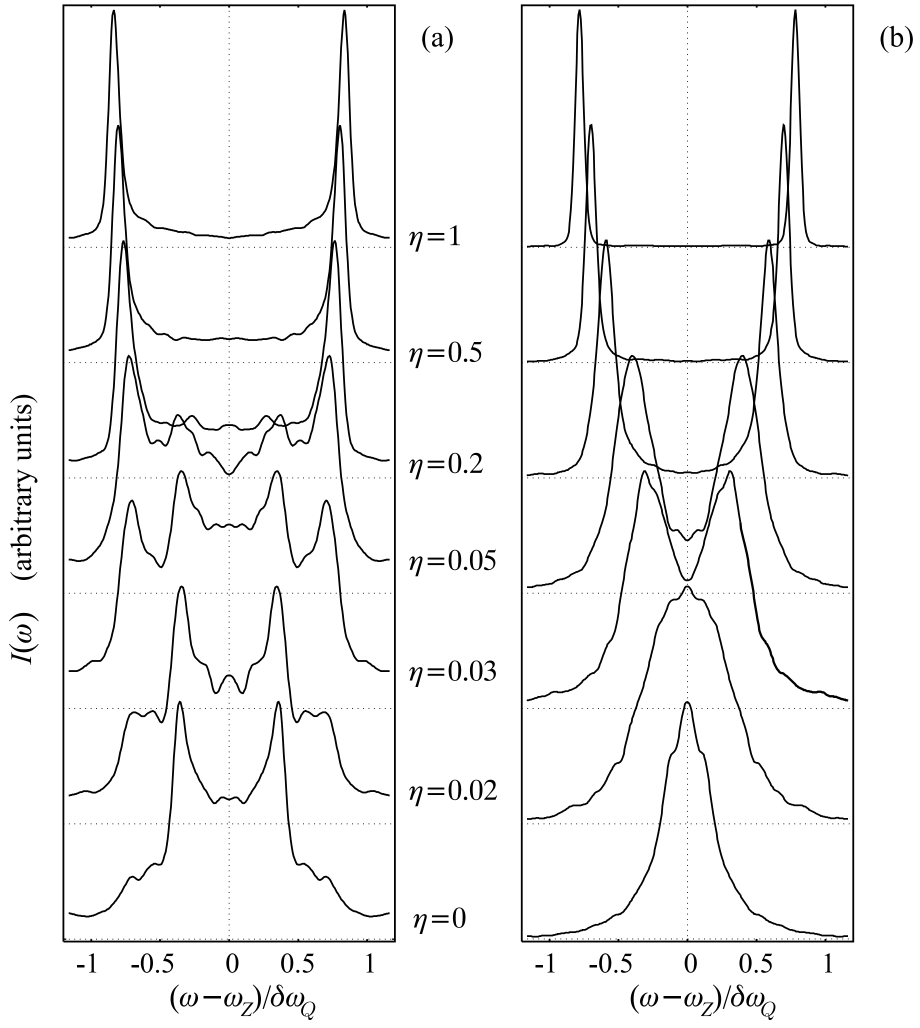

Slika 15 Simulirani spektri ^{2}H NMR radialne kapljice v nematski fazi za $T^* = 0.8$ in različne η; (a) brez difuzije, (b) s hitro difuzijo. S povečevanjem η pride do prehoda med radialno strukturo in strukturo z večino molekul usmerjenih vzdolž zunanjega polja.

urejanje jasno izraženo.

Namignili smo že, da je difuzija pomembna zlasti v majhnih kapljah. Če vzamemo $\delta\omega_Q \approx 2\pi \times 40$ kHz, $D \approx 4 \times 10^{-11}$ m^2/s in $S \approx 0.8$ (v povprečju), lahko ocenimo, da so spektri kapljic s polmeri pod $R \approx 60$ nm znatno difuzijsko izpovprečeni. Po drugi strani simulacije sprektrov kažejo, da pri istih podatkih v kapljicah polmerov nad $R \approx 330$ nm učinki difuzije niso več zaznavni. Zaradi omejitve z velikostjo vzorca ($R = 12a$ in $a \lesssim 5$ nm) so v predstavljenih simulacijah realistični predvsem primeri z $R \lesssim 60$ nm, ko smo že v limiti hitre difuzije.

Do zdaj smo predpostavljali, da je difuzija prostorsko homogena. Hkrati eksperimenti kažejo, da je lahko v bližini ograjujočih sten znatno upočasnjena, to pa je posebej opazno v močno ograjenih sistemih [96,166]. Tedaj so izračunani spektri sestavljeni iz superpozicije difuzijsko izpovprečenega prispevka notranjosti kapljic in prispevka površinske plasti, kjer difuzija ne igra pomembne vloge [97]. Če pa si poleg tega ogledamo še vzorec z mnogimi bipolarnimi kapljami, katerih simetrijske osi so usmerjene po prostoru naključno, ponovno naletimo na spekter Pakeove vrste [97]. Vzorec je namreč makroskopsko izotropen, čeprav posamezne kapljice niso. Tudi hitra difuzija Pakeov spekter ohrani, le da je ta nekoliko ožji kot v primeru brez difuzije.

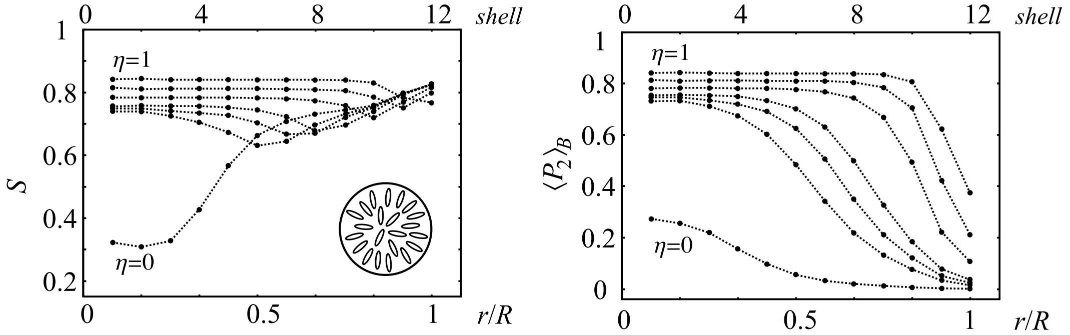

Slika 16 Parametri urejenosti za radialno kapljico pri $T^* = 0.8$: (a) S in (b) $\langle P_2\rangle_B$ kot funkcija razdalje od središča r. Krivulje so narisane za $\eta = 1$, $\eta = 0.5$, $\eta = 0.2$, $\eta = 0.05$, $\eta = 0.03$, $\eta = 0.02$ in $\eta = 0$ (od zgoraj navzdol). Jedro defekta se z višanjem poljske jakosti pretvori v strukturo, urejeno v smeri polja.

Priključimo sedaj zunanje polje, ki naj bo dovolj močno, da dodatno uredi nematik v kapljicah ($R \gg \xi_m$). V simulaciji sklopitev nematskih delcev z zunanjim poljem opisuje izraz (11), ki za $\eta > 0$ privede do urejanja delcev v smeri polja **f**. V primeru bipolarnih kapljic je prvi učinek zunanjega polja reorientacija bipolarnih osi, ki se obrnejo v smer polja [25,90]. Tukaj bomo obravnavali primer, ko je **f** že vzporeden bipolarnim osem. Tako spektri (slika 13) kot profili parametrov urejenosti (slika 14) kažejo, da zunanje polje povzroči dodatno urejanje molekul v smeri polja, hkrati pa tudi poviša stopnjo urejenosti S [117]. Oboje se odraža v povečanju kvadrupolnega razcepa, kar opazimo ne glede na stopnjo difuzijske izpovprečenosti spektrov. Zavedati pa se moramo, da so obravnavana zunanja polja izjemno močna, saj so tudi simulirane kapljice relativno majhne. Tako imamo v magnetnem primeru pri $\eta = 0.2$ za značilen nematik ($\epsilon = 0.023$ eV, $\chi_a S \approx 10^{-6}$ in $V_0 \approx 100$ nm^3) $B \approx 150$ T, kar je precej nad trenutnimi eksperimentalnimi zmožnostmi. Na podobne težave naletimo tudi pri uporabi električnih polj.

V primeru radialnih kapljic so spremembe, ki jih povzroči zunanje polje, bolj dramatične: defektno strukturo v središču kaplje polje razbije in delce uredi v smeri **f**. Urejeno jedro obkroža defektna linija moči $\frac{1}{2}$, ki se z višanjem η razteza, medtem ko je v plasteh ob površini za ne prevelik η radialno urejanje še vedno prisotno (slika 16). Takšno obnašanje lahko razberemo tudi iz izračunanih spektrov (slika 15), ki jih v odsotnosti difuzije uteženo sestavljata prispevek urejene sredice in Pakeov vzorec. V primeru hitre difuzije se spekter z enim vrhom pri $\omega_Q \approx 0$ v dovolj močnem polju prelevi v dvovrhega.

Če dvignemo temperaturo do $T^* = 1.2$ nad temperaturo prehoda v izotropno fazo, opazimo že v odsotnosti zunanjega polja ($\eta = 0$) ob steni kapljice urejeno paranematsko fazo. Če poleg tega vključimo še močno zunanje polje, se nematsko urejanje razširi po vsej kapljici [118], to pa ponovno privede do znatnega kvadrupolnega razcepa. Ta pojav je lahko opazen zlasti zato, ker je — kot že rečeno — jakost zunanjega polja izjemno visoka.

Kljub temu, da predstavljena metodologija za izračun spektrov dobro opiše dinamiko molekul in vplive zunanjih polj, pa sedanji rezultati za bolj natančno kvantitativno primerjavo z eksperimentalnimi še niso zreli: zaradi relativno majhnega števila delcev v simulaciji so spektri precej zašumljeni, konvolucije pa jih sicer zgladijo, a s tem tudi nekoliko prizadenejo njihovo obliko.

Nematiki z dispergiranimi polimernimi mrežami

Zadnje poglavje bo obravnavalo simulacije nematskega urejanja v sistemih z dispergiranimi polimernimi mrežami. Te sestavljajo tanka (nanometrska) polimerna vlakna ali nekoliko debelejši snopiči vlaken. Topografija mrež je lahko precej nepravilna, zato predstavljajo najzapletenejšo vrsto v tem delu obravnavanih ograditev [15,101].

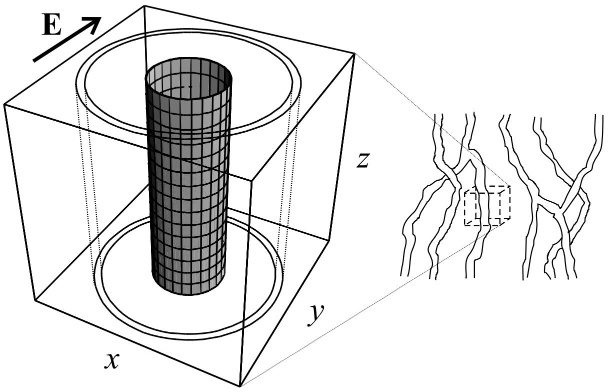

Slika 17 Shematski prikaz polimerne mreže (*desno*) in simulacijska škatla z valjastim vlaknom in eno izmed valjastih plasti (*levo*). Označena je tudi smer zunanjega polja **E**.

Najpomembnejša značilnost mrež je ta, da lahko že pri nizki koncentraciji uredijo okoliški tekoči kristal [5,26,39] in so kot take zanimive za uporabo v različnih optičnih elementih. V nadaljevanju si bomo ogledali učinke grobosti površine na ureditveno sposobnost mreže [102], topološke defekte [103], pojav preklapljanja orientacije molekul v zunanjem polju pri različnih mrežnih topografijah in paranematsko urejanje nad prehodom v izotropno fazo. Navedene pojave bomo spremljali tudi skozi opazljivke, kot so ^{2}H NMR, električna kapacitivnost in optična prepustnost.

Kot prvi korak k modeliranju polimerne mreže si oglejmo valjasto vlakno v simulacijski škatli s periodičnimi robnimi pogoji, kot kaže slika 17. Na ta način dobimo pravilno mrežo ravnih in vzporednih vlaken. Simulacije so bile — podobno kot v prejšnjem poglavju za kapljice — izpeljane v okviru modela Lebwohla in Lasherja. Površino vlakna tudi tukaj modeliramo z zamrznjenimi delci "duhovi", robni pogoji pa zajemajo planarno sidranje (vzdolž smeri vlaken, $\mathbf{z}$), homeotropno (pravokotno na lokalno površino) in delno ali v celoti neurejeno (groba površina). Stopnjo grobosti površine lahko kvantitativno podamo s parametrom urejenosti $\langle P_2\rangle_g$, ki predstavlja po absolutni vrednosti največjo lastno vrednost ureditvene matrike $\underline{Q}$, izračunane za spine "duhove". $\langle P_2\rangle_g = 1$ tako ustreza idealnemu planarnemu urejanju, $\langle P_2\rangle_g = -0.5$ idealnemu homeotropnemu, $\langle P_2\rangle_g \approx 0$ pa popolnoma naključni orientacijski porazdelitvi (merjeno vsakič glede na $\mathbf{z}$). Vmesne vrednosti ustrezajo delno urejeni — grobi — površini.

Pri izbranem polmeru vlakna $R = 5a$ in velikosti škatle $30\times30\times30$ delcev imamo v sistemu 24600 nematskih delcev in 840 površinskih delcev "duhov". Simulacije so bile zagnane iz popolnoma naključnih konfiguracij in uravnovešane vsaj 6×10^4 korakov na enak način kot v primeru PDLC kapljic. Nato je bilo 6.6×10^4 zaporednih konfiguracij uporabljenih za izračun povrečij. Ta zajemajo komponente ureditvene matrike $\underline{Q}$ in parameter $\langle P_2^z\rangle = \frac{1}{2}\left[3\langle(\mathbf{u}_i\cdot\mathbf{z})^2\rangle - 1\right]$, ki opisuje stopnjo ureditve glede

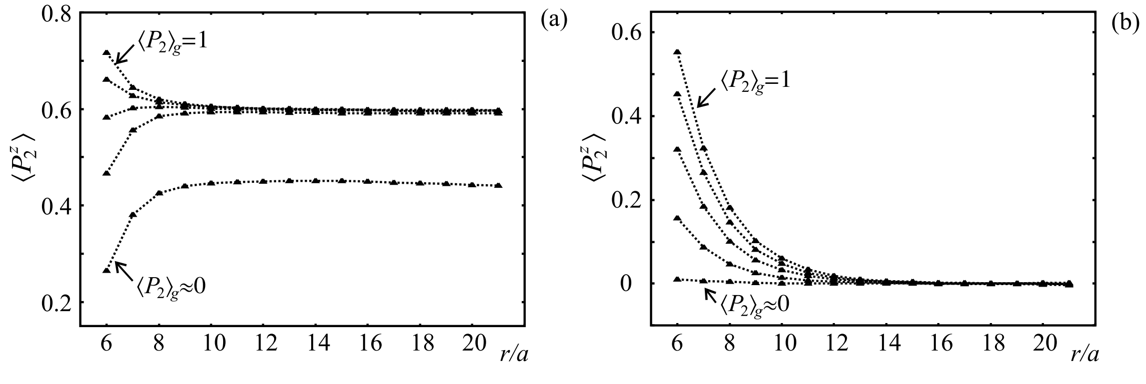

Slika 18 Pravilna mreža ravnih in vzporednih vlaken debeline $R = 5a$: odvisnost $\langle P_2^z\rangle$ od r (razdalje do središča simulacijske škatle); (a) nematska ($T^* = 1.0$) in (b) izotropna ($T^* = 1.2$) faza. Krivulje od zgoraj navzdol: $\langle P_2\rangle_g \approx 1.0$ (idealno planarno urejanje), 0.75, 0.50, 0.25 in 0 (naključna orientacijska porazdelitev).

na smer vlaken $\mathbf{z}$.

Slika 18 prikazuje radialne odvisnosti parametra urejenosti $\langle P_2^z \rangle$ za različne stopnje grobosti površine. V nematski fazi pri $T^* = 1.0$ za $\langle P_2 \rangle_g = 1$ je direktor usmerjen vzdolž $\mathbf{z}$, vrednost $\langle P_2^z \rangle$ pa sovpada s skalarnim parametrom urejenosti, S (pri izbrani $T^* = 1.0$ enaki $S \approx 0.6$). Vidimo lahko, da je S ob vlaknu rahlo povišan. V primeru delnega nereda $\langle P_2 \rangle_g < 1$ stopnja ureditve ob vlaknu upade, vendar je vlakno še vedno sposobno urediti nematik vzdolž $\mathbf{z}$. Zdi se, da to zmožnost izgubi šele za $\langle P_2 \rangle_g \approx 0$, saj direktor takrat več ni vzporeden $\mathbf{z}$. Pri višji temperaturi $T^* = 1.2$ (nad T^*_{NI}) tudi v sistemu vlaken opazimo paranematsko urejenje, ki je tem šibkejše, čim bolj grobo je vlakno. Vse spremembe v stopnji urejenosti ob vlaknu se dogajajo na razdalji korelacijske dolžine ξ (4), ki je reda velikosti nekaj a. Zgornje ugotovitve potrjujejo tudi spektri ^{2}H NMR, ki jih lahko izračunamo po metodologiji, razviti za nematske kapljice.

Do podobnih izsledkov glede grobosti vlakna in sposobnosti urejenja pridemo tudi za $\langle P_2 \rangle_g < 0$, homeotropno sidranje. V idealno homeotropnem primeru postane nematska ureditev še posebej zanimiva: v bližini vlakna pride v sistemu do tvorbe topoloških defektov (pravzaprav linij, ki tečejo vzdolž vlakna). Levi del slike 19 prikazuje direktorsko polje v na vlakno pravokotni ravnini, skupaj s pripadajočo stopnjo urejenosti S (oboje dobimo z diagonalizacijo lokalnih ureditvenih matrik

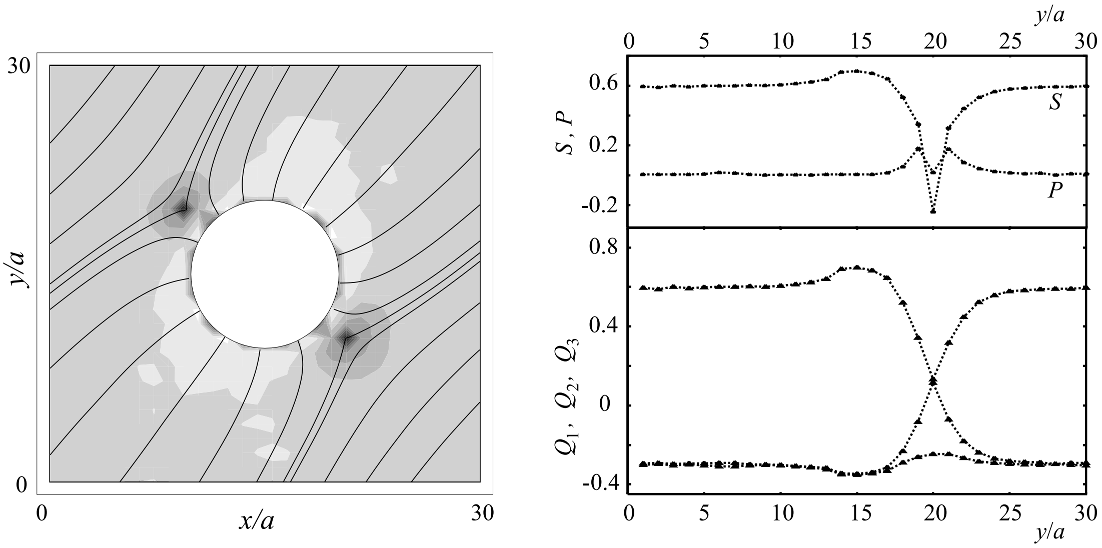

Slika 19 Nematsko urejanje v ob ravnem homeotropnem vlaknu. *Levo:* prerez direktorskega polja $\mathbf{n}(x, y)$ ($\mathbf{n}$ predstavljen s tokovnicami). Stopnja osenčenosti predstavlja skalarni parameter urejenosti $S(x, y)$ (temna območja ustrezajo nizkemu S). Par defektov moči $-\frac{1}{2}$ se pojavi blizu diagonale prikazanega prereza. *Desno:* lastne vrednosti ureditvene matrike $\underline{Q}$ (Q_1, Q_2 in Q_3), narisane skozi levega izmed obeh defektov vzdolž osi y. Zgornji del slike prikazuje pripadajoča poteka parametra urejenosti S in stopnje dvoosnosti P. Nesimetrijo glede na jedro defekta (to leži pri $y/a = 20$) povzroča prisotnost vlakna. Ostali parametri: $T^* = 1.0$ in $R/a = 5$.

$\underline{Q}$). Desni del slike 19 kaže obnašanje lastnih vrednosti $\underline{Q}$, ko prečkamo defekt. Vidimo, da je daleč od jedra defekta urejanje enoosno. Ko se bližamo jedru, začne stopnja urejenosti S padati, hkrati pa naraste dvoosnost P. V samem jedru je ureditev ponovno enoosna, vendar s $S < 0$, pri čemer je direktor usmerjen vzdolž smeri vlakna, $\mathbf{z}$. To obnašanje je v skladu s fenomenološkimi napovedmi [104,105]. Med drugim opazimo tudi, da do tvorbe defektov vselej pride blizu ene od diagonal simulacijske škatle. To lahko pripišemo zlasti odboju med defektoma, deloma pa tudi kolektivnim fluktuacijam v kockasti simulacijski škatli [168]. Topološko je v obravnavanem sistemu dopustna tudi ena sama defektna linija moči -1, vendar ni stabilna [24].

Oglejmo si še pojav preklapljanja orientacije molekul z zunanjim poljem. Sidranje naj bo idealno planarno vzdolž vlaken (osi z), zunanje polje $\mathbf{E}$ pa naj bo usmerjeno pravokotno nanje (vzdolž osi y) — slika 17. Obnašanje pravilnega sistema vzporednih vlaken v zunanjem polju je podobno obnašanju nematske celice (glej poglavje o fenomenološkem opisu nematika): pri višanju poljske jakosti do Fréederickszovega prehoda opazimo homogeno strukturo (h) z $\mathbf{n}||\mathbf{z}$, nad njim deformirano strukturo (d), nad saturacijskim prehodom pa zasičeno strukturo (s) z molekulami usmerjenimi v smeri polja $\mathbf{n}||\mathbf{E}||\mathbf{y}$. Ker sta kritični poljski jakosti za oba prehoda odvisni od jakosti sidranja, si bomo ogledali primere z različnim $w = \epsilon_g/\epsilon$. Tukaj ϵ_g pomeni jakost interakcije med molekulami nematika in polimernega vlakna, ϵ pa jakost interakcij med molekulami nematika samimi [enačba (10)].

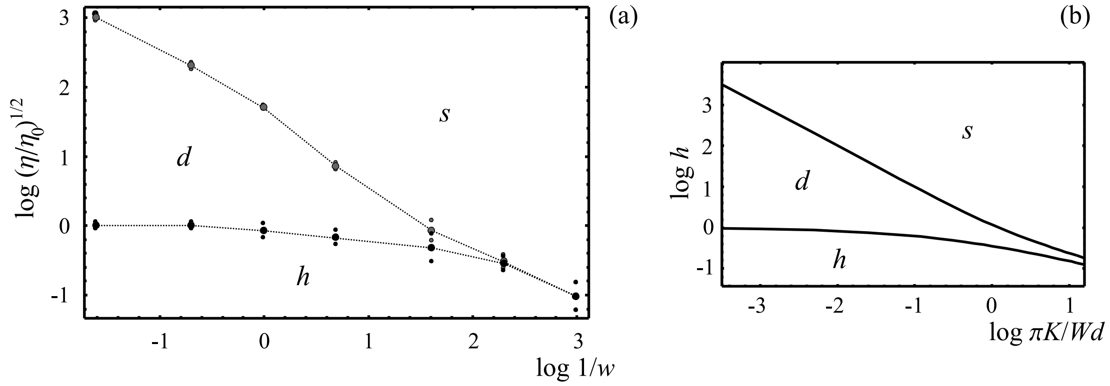

Slika 20 Pravilna mreža vzporednih vlaken in preklapljanje v zunanjem polju: (a) strukturni fazni diagram za $T^* = 1.0$ in $R/a = 5$; η_0 pomeni točko Fréederickszovega prehoda pri $w = 5$. (b) Primerljiv fazni diagram za navadno plast nematika (iz [115]); h je sorazmerna jakosti polja.

Simulacije so bile izvedene pri $T^* = 1.0$ v sistemu $30 \times 30 \times 30$ delcev s polmerom vlakna $R = 5a$. Pri danem w je bilo pri vsaki vrednosti η potrebnih 1.2×10^5 korakov za uravnovešanje in nadaljnjih 1.2×10^5 za izračun opazljivk. Simulacije so potekale tako, da je vrednost η naraščala postopoma od $\eta = 0$ do najvišje vrednosti (onstran saturacijskega prehoda), nato pa postopoma padala nazaj k $\eta = 0$, kar naj bi omogočilo razkritje morebitnih pojavov histereze. Pričakovana strukturna prehoda lahko iščemo z opazovanjem parametra $P_2^y = \frac{1}{2}[3\langle(\mathbf{u}_i \cdot \mathbf{y})^2\rangle - 1]$: če teče povprečje $\langle ... \rangle$ preko vsega vzorca, je P_2^y občutljiv na Fréederickszov prehod, če pa le po tanki plasti tik ob površini vlakna, pa na saturacijskega. Še bolj zanesljivo je opazovanje pripadajočega efektivnega odmika σ^y, saj fluktuacije P_2^y ob strukturnih prehodih opazno narastejo.

S slike 20 lahko razberemo območja stabilnosti treh napovedanih struktur, za primerjavo pa je prikazan enakovreden diagram za plast nematika [115]. Kvalitativno ujemanje med obema je dobro. V šibkem polju vselej opazimo homogeno strukturo h, v zelo močnem pa zasičeno strukturo s. Med njuni območji stabilnosti se vriva območje deformirane strukture d, ki postane pri šibkem sidranju (majhni w) zelo ozka. Kljub temu kaže, da neposrednega prehoda $h \leftrightarrow s$ ni, s tem pa tudi ne trojne točke v diagramu. Poleg tega ni opaziti histereze, iz česar sklepamo, da sta oba prehoda zvezna.

Kot kažejo slike elektronske mikroskopije [26,39], je topografija polimernih mrež precej bolj nepravilna, kot smo jo bili zmožni opisati s preprostim modelom s slike 17 (imenujmo ga "vzorec A"). Vlakna so lahko zavita in naključno razporejena po prostoru, vendar s še vedno dovolj dobro določeno povprečno smerjo. Prvi korak k takšni topografiji mreže predstavljajo ravna in vzporedna vlakna, ki so razporejena naključno po nekoliko povečani simulacijski škatli ("vzorec B"). Tudi v takem primeru pride v zunanjem polju do Fréederickszovega prehoda, vendar pri nižji poljski jakosti kot pri pravilni mreži z enako debelino in koncentracijo vlaken. Vzrok za tak premik je najti v porazdelitvi razdalj med vlakni, saj do Fréederickszovega prehoda pride, ko postane koherenčna dolžina zunanjega polja ξ_m primerljiva z najdaljšo izmed njih. Zaradi tega prihaja do preklapljanja molekulskih orientacij v vzorcu postopoma, in sicer najkasneje v področjih, kjer so vlakna razporejena nadpovprečno gosto.

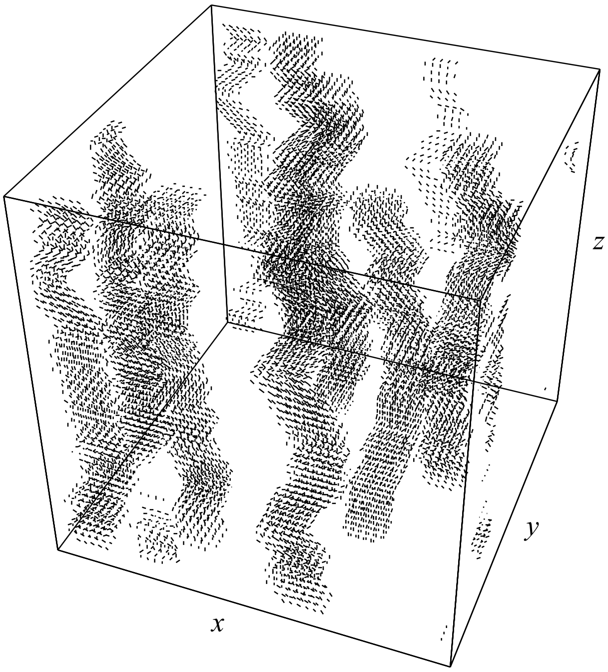

Slika 21 Polimerna mreža z neravnimi vlakni (vzorec C): delci "duhovi" predstavljajo togo mrežo. Sidranje na površini vlaken je planarno.

Najzapletenejši od vzorcev s polimernimi mrežami — “vzorec C” — vključuje neravna vlakna in je prikazan na sliki 21. Kot pri vzorcu B so bile simulacije izvedene v vzorcu 50 × 50 × 50 delcev z osmimi vlakni premera $R = 3a$ (usmerjenimi v povprečju vzdolž $\mathbf{z}$) ter s planarnim sidranjem jakosti $w = 1$ vzdolž lokalne tangentne smeri vlaken. Zdaj si bomo ponovno ogledali pojav preklapljanja v zunanjem polju, pri tem pa primerjali obnašanje topografsko različnih vzorcev A, B in C s približno enakimi koncentracijami polimernih vlaken (9%). V vzorcih B in C je bilo narejenih 8×10^4 simulacijskih korakov za uravnovešanje in 6.6×10^4 za računanje povprečij, v manjšem vzorcu vrste A (velikosti 18 × 18 × 18 delcev) pa je bilo uravnovešanje skrajšano na 6×10^4 korakov. Rezultate bomo predstavili v obliki izbranih eksperimentalnih opazljivk.

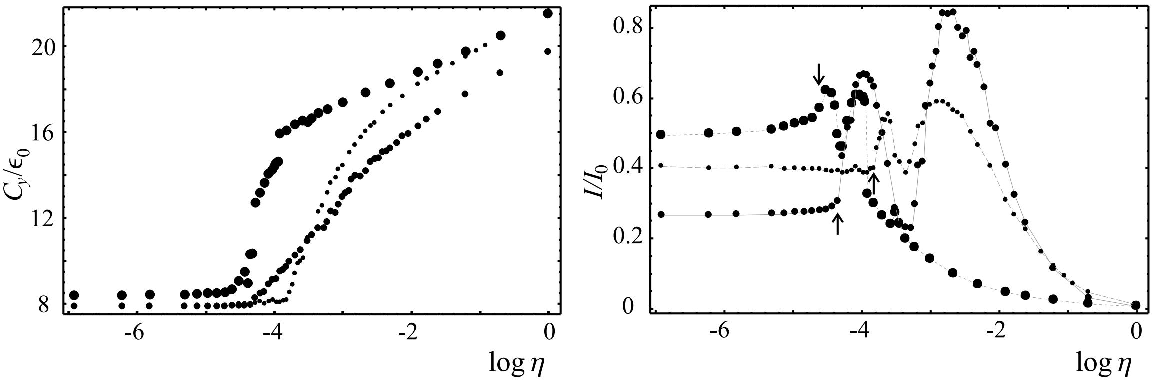

Slika 22 Preklapljanje orientacije molekul v zunanjem polju: meritve kapacitivnosti (*levo*) in intenzitete skozi vzorec prepuščene svetlobe (*desno*, I_0 označuje intenziteto vpadne svetlobe); vzorec A (majhne pike), vzorec B (večje pike) in vzorec C (največje pike). V desni sliki puščice označujejo kritične vrednosti η, kot jih odberemo z leve.

Začnimo z električno kapacitivnostjo C_y, opazovano vzdolž smeri zunanjega polja ($\mathbf{E}||\mathbf{y}$) — glej poglavje o eksperimentalnih opazljivkah. Slika 22 prikazuje odvisnost $C_y(\log\eta)$. V primeru idealne ureditve delcev bi dobili $C_y/\epsilon_0 = \epsilon_\perp$ za ureditev vzdolž smeri vlaken ($\mathbf{z}$) in $C_y/\epsilon_0 = \epsilon_{||}$ za ureditev vzdolž zunanjega polja, iz česar sledi, da lahko iz vedenja količine C_y izluščimo informacijo o orientaciji molekul v vzorcu. Tukaj pomenita $\epsilon_\perp$ in $\epsilon_{||}$ lastni vrednosti molekulskega dielektričnega tenzorja (v pričujoči simulaciji $\epsilon_\perp = 6.1$ in $\epsilon_{||} = 29.8$). S slike 22 lahko razberemo lego Fréederickszovega prehoda — ta zajame veliko število delcev — za vsakega izmed treh vzorcev, medtem ko saturacijskega prehoda C_y ne more razkriti. Fréederickszov prehod na prikazanih grafih sovpada s točko, kjer C_y občutno naraste [39]. Ocenjene kritične vrednosti so $\eta_A = 0.022 \pm 0.01$ za vzorec A, $\eta_B = 0.013 \pm 0.01$ za vzorec B in $\eta_C = 0.010 \pm 0.01$ za vzorec C. Kot že omenjeno, velja $\eta_B < \eta_A$ zaradi porazdelitve efektivnih razdalj med vlakni. Nadalje imamo $\eta_C < \eta_B$, kar izvira iz dejstva, da v vzorcu C delci pri nizkih η niso usmerjeni natanko vzdolž $\mathbf{z}$ in deluje magnetni navor nanje že za poljubno majhen η. Zaradi tega v vzorcu C pravzaprav ne smemo govoriti o ostrem Fréedrickszovem prehodu. Preklapljanje je najpočasnejše v vzorcu B (krivulja C_y najpoložnejša), kjer se nematik v delih vzorca z visoko gostoto vlaken uredi v smeri polja šele pri zelo visokih η. Povedati je treba, da je tudi tukaj zunanje polje zelo močno (glej oceno v prejšnjem poglavju) in da gre naraščanje C_y pri najvišjih η na račun povečevanja stopnje ureditve S [117], ne pa na račun reorientacije molekul.

Vzorec lahko postavimo tudi med prekrižana polarizator in analizator in merimo intenziteto prepuščene svetlobe (I), kot je bilo nakazano v poglavju o eksperimentalnih opazljivkah. Intenziteta I je sorazmerna $\sin^2(\Delta\Phi/2)$ (18), kjer $\Delta\Phi$ pomeni razliko med fazama rednega in izrednega žarka, ki se nabere, ko prepotujeta vzorec. Če v izbrani geometriji svetimo vzdolž smeri zunanjega polja, se količina $\Delta\Phi$ spremeni s končne vrednosti pri $\eta = 0$ do zelo majhne vrednosti za velike η, kar vodi do nihajočega obnašanja v odvisnosti $I(\eta)$ takoj, ko v vzorcu pride do preklapljanja molekulskih orientacij [116]. Tako obnašanje zares opazimo tudi na sliki 22, ki nudi enake zaključke glede kritičnih poljskih jakosti in hitrosti preklapljanja kot opazovanje C_y. Krivulje so bile simulirane za svetlobo valovne dolžine 632 nm, efektivno debelino vzorca 10 μm in lomna količnika nematika 1.5270 za redno polarizacijo ter 1.7445 za izredno (največja možna vrednost). Omenimo le še to, da se tudi izračunani spektri ^{2}H NMR dobro ujemajo z rezultati obeh predstavljenih eksperimentov.

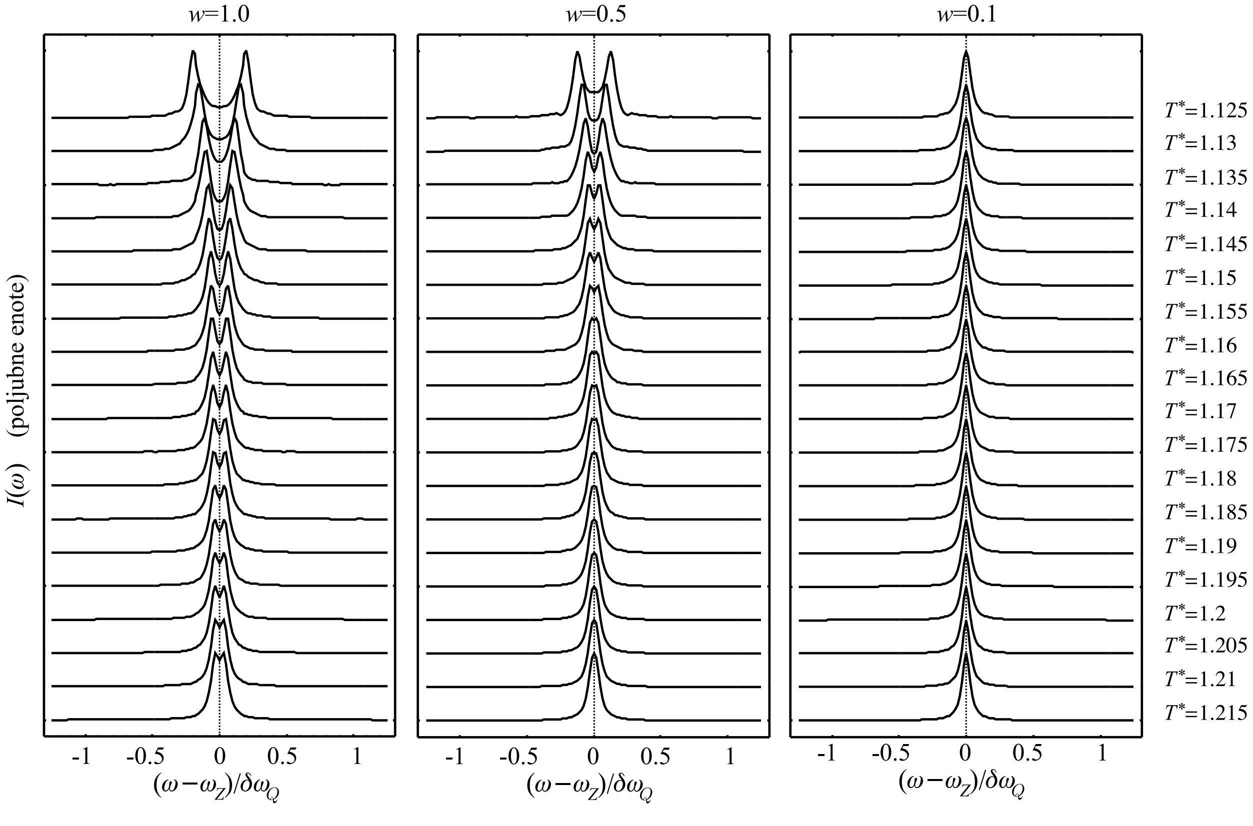

Slika 23 Paranematsko urejanje v vzorcu C: difuzijsko izpovprečeni spektri ^{2}H NMR v odvisnosti od T^* za različne jakosti sidranja: $w = 0.1$ (*levo*), $w = 0.5$ (*sredina*) in $w = 0.1$ (*desno*).

Zadnji od predstavljenih pojavov bo paranematsko urejanje nad temperaturo prehoda v izotropno fazo, ki ga povzroča površina. Opazili smo ga že v vzorcu A [slika 18 (b)], tu pa si bomo ogledali simulacije v vzorcu C (slika 21). Parametri simulacije so bili enaki kot v primeru preklapljanja, le da je bila izvedena za planarno sidranje z različnimi vrednostmi w, brez zunanjega polja ($\eta = 0$) in za različne temperature nad $T_{NI}^* = 1.1232$. Kot smo že opazili na sliki 18 (b), imamo blizu vlaken nezanemarljivo stopnjo nematske ureditve, ki pade proti nič na korelacijski razdalji $\xi \approx 5a$. Ta red lahko zaznamo z optičnimi metodami (med prekrižanima polarizatorjem in analizatorjem kakor zgoraj) [26] ali pa z ^{2}H NMR (slika 23). Spektri so bili računani v limiti hitre difuzije, polje spektrometra pa je bilo usmerjeno vzdolž $\mathbf{z}$. Dvovrhi spektri so posledica urejanja ob vlaknih, kvadrupolni razcep pa je tem večji, čim višja je stopnja ureditve. Vidimo, da razcep pada z višanjem temperature in z nižanjem jakosti sidranja, saj se s tem zmanjšuje tudi stopnja urejenosti. Do podobnih opažanj pridemo tudi pri simulacijah intenzitete prepuščene svetlobe.

Zaključki

V zaključku preglejmo glavne rezultate pričujočega dela, skupaj s še odprtimi vprašanji in nekaterimi smernicami za prihodnost. V delu smo se dotaknili izbranih problemov modeliranja ograjenih tekočekristalnih sistemov, v ta namen pa uporabili fenomenološki Landau-de Gennesov opis in, v še večjem merilu, mikroskopsko simulacijsko metodo Monte Carlo.

Izzvani z eksperimenti, ki kažejo na znatne elastične deformacije ob površini nematika, smo najprej obdelali urejanje ob stenah nematske plasti. V okviru Landau-de Gennesovega pristopa smo pokazali, da spreminjanje stopnje urejenosti ob površini lahko vodi do pojava lokaliziranih elastičnih deformacij, hkrati pa tudi do notranjega prispevka k površinskemu sidranju (oboje le takrat, če Frankove elastične konstante niso vse enake). Omenjene lokalizirane deformacije smo opazili le pri omejitvi na ravninske deformacije, ne pa tudi pri neravninskih zvojnih, in ne izvirajo iz spornega člena s pahljačno-upogibno elastično konstanto. Če sklopitev nematika z ograjujočo površino prilagodimo tako, da ekstrapolacijska dolžina zunanjega in notranjega sidranja doseže značilne eksperimentalne vrednosti okoli 100 nm, postanejo deformacije ob površini tako šibke, da z njimi ne moremo pojasniti eksperimentalno opaženih.

Zgornjo fenomenološko študijo smo nato dopolnili z mikroskopsko, temelječo na metodi Monte Carlo in modelu s šestkotniško mrežo ter prostorsko anizotropnimi interakcijami med induciranimi dipoli. Glavni namen te študije je bil podrobneje raziskati notranje sidranje, ki je pri dovolj nizkih stopnjah interakcijske anizotropije homeotropno in tudi takrat še vedno precej močno: pripadajoče ekstrapolacijske dolžine ℓ so mikroskopske — reda nekaj molekulskih razsežnosti. Poleg tega za razliko od eksperimentov v realističnih sistemih ℓ ne kaže znatne temperaturne odvisnosti, ko se bližamo prehodu v izotropno fazo. Navedena opažanja je moč pripisati preprostosti modela: nadaljnji koraki bi lahko zajemali opustitev mrežnega približka, kar bi omogočilo vključitev spreminjanja gostote blizu površine, ter opis grobih površin. Od obojega je pričakovati znižanje jakosti sidranja.

Zatem so bile obravnavane kompleksnejše vrste ograditev: nematske kapljice in nematiki z dispergiranimi polimernimi mrežami. Obeh smo se lotili s preprostim mikroskopskim mrežnim modelom Lebwohla in Lasherja, spet z uporabo metode Monte Carlo.

V primeru kapljic — najdemo jih v sistemih PDLC — smo obravnavali radialne in bipolarne robne pogoje ter se posvetili zvezi med numeričnimi rezultati simulacij in spektri ^{2}H NMR kot eni izmed možnih eksperimentalnih opazljivk. Razvita je bila metodologija za napoved spektrov v prisotnosti znatnega gibanja molekul — fluktuacij molekulskih dolgih osi ter translacijske difuzije (homogene in nehomogene), kvalitativno ujemanje z eksperimenti pa je dobro. Tudi urejujoči učinki zunanjega polja se jasno odražajo v računanih spektrih: zunanje polje molekule reorientira, a tudi zviša stopnjo urejenosti nematika. V poljih visoke jakosti pride do nematskega urejanja celo daleč nad temperaturo prehoda v izotropno fazo.

Zadnjo in najkompleksnejšo izmed obravnavanih ograditev so predstavljali nematiki z vključki polimernih mrež. Sprva smo se posvetili pravilni mreži ravnih in med seboj vzporednih vlaken ter vplivu grobosti njihove površine na ureditvene sposobnosti take mreže. Rezultati kažejo, da mreža ohrani svojo sposobnost urejanja nematika tako dolgo, dokler površina vlaken ni popolnoma neurejena. V primeru gladkih vlaken in homeotropnega sidranja v sistemu opazimo topološke defekte, katerih notranjo strukturo smo lahko razbrali iz rezultatov simulacij: jedro defekta obdaja prstan dvoosne ureditve, v kateri je stopnja urejenosti S zmanjšana, v samem jedru pa je ureditev enoosna, toda z negativnim S. Nadaljevali smo s študijami preklapljanja molekulskih orientacij z zunanjim poljem. Obnašanje pravilnega sistema vzporednih vlaken v zunanjem polju smo predstavili v faznem diagramu, iz katerega lahko razberemo premikanje Fréedericksovega in saturacijskega prehoda s spreminjajočo se jakostjo zunanjega sidranja. Obnašanje je podobno kot v navadni nematski plasti. Ogledali smo si tudi preklapljanje v vzorcih z bolj zapleteno topografijo mreže, kjer so bila ravna ali neravna vlakna nameščena po prostoru naključno. Preklapljanje smo spremljali z opazovanjem simuliranih spektrov ^{2}H NMR, električne kapacitivnosti in intenzitete prepuščene svetlobe. Vse navedene opazljivke kažejo, da igra topografija mreže polimernih vlaken pri procesu preklapljanja izjemno pomembno vlogo. Za konec smo si ogledali še paranematsko urejanje nad temperaturo prehoda v izotropno fazo. Nekatere od zgornjih zaključkov lahko prenesemo tudi v sorodne kompleksne sisteme: nematske gele in koloide.

Na koncu lahko rečemo, da je simulacijski del postregel s številnimi sicer že znanimi pojavi, vendar je pomembnost predstavljenih rezultatov in metod zlasti v tem, da so omogočili vzpostavitev povezave med podrobnostmi na mikroskopski ravni in makroskopskim obnašanjem vzorca. Zaradi majhnosti obravnavanih sistemov iskanje kvantitativnega ujemanja z eksperimenti za zdaj ni prav uspešno, kar pa se bo z naraščanjem razpoložljive računalniške moči s časom gotovo spremenilo.

* * *

1

Introduction

To those not familiar with the subject, the expression *liquid crystals* may at first seem somewhat self-contradictory. Indeed, the term refers both to liquid and solid-like properties of matter, and appears to suggest that in a liquid-crystalline substance both are manifested simultaneously. Without usually being aware of the very subtle nature of these complex materials, most people regularly use liquid crystal-based devices in everyday life. These devices mainly comprise various types of displays, ranging from simple seven-segment watch displays that became operational already in the early 1970s, to sophisticated color displays built into up-to-date laptop computers. The smallness and low energy consumption were the features that made such displays suitable for mass production, resulting in a subsequent boom in electronic industry. Other related applications are switchable windows and rapid light shutters, the latter being very promising in the field of optical telecommunications. Despite this vast development over the last decades, a conventional cathode-ray tube display (still cheaper than a state-of-the-art liquid-crystal display of comparable performance) was used to display results of the research presented in this thesis, and, eventually, also for typing it.

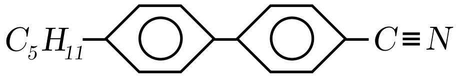

Figure 1.1 Structural formula of *4′-pentyl-4-cyanobiphenyl* (5CB), an elongated molecule showing liquid-crystalline behavior.

Roughly speaking, liquid crystals are anisotropic fluids made up of rodlike or discotic organic molecules. While the main liquid-like property is the ability to flow, the solid-like character comprises anisotropies of dielectric, magnetic, and optical properties, which all originate in the strong anisotropy of the effective molecular shape. The first liquid-crystalline compound — cholesteryl benzoate — was studied by the botanist Reinitzer [1] as early as in 1888, followed by Lehmann a year later [2]. Performing polarizing microscopy experiments, Reinitzer observed two first-order phase transitions upon heating the solid compound: first it melted into an unusual turbid fluid state, which at a higher temperature transformed into a clear liquid. Studying the intermediate turbid phase, Lehmann realized that it is birefringent, i.e., optically anisotropic, and called it *liquid crystal.* Today a rather wide collection of different liquid-crystalline phases is known and, as they are dwelling in between the ordinary solid and liquid phases, the preferred common description for them is *mesophases*. The mesophases can be divided into two broad categories, *thermotropics* and *lyotropics*. Thermotropics are one-component systems and have temperature-dependent phase behavior, while lyotropics are solutions of a liquid-crystalline solute in a solvent (e.g., water) and exhibit concentration-dependent phase behavior.

The simplest of all thermotropics are the *nematic* liquid crystals (*nematics*), owing their name to a translation from the Greek word $\nu\eta\mu\alpha$ ("thread") by Friedel who, in the early 1900s, observed the threadlike appearance of topological defects under a microscope between crossed polarizers [3]. Nematics consist of rodlike molecules whose elongated and rigid torso is typically formed by two or more aromatic rings, while the flexible limbs are usually made of alkyl chains (Fig. 1.1). Macroscopically, a nematic sample is fluid and, like in an ordinary liquid, there is no positional order in center of mass positions. There is, however, significant long-range orientational order in orientations of molecular long axes, and in a large (bulk) sample nematic molecules on the average align along a well-defined (but arbitrary) direction, denoted by a unit vector, the *director* **n** (see Fig. 1.2) [4]. Note that in ordinary nematics states described by **n** and −**n** cannot be distinguished. Moreover, at finite temperatures the ordering along **n** is not perfect. The corresponding degree of order decreases with increasing temperature. In absence of severe external constraints, such as confinement and electric or magnetic fields, the orientational distribution of molecules around **n** is uniform, corresponding to uniaxial symmetry. The optical axis in such *uniaxial* nematics then also coincides with **n**. Under strong external constraints, however, the uniaxiality in ordering may be lost and a second characteristic direction occurs in the mesophase, now called *biaxial*.

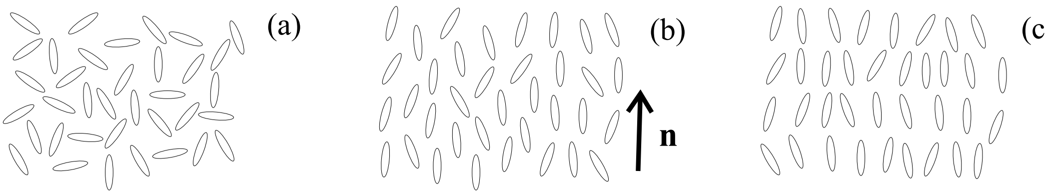

Figure 1.2 Molecular ordering in the isotropic (a), nematic (b), and one of the possible smectic phases (c). **n** denotes the nematic director.

When in a nematic sample temperature is increased far enough, a first-order phase transition takes place. The long-range orientational order is now lost and the resulting *isotropic* phase behaves as an ordinary liquid. If, on the other hand, temperature is decreased, either a direct transition to a solid or to one of the *smectic* mesophases can follow, depending on the exact nature of the liquid-crystalline species. On the average, in smectics molecular centers of mass are arranged into parallel layers (see Fig. 1.2), thereby exhibiting one-dimensional positional order, in addition to orientational order present already in nematics. The term "smectic" is common to a rich variety of mesophases and comes from the Greek expression for soap ($\sigma\mu\varepsilon\gamma\mu\alpha$), a substance also capable of forming thin molecular layers. In general, smectic phases possess two characteristic directions and are therefore optically biaxial. In this thesis, however, the emphasis will be given to thermotropic nematics. One of the reasons for this lies in the fact that it is mostly nematic materials that are currently being used for applicative purposes, while other mesophases are primarily a matter of fundamental research.

The behavior of nematics (as well as other mesophases) becomes even more interesting if they are *confined* to microcavities like droplets and pores [5], or simply in between two parallel plates. In such systems, the aligning tendency of solid substrates significantly affects the equilibrium molecular ordering, especially in *strongly confined* systems with a high surface-to-volume ratio. Solid substrates can impose different types of alignment or *anchoring*, the possibilities being planar, homeotropic, and tilted [6]. Close enough to the substrates surface-induced *paranematic* phase can persist even above the nematic-isotropic transition temperature. *Planar* alignment in the plane of the confining substrate can be achieved by unidirectional rubbing of the clean or coated substrate [7–10]. *Homeotropic* alignment (normal to the substrate), on the other hand, can be provided by treating the substrate with a surfactant [11–13], while *tilted* anchoring conditions can be achieved through oblique evaporation of silicon oxide onto glass plates [14]. Alternatively, directionless evaporation can result in a substrate with irregular surface topography, acting disorderly rather than orderly. Similar completely or partially random topography can be encountered on polymer surfaces, and depends sensitively on the polymerization parameters [15]. Analogous (dis)ordering effects can be expected also at a free nematic surface, or at the nematic-isotropic interface [16]. Indeed, in a liquid crystal intermolecular interactions are highly anisotropic, and missing-neighbor effects can account for the aligning tendencies at such interfaces [17]. The actual preferred orientation (the *easy axis*) is intimately related to individual properties and molecular structure of the given nematic species. The free-surface orienting effects are an intrinsic property of the nematic and are therefore often referred to as *intrinsic anchoring* (as opposed to the solid substrate-imposed *external anchoring* discussed above).

Under strong confinement, different easy axes at the opposing substrates (as in a slab) or more complex geometric constraints (in droplets and pores) give rise to a conflict in determining the average molecular orientation. In other words, the director becomes spatially dependent, $\mathbf{n} = \mathbf{n}(\mathbf{r})$, in order to meet all boundary conditions imposed by the confining substrates. Any deviation from the *homogeneous* bulk director profile with $\mathbf{n} \neq \mathbf{n}(\mathbf{r})$ represents an *elastic deformation*, accompanied by an increase in the deformation free energy [18–20]. In addition, if the actual surface molecular orientation is to deviate from the local anchoring easy axis, this is also penalized by an increase in free energy [21,22]. Then, the equilibrium director profile is the one minimizing the total free energy. Unlike in solids, the elasticity encountered in nematics is referred to as *curvature elasticity*. While still being able to flow (and thus unable to resist shear deformations), nematics are able to transmit substrate-imposed torques through the curvature of the director field. There is no characteristic length scale associated with such elasticity: the elastic distortion spreads smoothly throughout the sample. In certain geometries, however, the director field may contain places where the director — for topological reasons — cannot be defined. Such point, line, or wall-like singularities, accompanied by a strong variation in the degree of ordering, are called *topological defects* [4,23,24].

A further consequence of the non-spherical molecular shape is the anisotropy in the dielectric and magnetic susceptibility tensor of nematics. Consequently, in an external (electric or magnetic) field an orienting torque acts on nematic molecules, thereby allowing for a controllable variation of the director orientation [4,20]. At the same time, the orientation of the optical axis (**n**) is varied as well, which is the main effect liquid-crystalline optical devices are based on. Inevitably, external fields conflict with confining substrates, and — unless extremely strong — they are unable to reorient the nematic in the very vicinity of the confining wall. The thickness of this region is given by the *electric* or *magnetic coherence length* and decreases with increasing field strength [4].

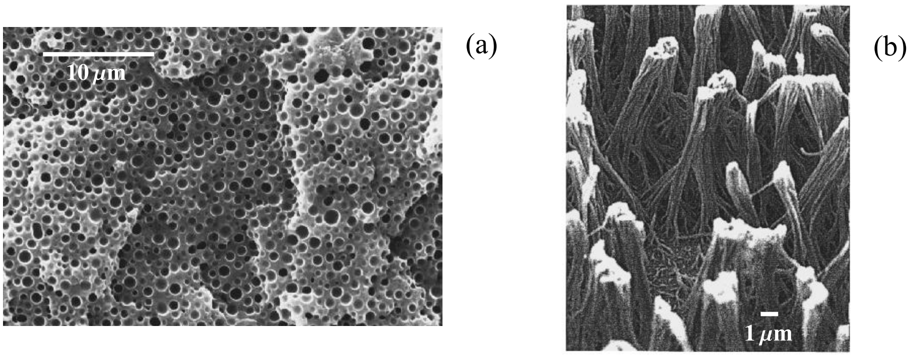

Figure 1.3 Scanning electron microscopy pictures taken after removal of the nematic. (a) PDLC sample with nematic droplets [25], (b) polymer networks dispersed in nematics [26].

The simplest type of confinement can be encountered in every nematic cell, including displays, where the liquid crystal is sandwiched between two flat (usually parallel) plates, or in any thin (also free-standing) liquid crystal film. However, more recent developments in material science have provided novel confining matrices, which are attractive both for basic research, as well as for applicative purposes. *Nucleopore* and *Anopore membranes* are thin membranes penetrated by channels providing cylindrical confinement, the channel radii being of the order of 1 μm [27]. *Polymer-dispersed liquid crystals* (PDLCs) consist of roughly spherical nematic droplets, with typical radii from a few hundred Ångström to well above a micron, embedded in a polymer matrix [see Fig. 1.3 (a)] [28]. They can be used to design switchable windows, projection devices, reflective holographic displays [29] etc. Low concentration *polymer networks* consist of thin polymer fibers (even nanometric in diameter), or of somewhat thicker fiber bundles [see Fig. 1.3 (b)]. They are capable of orienting the surrounding liquid crystal [30], being useful in building bulk-stabilized optical switches [31], and even allow for the formation of paranematic order [26]. Other types of complex confinement include also *filled nematics* and *aerogels*, where agglomerates of nanometric silica particles are dispersed in a nematic host, dividing it into several domains, each with its own local order [5].

Until now, confined systems have been studied extensively both theoretically and experimentally. Theoretically, most widespread are the analyses performed within the *phenomenological Landau-de Gennes theory*, which is based on describing the rather complex molecular ordering by introducing a macroscopic order parameter. Then a free energy functional is constructed [16,32] and minimized with respect to order parameter profiles for the given boundary conditions. The second class of approaches stems from the statistical mechanics-based *density functional theory.* Here the molecular ordering is described in terms of the density and orientational distribution function profiles, the equilibrium being found by minimizing the grand potential with respect to these profiles [33–35]. Unlike the phenomenological Landau-de Gennes theory, this approach includes microscopic intermolecular interactions and is therefore somewhat more fundamental.

With the advent of fast computing machines in the late 1940s, the field of molecular simulations began to burgeon. Indeed, from then on it was possible to simulate an ensemble of particles with microscopic degrees of freedom, such as particle position and orientation, and express the simulation output in terms of macroscopic thermodynamic averages and experimental observables. In such studies, the system evolution can be provided either from integrating Newton's equations of motion (*molecular dynamics simulations* [36]), or performing an appropriately weighted random walk in phase space (*Monte Carlo simulations* [37]). Both approaches are based on intermolecular interactions and are in ergodic systems supposed to yield equivalent results for thermodynamic averages.

Experimentally, *polarizing microscopy* was one of the first tools used for the study of liquid crystals [1,2], whereby the sample is put between two crossed polarizers and the transmitted light pattern (or just the intensity) is analyzed. The method relies on the birefringence of the liquid-crystalline material, in particular on its molecular orientation-dependent index of refraction. It has been successfully applied, e.g., to distinguish between different director structures in supramicron confined systems [38], to detect paranematic order in a system with dispersed polymer networks [26], as well as for investigations of defects [23], to name just a few examples. Similarly, *capacitance* measurements reckon on the anisotropy of the static dielectric constant of the material and can therefore give information on significant molecular reorientation in the sample, such as director switching in an external field [39]. Yet another experimental technique is the *deuterium nuclear magnetic resonance* (^{2}H NMR) [5]. It is extremely powerful for the recognition of nematic structures, especially in submicron cavities not accessible to optical techniques due to limitations set by the light wavelength [40]. The method can provide information on molecular ordering either through spectra governed by the molecular orientation and order-dependent quadrupolar splitting, or through nuclear spin relaxation phenomena [5,41]. A further optical technique is the *second harmonic generation* (SHG) which is a non-linear optical phenomenon and — contrary to the previous "bulk" techniques — gives information on molecular ordering in a thin subsurface layer [42]. Therefore, combined with conventional "bulk" methods, it is suitable for investigations of possible subsurface variations in molecular orientation [43]. Similar information on molecular alignment in thin films can be extracted also from the characteristics of reflected or transmitted polarized light in *ellipsometry* measurements [44]. Information on surface anchoring strength can be deduced from *dynamic light scattering* experiments, analyzing the light scattered by collective director fluctuations in a nematic confined to a cell [45] or to cylindrical pores [46]. Further, *calorimetry* (i.e., measurements of the heat capacity) has been applied to study phase transitions, also in confined systems [47].

This thesis aims at covering some selected modeling problems in the physics of strongly confined liquid crystals. Two main objectives will be followed: (i) a better understanding of mechanisms driving the nematic ordering close to an interface (still not fully understood as of now) and (ii) gaining more insight into nematic ordering in complex (even irregular) types of confinement. The geometries treated here will include a simple nematic slab [to cover objective (i)], nematic droplets (as encountered in ordinary and holographic PDLCs, covering objective (ii)], and nematics with dispersed polymer networks [objective (ii); related systems comprising colloids and gels]. Especially the two latter confinement types are particularly interesting also for applicative purposes, as already mentioned. In the analysis, phenomenological Landau-de Gennes-type modeling and simple large-scale molecular simulations will be combined. Therefore, the next Chapter will be devoted to these approaches, as well as to methods used for calculating selected experimental observables from the simulation data.

Starting with the simplest type of confinement, Chapter 3 will be dealing with molecular ordering in a thin nematic slab, giving particular emphasis to variations of the degree of nematic order, as well as to the resulting intrinsic anchoring and subsurface deformations. In fact, a number of experimental investigations [43,48–51] shows that liquid crystal molecules in the surface layer can have an orientation different from that in the bulk material. In some cases this can be attributed to the variation of nematic order [50,51] and biaxiality [43]. On the other hand, theoretical predictions about subsurface deformations have been published by different groups, mainly in connection with the splay-bend (K_{13}) elastic constant introduced long ago in the Landau-de Gennes phenomenological description [52,53]. As the splay-bend contribution to the elastic free energy can be shown not to be bounded from below [54], an additional higher-order term is to be included in the free energy density for stabilization [55–58], producing a strongly localized (but finite) subsurface deformation. Based on elastic theory and yielding strong deformations, this description raised many questions and was followed by alternatives avoiding the strong deformations [59–61]. Possible variations of the nematic order were not taken into account, and tacitly the scalar order parameter was assumed constant. More recent macroscopic considerations indicate that for an ideal flat nematic interface with a step-like density profile and no order variation $K_{13} = 0$ holds [62–65]. This then apparently solves the problem of strong subsurface deformations in the macroscopic description, but does not specify the microscopic source of deformations observed experimentally. However, a nonzero K_{13} is recovered if one allows either for a variation of density close to the nematic interface, or for a variation in the degree of nematic order [66,67]. The analysis presented in this Chapter will first focus on planar deformations, allowing for order (but not density) variations [68], aiming to explore the coupling between subsurface order variations and elastic deformations similar to those induced by the splay-bend elastic contribution in case of constant nematic order. For this purpose, the free energy will be expanded only up to first spatial derivatives of the order parameter, thereby explicitly avoiding the controversial splay-bend constant. Complementary analyses in a similar system have been performed also by other authors [50,51,69,70]. In addition, the present analysis will be extended to twist deformations [71].

The second part of Chapter 3 will still be concerned with the nematic slab, however, omitting the phenomenological description used in the first part and replacing it with a simple microscopic hexagonal lattice model presented in Ref. [17]. According to Ref. [17], the essential mechanism in aligning nematic molecules close to an interface seems to be the competition between intrinsic and external anchoring, the same conclusion coming also from the density functional approach [72]. Therefore, in this Chapter intrinsic anchoring will be investigated in some more detail. Like in Ref. [17], the simple hexagonal lattice model will be considered, which — combined with the spatially anisotropic induced dipole-induced dipole interaction — can reproduce the intrinsic anchoring at a nematic interface. The current analysis will be extended to nonzero temperatures, performing Monte Carlo simulations in the abovementioned model system. In particular, the intrinsic anchoring strength, including its temperature dependence, will be estimated by imposing a bend deformation in a hybrid cell-like system. In the past, intrinsic anchoring has been studied, e.g., in a pseudomolecular continuum approach with ellipsoidal molecules [73], analyzing a nematic-vapor or nematic-isotropic interface for Gay-Berne particles [74–78], and considering a system of hard ellipsoids in contact with a hard wall [79,80]. The anchoring energy (if reported) mostly shows that anchoring reproduced by these model systems is rather strong, exceeding experimental values [6] by one or two orders of magnitude. Moreover, simulations in similar systems yield different anchoring easy axes for intrinsic anchoring [75,76], depending sensitively on parameters entering the intermolecular potential [78]. A number of other (zero-temperature) lattice or continuum approaches has also been devised, mainly to study subsurface deformations in nematics [81–83]. Further, molecular dynamics simulations of particles interacting via the Gay-Berne potential show a substrate-induced spatial variation of the nematic scalar order parameter, accompanied by density modulations and smectic ordering [84–87], seen also experimentally [88,89].

Moving now to more complex confining geometries, Chapter 4 will cover nematic ordering in spherical PDLC nematic droplets. The molecular ordering in such confined systems is affected by the competition between ordering effects of the polymer matrix (anchoring) and of external fields, plus by disordering temperature effects. Depending on the polymer matrix and on the surface treatment methods, different director structures — including topological defects — can be encountered inside droplets. The discussion in this Chapter will be limited to *radial* [40,38] and *bipolar* droplets [38,40,90] with homeotropic and planar anchoring conditions, respectively (see Fig. 1.4). Applying an external electric or magnetic field, additional ordering effects can be observed [40,90], and turn out to be of great importance for technical applications. Experimentally, deuterium nuclear magnetic resonance (^{2}H NMR) [40,90] and polarizing microscopy [38] are the usual techniques to study PDLCs. From the theoretical point of view, however, Landau-de Gennes-type elastic continuum approaches [5] and Monte Carlo (MC) simulations [91] have been widely used to study PDLC in a variety of physical situations, including ellipsoidal droplets [25,92]. The simulations were mostly based on the simple Lebwohl-Lasher lattice model [93]. In particular, the MC technique has proved to be a powerful method not only for investigating the thermodynamical behavior of confined nematics, but also for the prediction of quantities directly observable in experiments. The observables simulated to date include static ^{2}H NMR spectra and polarizing microscopy patterns, thereby bridging the gap between simulation and experiment [91,94]. Chapter 4 will present a novel and widely applicable methodology for the calculation of ^{2}H NMR spectra that also starts from MC configurations, but takes into account dynamical effects as well [95]. These include fluctuations of molecular long axes and translational molecular diffusion (also spatially inhomogeneous [96,97]). A many-bipolar droplet sample will also be considered [97]. To conclude this Chapter, external field-induced changes in spectra will be studied in great detail [98]. Note that analyses presented in Refs. [99,100] already deliver thorough studies of external field effects in radial and bipolar droplets, containing also the corresponding ^{2}H NMR spectra, but none of these studies presents a line shape calculation in the presence of significant molecular motion.

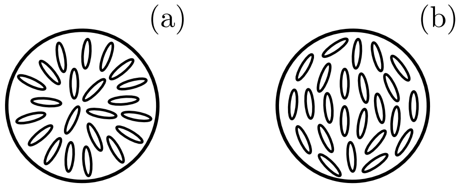

Figure 1.4 Director configurations in a PDLC droplet: (a) radial, (b) bipolar.

The following Chapter 5 will be concerned with nematic samples containing dispersed polymer networks. These can be topographically quite irregular and, consequently, this is the most complex confinement type presented in the thesis. Having a rather high surface-to-volume ratio, even at low network concentrations these composite systems are similar to "ordinary" confined systems with "closed" cavities [5]. Again, apart from exhibiting a variety of interesting ordering and confinement-related phenomena, composite materials like liquid crystal-dispersed polymer networks are promising also for the construction of novel bulk-stabilized electrooptical devices, which are usually based on the *switching* phenomenon. This phenomenon consists of changing the molecular orientation — initially imposed by the polymer network — by applying an aligning external electric field. Above a certain threshold the net molecular orientation changes, which can be observed through changes in optical transmission, electric capacitance, or by ^{2}H NMR spectroscopy [31,39]. Both the nature of the switching process and the performance of electrooptical devices are intimately related to the anchoring and ordering conditions at the fiber surface, as well as to the topography of the network. These properties can all be regulated during the network formation process [15,101], and by surface treatment after the network has been formed. The existing experimental studies were usually accompanied by phenomenological (Landau-de Gennes-type) analyses [5,26,31,39], but so far almost nothing has been done for such network-like confinement at the microscopic level. For all these reasons here a thorough microscopic simulation study of the orientational coupling between polymer fibers and the surrounding liquid crystal will be presented. Again, the analysis will be based on the Lebwohl-Lasher model [93], focusing on polymer networks with a well-defined fiber net direction (as in Fig. 1.3), and on effects of roughness at the fiber surface [102]. Furthermore, for homeotropic anchoring, due to topological constraints defects in nematic ordering can be expected to form [103]. Their inner structure will then be explored and compared with the existing phenomenological studies [104,105]. Moreover, the switching process in an external field will be simulated and the role of network irregularities in switching characteristics (threshold etc.) will be examined. For a regular polymer fiber array (also applicable to model colloidal crystals), a simple stability phase diagram will be derived for the director structures observed in an external field. Finally, paranematic surface-induced ordering above the bulk nematic-isotropic transition temperature will be explored in the system. For practical purposes, the simulation output will be expressed in terms of selected experimental observables, that is ^{2}H NMR spectra, electric capacitance, and transmitted intensity of polarized light.

The final Chapter — the Conclusion — will summarize the main achievements and findings presented in the thesis, together with open problems and possible future directions.

2

Theoretical background

In this Chapter a brief review of theoretical and simulation approaches for treating confined nematics will be given, together with selected experimental methodologies applicable to these systems.

2.1 Phenomenological Landau-de Gennes theory

Unlike in rare gases or idealized solids, in liquids (including liquid crystals) a full statistical mechanics treatment is highly nontrivial. On the other hand, with present computing power also molecular simulation studies of macroscopic liquid samples are still not within reach. In addition, very often the detailed microscopic description of the system is not even necessary to predict its macroscopic properties sufficiently well. Therefore, in such cases a phenomenological Landau-type description can be suitable. Within this description type, an appropriate macroscopic *order parameter* must be introduced first. The order parameter is supposed to reflect the microscopic state of the system and should be in agreement with its symmetry. The equilibrium state of the system is then searched for by minimizing the appropriate thermodynamic potential with respect to the order parameter.

2.1.1 Nematic order parameter

An isotropic liquid possesses neither positional nor orientational order and has thereby the highest possible symmetry. The nematic phase, on the other hand, is orientationally ordered, while positional ordering is still absent. A smectic phase, however, possesses both orientational and positional long-range order. In the following we are going to omit smectic phases and treat exclusively nematics. Consequently, an order parameter containing information on solely orientational ordering of molecules will be sufficient to characterize nematics and distinguish them from isotropic liquids.

Nematics consist of elongated molecules whose orientations can be characterized by unit vectors **u** along the molecular long axes. Due to rapid tumbling, the effective molecular shape is cylindrically symmetric. For the same reason, the molecular "head" and "tail" also cannot be distinguished on the average, although the head-tail symmetry is not an inherent property of such molecules. Consequently, nematic molecules can be regarded as directionless objects with a well-defined orientation (note that terms *direction* and *orientation* are not used as synonyms here). In a reference frame where the z-axis is chosen to coincide with the director $\mathbf{n}$, molecular orientations $\mathbf{u}$ for each molecule can be defined by the polar and azimuthal angles, θ and ϕ, respectively, with $\cos\theta = \mathbf{n}\cdot\mathbf{u}$. Then the state of molecular alignment can be described by an orientational distribution function $f(\theta,\phi)$, giving the probability to find molecules oriented within a solid angle $d\Omega$, $\Omega^{-1}\int f(\theta,\phi)d\Omega$. The distribution $f(\theta,\phi)$ should be normalized so that $\Omega^{-1}\int f(\theta,\phi)d\Omega = 1$, if integrated over the whole solid angle. In an unconstrained sample $f(\theta,\phi)$ is *uniaxial* — axially symmetric with respect to $\mathbf{n}$ — and hence ϕ-independent. In such uniaxial nematics $f = f(\theta)$ can be expanded as

$$f(\theta) = \sum_{n=0}^{\infty} f_n P_n(\cos\theta), \tag{2.1}$$

where $P_n(x)$ is the nth Legendre polynomial and $f_n = (2n+1)\Omega^{-1}\int f(\theta)P_n(\cos\theta)d\Omega$ are the expansion coefficients. The monopole term is a constant, $f_0 = 1$, and therefore not sensitive to any type of orientational molecular ordering. Hence, higher-order terms are to be considered in the quest for an appropriate order parameter. Given the head-tail symmetry of the nematic phase, $f(\theta) = f(\pi-\theta)$ holds, which results in $f_n = 0$ if n is odd and in $f_n \neq 0$ otherwise. The first nonzero contribution thus comes from the quadrupolar term

$$f_2 = 5\Omega^{-1}\int f(\theta)P_2(\cos\theta)d\Omega = 5\langle P_2(\cos\theta)\rangle \equiv 5S, \tag{2.2}$$

defining the *scalar order parameter* $S = \langle \frac{1}{2}(3\cos^2\theta - 1)\rangle$, where the average $\langle ...\rangle$ is to be performed over an ensemble of molecules. The order parameter defined in this way is able to quantify the degree of nematic ordering with respect to $\mathbf{n}$: in a perfectly aligned nematic with $\mathbf{u}||\mathbf{n}$ one has $S = 1$, while in the isotropic phase with $f(\theta)$ uniform also in θ, $\langle\cos^2\theta\rangle = \frac{1}{3}$ holds and the order parameter vanishes, i.e., $S = 0$. A meaning can be assigned also to negative values of S; $S = -\frac{1}{2}$ corresponds to perfect ordering in the plane perpendicular to $\mathbf{n}$. Up to the first nontrivial term the orientational distribution can now be rewritten as

$$\begin{aligned} f(\theta) &= 1 + 5SP_2(\cos\theta) = 1 + \frac{5S}{2}\left[3(\mathbf{n}\cdot\mathbf{u})^2 - 1\right] \\ &= 1 + \frac{5S}{2}\left[3n_i n_j - \delta_{ij}\right]u_i u_j = 1 + 5\,\mathsf{Q}_{ij}u_i u_j, \end{aligned} \tag{2.3}$$

(assuming summation over repeated indices), where Q given by

$$\mathsf{Q} = \frac{S}{2}\left[3\,\mathbf{n}\otimes\mathbf{n} - \mathsf{I}\right] \tag{2.4}$$

is the *tensorial order parameter* [4] — the quadrupolar moment of the orientational distribution $f(\theta)$ — and I the identity matrix. The Q-tensor contains the information both on the average molecular orientation $\mathbf{n}$ and on the degree of order S.

Alternatively, nematic ordering can be described also in terms of the symmetric and traceless *ordering matrix* [4],

$$\underline{Q} = \frac{1}{2}\left[3\langle \mathbf{u} \otimes \mathbf{u} \rangle - \mathsf{I}\right], \tag{2.5}$$

where the eigenvalue with the largest absolute value can be identified as S and the corresponding eigenvector as $\mathbf{n}$. In the uniaxial case, the other two eigenvalues are then both equal to $-\frac{1}{2}S$ and the eigenvectors perpendicular to $\mathbf{n}$.

Under external constraints such as electric and magnetic fields, or severe confinement, elastic deformations can break the cylindrical symmetry of the $f(\theta, \phi)$ distribution function assumed so far. In addition to the director $\mathbf{n}$, two additional characteristic directions appear in the system, $\mathbf{e}_1$ and $\mathbf{e}_2$, forming an orthonormal triad together with $\mathbf{n}$. In such *biaxial* nematics the tensorial order parameter becomes somewhat more complicated and reads

$$\mathsf{Q} = \frac{S}{2}\left[3\,\mathbf{n} \otimes \mathbf{n} - \mathsf{I}\right] + \frac{P}{2}\left[\mathbf{e}_1 \otimes \mathbf{e}_1 - \mathbf{e}_2 \otimes \mathbf{e}_2\right], \tag{2.6}$$

introducing $P = \frac{3}{2}\langle \sin^2\theta \cos 2\phi \rangle$ as the *biaxiality.* Diagonalizing the ordering matrix (2.5) now gives three eigenvalues that are different, S, $-\frac{1}{2}(S{+}P)$, and $-\frac{1}{2}(S{-}P)$, the respective eigenvectors being $\mathbf{n}$, $\mathbf{e}_1$, and $\mathbf{e}_2$. The ordering matrix and the Q tensor both consist of nine elements, but are symmetric and traceless by construction, hence only five out of nine elements are independent. This agrees with the fact that five parameters are enough to determine the orientational distribution $f(\theta, \phi)$ (up to the quadrupolar term): the two angles defining $\mathbf{n}$, the scalar order parameter S, one further angle to determine $\mathbf{e}_1$ (or, alternatively, $\mathbf{e}_2$), and the biaxiality P.

The microscopic order represented by the order parameter Q (or by the ordering matrix) is also reflected in macroscopic quantities like dielectric or magnetic susceptibility χ, as well as in the index of refraction. In an anisotropic medium like nematics, χ is a tensorial quantity and is closely related to the order parameter Q. Denoting the eigenvalues of $\underline{\chi}$ by χ_1, χ_2, and χ_3 (the corresponding eigenvectors coinciding with $\mathbf{e}_1$, $\mathbf{e}_2$, and $\mathbf{n}$), one can write

$$\underline{\chi} = \frac{2}{3}\chi_a\left[\frac{S}{2}(3\,\mathbf{n} \otimes \mathbf{n} - \mathsf{I})\right] + \chi_b\left[\frac{P}{2}(\mathbf{e}_1 \otimes \mathbf{e}_1 - \mathbf{e}_2 \otimes \mathbf{e}_2)\right] + \chi_i \mathsf{I}. \tag{2.7}$$

Here $\chi_a = \chi_3' - \frac{1}{2}(\chi_1' + \chi_2')$ is the anisotropy of the molecular susceptibility, i.e., the anisotropy for a perfectly ordered nematic ($S = 1$), where $\chi_k' S = \chi_k$ (recall that χ_k are macroscopic parameters obtained at finite temperatures and $S < 1$). Further, $\chi_b = \chi_1'' - \chi_2''$ is nonzero in case of biaxial ordering ($\chi_k'' P = \chi_k$) and $\chi_i = \frac{1}{3}(\chi_1 + \chi_2 + \chi_3)$ denotes the average susceptibility, i.e., its isotropic part.

2.1.2 Nematic-isotropic phase transition

In *phase transitions* matter undergoes changes in microstructure and symmetry. A phase transition is accompanied by an abrupt change of a macroscopic observable like density, electric or magnetic polarization, or similar. While the relevant thermodynamic potential — determining the equilibrium state in a system for given parameters (e.g., free energy F for well-defined temperature, volume, and particle number) — remains continuous across the transition, its derivatives may not. Phase transitions characterized by a discontinuity in, e.g., entropy $\mathcal{S} = -(\partial F/\partial T)_V$, are referred to as *discontinuous* (or *first-order*), while the ones with no discontinuity in $\mathcal{S}$ are called *continuous* (or *second-order*). As opposed to continuous phase transitions, discontinuous transitions present also a discontinuity in the aforementioned macroscopic observable playing the role of the order parameter. In addition, the possible discontinuity in entropy, $\Delta\mathcal{S}$, results in an exchange of *latent heat* $\mathcal{Q} = T_c\Delta\mathcal{S}$, where T_c stands for the transition temperature. Moreover, metastable states can be found in the vicinity of discontinuous transitions.

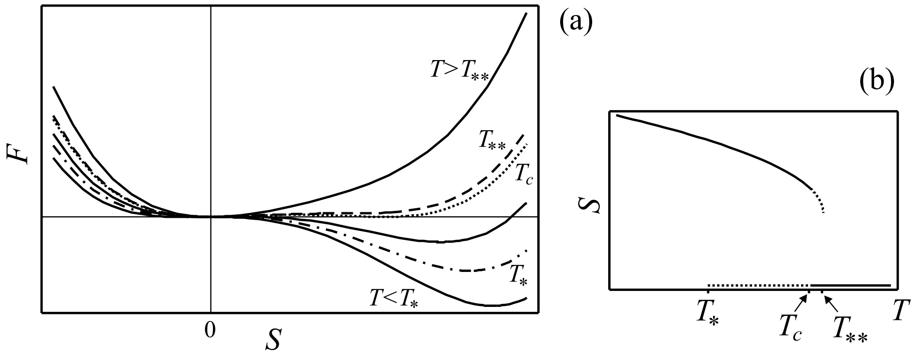

Figure 2.1 Nematic-isotropic transition: free energy vs. order parameter at different temperatures (a), equilibrium order parameter vs. temperature (b).

The macroscopic observable sufficient to characterize uniaxial ordering in a bulk nematic sample is the scalar order parameter S introduced in the previous Section. Experimental studies have shown that the nematic-to-isotropic transition is accompanied both by a discontinuous drop in S and by absorption of latent heat [4]. Moreover, metastable supercooled isotropic and superheated nematic phase could be observed as well. These findings all indicate that the nematic-isotropic (NI) transition is discontinuous. Following the Landau description of phase transitions, the free energy density of the system is to be written in terms of the order parameter in form of a simple polynomial expansion [32]. Close enough to the transition this expansion converges and may hence contain a small number of lowest-order terms, that is

$$f_0(S,T) = f_i(T) + \frac{1}{2}a(T - T_*)S^2 - \frac{1}{3}BS^3 + \frac{1}{4}CS^4 \tag{2.8}$$

Here $a > 0$, $B > 0$, and $C > 0$ are positive phenomenological material constants, while T_* is the lowest temperature still allowing for the existence of the supercooled isotropic phase. Typically, a is of the order of 10^5 J/m^{3}K, while B and C range around few times 10^6 J/m^3. Further, f_i denotes the free energy density of the isotropic phase. The expression (2.8) ensures with $C > 0$ that F is bounded from below and agrees with the symmetry of the order parameter S. In particular, odd-order S^3-term is allowed because of the non-equivalence of S and $-S$, while the linear S-term is prohibited so as to obtain $S = 0$ in the isotropic phase if external fields are absent. Unlike constants B and C, the proportionality constant of the S^2-term $a(T - T_*)$ is taken to be temperature-dependent and therefore plays an important role in driving the phase transition. The equilibrium in the system is then found by minimizing the free energy $F(S,T) = \int f_0(S,T)dV$ [see Fig. 2.1 (a)] at fixed temperature with respect to S, yielding

$$S(T) = \begin{cases} 0, & T > T_c, \\ \frac{B}{2C}\left(1 + \sqrt{1 - \frac{4aC}{B^2}(T - T_*)}\right), & T < T_c. \end{cases} \tag{2.9}$$

The full $S(T)$-dependence is shown in Fig. 2.1 (b). Analyzing the stability of the solutions given in Eq. (2.9) leads to the following relations: the phase transition temperature T_c is related to T_* via $T_c = T_* + 2B^2/9aC$, while the highest temperature of the superheated nematic phase T_{**} is given by $T_{**} = T_* + B^2/4aC$. Therefore, below T_* only the nematic phase can exist. For $T_* < T < T_c$ the nematic phase is stable and the isotropic metastable, and the opposite for $T_c < T < T_{**}$. Above T_{**} only the isotropic phase is stable. The stability range for metastable phases is with $T_c - T_* \sim 1$ K and $T_{**} - T_c \sim 0.1$ K relatively narrow, therefore the NI transition is said to be weakly first-order. Finally, for a transition at T_c, from the difference in entropies of both phases the latent heat is found to be $\mathcal{Q} = T_c \Delta \mathcal{S} = \frac{1}{2} a T_c V S_c^2$, where $S_c = S(T_c)$ and V denotes the sample volume. For a typical liquid crystal $\mathcal{Q}$ is of the order of 10^6 J/m^3, which roughly amounts to only 0.3 % of the latent heat for ice melting. This is, however, in agreement with the weakly first-order transition character.

The phenomenological Landau approach [32] relies on a well-defined phenomenological order parameter. Representing an ensemble average over a certain number of molecules, due to thermal (spatial and temporal) fluctuations the order parameter may deviate from its average value. If neither the correlation length of such fluctuations, nor their amplitude is too large, the average value of the order parameter used for the free energy expansion still seems to provide an adequate description of the system. Following the more quantitative *Ginzburg criterion* [106], in a three-dimensional system order parameter fluctuations are insignificant either far enough from the phase transition temperature, or in systems involving long-range interactions. In the phenomenological part of this thesis the phase transition will never be approached and the Landau approach will be applied without any reservation.

2.1.3 Inhomogeneous phases and curvature elasticity

In a confined system, the effect of the solid substrate or a free surface is to impose a degree of order typically different from the equilibrium bulk value given by Eq. (2.9), and, as a consequence, S becomes spatially-dependent. If the characteristic length associated with S-variations is larger than the molecular dimension (typically 1 nm), the continuum picture of the system is adequate. In other words, the sample can be divided into mesoscopic "bins" containing a sufficient number of molecules to still allow for a reliable definition of the order parameter profile, $S = S(\mathbf{r})$. In such *inhomogeneous* samples the free energy density also becomes spatially-dependent and contains additional gradient terms penalizing variations of S. The simplest generalization with first-order gradients only (valid for weak enough variations) is given by

$$f(\mathbf{r}) = f_0(S,T) + \frac{3}{4}L(\nabla S)^2, \tag{2.10}$$

where L is another material constant ($L \sim 10^{-11}$ N). To find the equilibrium S-profile, the total free energy functional $F = \int f(\mathbf{r})dV$ has to be minimized with respect to $S(\mathbf{r})$, yielding the Euler-Lagrange differential equation $\frac{d}{d\mathbf{r}}(\frac{\partial f}{\partial \nabla S}) = (\frac{\partial f}{\partial S})$.

Consider now a simple one-dimensional case where the surface degree of order is fixed, e.g., to S_0 by a single planar wall, while the equilibrium bulk value is denoted by $S_b \neq S_0$. The z-axis is taken to be the wall normal. Writing $S(z) = S_b + \delta S(z)$, retaining only lowest-order terms in the correction $\delta S(z) \ll S_b$, and solving the resulting Euler-Lagrange equation yields $\delta S(z) = (S_0 - S_b)e^{-z/\xi}$, thereby introducing the characteristic length of the S-variation, the *correlation length* ξ. Note that $S(z)$ is a monotonic function of z. From this calculation, ξ is given by

$$\xi = \sqrt{\frac{3L}{2a(T-T_*) - 4BS_b + 6CS_b^2}}, \tag{2.11}$$

with $S_b = 0$ in the isotropic phase ($T > T_c$) and $S_b \neq 0$ following Eq. (2.9) in the nematic phase ($T < T_c$). The correlation length ξ increases on approaching the transition temperature T_c from either side, but does not diverge. For a typical nematic, ξ can be evaluated to be of the order of $\sim$ 10 nm at T_c. A similar characteristic length can be derived for biaxiality (P) variations as well.

As soon as the average molecular orientation is subject to spatial variations, too, it is more convenient to write the free energy density in terms of the tensor order parameter Q and its gradients. For simplicity, only uniaxial cases will be treated here, and Q will be given by Eq. (2.4). As free energy is a scalar quantity, scalar invariants have to be constructed from the Q tensor, the candidates being the trace and the determinant. At the same time, the free energy expression must be invariant to all symmetry operations allowed in the high-symmetry (isotropic) phase possessing full symmetry, including invariance to rotations and reflections. The tensor trace is then the only scalar meeting these invariance requirements. For this reason, the homogeneous part of the free energy density (2.8) can be written in terms of traces of powers of Q, i.e., $\mathrm{tr}\mathsf{Q}^2 = \frac{3}{2}S^2$, $\mathrm{tr}\mathsf{Q}^3 = \frac{3}{4}S^3$, and $(\mathrm{tr}\mathsf{Q}^2)^2 = \frac{9}{4}S^4$. Note that the first-order term $\mathrm{tr}\mathsf{Q}$ is absent because it is zero by definition, and that another fourth-order term is possible, $\mathrm{tr}\mathsf{Q}^4$, but is just proportional to $(\mathrm{tr}\mathsf{Q}^2)^2$. In absence of external fields, the free energy density for a homogeneous (undeformed) sample f_0 (2.8) in tensor notation then reads

$$f_0(\mathsf{Q},T) = f_i(T) + \frac{1}{3}a(T-T_*)\mathrm{tr}\mathsf{Q}^2 - \frac{4}{9}B\mathrm{tr}\mathsf{Q}^3 + \frac{1}{9}C(\mathrm{tr}\mathsf{Q}^2)^2. \tag{2.12}$$

In inhomogeneous phases, the Q-tensor components become spatially-dependent. In the weak deformation (continuum) limit the first-order derivatives $\mathsf{Q}_{ij,k} = \partial \mathsf{Q}_{ij}/\partial x_k$ are small quantities. They can be used to construct additional scalar invariants with proper symmetry, representing free energy contributions associated with elastic distortions. The free energy density in a deformed sample can now be written as [4,107]

$$f(\mathbf{r}) = f_0(\mathsf{Q}, T) + \frac{1}{2} L_1 \mathsf{Q}_{ij,k}\mathsf{Q}_{ij,k} + \frac{1}{2} L_2 \mathsf{Q}_{ij,j}\mathsf{Q}_{ik,k} + \frac{1}{2} L_3 \mathsf{Q}_{ij,k}\mathsf{Q}_{ik,j}, \tag{2.13}$$

where L_1, L_2 and L_3 are the "elastic parameters" entering this phenomenological Landau-de Gennes model. For a deformed state $f \geq f_0(\mathsf{Q}, T)$ is expected, therefore in Eq. (2.13) there are no linear terms in the first-order derivative of Q_{ij}, and, further, all terms quadratic in $\mathsf{Q}_{ij,k}$ are assumed to be positive definite. This yields the following restrictions: $L_1 > 0$ and $L_2 + L_3 > -\frac{3}{2} L_1$ [107].

Using the definition of Q (2.4) and taking into account that $\mathbf{n}$ is normalized ($\mathbf{n} \cdot \mathbf{n} = 1$ and hence $n_i n_{i,j} = 0$), it is possible to rewrite $f(\mathbf{r})$ given by Eq. (2.13) in terms of the director $\mathbf{n}$ and the scalar order parameter S. In the resulting expression the variations of S and $\mathbf{n}$ are highly coupled. Neglecting for the moment variations of S to treat only curvature elasticity (setting $\nabla S = 0$ and $S = S_b$), one is left with

$$\begin{aligned} f(\mathbf{r}) = f_0(S_b, T) + \frac{9}{8} S_b^2 \Big[& (2L_1 + L_2 + L_3)\{(\nabla \cdot \mathbf{n})^2 + (\mathbf{n} \times (\nabla \times \mathbf{n}))^2\} \qquad (2.14) \\ & + 2L_1 (\mathbf{n} \cdot (\nabla \times \mathbf{n}))^2 - (2L_1 + L_3) \nabla \cdot (\mathbf{n}(\nabla \cdot \mathbf{n}) + \mathbf{n} \times (\nabla \times \mathbf{n})) \Big], \end{aligned}$$

or, equivalently, $f(\mathbf{r}) = f_0(S_b, T) + f_F(\mathbf{r})$. Here

$$\begin{aligned} f_F(\mathbf{r}) = \frac{1}{2} \Big\{ & K_{11} \left[\nabla \cdot \mathbf{n}\right]^2 + K_{22} \left[\mathbf{n} \cdot (\nabla \times \mathbf{n})\right]^2 + K_{33} \left[\mathbf{n} \times (\nabla \times \mathbf{n})\right]^2 \Big\} \\ & - K_{24} \nabla \cdot \left[\mathbf{n} \left(\nabla \cdot \mathbf{n}\right) + \mathbf{n} \times (\nabla \times \mathbf{n})\right] \qquad (2.15) \end{aligned}$$

is the standard Frank elastic free energy density [18], and K_{11}, K_{22}, and K_{33} are the Frank elastic constants for the corresponding deformation modes: K_{11} for *splay* with $(\nabla \cdot \mathbf{n})^2 \neq 0$, K_{22} for *twist* with $(\mathbf{n} \cdot (\nabla \times \mathbf{n}))^2 \neq 0$, and K_{33} for *bend* with $(\mathbf{n} \times (\nabla \times \mathbf{n}))^2 \neq 0$; see Fig. 2.2. The last divergence term belongs to the *saddle-splay* deformation and is nonzero if $\mathbf{n}$ depends on more than one Cartesian coordinate, introducing the K_{24} elastic constant.

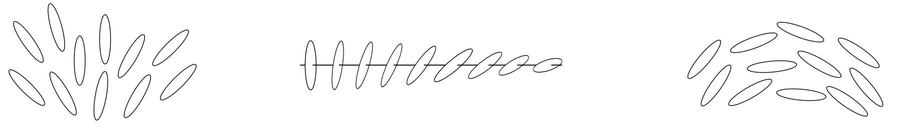

Figure 2.2 Frank elastic deformation modes: splay (a), twist (b), and bend (c).

Comparing Eqs. (2.14) and (2.15), following relations are found: $K_{11} = K_{33} = \frac{9}{4} S_b^2 (2L_1 + L_2 + L_3)$, $K_{22} = \frac{9}{2} S_b^2 L_1$, and $K_{24} = \frac{9}{4} S_b^2 (2L_1 + L_3)$, showing that within this approach the splay and bend constants are equal and different from the twist elastic constant. Only in the special case with $L_2+L_3=0$, all three Frank elastic constants have the same value $K_{11}=K_{22}=K_{33}=K=\frac{9}{2}S_b^2L_1$ (*one-constant approximation*), while the value of the saddle-splay K_{24} elastic constant is still different. The typical magnitude of Frank elastic constants is $K\sim 5\times 10^{-12}$ N. They can be measured reliably, e.g., by studying elastic distortions in an external field (described in more detail later) [108,109]. The K_{24} constant, on the other hand, can be deduced, e.g., by investigating three-dimensional structures in capillaries [110], its magnitude being similar to that of Frank elastic constants.

Mathematically, the saddle-splay contribution is a divergence term and therefore does not contribute to the bulk Euler-Lagrange equations, while it modifies the surface boundary conditions. Another divergence term derived in the past together with the K_{24} term was the *splay-bend* term $f_{13}(\mathbf{r})=K_{13}\nabla\cdot[\mathbf{n}\,(\nabla\cdot\mathbf{n})]$ [52,53]. Unlike the K_{24} term, it explicitly contains second-order derivatives of $\mathbf{n}$ and could therefore not be recovered from Eq. (2.13) containing first derivatives only. It is unbounded from below unless an additional higher-order stabilizing contribution is added to the bulk free energy density. In this case it induces a strong subsurface variation of $\mathbf{n}$ [55–58]. More recent studies show that for a step-like nematic density profile at a flat interface it is canceled by the spontaneous splay contribution $K_1(\nabla\cdot\mathbf{n})$ [111], which is prohibited in the bulk due to inversion symmetry, but allowed in a thin subsurface layer whose thickness is related to the range of intermolecular forces [62,65]. Due to its controversy coming from the strength of the subsurface deformation it produces, the K_{13} contribution is usually excluded from considerations of confined systems.

2.1.4 External anchoring

Phenomenologically, the effect of the bounding interface is to impose a certain degree of ordering and a preferred average molecular orientation, the easy axis (or, alternatively, the "easy" Q-tensor denoted by Q_0). Any deviations from the interface-imposed ordering are penalized by a surface contribution to free energy, which can — similarly as in the bulk case — be written in terms of appropriate scalar invariants. These are now constructed from the tensor $\mathsf{Q}_s-\mathsf{Q}_0$ measuring the deviation of the actual surface ordering Q_s from Q_0. The corresponding bulk free energy density reads

$$f_a(\mathbf{r})=\frac{W_e}{2}\Big[\mathrm{tr}(\mathsf{Q}_s-\mathsf{Q}_0)^2+\mu\Big\{\mathrm{tr}(\mathsf{Q}_s-\mathsf{Q}_0)^2\Big\}^2\Big]\,\delta(\mathbf{r}-\mathbf{r}_0). \tag{2.16}$$

Often it is enough to consider the first contribution only, setting $\mu=0$ [22]. Since the close-packing and van der Waals forces (mainly) responsible for anchoring effects are relatively short-ranged, f_a is regarded as a purely contact term, $\mathbf{r}_0$ representing the locus of points defining the interface. The quantity W_e has units of energy and is related to the strength of anchoring. For uniaxial nematics with $\mathsf{Q}_0=\frac{1}{2}S_0(3\mathbf{n}_0\otimes\mathbf{n}_0-\mathsf{I})$ and $\mathsf{Q}_s=\frac{1}{2}S_s(3\mathbf{n}_s\otimes\mathbf{n}_s-\mathsf{I})$ the lowest-order term in expression (2.16) reduces to a surface free energy density

$$f_s = \frac{9W_e}{8}\Big[\frac{2}{3}S_s^2 + \frac{2}{3}S_0^2 - 2S_sS_0\Big\{(\mathbf{n}_s \cdot \mathbf{n}_0)^2 - \frac{1}{3}\Big\}\Big]. \tag{2.17}$$

Now $\mathbf{n}_0$ and S_0 stand for the direction of the easy axis and for the surface-induced value of S, respectively, while $\mathbf{n}_s$ and S_s are their actual surface values. In cases without S-variation, i.e., for $S_0 = S_s = S_b$, the above expression simplifies to

$$f_s^{RP} = -\frac{W}{2}\cos^2\alpha, \tag{2.18}$$

retaining the term with angular dependence only. This *Rapini-Papoular form* [21] often represents a simple and a good enough approximation for the anchoring energy. Here $\cos\alpha = \mathbf{n}_s \cdot \mathbf{n}_0$ has been introduced and α is the angular deviation of the surface director $\mathbf{n}_s$ from the easy axis $\mathbf{n}_0$. Further, the *anchoring strength* W has been introduced as $W = \frac{9}{2}W_eS_b^2$. Typically, values of W range from 10^{-6} J/m^2 to 10^{-4} J/m^2 [6]. Expressed in terms of the Kléman-de Gennes *extrapolation length* K/W (where K is the effective Frank elastic constant) [4], this translates into K/W between 50 nm and 5 μm. There are several method types for measuring the anchoring strength, mostly relying on tilting the actual molecular surface orientation away from the easy axis (for an extensive review see Ref. [6]). This is usually accomplished in a cell by applying an external electric or magnetic field, or through antagonistic boundary conditions at the opposite surface. Other indirect methods include, e.g., the stability analysis of director structures in nematic droplets [112] and pores [113], or the study of fluctuation modes in confined systems [45,46].

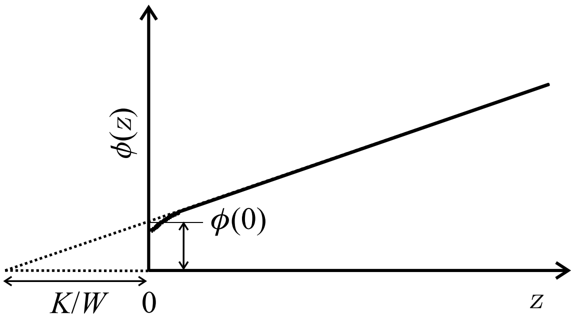

Figure 2.3 Definition of the Kléman-de Gennes extrapolation length K/W [4].

Imagine now a nematic slab of thickness d, with the z-axis along its normal, and ϕ denoting the angle between the director $\mathbf{n}$ and the sample normal z. Assume further that the $z = 0$ surface promotes homeotropic alignment with $\phi_0 = 0$ and a finite anchoring strength, and that the anchoring at the opposite ($z = d$) surface is infinitely strong with a different easy axis. In a thick enough sample such a set-up induces an elastic deformation [114] and the deviation of the actual surface tilt $\phi(0)$ from the easy axis $\phi_0 = 0$ at $z = 0$ will yield an information on the anchoring strength. Then, in terms of the $\phi(z)$ profile the total [bulk (2.15) plus surface (2.18)] free energy per unit surface is given by $F = \int_0^d f_F(z)dz + f_s = \frac{1}{2}\int_0^d K\phi'^2 dz + \frac{1}{2}W\sin^2\phi(0)$ (in the one-constant approximation and assuming the degree of order not to vary, i.e., $S = S_b$), the prime $'$ denoting derivation with respect to z. Minimizing F with respect to $\phi(z)$, the solution of the Euler-Lagrange equation $\frac{d}{dz}(\frac{\partial f_F}{\partial \phi'}) = K\phi'' = 0$ is found to be a linear director profile $\phi(z) = C_1 z + C_0$, the constants C_i to be determined from the boundary conditions at both sample walls. At the $z = 0$ wall the boundary condition reads $(\frac{\partial f_F}{\partial \phi'})_{z=0} = \frac{\partial f_s}{\partial \phi(0)}$ or $(d\phi/dz)_{z=0} = \frac{1}{2}(W/K)\sin 2\phi(0)$ and represents the surface torque balance condition. This relation enables one to deduce K/W from estimated $(d\phi/dz)_{z=0}$ and $\phi(0)$. Note that for small $\phi(0)$ (i.e., strong enough anchoring) the above condition simplifies to $(d\phi/dz)_{z=0} = (W/K)\phi(0)$ and makes it possible to determine K/W simply by extrapolating the profile $\phi(z)$ graphically across the sample boundary to $\phi = 0$ corresponding to the homeotropic easy axis (see Fig. 2.3). Note also that if the degree of nematic order is allowed to vary — which usually is the case near confining boundaries — the profile $\phi(z)$ may deviate from the linear behavior predicted above. In this case the extrapolation of the profile towards the surface must be performed from far enough in the bulk where the order parameter profile is constant.

2.1.5 External fields

If nematic molecules are exposed to an external field, an additional contribution appears in the bulk free energy density. In the following, the derivation will be performed for magnetic fields, but the procedure for an electric field would be identical.

Denoting the external field strength by $\mathbf{H}$, the resulting magnetization can be written as $\mathbf{M} = \underline{\chi}\mathbf{H}$, with the magnetic susceptibility tensor $\underline{\chi}$ given by Eq. (2.7). In case of uniaxial ordering ($P = 0$) $\underline{\chi}$ has only two different eigenvalues, $\chi_3 = \chi_3' S = \chi_{||}$ and $\chi_{1,2} = \chi_{1,2}' S = \chi_\perp$, corresponding to directions parallel to the director $\mathbf{n}$ and perpendicular to it. Splitting the field strength into components parallel and perpendicular to $\mathbf{n}$, one has $\mathbf{H}_{||} = \mathbf{n}(\mathbf{H}\cdot\mathbf{n})$ and $\mathbf{H}_\perp = \mathbf{H} - \mathbf{n}(\mathbf{H}\cdot\mathbf{n})$. Consequently, the magnetization reads

$$\mathbf{M} = \chi_\perp \mathbf{H} + (\chi_{||} - \chi_\perp)(\mathbf{n}\cdot\mathbf{H})\mathbf{n}. \tag{2.19}$$

In an experiment performed in an external field with strength fixed, the additonal free energy density contribution reads $f_m = -\mu_0 \int_0^H \mathbf{M}\cdot d\mathbf{H}$ (μ_0 standing for the permittivity of the vacuum) and, taking into account (2.19), becomes

$$f_m(\mathbf{r}) = -\frac{\mu_0}{2}\Big[\chi_\perp H^2 + (\chi_{||} - \chi_\perp)(\mathbf{n}\cdot\mathbf{H})^2\Big]. \tag{2.20}$$

The second term is orientation-dependent and shows that for positive $\chi_a S = \chi_{||} - \chi_\perp$ the field free energy is smallest when the director is aligned along $\mathbf{H}$, the field direction. Similarly, $\chi_a < 0$ would have resulted in an alignment perpendicular to $\mathbf{H}$. This orienting mechanism stems exclusively from the nonzero anisotropy χ_a and is not present in media where the molecules (and the tensor $\underline{\chi}$) are isotropic. Denoting the angle between $\mathbf{n}$ and $\mathbf{H}$ with β ($\cos\beta = \mathbf{n}\cdot\mathbf{H}/H$), Eq. (2.20) can be simplified to

$$f_m(\mathbf{r}) = f_m^0(H) - \frac{1}{2}\mu_0 \chi_a S H^2 \cos^2\beta, \tag{2.21}$$

where the orientation-independent term has been denoted by $f_m^0(H)$. Analogously, in an external electric field $\mathbf{E}$ directed at an angle β with respect to $\mathbf{n}$, the field free energy contribution is given by

$$f_e(\mathbf{r}) = f_e^0(E) - \frac{1}{2}\epsilon_0\epsilon_a S E^2 \cos^2\beta, \tag{2.22}$$

where $\epsilon_a = (\epsilon_{||} - \epsilon_\perp)/S$ is the dielectric constant anisotropy and ϵ_0 the dielectric constant of the vacuum. Note that both f_m and f_e are position-dependent through the $\beta = \beta(\mathbf{r})$ dependence.

Liquid crystals are — like most organic molecules — diamagnetic: nematic molecules usually contain aromatic rings capable of carrying magnetic field-induced currents (see Fig. 1.1). Consequently, both $\chi_{||}$ and $\chi_\perp$ are negative and small, with typical absolute values around $10^{-7} - 10^{-6}$, and the macroscopic anisotropy $\chi_a S = \chi_{||} - \chi_\perp$ is also in this range [4]. In the magnetic case one usually has $\chi_a > 0$. On the other hand, in the electric field case the anisotropy of the dielectric constant comes from the anisotropic molecular polarizability, as well as from permanent dipoles associated with strongly polar (e.g., cyano) groups — Fig. 1.1. The typical values for the dielectric constant are of the order of ~ 5, with $\epsilon_a \sim 0.2$ (magnitude and sign strongly dependent on the chemical structure of the given nematic species) [4].

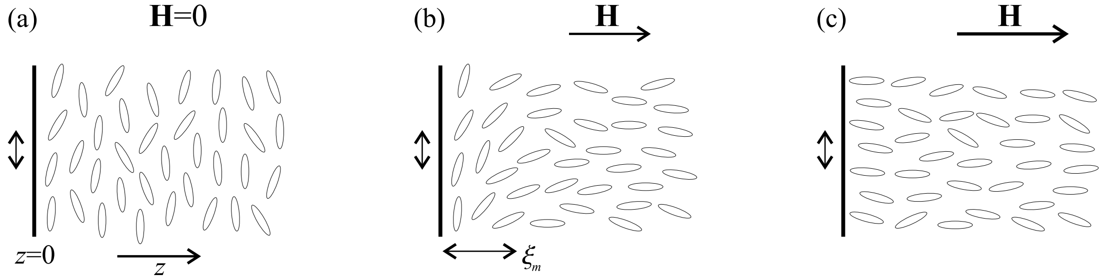

Figure 2.4 Semi-infinite nematic sample with planar anchoring in an external field **H** applied along the surface normal: undeformed zero-field structure (a), deformed structure (b), and saturated structure (c).

Imagine now a semi-infinite nematic sample (as shown in Fig. 2.4) whose substrates promote planar molecular alignment, the z-axis being the substrate normal. Let further ϕ denote the angle between $\mathbf{n}$ and the z-axis. In absence of external fields, one has $\phi = \pi/2$ throughout the sample [Fig. 2.4 (a)]. However, once an external field is applied along z, the conflict between the field and the confining substrate produces an in-plane elastic deformation [Fig. 2.4 (b)]. The minimization of the Frank (2.15) plus field (2.21) free energy $F = \int_0^\infty f(z)dz = \frac{1}{2}\int_0^\infty [K\phi'^2 + \mu_0\chi_a S_b \sin^2\phi]dz$ (written per unit surface in one-constant approximation, again assuming that $S = S_b$ is constant) yields the Euler-Lagrange equation $\frac{d}{dz}(\frac{\partial f}{\partial \phi'}) = (\frac{\partial f}{\partial \phi})$. This equation, if solved for infinitely strong surface anchoring (i.e., no deviations from the surface easy axis $\phi_0 = \pi/2$ are allowed), gives the director profile $\phi(z) = 2\arctan(e^{-z/\xi_m})$. Hereby the characteristic length of the distortion

$$\xi_m = \sqrt{\frac{K}{\mu_0 \chi_a S_b H^2}}, \tag{2.23}$$

called also *magnetic coherence length*, has been introduced [4]. For $z \gg \xi_m$ nematic molecules are aligned along the field and ξ_m can be regarded as the thickness of the deformed layer. Note that the thickness ξ_m is inversely proportional to the field strength H: the stronger the field, the smaller ξ_m. In a 1 T magnetic field for a typical nematic ξ_m can be estimated to be of the order of 10 μm, which means that in order to align the nematic in submicron cavities external fields of extreme strength are required. Similarly, the electric counterpart of ξ_m — the *electric coherence length* — is given by $\xi_e = (K/\epsilon_0 \epsilon_a S_b E^2)^{1/2}$.

In cases where the anchoring strength W is finite [and modeled, e.g., by the Rapini-Papoular form (2.18)], the qualitative character of $\phi(z)$ profiles remains unchanged (except for the angular deviation from the surface easy axis). Increasing the field strength, at first the deformed layer gets thinner (ξ_m decreases), but once ξ_m drops below the extrapolation length K/W, the anchoring cannot oppose the aligning effect of the field any longer and the nematic aligns along the field ($\phi = 0$) also in the vicinity of the substrates [see Fig. 2.4 (c)]. The structural transition from the deformed to field-aligned structure is continuous and is called *saturation transition* [6].

Note that in the semi-infinite sample already an arbitrarily weak external field can induce the elastic deformation. In a cell with planar anchoring where the nematic is sandwiched between two flat and parallel substrates, however, in weak fields applied along the cell normal the nematic remains undeformed. The deformation then appears only above a certain threshold field strength that is inversely proportional to the sample thickness d [108,109], which is a phenomenon known as the *Fréedericksz transition.* It is a continuous structural transition whose threshold can be estimated by studying the stability of the $\phi(z) = \pi/2$ zero-field solution with respect to small perturbations. Decomposing these into Fourier components, the component with the largest possible wavelength is found to be destabilized first (i.e., at the lowest field strength). Expressed in terms of coherence length, for strong anchoring the Fréedericksz transition occurs at $\xi_m^F = d/\pi$ [4]. For finite anchoring, however, the threshold shifts towards lower field strengths. For $K/W \ll d$, ξ_m^F is modified to $\xi_m^F = (d/\pi)(1 + 2K/Wd)$ [6]. Like in a semi-infinite sample, at high enough field strengths the saturation transition takes place. A full stability phase diagram for the undeformed, deformed, and saturated structure has been derived for the slab geometry numerically in Ref. [115].

Choosing an appropriate geometrical set-up (anchoring and field direction), cells with strong anchoring can be used to measure all three Frank elastic constants (recall that they also enter ξ_m^F). The switching of the molecular orientation can be monitored, e.g., by polarizing microscopy and allows for a reliable estimation of the elastic constants [116]. In cells with weak anchoring, the Fréedericksz switching experiment was commonly used also to measure the anchoring strength W (a review of these studies can be found in Ref. [6]).

Finally, note that even in a large and undistorted bulk sample the external field modifies the expression for the homogeneous free energy density (2.8). The additional term is given by Eq. (2.21), and, having set $\beta = 0$, one ends up with $-\frac{1}{2}\mu_0\chi_a S_b H^2$. Note that this contribution is proportional to S_b, whereby the equilibrium value of S_b can be altered by the field [117] and the existence of the nematic phase can be enforced even above the NI transition temperature [118]. Both effects can be seen also experimentally.

2.1.6 Topological defects

In a real unconstrained macroscopic sample one almost never encounters the perfect homogeneous (undeformed) director pattern, but typically finds a distribution of arbitrarily oriented nematic domains instead. Wherever these domains meet, topological defects can emerge. These are points, lines, or walls where there is a singularity in the director field — the director is not well-defined. The vicinity of defects is usually characterized by a considerable distortion in the director field, accompanied both by a significant decrease in the degree of nematic ordering (S) to avoid the high deformation free energy cost, and by non-negligible biaxiality (P). Defect-rich configurations in bulk unconstrained samples can be regarded as long-lived excitations whose free energy is higher than that of the perfectly homogeneous "ground state". On the other hand, the formation of defects can be enforced also by appropriate confinement.

Consider now a two-dimensional case where the director $\mathbf{n} = \mathbf{n}(x, y)$ is lying in the xy-plane. Within this plane, let the director be parametrized by the angle $\theta(x, y)$, leading to $\mathbf{n} = (\cos\theta, \sin\theta)$. The following analysis can be applied without modifications also to straight defect lines (*disclinations*). Suppose further that the defect is located at the origin of the coordinate system. Now imagine a closed loop encircling the defect. Moving along this loop, the local $\mathbf{n}$ rotates and, after having encircled the defect once, satisfying the continuity requirement for $\mathbf{n}$ one finds that $\theta(\varphi + 2\pi) = \theta(\varphi) + 2\pi m$ (φ here denotes the polar angle in the xy-plane). Here m is an integer or half-integer number, also called *defect strength.* Note that the shape of the closed loop may be completely arbitrary and that no length scale has been introduced in the problem so far. Therefore, the director field must depend only on the polar angle φ and not on the distance r from the defect center. As a consequence, $\mathbf{n}$ can be parametrized solely by $\theta = \theta(\varphi)$.

To find the actual director field surrounding the defect, one has to consider the corresponding free energy contributions. Assuming that far from the defect core the degree of nematic ordering is almost constant, in the one-constant approximation the bulk elastic free energy associated with the director field distortion (2.15) is given by $F_d = \frac{K}{2}\int dV(\nabla\theta)^2$. Minimizing F_d with respect to $\theta(\varphi)$ yields the Euler-Lagrange equation $\nabla^2\theta = 0$, whose solution, choosing $\theta(0) = 0$, is

$$\theta(\varphi) = m\varphi, \qquad m = 0, \pm\tfrac{1}{2}, \pm 1, \pm\tfrac{3}{2}, \ldots \tag{2.24}$$

agreeing also with the continuity requirement for θ. The above choice for $\theta(0)$ merely defines the orientation of the coordinate system. Director fields for some defect types

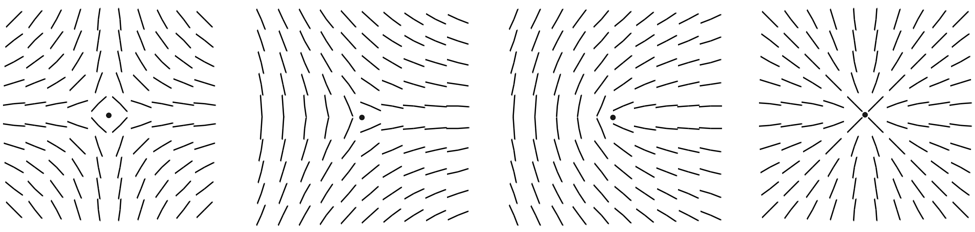

$m=-1$ $m=-1/2$ $m=1/2$ $m=1$

Figure 2.5 Director fields surrounding topological defects of different strength m.

are shown in Fig. 2.5. Then, in the polar coordinate system F_d (per unit length) can be calculated as

$$F_d = \frac{K}{2}\int_{r_0}^{R} r dr \int_0^{2\pi} \frac{1}{r^2}\left(\frac{d\theta}{d\varphi}\right)^2 d\varphi = \pi K m^2 \log\frac{R}{r_0}, \tag{2.25}$$

where R is a characteristic dimension of the confined system and r_0 the radius of the defect core where the degree of order cannot be assumed constant. Note that — ignoring the possible m-dependence in r_0 — the elastic free energy of the director field distortion caused by the defect is proportional to m^2.

In a simplified picture, the core of the defect can be regarded as a tiny region of a molten-down nematic, i.e., as a completely isotropic liquid. The core free energy F_c per unit length can then be estimated as $F_c = \pi r_0^2 \Delta f$, where Δf is the difference between the free energy densities of the isotopic and nematic phase (2.8). Now the quantity r_0 can be estimated by minimizing $F_d + F_c$, leading to $r_0 = |m|(K/2\Delta f)^{1/2}$. Note that also the core size depends on the defect strength m and that within the present simple estimate the core free energy is also proportional to m^2. Taking into account the m-dependence in r_0, the total (distortion plus core) free energy can be written as [24]

$$F_d + F_c = \pi K m^2\Big(\log\frac{R}{m\xi} + \frac{1}{2}\Big), \tag{2.26}$$

where ξ is the correlation length associated with the variation of the degree of order (2.11). In large enough samples with $R \gg \xi$, the core energy can be ignored in comparison with the elastic contribution. Note that in this case and for low (and relevant) values of m the total energy $F_d + F_c$ is an increasing function of m and that, consequently, high strength-defects are less likely to form.

If there are two (or more) defects positioned at different locations in the sample, the overall director field is a linear combination of director fields obtained for separate defects (this follows from the linearity of the Euler-Lagrange equation). Then the free energy for the director field deformation for, e.g., two defects of strength m_1 and m_2 separated by b is given by [24]

$$F_d = F_d^1 + F_d^2 + 2\pi K m_1 m_2 \log\frac{R}{b}, \tag{2.27}$$

where $F_d^1 + F_d^2$ is the distortion energy of the isolated defects and the last term is the "interaction" term. From (2.27) it follows that defects of opposite strength sign attract (and, eventually, annihilate), while those of equal strength sign repel. This attraction/repulsion is mediated by the long-range curvature elasticity of the director field.

Moreover, defects of given strength can split into several lower-strength ones, thereby maintaining the total defect strength $m = \sum_i m_i$. For example, a -1 strength defect can split into two $-\frac{1}{2}$ strength ones. Combining Eqs. (2.25)-(2.27) gives

$$F_d = \pi K (m_1 + m_2)^2 \log \frac{R}{r_0} - 2\pi K m_1 m_2 \log \frac{b}{r_0} \tag{2.28}$$

for the deformation free energy of two interacting defects and implies that a pair of, e.g., $-\frac{1}{2}$ strength defects indeed is more stable than a single -1 strength one [24]. Here, however, both the defect core free energy and difference in core sizes were ignored, but more detailed analyses still suggest that it is favorable for a defect of higher strength to split into several lower strength-ones. Very often a simple "rule of thumb" for the defect stability analysis is used, according to which the leading contribution in the corresponding free energy is simply proportional to m^2.

2.2 Molecular simulations and lattice models

The second class of approaches addressed in this thesis will be based on simple microscopic models of the nematic, starting from a given interparticle pairwise interaction law. Such approaches become inevitable if one is interested, e.g., in performing detailed studies of phase transitions accompanied by significant fluctuations of the phenomenological order parameter, studying cases where the order parameter shows spatial variations too strong to be accommodated within continuum theories, or, simply, if one is merely interested in relating a certain parameter entering the intermolecular potential with macroscopic observables.

2.2.1 Lebwohl-Lasher model

On the molecular level, two main interaction types are responsible for the formation of the nematic phase. The first type is the pure steric intermolecular repulsion, with no long-range attraction. In fact, if the particle density in a system of strongly elongated molecules is increased, following Onsager a nematic-to-isotropic transition takes place [119]. On the other hand, a temperature-driven first-order nematic-to-isotropic transition was shown to happen (by Maier and Saupe) also in a system of molecules with a large anisotropy in the molecular polarizability resulting in anisotropic attractive dispersion (van der Waals) forces [120,121]. To overcome the mean-field approximation used in Refs. [120,121], a simple microscopic lattice model was put forward by Lebwohl and Lasher, evolving into a computer simulation study of the nematic-isotropic (NI) transition [93,122]. The lattice approximation was particularly suitable for the pioneering computer studies because of its computational

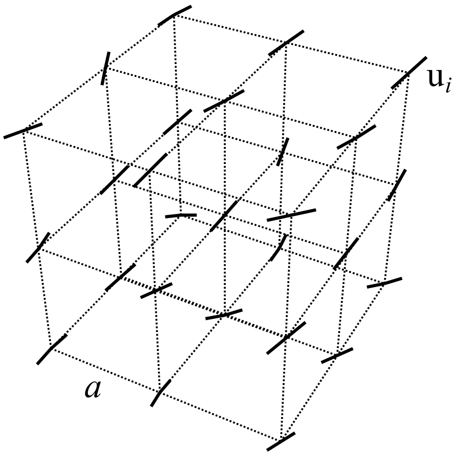

Figure 2.6 Lebwohl-Lasher lattice model of a nematic: particles $\mathbf{u}_i$ attached to a cubic lattice of spacing a.

cheapness in comparison to the off-lattice models. With the enormous increase of the computing power in the past decades, lattice models are still appealing because they facilitate the performance of large-scale simulations, as well as simulations in medium-size systems for a broad range of physical parameters.

In the framework of the *Lebwohl-Lasher* (LL) *lattice model* uniaxial nematic molecules are represented by particles that can rotate freely, but are arranged into a simple cubic lattice with spacing a (Fig. 2.6). Thereby there are no translational degrees of freedom in the system, but despite this the model can be seen to reproduce the orientational behavior well enough. Equivalently, particles may also be regarded as close-packed molecular clusters (consisting of up to 10^2 molecules), maintaining their short-range orientational order in the relatively narrow temperature existence range of the nematic, as well as across the NI phase transition [94,100]). Supposing that the effective volume occupied by one molecule is $\sim 1\ \mathrm{nm}^3$, the lattice spacing a can be estimated by $a \lesssim 5$ nm.

The orientation of the particle located at the ith lattice site is denoted by a three-dimensional unit vector $\mathbf{u}_i$. The particles i and j then interact through a pair potential given by

$$U_{ij} = -\epsilon_{ij} P_2(\cos\beta_{ij}) = -\epsilon_{ij}\Big[\frac{3}{2}(\mathbf{u}_i\cdot\mathbf{u}_j)^2 - \frac{1}{2}\Big], \tag{2.29}$$

where $\epsilon_{ij} = \epsilon$ is a positive constant (of the order of ~0.02 eV) if i and j are nearest neighbors, and $\epsilon_{ij} = 0$ otherwise. Further, P_2 is the second-rank Legendre polynomial and β_{ij} the angle between $\mathbf{u}_i$ and $\mathbf{u}_j$. In this sense the LL model is similar to the Heisenberg model used for modeling magnetic systems, yet accounting also for the head-tail symmetry encountered in nematics. The effect of the interaction (2.29) is to align neighboring particles parallel to each other and is at low enough temperatures sufficient to induce nematic ordering.

Simulating bulk systems, standard periodic boundary conditions are usually applied [93,122,123]. An improved "cluster" boundary condition has also been devised where particle orientations at the simulation box surface are sampled from a distribution with the same value of the order parameter S as calculated for particles inside the box [124]. On the other hand, in confined systems a certain fraction of nematic particles (the *"ghost" particles*) is used to fix the boundary conditions. For example, to model a PDLC droplet, a jagged sphere is carved from the cubic lattice by considering all molecules lying closer than R (the droplet radius) to the chosen center [91]. Then the interaction with the confining polymer substrate is mimicked by assuming an additional layer of ghost particles whose orientations are chosen in accordance with the desired boundary conditions and are kept fixed during the simulation [125]. Both nematic-nematic and nematic-ghost interactions are modeled by the interaction law (2.29), but the interaction strengths ϵ_{ij} are not necessarily equal for both interaction types.

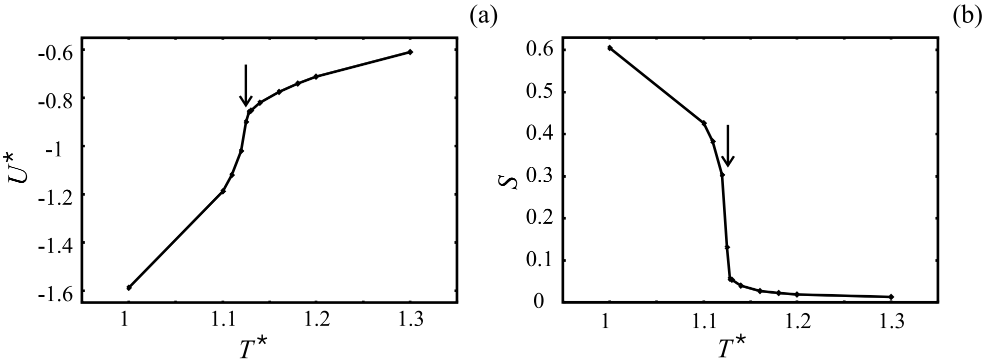

Figure 2.7 Bulk Lebwohl-Lasher system: temperature dependence of reduced internal energy $U^* = U/\epsilon$ (a) and scalar order parameter S (b). The NI phase transition occurs at $T^* = k_B T/\epsilon = 1.1232$ in reduced units, as indicated by the arrows [123].

Performing Monte Carlo simulations (described in more detail later in this Chapter), it was shown that the LL model reproduces a weakly first-order NI transition in a bulk system — a large sample with periodic boundary conditions [93,123] — while in confined systems (e.g., droplets) of sufficiently small size the phase transition is suppressed [126,127], which is in agreement with experimental data. The temperature dependences of the total internal energy $U = \sum_{\langle i<j \rangle} U_{ij}$ and of the scalar order parameter S are shown in Fig. 2.7. A biaxial version of the pair potential (2.29) has also been devised, leading to a biaxial nematic [128].

The LL model can be easily modified to account for external field effects as well. Following the same physical reasoning as in Sect. 2.1.5, the coupling energy of each nematic particle $\mathbf{u}_i$ to an external (electric or magnetic) field can be modeled by

$$U_i^f = -\epsilon\eta P_2(\cos\beta_i) = -\epsilon\eta\Big[\frac{3}{2}(\mathbf{u}_i \cdot \mathbf{f})^2 - \frac{1}{2}\Big], \tag{2.30}$$

where $\mathbf{f}$ is the unit vector giving the orientation of the external field and β_i is the angle between $\mathbf{f}$ and $\mathbf{u}_i$. Further, η is the constant describing the strength of the coupling with the external field. In the magnetic field case the dimensionless η is defined by $\epsilon\eta = \chi_a V_0 B^2/3\mu_0$, where $B \approx \mu_0 H$ stands for the magnetic induction,

$\chi_a = (\chi_{||} - \chi_{\perp})/S$ again denotes the anisotropy of the microscopic magnetic susceptibility ($||$ and $\perp$ referring to the direction of $\mathbf{u}_i$), and V_0 stands for the volume of space occupied by one nematic particle (see, e.g., [99]). For $\eta > 0$ ($\chi_a > 0$) nematic particles are aligned along $\mathbf{f}$. Matching aligning effects in the electric and the magnetic field, for a given nematic species one can translate any magnetic field strength (or B) into an equivalent strength of the electric field (E) [99]. In the electric case one then has $\epsilon\eta = \epsilon_a \epsilon_0 V_0 E^2/3$, where $\epsilon_a = (\epsilon_{||} - \epsilon_{\perp})/S$.

2.2.2 Hexagonal lattice model

The Maier-Saupe theory [120,121] has been devised from anisotropic van der Waals forces in the mean-field approximation that can be believed to work well deep enough in the bulk. The Lebwohl-Lasher model [93] goes beyond the mean-field approximation, but still assumes the interparticle interaction to promote strictly parallel alignment, regardless of the relative position of particles. While certainly reasonable in the bulk, close to a confining substrate such a simplified picture is not necessarily appropriate. Therefore, in what follows, anisotropic van der Waals forces will be reconsidered, leading to a generalization of the interaction law (2.29): the *induced dipole-induced dipole* interaction.

In a simplified picture, a nematic molecule can be thought of as an elongated and electrically neutral cloud of positive and negative charge. Due to thermal fluctuations, centers of mass for the positive and negative charge do not overlap. The characteristic time for these charge fluctuations is much shorter than the times associated with the reorientation of the molecule as a whole. Then, in a given moment, in the molecule an instantaneous electric dipole $\mathbf{p}_e$ is created whose time-averaged value equals zero. However, during its existence $\mathbf{p}_e$ gives rise to a dipolar electric field

$$\mathbf{E}(\mathbf{r}) \propto \frac{1}{r^3}\Big[3\frac{(\mathbf{p_e}\cdot\mathbf{r})\mathbf{r}}{r^2} - \mathbf{p}_e\Big]. \tag{2.31}$$

The electric field (2.31) polarizes neighboring molecules, thereby inducing electric dipoles $\mathbf{p}'_e(\mathbf{u}',\mathbf{r})$, where $\mathbf{r}$ and $\mathbf{u}'$ denote molecular positions and orientations, respectively, and $r = |\mathbf{r}|$. Assuming that nematic molecules are on the average uniaxial, the molecular polarizability tensor $\underline{\alpha}$ has only two different eigenvalues, $\alpha_{||}$ and $\alpha_{\perp}$, referring to an electric field aligned along the molecular long axis $\mathbf{u}'$ and perpendicular to it, respectively. The dipole moment $\mathbf{p}'_e$ induced by the electric field $\mathbf{E}(\mathbf{r})$ can now be written as

$$\mathbf{p}'_e(\mathbf{u}',\mathbf{r}) = \underline{\alpha}\,\mathbf{E}(\mathbf{r}) = \alpha_{\perp}\mathbf{E}(\mathbf{r}) + (\alpha_{||} - \alpha_{\perp})(\mathbf{E}(\mathbf{r})\cdot\mathbf{u}')\mathbf{u}' \tag{2.32}$$

and the corresponding interaction energy as

$$U = -\mathbf{p}'_e(\mathbf{u}',\mathbf{r})\cdot\mathbf{E}(\mathbf{r}) \propto -\alpha_{\perp}E^2 - (\alpha_{||} - \alpha_{\perp})(\mathbf{E}(\mathbf{r})\cdot\mathbf{u}')^{\mathbf{2}}. \tag{2.33}$$

Note that the molecular orientation-dependent term $\mathbf{E}(\mathbf{r})\cdot\mathbf{u}'$ enters Eq. (2.33) as a square and therefore always yields a nonzero average if averaged over rapid thermal fluctuations of the molecular charge (and $\mathbf{p}_e$), regardless of the fact that the instantaneous $\mathbf{p}_e$ is actually averaged to zero. Further, given a high anisotropy of the molecular polarizability with $\alpha_{||} \gg \alpha_{\perp}$, one can assume that the most probable orientation of the instantaneous fluctuation-induced $\mathbf{p}_e$ is along the molecular long axis $\mathbf{u}$. Then, taking the expression (2.31) for the dipolar field $\mathbf{E}(\mathbf{r})$, the orientation-dependent part of the interaction energy is given by

$$U(\mathbf{u}, \mathbf{u}', \mathbf{r}) = -\frac{\epsilon'}{r^6}\Big[\mathbf{u} \cdot \mathbf{u}' - 3\nu\Big(\mathbf{u} \cdot \frac{\mathbf{r}}{r}\Big)\Big(\mathbf{u}' \cdot \frac{\mathbf{r}}{r}\Big)\Big]^2. \tag{2.34}$$

Here ν — the interaction anisotropy parameter — has been introduced: for $\nu = 1$ the expression (2.34) represents the induced dipole-induced dipole interaction, while for $\nu = 0$ it reduces to the Maier-Saupe interaction used in the LL model. The magnitude of interaction strength ϵ' is similar to that of ϵ introduced in Eq. (2.29) for the LL model. Having assumed $\alpha_{||} \gg \alpha_{\perp}$, ϵ' is positive and the interaction is attractive. It is also decreasing rapidly with the interparticle distance r. Unlike the Maier-Saupe interaction law used in the LL model (2.29), the interaction energy U is a function not only of the particle orientations $\mathbf{u}$ and $\mathbf{u}'$, but also of their relative position $\mathbf{r}$, and is therefore *spatially anisotropic*. The anisotropy parameter ν allows one to continuously vary the importance of the anisotropic ($\mathbf{r}$-dependent) contribution in the interaction law (2.34). Then, a nonzero ν results in orienting effects at the sample surface [17,81] and in an anisotropy of Frank elastic constants. In fact, the Maier-Saupe interaction corresponds to the one-constant approximation, while for $\nu \neq 0$ the twist elastic constant is different from the splay and bend ones [129].

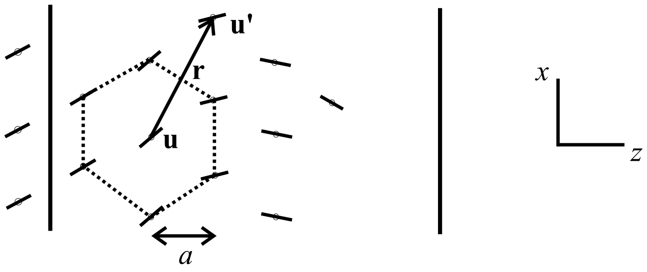

Figure 2.8 Simple hexagonal lattice model.

Having a spatially anisotropic pairwise potential, a question should be posed as to whether discrete lattice models can still be used together with such potentials. In principle, in this case artificial lattice approximation-induced bulk easy axes could appear, depending on the lattice geometry. Indeed, the effect of the LL potential is merely to impose parallel alignment of neighboring particles, regardless of their relative position, and for this potential none of the lattices imposes any bulk easy axes. Using the induced dipole-induced dipole interaction together with, e.g., the simple cubic lattice (as in Ref. [81]) is inappropriate because easy axes appear along the three main lattice directions. Then the model is not capable of reproducing the soft curvature elasticity in the bulk and is hence useless for studying nematics. Alternatively, one can use the *simple hexagonal lattice* — see Fig. 2.8. In this case, for in-hexagonal-plane molecular alignment, on the average bulk easy axes can be seen to vanish [17], and planar elastic deformations in nematics can be treated appropriately with this model system. The most striking leftover from the lattice approximation is the existence of periodic solid-like solutions for the director profile, which — at low enough temperatures — are more stable than the smooth nematic ones [17]. One can avoid, however, these difficulties by reducing the anisotropy parameter ν to below $\nu \approx 0.3$. Then solid-like solutions disappear and the smooth nematic ones become stable, while the spatially anisotropic interaction character is still retained since $\nu \neq 0$. In fact, for $\nu \lesssim 0.3$ side-to-side molecular alignment is favored (similar to that of the Gay-Berne interaction [130]), promoting parallel ordering. This result is compatible with the one obtained in the mean-field analysis by Maier and Saupe, as well as with the behavior of the LL model. However, while disguised in the bulk, the anisotropic interaction character reappears in form of orienting effects close to the sample surface (absent in the LL model), which can be interpreted as intrinsic anchoring. To cover these phenomena qualitatively, it is sufficient to consider nearest-neighbor interactions.

2.2.3 Monte Carlo simulation technique

This Section will be devoted to Monte Carlo simulations that can be applied to the above model systems for finding equilibrium molecular configurations, as well as for the calculation of macroscopic observables.

While molecular dynamics simulations aim at mimicking the "natural" dynamics of the simulated system, the system evolution provided by Monte Carlo-type simulations is different. Molecular dynamics consists of the brute-force step-by-step solution of Newton's equations of motion, thereby tracing the system in time, which corresponds to a realistic experimental situation. In this case it is possible to calculate time averages of thermodynamic quantities ($\bar{\mathcal{A}}$). On the other hand, the Monte Carlo method can be interpreted as a procedure for sampling many-particle configurations from the statistical ensemble. This method then enables one to calculate ensemble averages $\langle\mathcal{A}\rangle$. Then, assuming that the ergodic hypothesis for a given system holds ($\bar{\mathcal{A}} = \langle\mathcal{A}\rangle$), both molecular dynamics and Monte Carlo techniques should yield equivalent results for the averages of interest. However, the advantage of Monte Carlo methods is that — in contrast to molecular dynamics simulations — they do not require any calculations of forces and torques. Moreover, in highly simplified model systems like the lattice ones ("non-natural" by construction), Monte Carlo simulations seem to be the method of choice.

In lattice models the microscopic state of the system consisting of N particles is univocally defined by specifying all particle orientations $\mathbf{u}_i$. In the N-particle configuration space the set of all orientations $\mathbf{u}_i$ can be given by a single long vector $\mathbf{u}^N$. In the LL model system (Sect. 2.2.1), for example, the Hamiltonian $\mathcal{H}(\mathbf{u}^N)$ in presence of an external field reads

$$\mathcal{H}(\mathbf{u}^N) = -\epsilon \sum_{\langle i<j\rangle} P_2(\mathbf{u}_i \cdot \mathbf{u}_j) - \epsilon\eta \sum_{i=1}^{N} P_2(\mathbf{u}_i \cdot \mathbf{f}), \tag{2.35}$$

the first sum $\sum_{\langle i<j\rangle}$ to be taken over nearest neighbors only. The aim is to calculate

the ensemble average of a given quantity $\mathcal{A}(\mathbf{u}^N)$

$$\langle \mathcal{A} \rangle = \frac{\int d\mathbf{u}^N \mathcal{A}(\mathbf{u}^N)\ e^{-\beta\mathcal{H}(\mathbf{u}^N)}}{\int d\mathbf{u}^N\ e^{-\beta\mathcal{H}(\mathbf{u}^N)}} \tag{2.36}$$

where $\beta^{-1} = k_B T$, k_B being the Boltzmann constant and T the absolute temperature. Straightforward integration of expression (2.36) is doomed to failure. This is because the integration area — the configuration space — becomes enormously huge with the growing number of particles. Moreover, when integrating, most of the time is spent in regions where the Boltzmann weight $e^{-\beta\mathcal{H}(\mathbf{u}^N)}$ is negligibly small.

Obviously, the direct evaluation of integrals like $Z = \int d\mathbf{u}^N\, e^{-\beta\mathcal{H}(\mathbf{u}^N)}$ (the partition function) is not possible. However, when one calculates $\langle \mathcal{A} \rangle$, merely a ratio of two integrals of that kind is to be found. In other words, it is enough to know the relative probability of sampled states rather than the absolute one. This is the underlying idea of the *Metropolis algorithm* [37] for calculating $\langle \mathcal{A} \rangle$, described in what follows.

Suppose now that one is able to generate random points in configuration space according to the canonical probability distribution $\mathcal{N}(\mathbf{u}^N) \propto e^{-\beta\mathcal{H}(\mathbf{u}^N)}$, characterizing systems with well-defined temperature. Suppose that L points have been generated. The number of points per unit volume in the neighborhood of the point $\mathbf{u}_k^N$ is $n_k = L\mathcal{N}(\mathbf{u}_k^N)$. The average $\langle \mathcal{A} \rangle$ can now be calculated as follows:

$$\langle \mathcal{A} \rangle \approx \frac{1}{L} \sum_k n_k \mathcal{A}(\mathbf{u}_k^N). \tag{2.37}$$

In this way one chooses (samples) only important states (i.e., those having a high Boltzmann weight). The sampling scheme is hence called *importance sampling.*

Now an algorithm is needed to generate the L sample points $\mathbf{u}_k^N$ according to the scheme just introduced. Instead of generating all of them at once, one can simulate a random walk in configuration space, producing a trajectory of states that obeys the probability distribution $\mathcal{N}(\mathbf{u}^N)$. Let the random walk start with the configuration $\mathbf{u}^N$, referred to as "o" (old). Now generate a new trial configuration $\mathbf{u}'^N$, labeled as "n" (new), by adding a random displacement to $\mathbf{u}^N$. The probability for such a move to occur is denoted by $\pi(o \to n)$. It is a product of the probability to generate such a *trial move* $\alpha(o \to n)$, and the probability to accept it $acc(o \to n)$. The sampling scheme described by the probability matrix π must necessarily be *ergodic*, i.e., the scheme must be able to reach every accessible point in configuration space in a finite number of steps from any other point of that space. Here it has already been assumed that the simulated system is ergodic in itself.

The old and new states have a different Boltzmann weight factor and thus different probabilities $\mathcal{N}(o)$ and $\mathcal{N}(n)$ of finding the equilibrated system in one of these states. If $\mathcal{N}(n) > \mathcal{N}(o)$, i.e., the new state is more likely, the move should automatically be accepted. Otherwise, it should be accepted with a certain probability depending on both $\mathcal{N}(n)$ and $\mathcal{N}(o)$. To find this acceptance criterion, one has to notice that the transitions $o \to n$ and $n \to o$ should not destroy the equilibrium probability distribution $\mathcal{N}(\mathbf{u}^N)$ once it has been reached. Thus, the number of moves

$o \to n$ must be exactly canceled by moves $n \to o$, which gives rise to the *detailed balance condition*:

$$\mathcal{N}(o)\pi(o \to n) = \mathcal{N}(n)\pi(n \to o). \tag{2.38}$$

Assume that $\alpha(o \to n) = \alpha(n \to o)$, i.e., the moves $o \to n$ and the reverse move are attempted with equal probabilities. Then one can rewrite the detailed balance condition as

$$\frac{acc(o \to n)}{acc(n \to o)} = \frac{\mathcal{N}(n)}{\mathcal{N}(o)} = e^{-\beta[\mathcal{H}(n)-\mathcal{H}(o)]}. \tag{2.39}$$

Consequently, the above procedure is in agreement with the detailed balance condition if the acceptance probability in trial moves with $\mathcal{N}(n) < \mathcal{N}(o)$ is set to $acc(o \to n) = \mathcal{N}(n)/\mathcal{N}(0) = e^{-\beta[\mathcal{H}(n)-\mathcal{H}(o)]}$. At the same time, for trial moves with $\mathcal{N}(n) > \mathcal{N}(o)$, $acc(o \to n) = 1$ must hold. Summarizing, a basic Monte Carlo algorithm for a N-particle system has the form:

1. Take the configuration $\mathbf{u}^N$; calculate its energy $\mathcal{H}(\mathbf{u}^N) = \mathcal{H}(o)$.
2. Select one particle from the old configuration at random; move the selected particle randomly to obtain the new trial configuration $\mathbf{u}'^N$; calculate the energy of the new configuration $\mathcal{H}(\mathbf{u}'^N) = \mathcal{H}(n)$.
3. Accept the move $\mathbf{u}^N \to \mathbf{u}'^N$ $(o \to n)$ with a probability
$$acc(o \to n) = \min\left[1, e^{-\beta[\mathcal{H}(n)-\mathcal{H}(o)]}\right].$$
4. Return to step 2 of this algorithm.

At each step of the algorithm the quantity $\mathcal{A}$, whose average is to be evaluated, has to be sampled. It must be stressed that a sample must be taken also if the trial move has been rejected since $\pi(o \to o) = 1 - \sum_{n \neq o} \pi(o \to n) \neq 0$. Not sampling $\mathcal{A}$ in such cases can result in non-negligible systematic errors.

Moreover, the instantaneous value of the quantity $\mathcal{A}$ is subject to fluctuations. Also the fluctuations of $\mathcal{A}$ can, beside the average $\langle \mathcal{A} \rangle$, yield some interesting information. For example, in the canonical ensemble considered above, fluctuations of the total energy $\mathcal{H}$ are related to the specific heat C_V at constant volume $\sigma_{\mathcal{H}}^2 = \langle \mathcal{H}^2 \rangle - \langle \mathcal{H} \rangle^2 = k_B T^2 C_V$.

The ensemble average $\langle \mathcal{A} \rangle$ is due to fluctuations accompanied by an error $\Delta\mathcal{A}$. Suppose that one has performed M simulation steps and sampled $\mathcal{A}$ M times. As the period of a fluctuation is usually several simulation steps (typically of the order 10^2), all M samples of $\mathcal{A}$ are not uncorrelated. Let τ be the corresponding correlation time (measured in units of steps). Since M/τ is then approximately the number of independent sample points taken, the error of $\langle \mathcal{A} \rangle$ can be written as

$$\Delta\mathcal{A} \approx \sigma_{\mathcal{A}} \sqrt{\frac{\tau}{M}}, \tag{2.40}$$

$\sigma_{\mathcal{A}}$ standing for $(\langle \mathcal{A}^2 \rangle - \langle \mathcal{A} \rangle^2)^{1/2}$. If $\langle \mathcal{A} \rangle \propto N$, $\sigma_{\mathcal{A}} \propto \sqrt{N}$ holds, and the relative error $\Delta\mathcal{A}/\langle \mathcal{A} \rangle$ decreases with the increasing number of particles as $1/\sqrt{N}$. Moreover, it decreases also with the number of Monte Carlo steps as $1/\sqrt{M}$.

There is also the issue of how to generate trial moves — the $\mathbf{u}_i$ reorientations. For instance, the Lebwohl-Lasher model simulations presented in this thesis have followed the *Barker-Watts* technique [131]. It was first applied to perform simulations of water structure [131], but was then used extensively together with the LL model. In all cases it proved to ensure appropriate and ergodic sampling in configuration space [91]. The technique consists of selecting an individual particle at random, then selecting one of the three fixed coordinate axes in the Cartesian laboratory reference frame (again at random), and performing a rotation of the unit vector $\mathbf{u}_i$ around the chosen axis. The rotation angle and direction are also chosen at random, the maximum rotation magnitude being an important simulation parameter. Indeed, if the moves are too small, the random walk will visit only a small fraction of the configuration space and the estimate for $\langle \mathcal{A} \rangle$ will be poor. On the other hand, if the trial move is too large, it is very likely to be rejected due to the low probability $\mathcal{N}(n)$ of the new state. Although more sophisticated criteria for the selection of the trial move magnitude exist, here a "rule of thumb" will be adopted, stating that on the average 50% of attempted trial moves be accepted. Instead of performing individual trial moves, collective moves involving several particles can be performed as well. Efficient collective moves can, however, be constructed only if the displacements of individual particles are not chosen independently, but follow, e.g., Newton's equations of motion as in molecular dynamics simulations, leading to the *hybrid Monte Carlo* technique.

Performing Monte Carlo simulations with the hexagonal lattice model (Sect. 2.2.2), a procedure similar to that used for the LL model can be adopted. The main difference between the two models comes from the fact that here nematic particles must be prevented from moving out of hexagon planes, thereby avoiding bulk easy axes. Again the Metropolis algorithm can be applied, however, the generation of trial moves has to be reduced to a simple particle rotation, so as to meet the in-plane constraint for particle orientations.

Another important topic are the initial conditions. In an ergodic system, after equilibration the simulation results are supposed not to be initial configuration-dependent. Yet some caution is necessary whenever the system can be trapped in metastable states (especially if the simulation run is too short).

Finally, it is necessary to specify the quantity $\mathcal{A}$ to be sampled during the MC evolution provided by the Metropolis algorithm. In analyses of confined nematics, it is convenient to accumulate the ordering matrix $\underline{Q}$ components (2.5) to obtain the order parameter, biaxiality, and director maps. Further, one can define and accumulate $P_2^v = \frac{1}{2}\langle 3(\mathbf{v}\cdot\mathbf{u}_i)^2 - 1\rangle_i$, where $\mathbf{v}$ is a fixed unit vector (also spatially-dependent, if needed), quantifying the degree of order with respect to a given direction ($\mathbf{v}$) or a given pattern $\mathbf{v} = \mathbf{v}(\mathbf{r})$. Moreover, various types of positional and orientational correlation functions can be sampled (only the latter being relevant in case of lattice models). Another important class of observables are the ones detectable experimentally. Some of the examples are ^{2}H NMR line shapes, electric capacitance, and transmitted polarized light intensity. They will be discussed in more detail in Sect. 2.3 and later on.

2.3 Experimental observables

An essential part of any theoretical or simulation work is to bridge the gap between these approaches and experimental observables. Attempting to do this, from the broad variety of experimental techniques listed in the introductory Chapter, here three will be treated in more detail: deuterium nuclear magnetic resonance, measurements of electric capacitance, and measurements of light intensity transmitted through a sample between two crossed polarizers.

2.3.1 ^{2}H NMR

Deuterium nuclear magnetic resonance (^{2}H NMR) is a powerful technique, frequently applied to investigate confined nematics such as PDLC and systems with dispersed polymer networks [25,40,132,133]. The technique is very convenient for the study of such heterogeneous systems since, if applied to deuterated nematics, it only gives direct information on the behavior of the confined liquid crystal — rather than on the non-deuterated confining matrix. Further, it is applicable also for small, i.e., submicron cavities, where optical methods fail to yield useful information because the light wavelength is too large in comparison to the cavity diameter. Moreover, ^{2}H NMR spectra can give a complete idea about orientational molecular ordering, that is both about director configurations and dynamic processes like fluctuations of molecular long axes and translational diffusion.

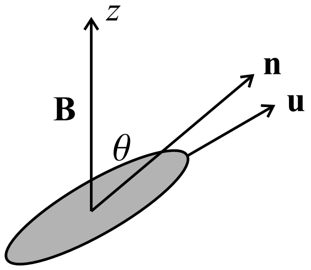

Figure 2.9 ^{2}H NMR and geometry: **u** molecular long axis, **n** nematic director, and **B** spectrometer magnetic field.

A ^{2}H NMR spectrum of a selectively deuterated nematic in the bulk isotropic phase consists of a single line whose position in the spectrum is determined by the Zeeman splitting of deuteron energy levels in the spectrometer magnetic field. The corresponding line width is well below $2\pi \times 100$ Hz. Since deuterons possess a nonzero quadrupolar moment and interact with the electric field gradient (EFG) of C–^{2}H bonds in nematic molecules, there is an additional quadrupolar perturbative contribution to their energy levels. This contribution is averaged out by molecular motions in the isotropic, but not in the nematic phase. Indeed, once in an undistorted nematic, the single narrow line splits into a doublet, the frequency splitting now being typically of the order of $\omega_Q \sim 2\pi \times 40$ kHz. In general, the splitting ω_Q depends on the relative orientation of the EFG tensor and the direction of the NMR spectrometer magnetic field **B**.

In deriving the expression for ω_Q, one usually assumes that nematic molecules exhibit fast rotations, mainly around the long molecular axis. These occur on a time scale much faster than any other motion type and lead to an averaged EFG tensor that is uniaxial, with the principal axis along the long molecular axis $\mathbf{u}$. The instantaneous quadrupolar frequency splitting so depends only on the relative orientation of $\mathbf{u}$ and $\mathbf{B}$, and is given by $\Omega_Q = \pm\delta\omega_Q \, \frac{1}{2} \, [3(\mathbf{u}\cdot\mathbf{B}/B)^2 - 1]$, where $\delta\omega_Q$ represents the maximum effective splitting (averaged over fast molecular rotations). In a nematic, however, molecular long axes $\mathbf{u}$ are not fixed and fluctuate also themselves around the director $\mathbf{n}$. An average over these fluctuations can be easily performed only if they are also rapid enough on the NMR time scale given by $t_0 \approx 2\pi/\delta\omega_Q$ and results in a reduction of the quadrupolar splitting. Neglecting biaxiality in molecular ordering, this effective splitting can be written as (see, for instance, Refs. [5,134,135])

$$\omega_Q = \pm\delta\omega_Q \, S\Big[\frac{3\cos^2\theta - 1}{2}\Big], \tag{2.41}$$

where $S = \langle \frac{1}{2}[3(\mathbf{n}\cdot\mathbf{u})^2 - 1]\rangle$ is the usual uniaxial nematic order parameter (2.2) and θ the angle between the local director $\mathbf{n}$ and the spectrometer magnetic field $\mathbf{B}$ (see Fig. 2.9).

In a confined system, both $\mathbf{n}$ and S become position-dependent. Since the NMR spectrum corresponds to the overall response of all molecules in the sample, the $\mathbf{n} = \mathbf{n}(\mathbf{r})$ and $S = S(\mathbf{r})$ dependences reflect in NMR spectra via the spatial dependence of the local value of the quadrupolar splitting $\omega_Q = \omega_Q(\mathbf{r})$. The resulting characteristic spectral patterns make it then possible, e.g., to distinguish between different structures inside PDLC droplets, or to monitor the switching of the molecular orientation in a nematic with dispersed polymer fibers. The identification of director configurations can, however, become very problematic in small cavities where translational self-diffusion significantly affects the ^{2}H NMR line shape.

One of the ways to calculate spectra is a simple superimposition of individual molecular static Lorentzian lines from all over the sample, positioning them into the spectrum either according to $\mathbf{n}(\mathbf{r})$ and $S(\mathbf{r})$ profiles [136], or according to molecular configurations obtained from MC simulations [94,99], in both cases following Eq. (2.41). Note that such a procedure is correct only in absence of significant diffusive motion or, alternatively, in systems where the confinement is less severe and the spatial dependence $\omega_Q = \omega_Q(\mathbf{r})$ is weak.

To properly take into account any kind of motional effects, it is convenient to use a semiclassical approach with the time-dependent deuteron spin Hamiltonian [135]. This approach consists of generating the relaxation function

$$G(t) = \exp(i\omega_Z t)\Big\langle \exp\big(i\int_0^t \Omega_Q[\mathbf{r}_i(t'), t']\, dt'\big)\Big\rangle_i, \tag{2.42}$$

with $\Omega_Q[\mathbf{r}_i(t), t] = \pm\delta\omega_Q \, \frac{1}{2} \, [3(\mathbf{u}_i\cdot\mathbf{B}/B)^2 - 1]$, the "instantaneous" quadrupolar splitting [not to be confused with ω_Q from Eq. (2.41) where an average over fluctuations of $\mathbf{u}_i$ has already been performed]. Further, in Eq. (2.42) ω_Z denotes the Zeeman frequency, while the brackets $\langle ... \rangle_i$ stand for the ensemble average over all molecules in the sample. The resonance frequency of the ith molecule located at $\mathbf{r}_i$ is given by $\omega_Z + \Omega_Q[\mathbf{r}_i(t), t]$ and depends on time (t) through $\mathbf{u}_i = \mathbf{u}_i[\mathbf{r}_i(t), t]$, i.e., the instantaneous orientation of the molecular long axis. Generating $G(t)$ is equivalent to mimicking an actual pulsed-NMR experiment. In fact, placing the nematic sample into the spectrometer magnetic field $\mathbf{B}$ gives rise to a net magnetization $\mathbf{M}$ along $\mathbf{B}$, coming from ^{2}H spins. Then, applying a so-called $\pi/2$ magnetic field pulse with a coil mounted perpendicular to $\mathbf{B}$, $\mathbf{M}$ is switched into a plane perpendicular to $\mathbf{B}$. Now, to withstand the torque exerted by $\mathbf{B}$, $\mathbf{M}$ starts to precess (still in the plane perpendicular to $\mathbf{B}$ if spin-lattice relaxation phenomena are neglected). Then, in the coil (same as used to apply the $\pi/2$-pulse) a periodic induced voltage is detected and coincides with the relaxation function $G(t)$ introduced above. Then the ^{2}H NMR line shape $I(\omega)$ is calculated as the Fourier transform of $G(t)$, namely

$$I(\omega) = \int e^{i\omega t}\, G(t)\, dt. \tag{2.43}$$

This procedure for calculating $I(\omega)$ can establish a correct link between any type of molecular motion and the spectra. The information on the motion enters $G(t)$ via the $\mathbf{u}_i = \mathbf{u}_i[\mathbf{r}_i(t), t]$ dependence. The motion is dominated by two processess: fluctuations of molecular long axes and translational self-diffusion. Neglecting for the moment the diffusion, the coordinates of a given molecule $\mathbf{r}_i$ can be taken as fixed and time-independent during the $G(t)$ acquisition. The long molecular axis $\mathbf{u}_i$, however, still fluctuates around the local average, i.e., the director $\mathbf{n}(\mathbf{r}_i)$, and thus still depends on t. Hence, the time dependence in Ω_Q is caused solely by $\mathbf{u}_i$ fluctuations, while the average $\mathbf{u}_i$ (the director) remains unchanged. The characteristic time scale for such fluctuations t_F in a typical liquid crystal is of the order of $\sim 10^{-8}$ s and is much shorter than the typical NMR time scale $t_0 \sim 2.5 \times 10^{-5}$ s [41]. If now translational diffusion is considered as well, also the molecular coordinates change during the NMR experiment: $\mathbf{r}_i = \mathbf{r}_i(t)$. Thereby the average $\mathbf{u}_i$ for a given molecule changes with time since — in a confined system — $\mathbf{n} = \mathbf{n}(\mathbf{r}_i)$. Then the instantaneous Ω_Q depends on t also indirectly through $\mathbf{r}_i = \mathbf{r}_i(t)$. The typical time scale t_D for diffusion to yield a molecular displacement of approximately one molecular length (~ 1 nm) is, like t_F, also of the order of $\sim 10^{-8}$ s [41]. It is, however, more relevant to know the time t'_D needed for molecular diffusion to yield a displacement over which the average molecular orientation $\mathbf{n}(\mathbf{r})$ changes noticeably. The time scale t'_D obviously varies with system size and can become much larger than t_D, especially in systems where the confinement is weak.

In order to estimate how dynamic processes influence the spectra, it is necessary to compare their characteristic time scales to the characteristic NMR time scale t_0. If the molecular motion is sufficiently slow on the t_0 time scale, the spectra can be calculated as $I(\omega) = \langle \delta[\omega - \omega_Z \pm |\omega_Q(\mathbf{r}_i)|] \rangle_i$ [40], i.e., it is possible to use the static approach used in Refs. [94,99]. If, at the other extreme, molecular motion is very fast on the t_0 scale, the spectrum is completely motionally averaged and consists of a sharp doublet $I(\omega) = \delta[\omega - \omega_Z \pm |\langle \omega_Q(\mathbf{r}_i) \rangle_i|]$ whose peaks are positioned at average frequencies $\omega_Z \pm |\langle \omega_Q(\mathbf{r}_i) \rangle_i|$ [40].

2.3.2 Electric capacitance

Alternatively, confined nematics can be studied also by electric capacitance measurements. As already discussed, the anisotropic shape of nematic molecules gives rise to an anisotropy in the dielectric constant. In an external electric field $\mathbf{E}$ the dielectric displacement $\mathbf{D}$ can be written as $\mathbf{D} = \epsilon_0 \underline{\epsilon}\mathbf{E}$, where $\underline{\epsilon}$ is the dielectric constant tensor. Therefore, for a given $\mathbf{E}$ the displacement $\mathbf{D}$ and the effective value of the dielectric constant depend on the relative orientation of the principal axes of $\underline{\epsilon}$ (being in an intimate relation with the director $\mathbf{n}$) and $\mathbf{E}$. As a consequence, a measurement of electric capacitance can yield information on the orientation of nematic molecules, i.e., $\mathbf{n}$. Inversely, capacitance can also be predicted from known director profiles derived phenomenologically [39], or directly from molecular simulation providing configurations of molecular orientations $\mathbf{u}(\mathbf{r})$.

Consider now a nematic slab of thickness d between two capacitor plates where an external electric field $\mathbf{E}$ is applied along $\mathbf{z}$, the unit vector along the sample normal, while the plates are parallel to the xy-plane. For simplicity, it will be assumed that the local electric field is everywhere directed along $\mathbf{z}$. Although in an inhomogeneous dielectric sample this is not strictly true, a full solution of electrostatic Maxwell equations to determine the correct $\mathbf{E}(\mathbf{r})$ dependence is beyond the scope of this analysis. Given the above assumption, one can write for the normal component of the dielectric displacement at the site of each molecule $D_z(x, y) = \epsilon_0 \epsilon(x, y, z) E_z(x, y, z)$, where the molecular $\epsilon(x, y, z)$ is defined as

$$\epsilon(x, y, z) = \epsilon'_{\perp} + (\epsilon'_{||} - \epsilon'_{\perp})(\mathbf{u} \cdot \mathbf{z})^2. \tag{2.44}$$

Here $\epsilon'_{||}$ and $\epsilon'_{\perp}$ denote the eigenvalues of the molecular dielectric tensor, and $\mathbf{u}$ stands for the orientation of the long molecular axis. Following the Gauß theorem $\oint_S \mathbf{D} \cdot d\mathbf{S} = 0$ in absence of free (e.g., ionic impurity) charges, and provided that spatial variations of $\mathbf{u}$ within the xy-plane are weak, for given x and y D_z can be taken to be z-independent. Then D_z has to be same both for $z = 0$ (at the sample surface) and for any other value of z, resulting in $\epsilon(x, y, z) E_z(x, y, z) = \epsilon(x, y, 0) E_z(x, y, 0)$. Moreover, the voltage $\mathcal{V}$ across the sample is independent of where at the plates it is measured, i.e., $\mathcal{V} = \int_0^d E_z(x, y, z) dz = \int_0^d E_z(0, 0, z) dz$. At the same time, the electric charge loaded onto a $a \times b$ portion of the capacitor plates is given by $e = \int_0^a dx \int_0^b dy \, D_z(x, y)$. Assembling all the above relations, the capacitance of the sample can be identified as

$$C = \frac{e}{\mathcal{V}} = \epsilon_0 \int_0^a dx \int_0^b dy \left(\int_0^d \frac{dz}{\epsilon(x, y, z)} \right)^{-1}. \tag{2.45}$$

This formula can be interpreted as follows. The aforementioned assumptions are equivalent to replacing the sample with a circuit of small capacitors, each with its own capacitance proportional to $\epsilon(x, y, z)$. These capacitors are connected in series along the z-axis and, after this, these capacitor series are connected in parallel within the xy-plane. The expression (2.45) then represents the effective capacitance of such a circuit.

2.3.3 Polarized light transmission

Historically, optical methods were the first to reveal the unusual phase behavior of liquid-crystalline materials [1,2]. Like the static dielectric constant, its high-frequency counterpart — the refractive index — is anisotropic, too. Solving the electromagnetic wave equation in an anisotropic dielectric medium, one finds two principal ray types with different polarization, *ordinary* and *extraordinary*, characterized by different values of the refractive index and hence also by different propagation speeds. In the following, exclusively polarized and monochromatic light beams will be considered. Note that the polarization in an anisotropic medium is given by the dielectric displacement vector **D** that is perpendicular to the direction of beam propagation, **k** (the wave vector). As nematic molecules are anisotropic in shape, it is important to know how the polarization **D** of incident light is oriented with respect to the principal axes of the dielectric tensor. For uniaxial molecules, only two out of three eigenvalues are different, $\epsilon_{||}^{\infty}$ and $\epsilon_{\perp}^{\infty}$, symbols $||$ and $\perp$ again referring to the molecular long axis **u**. The eigenvector corresponding to the non-degenerate eigenvalue $\epsilon_{||}^{\infty}$ is identified as the *optical axis* (here denoted by the unit vector **a**) and in a macroscopic sample coincides with the director **n**, while at the molecular level it can be taken along the long molecular axis **u**.

If now the incident light polarization **D** — always perpendicular to **k** — is perpendicular also to the optical axis **a**, one is dealing with the ordinary ray. The ordinary refractive index is given by $n_o = \sqrt{\epsilon_{\perp}^{\infty}}$ and does not depend on the relative orientation of **k** and **a**, i.e., on $\cos\theta = \mathbf{a}\cdot\mathbf{k}/k$. On the other hand, if **D** is lying in the plane defined by **a** and **k**, the corresponding ray is referred to as extraordinary. For the extraordinary ray, however, the (extraordinary) refractive index n_e becomes θ-dependent [137] and satisfies

$$\frac{1}{n_e^2} = \frac{\cos^2\theta}{\epsilon_{\perp}^{\infty}} + \frac{\sin^2\theta}{\epsilon_{||}^{\infty}}. \tag{2.46}$$

Consequently, any arbitrary polarization vector **D** can be decomposed into ordinary and extraordinary polarization components, each of them propagating through the sample with the corresponding index of refraction. Note that if the light beam is directed along the optical axis ($\mathbf{k}||\mathbf{a}$), the refractive indices of both components are equal, $n_o = n_e = \sqrt{\epsilon_{\perp}^{\infty}}$.

The polarization vector $\mathbf{D}(\mathbf{r})$ at a given point **r** in the sample can be conveniently described in terms of the *Jones vector* with components in the plane perpendicular to **k**. These can also be complex, which corresponds to a general elliptical polarization of the light. Assume again that the nematic is confined to slab geometry and that **z** is the slab normal, coinciding with the incident light direction, **k**. Assume further that diffractive and interference phenomena can be neglected and let the sample be split into thin layers normal to **k**, of thickness δz each. Considering a single layer at z, the polarizations of incident and propagated light, $\mathbf{D}(z)$ and $\mathbf{D}(z+\delta z)$, respectively, and are related via $\mathbf{D}(z+\delta z) = \mathsf{A}(z)\mathbf{D}(z)$, where the matrix $\mathsf{A}(z)$ is given by

$$\mathsf{A}(z) = e^{i2\pi n_o \delta z/\lambda} \left[\begin{pmatrix} 1 & 0 \\ 0 & 1 \end{pmatrix} + \frac{e^{i2\pi[n_e(z)-n_o]\delta z/\lambda} - 1}{a_x^2 + a_y^2} \begin{pmatrix} a_x^2 & a_x a_y \\ a_x a_y & a_y^2 \end{pmatrix} \right], \tag{2.47}$$

$a_i = a_i(z)$ are the components of $\mathbf{a}$, and λ is the light wavelength in vacuum. Propagating through the whole sample, the incoming and outcoming polarizations $\mathbf{D}_0 = \mathbf{D}(z = 0)$ and $\mathbf{D}' = \mathbf{D}(z = d)$ are related by $\mathbf{D}' = \mathsf{B}\,\mathbf{D}_0$, where B is given by the matrix product $\mathsf{B} = \prod_{n=1}^{N} \mathsf{A}(n\,\delta z)$ and $N = d/\delta z$ is the number of layers in the sample.

A typical experimental set-up consists of putting the sample between two polarizers crossed at right angle and measuring the intensity of transmitted light $I \propto D_a'(D_a')^* = [\Re(D_a')]^2 + [\Im(D_a')]^2$. Here D_a' is the component of the Jones vector $\mathbf{D}'$ along the direction of the polarizer analyzing the outcoming light and $(D_a')^*$ its complex conjugate. Assuming that the director is homogeneous (and $\mathbf{a}$ constant) and directed at an angle φ_0 with respect to the polarizer, the transmitted intensity I can be written as [138]

$$I = I_0 \sin^2(2\varphi_0)\sin^2(\Delta\Phi/2), \tag{2.48}$$

with I_0 denoting the intensity of the incoming polarized light. Moreover, $\Delta\Phi$ is the phase difference between the ordinary and extraordinary ray accumulated upon passing through the sample (also called *birefringence*) and is given by $\Delta\Phi = (2\pi/\lambda)\int_0^d [n_e(z) - n_o]dz$. According to Eq. (2.48), the maximum output intensity is obtained for $\varphi_0 = \pi/4$. The set-up described above has been used to monitor the switching of the molecular orientation in the Fréedericksz transition [116] to measure the temperature dependence of Frank elastic constants, to measure the anchoring strength [6], as well as for the detection of surface-induced paranematic order [26], to name just a few examples.

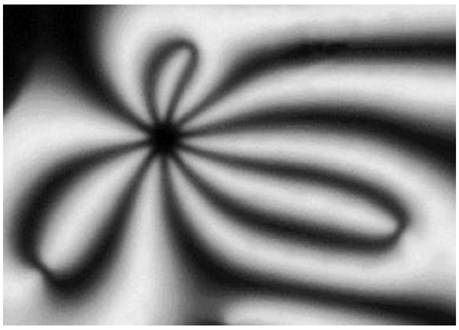

Figure 2.10 Defect structure in a nematic with polymer inclusions, as viewed between crossed polarizers (photo by I. Drevenšek).

In the above analysis it was tacitly assumed that the optical axis (and the nematic director) depends only on the normal z-coordinate, but not on the in-plane ones, x and y, as, for example, in PDLC droplets or nematics with dispersed polymer networks. If the director modulations in the x and y directions are occurring on length scales much shorter than the light wavelength, in an experiment one measures the light intensity averaged over the part of the xy-plane occupied by the probing light beam [26]. If, on the order hand, $\mathbf{n}$ variations are smoother, one ends up with a x-and-y-coordinate-resolved intensity pattern $I(x, y)$, which is the underlying mechanism, e.g., for the recognition of nematic structures in polarizing microscopy experiments [38] — see Fig. 2.10.

3

Nematic slab

This Chapter will be concerned with the simplest confining geometry, a nematic slab. The motivation for the following study comes from experimentally detected subsurface variations of the average molecular orientation, as discussed in the Introduction. In the first part of the Chapter (Sects. 3.1 and 3.2), the nematic orientation close to a flat solid substrate will be investigated by means of a Landau-de Gennes phenomenological model. In particular, it will be shown that when the splay and bend elastic constants are different from the twist elastic constant, a spatial variation of S near the bounding walls yields a subsurface deformation in the nematic director (and vice versa), as well as an intrinsic contribution to the anchoring strength. An expression for the quasi splay-bend elastic constant will be derived and the effective anchoring — a combination of the external and the intrinsic contribution — will be analyzed. Matching elastic and magnetic effects, the corresponding effective extrapolation length will be estimated. In conclusion, a non-planar twisted sample will be considered, analyzing the possibility of finding a localized subsurface deformation also in the twist angle profile. Such twisted-cell geometry is particularly interesting because it is widely used for display applications.

In the second part (Sect. 3.3), a microscopic Monte Carlo study of the intrinsic anchoring at a planar free nematic surface will be presented. To estimate the corresponding extrapolation length and its temperature dependence, a bend deformation in a hybrid cell-like nematic slab will be imposed (Sect. 2.1.4), while the simulation will be based on the simple hexagonal lattice model with nematic particles interacting via the spatially anisotropic modified induced dipole-induced dipole potential (see Sect. 2.2.2).

3.1 Planar cell: Landau-de Gennes analysis

Consider now a nematic sample sandwiched between two parallel plates. Let the sample normal be the z-axis, with the plates positioned at $z = \pm\frac{d}{2}$. Further, consider a uniaxial nematic and allow for planar deformations only. Then one has $S = S(z)$ and $\mathbf{n} = \mathbf{n}(z) = (\sin\phi(z), 0, \cos\phi(z))$, $\phi(z)$ being the angle between $\mathbf{n}$ and the sample normal. Parametrizing the tensorial order parameter Q (2.4) with $S(z)$ and $\phi(z)$, the Landau-de Gennes free energy density (2.13) in the one-constant approximation

($L_2 + L_3 = 0$) can be rewritten as

$$f = f_0(S,T) + \frac{3}{4} L_1 S'^2 + \frac{9}{4} L_1 S^2 \phi'^2, \tag{3.1}$$

where the prime denotes a derivative with respect to z. Note that in the planar geometry discussed here the contribution giving the K_{24} term vanishes identically. Expression (3.1) has been considered by different authors, mainly to describe the influence of the spatial variation of the elastic constant on the nematic tilt angle profile $\phi(z)$ [70,139–143]. A simple variational analysis shows that in a symmetric sample in the strong anchoring case, in which ϕ values at both walls of the nematic slab are equal and fixed, a possible $S = S(z)$ dependence does not induce any subsurface deformation. In fact, a minimum of f (3.1) corresponds to $\phi' = 0$. The spatial variation of S can induce an additional $\phi(z)$-variation only if the deformation is already present.

Consider now a more general case, where $L_2 + L_3 \neq 0$ and $K_{11} = K_{33} \neq K_{22}$. In the planar geometry the free energy density given by Eq. (2.13) has four terms

$$f = f_0(S,T) + f_1(\phi, S') + f_2(\phi', S) + f_3(\phi, \phi', S, S'), \tag{3.2}$$

introducing three elastic contributions (f_1, f_2, f_3). The f_1 term quadratic in S' depends also on ϕ:

$$f_1(\phi, S') = \frac{3}{4} L_1 \Big\{ 1 + \frac{L_2 + L_3}{2L_1} \Big(\cos^2\phi + \frac{1}{3} \Big) \Big\} S'^2. \tag{3.3}$$

The Frank elastic term

$$f_2(\phi', S) = \frac{9}{4} L_1 S^2 \Big\{ 1 + \frac{L_2 + L_3}{2L_1} \Big\} \phi'^2 \tag{3.4}$$

has similar structure as the corresponding term in Eq. (3.1). The third part of the free energy

$$f_3(\phi, \phi', S, S') = -\frac{3}{8} (L_2 + L_3) \sin(2\phi)\, \phi' S S' \tag{3.5}$$

is absent in the equal elastic constant case, coupling variations in ϕ and S. If the substrates impose a scalar order parameter different from the bulk one, the free energy f is no longer minimized by a solution with $\phi' = 0$. Hence a scalar order parameter spatial dependence — usually localized near the substrates — induces a spatial variation of the tilt angle ϕ [69]. The influence of f_3 on structural transitions in nematic liquid crystals has been partially analyzed by Jérôme [50,51].

3.1.1 Quasi splay-bend elastic constant and intrinsic anchoring energy

Assume for the moment that the nematic sample occupies the $z > 0$ half-space, and that in the planar one-dimensional case $S(0) = S_0$ and $\phi(0) = \phi_0$ are fixed by short-range forces. In the bulk the value of S depends only on temperature and is denoted by S_b [found by minimizing (2.8)]. Assuming further that $S_b \neq S_0$, $S(z)$ relaxes to S_b over a length which is of the order of the correlation length ξ (2.11). This characteristic length, in general, does not apply to ϕ-variations, since in absence of external fields there is no preferred orientation of nematic molecules ϕ_b in the bulk of the sample, which would be analogous to S_b. Bulk ϕ-variations, i.e., bulk elastic deformations, caused by external fields or confinements, occur usually over a scale considerably larger than ξ.

In the following, it will be shown that in a nematic layer thick compared to ξ it is possible to include a spatial variation of S in two additional surface energy terms, one corresponding to intrinsic anchoring and one to a quasi splay-bend elastic term. To show this, one has to consider the second and the fourth term of f defined in Eq. (3.2). The total energies per unit surface coming from these contributions are given by $\mathcal{W} = \int_0^\infty f_1(z)dz$ and $\mathcal{G} = \int_0^\infty f_3(z)dz$. Then for $\mathcal{W}$ one obtains

$$\mathcal{W} = \frac{3}{4}L_1\Big\{1 + \frac{L_2+L_3}{2L_1}\Big(\cos^2\phi(z^*) + \frac{1}{3}\Big)\Big\}\lambda^*\langle S'^2\rangle, \tag{3.6}$$

where $\langle S'^2\rangle = (\lambda^*)^{-1}\int_0^{\lambda^*} S'^2 dz$, λ^* being a length of the order of a few ξ. In Eq. (3.6) z^* is an effective distance in the range $(0, \lambda^*)$. Since λ^* is a mesoscopic length, $\mathcal{W}$ can be considered as an additional surface energy, whose anisotropic part $\frac{1}{2}W_i\cos^2\phi(z^*)$ can be interpreted as intrinsic anchoring with a strength defined by

$$W_i = \frac{3}{4}|L_2+L_3|\lambda^*\langle S'^2\rangle \approx \frac{3}{4}|L_2+L_3|\frac{(S_b-S_0)^2}{\lambda^*} = \frac{|K_{11}-K_{22}|}{3\lambda^*}\Big(1-\frac{S_0}{S_b}\Big)^2, \tag{3.7}$$

assuming that $\langle S'^2\rangle \approx (S_b-S_0)^2/(\lambda^*)^2$ and taking into account expressions for the elastic constants derived in Sect. 2.1.3. The sign of L_2+L_3 determines the direction of the easy axis, while the anchoring strength W_i is proportional merely to the modulus of L_2+L_3. The Kléman-de Gennes extrapolation length $l_i = K_{11}/W_i$ [4] is then given by

$$l_i \approx \frac{3K_{11}}{|K_{11}-K_{22}|}\Big(\frac{S_b}{S_b-S_0}\Big)^2\lambda^* \tag{3.8}$$

and depends strongly on the difference $S_b - S_0$.

Also the integral of the term coupling the order and angle variations $\mathcal{G}$ can be rewritten in an effective form as

$$\mathcal{G} = -\frac{3}{16}(L_2+L_3)\Big[\sin(2\phi)\,\phi'\Big]_{z^{**}}(S_b^2 - S_0^2), \tag{3.9}$$

taking into account that $S(z)$ is a monotonic function. The product $\sin(2\phi)\phi'$ is to be evaluated at some intermediate distance z^{**}. Since $0 < z^{**} < \lambda^*$, $\mathcal{G}$ can also be considered as an effective surface contribution having the characteristic angular functional form $\sin(2\phi)\,\phi'$ of the splay-bend elastic term introduced by Nehring and Saupe [52,53]. The corresponding *quasi splay-bend elastic constant* can then be identified as

$$\tilde{K}_{13} = -\frac{3}{8}(L_2+L_3)(S_b^2 - S_0^2) = \frac{K_{22}-K_{11}}{6}\Big[1 - \Big(\frac{S_0}{S_b}\Big)^2\Big]. \tag{3.10}$$

It should be stressed that $\mathcal{G}$ is only effectively a surface term and cannot produce any divergent subsurface deformation, as it is the case with the ordinary K_{13} term. Essentially, it is a bulk term effective only in a thin layer of thickness λ^*. Therefore the $\mathcal{G}$ term-induced subsurface deformations are stabilized by the bulk elastic terms f_1 and f_2. The detailed director profile, requiring a complete free energy minimization, will be discussed in the following.

The intrinsic anchoring strength W_i given by Eq. (3.7) and a quasi $\tilde{K}_{13}$ given by Eq. (3.10) are both temperature-dependent because both the bulk value of the scalar order parameter S_b and the length $\lambda^* \propto \xi$ exhibit a significant temperature dependence on approaching the nematic-isotropic (NI) phase transition.

According to the pseudomolecular model proposed by Vertogen [144,145], it is possible to evaluate elastic constants if the interparticle interaction $\mathcal{U}$ responsible for the formation of the nematic phase is known. In the framework of Vertogen's model it can be shown that if $\mathcal{U}$ is spatially isotropic (i.e., molecular orientations and their relative position are not coupled), the relations $K_{11} = K_{22} = K_{33}$ and $K_{13} = 0$ hold [146]. This is in accordance with the above result that the quasi $\tilde{K}_{13}$ vanishes in the one-constant approximation, i.e., for $L_2 + L_3 = 0$.

3.1.2 Numerical solution of the variational problem

To complete the previous approximate analysis, in the following a full minimization of the total free energy will be carried out by solving numerically the corresponding variational problem. Again a nematic slab of thickness d is considered, with the confining surfaces at $z = \pm\frac{d}{2}$, and again the deformation is assumed to be planar.

To solve the minimization problem, Euler-Lagrange equations and the corresponding boundary conditions must be derived first. The total free energy to be minimized can be written as

$$F = \int_V f_B[\phi(z), \phi'(z), S(z), S'(z)]dV + \int_S f_S[\phi(\pm\tfrac{d}{2}), \phi_0, S(\pm\tfrac{d}{2}), S_0]dS, \qquad (3.11)$$

where $f_B = f_0 + f_1 + f_2 + f_3$ and f_S (specified later) are the bulk and the surface free energy density, respectively, while ϕ_0 and S_0 denote the substrate-induced values of ϕ and S. The surface contribution f_S arising from external anchoring is nonzero only in the weak anchoring case. In presence of an external field also the field energy contribution must be added to f_B.

In the present case the Euler-Lagrange equations have the form

$$\frac{\partial f_B}{\partial \phi} - \frac{d}{dz}\frac{\partial f_B}{\partial \phi'} = 0 \quad \text{and} \quad \frac{\partial f_B}{\partial S} - \frac{d}{dz}\frac{\partial f_B}{\partial S'} = 0, \qquad (3.12)$$

and are both second-order. Hence there must be four boundary conditions for the variational problem to be well-posed. In the strong anchoring case and for a symmetric sample these read $\phi(\pm\frac{d}{2}) = \phi_0$ and $S(\pm\frac{d}{2}) = S_0$, while in the weak anchoring case they become

$$\pm\Big(\frac{\partial f_B}{\partial \phi'}\Big)_{z=\pm\frac{d}{2}} + \frac{\partial f_S}{\partial \phi(\pm\frac{d}{2})} = 0 \quad \text{and} \quad \pm\Big(\frac{\partial f_B}{\partial S'}\Big)_{z=\pm\frac{d}{2}} + \frac{\partial f_S}{\partial S(\pm\frac{d}{2})} = 0. \qquad (3.13)$$

The above system (3.12-3.13) was solved numerically by means of the relaxation method for boundary value problems [147]. First the case with infinitely strong anchoring will be considered. After this, it will be upgraded to a more general situation with an arbitrary strength of anchoring.

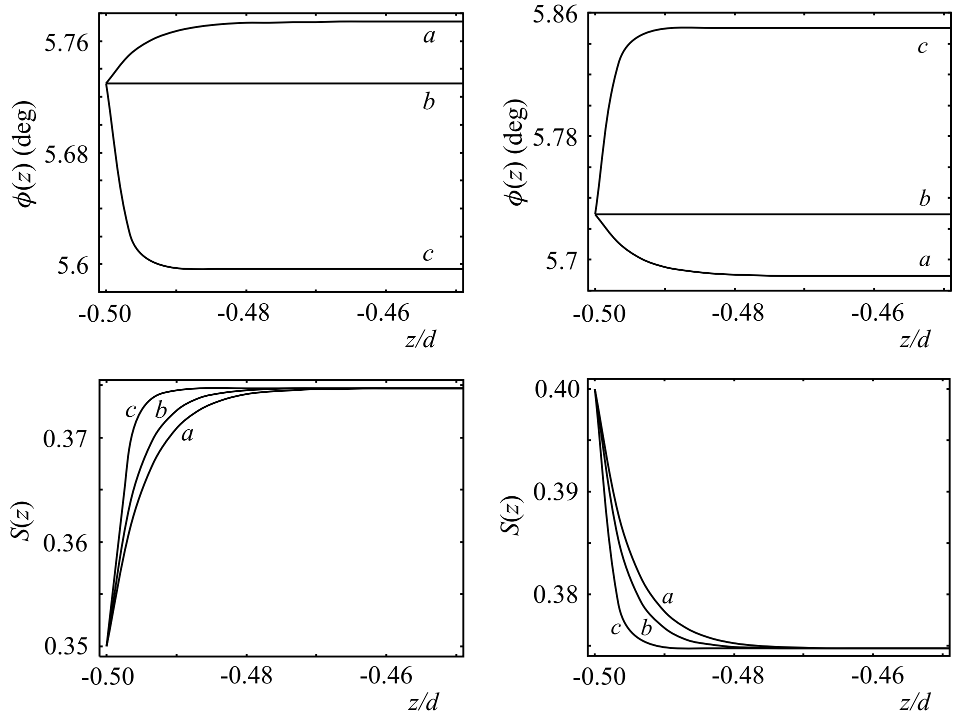

Figure 3.1 Nematic slab: $\phi(z)$ and $S(z)$ profiles in the strong anchoring case; $\phi_0 = 0.1(180^\circ/\pi) \approx 5.73^\circ$, $S_b \approx 0.3747$, and $L_2 + L_3 = +L_1, 0, -L_1$ [cases (a), (b), and (c), respectively]. Disordering ($S_0 = 0.35$, *left*) and ordering substrate ($S_0 = 0.4$, *right*). The sample thickness is equal to $d = 1$ μm, $a = 0.13 \times 10^6$ J/m^{3}K, $B = 1.6 \times 10^6$ J/m^3, $C = 3.9 \times 10^6$ J/m^3 (as measured for 5CB [148]), $T - T_* = 0.4$ K, and $L_1 \approx 10^{-11}$ N.

In the strong anchoring limit at the confining surfaces the scalar order parameter S is fixed to S_0 by surface treatment, while in the bulk it takes the temperature-determined value $S_b \neq S_0$. Further, the surface tilt angle $\phi(\pm\frac{d}{2})$ is fixed to ϕ_0. Although the actual surface tilt cannot vary, the S-variation induces a subsurface deformation. Some examples of director and scalar order parameter profiles are shown in Fig. 3.1. The S-variation occurs in a layer whose thickness is ~ 10 nm, which is indeed of the order of ξ, as predicted by a rough estimate in Sect. 3.1.1. In this region also the variation of ϕ — a subsurface deformation — occurs. The amplitude of the resulting deformation $\Delta\phi$, defined as $\Delta\phi = \phi_b - \phi_0$ (ϕ_b being the bulk tilt angle), is found to be proportional to the quasi $\tilde{K}_{13}$ elastic constant introduced above, similarly as in the case of normal K_{13} elastic constant. If the amplitude of the S-variation (i.e., $S_b - S_0$) is small enough to neglect the variation of the Frank elastic constant $K \propto S_b^2$ close to the interface, the same relation as for the ordinary K_{13} may be used to approximately predict the deformation amplitude [149]:

$$\Delta\phi \approx -\frac{\tilde{K}_{13}}{2K}\sin 2\phi(\pm\tfrac{d}{2}). \tag{3.14}$$

Note that whereas the deformation stabilization in Ref. [149] is governed by second-order elasticity, it is here by the positive definite first-order terms $f_1 \propto S'^2$ and $f_2 \propto \phi'^2$ introduced in Sect. 3.1.1.

The quasi $\tilde{K}_{13}$ elastic constant given by Eq. (3.14) depends on both $L_2 + L_3$ and the difference between the bulk and the surface scalar order parameter. The numerical solutions confirm that if L_2+L_3 changes sign, the deformation amplitude $\Delta\phi \propto \tilde{K}_{13}$ changes sign as well. If $L_2+L_3 = 0$, the subsurface deformation vanishes and $\Delta\phi = 0$. Further, the change in sign of $\Delta\phi$ occurs also if the sign of $S_0 - S_b$ is changed. From Fig. 3.1 it can be deduced that also the characteristic length of the subsurface distortion depends on $L_2 + L_3$. In comparison to cases with negative L_2+L_3, positive L_2+L_3 yield larger proportionality constants in the stabilizing terms f_1 and f_2 [see Eqs. (3.3-3.4)], indicating that stabilization effects for $L_2+L_3 > 0$ are stronger than for $L_2+L_3 < 0$. Hence the corresponding deformations are weaker, i.e., occurring over a larger distance and having smaller amplitude, the former holding for both $\phi(z)$ and $S(z)$ profiles, while the latter is true for $\phi(z)$ profiles only, since $S_b - S_0$ is fixed if anchoring is strong.

Consider now a more realistic nematic-surface coupling, i.e., an anchoring situation where actual surface values $S(\pm\frac{d}{2})$ and $\phi(\pm\frac{d}{2})$ are allowed to vary. Any deviation of these values from the surface-induced ones (S_0 and ϕ_0, respectively) is penalized with an increase of the anchoring energy. This short-range interaction free energy is usually modeled by (2.17) [22], i.e.,

$$f_S = \frac{9}{8}W_e\Big[\frac{2}{3}\Big\{S(\pm\tfrac{d}{2})^2 + S_0^2\Big\} - 2S(\pm\tfrac{d}{2})S_0\Big\{\cos^2\left[\phi(\pm\tfrac{d}{2}) - \phi_0\right] - \frac{1}{3}\Big\}\Big], \tag{3.15}$$

where W_e is related to the corresponding substrate (external) anchoring strength. Note that if there is no S-variation, the expression (3.15) reduces to the standard Rapini-Papoular formula (2.18) [21], while in cases without elastic distortion $[\phi(\pm\frac{d}{2}) = \phi_0]$ its form is $f_S \propto [S(\pm\frac{d}{2}) - S_0]^2$. In the most general case, however, S and ϕ-variations are coupled in the anchoring energy (3.15). The weak anchoring case has been considered previously in Ref. [141] in the one-constant approximation, in which the quasi splay-bend elastic constant is identically zero. Now this analysis shall be generalized by allowing $L_2 + L_3 \neq 0$.

The same Euler-Lagrange equations as in the strong anchoring case were solved, however, with modified boundary conditions. As the actual surface tilt angle is not fixed any more, effects of S-variation-induced intrinsic anchoring can now be revealed. The easy axis for this intrinsic anchoring contribution can be either planar (for $L_2+L_3 > 0$) or homeotropic (for $L_2+L_3 < 0$), as it follows from Eq. (3.6). The calculated $\phi(z)$ profiles confirm this prediction, which is evident from Fig. 3.2: for $L_2+L_3 < 0$ $\phi(\pm\frac{d}{2}) < \phi_0$, and for $L_2+L_3 > 0$ $\phi(\pm\frac{d}{2}) > \phi_0$. The subsurface deformation is still present and behaves in the same manner as in the strong anchoring case.

However, supposed the same S_b and S_0, it is weaker than in the strong anchoring case since $|S_b - S(\pm\frac{d}{2})| < |S_b - S_0|$.

It should be stressed that molecular models where, for instance, the intermolecular interaction is described as a superposition of the Maier-Saupe and the induced dipole-induced dipole coupling (2.34), yield $L_2+L_3 < 0$, i.e., $K_{11} = K_{33} < K_{22}$ [146], which corresponds to a homeotropic easy axis in our study. Thus further discussion will be restricted only to cases with $L_2 + L_3 < 0$.

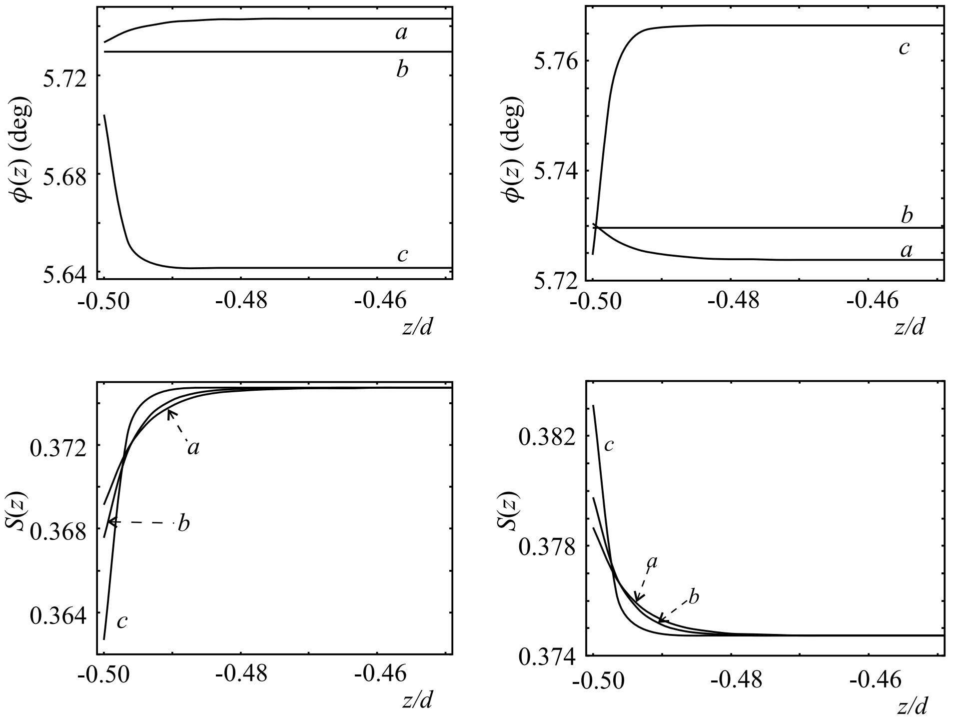

Figure 3.2 Nematic slab: $\phi(z)$ and $S(z)$ profiles in the weak anchoring case ($w_e = 10$); Disordering ($S_0 = 0.2$, *left*) and ordering substrate ($S_0 = 0.5$, *right*). All other parameters and labels are same as those in Fig. 3.1.

A suitable method to estimate the strength of the effective anchoring is to investigate its competition with a distortion-imposing magnetic field **H** [17] tilted at an angle α with respect to the surface normal. Therefore the magnetic energy term (2.21)

$$f_m = -\frac{1}{2}\mu_0\chi_a S(\mathbf{n}\cdot\mathbf{H})^2 = -\frac{1}{2}\mu_0\chi_a S H^2\cos^2\left(\phi(z) - \alpha\right) \tag{3.16}$$

should be added to the bulk free energy density (3.2). Then $\phi(z)$ and $S(z)$ profiles can again be calculated by solving the Euler-Lagrange equations, which now differ from those derived in absence of the additional magnetic free energy contribution. The influence of subsurface deformations on the large scale director profile enters only via the effective intrinsic anchoring contribution. Therefore, ignoring the thin subsurface layer in which the subsurface deformation occurs, one can for small ϕ fit the calculated $\phi(z)$ profiles by the ansatz (see Fig. 3.3)

$$\phi(z) = \alpha + A\frac{\cosh(z/\xi_m)}{\cosh(d/2\xi_m)} \tag{3.17}$$

following from the standard Frank elasticity, the parameter A being related to the amplitude of the deformation, d denoting the sample thickness, and ξ_m the characteristic length of this field-induced deformation — the magnetic coherence length (2.23) [4]. Fig. 3.3 (b) shows the enlarged subsurface region of Fig. 3.3 (a), in which the ansatz (3.17) describing the macroscopic director profile fails to match with the calculated profile. Since this region is of microscopic — nanometric — thickness, it will be neglected in the determination of the anchoring strength, as already stated above.

If ϕ_0 is the direction favored by the effective anchoring, the parameters of the fit

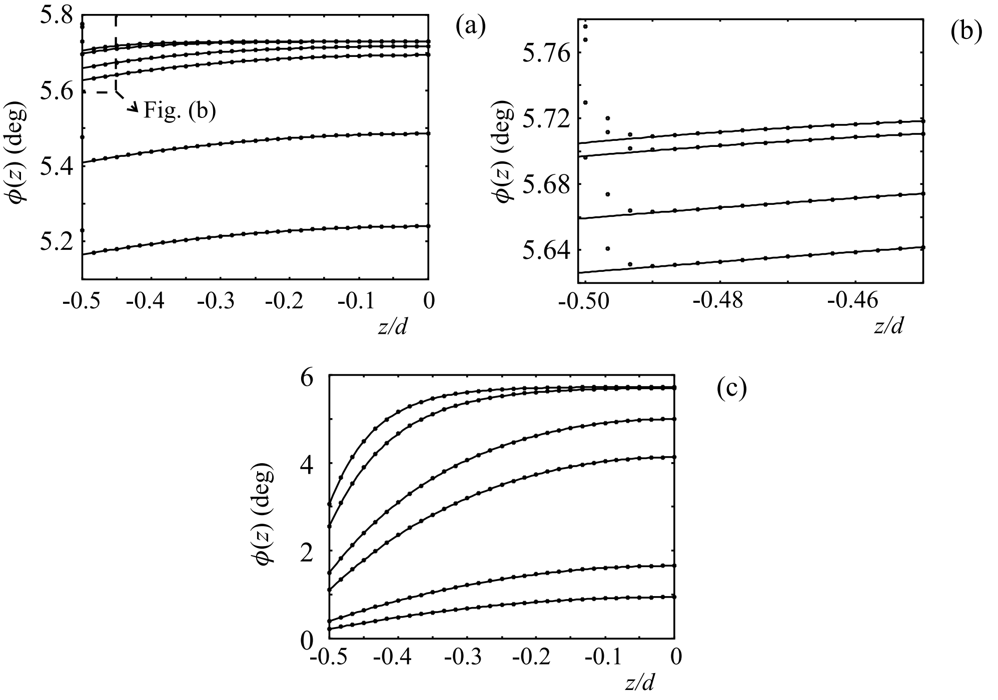

Figure 3.3 Calculated director profiles (dots) in magnetic field compared to the hyperbolic cosine fit (solid line): $w_e = 5$, $L_2 + L_3 = -L_1$, $S_b \approx 0.3747$, and $S_0 = 0$ [cases (a) and (b); no external anchoring] or $S_0 = 0.5$ [case (c); homeotropic external anchoring with $\phi_0 = 0°$]. The sample thickness is equal to $d = 1\mu$m, the magnetic field direction $\alpha = 0.1(180°/\pi) \approx 5.73°$. The magnetic field strengths expressed in terms of the coherence length ξ_m amount to ≈ 65 nm, 90 nm, 205 nm, 290 nm, 650 nm, and 920 nm; the first value corresponding to the top and the last to the bottom curves of Figs. (a) and (c). Comparing cases (a) and (c), it is evident that the external anchoring is considerably stronger than the intrinsic one. Fig. (b) presents the enlarged section of Fig. (a) marked with a dashed line. All other parameters are equal to those of Fig. 3.1.

$(A,\,\xi_m)$ for small $\phi_0-\alpha$ yield the effective extrapolation length [17]

$$l_{eff}=\frac{K}{W_{eff}}=\Big[\frac{\phi_0-\alpha}{A}-1\Big]\xi_m\coth(\frac{d}{2\xi_m}). \tag{3.18}$$

This anchoring is a superposition of the intrinsic and external contribution. From the analysis performed above, it is possible to estimate extrapolation lengths for both sources of anchoring separately. For intrinsic anchoring one can rewrite (3.8) as

$$l_i=\frac{3S_b^2}{[S_b-S(\pm\frac{d}{2})]^2}\Big|\frac{2L_1}{L_2+L_3}+1\Big|\lambda^*. \tag{3.19}$$

Provided that λ^* is known, the approximate value l_i (3.19) can be compared with the "measured" one, l_{eff} (3.18). Similarly, it is possible to derive an estimate for the external anchoring extrapolation length $l_e=K_{11}/W_E$. The external anchoring strength W_E can from Eq. (3.15) be identified as $W_E=\frac{9}{2}W_eS(\pm\frac{d}{2})S_0$, while the elastic constant K_{11} is still given by $K_{11}=\frac{9}{4}S_b^2(2L_1+L_2+L_3)$. In terms of the dimensionless anchoring strength $w_e=W_ed/L_1$ the length l_e can be expressed (for $S_0\neq 0$) as

$$l_e=\frac{S_b^2}{w_eS_0S(\pm\frac{d}{2})}\Big[1+\frac{L_2+L_3}{2L_1}\Big]d. \tag{3.20}$$

Assuming that both intrinsic and external anchoring have the same easy axis (e.g., homeotropic), the effective anchoring strength can be written as $W_{eff}=W_i+W_E$. Then for the corresponding extrapolation lengths the relation

$$\frac{1}{l_{eff}}=\frac{1}{l_i}+\frac{1}{l_e} \tag{3.21}$$

holds. If, e.g., $l_e\ll l_i$, then $l_{eff}\approx l_e$.

Imagine now a nematic slab confined by two substrates treated by silicon oxide-evaporation technique, such that $S_0=0$. In this case the angular dependence in (3.15) vanishes and hence the external anchoring in the Rapini-Papoular sense is absent. The choice $S_0=0$ enables one therefore to investigate pure intrinsic anchoring despite $w_e\neq 0$, and thus simplifies the analysis significantly. Setting $w_e\neq 0$ is, however, necessary to yield $S(\pm\frac{d}{2})\neq S_b$, which is required for intrinsic anchoring to occur at all. However, beside studying cases with $S_0=0$, it will be instructive to consider also those with $S_0\neq 0$ in order to see the increase of the effective anchoring strength when external anchoring is present as well.

$\phi(z)$ and $S(z)$ profiles in magnetic field were calculated for different values of the field strength H, the surface-imposed order parameter S_0, and anchoring strength w_e (the example $w_e=5$ is given in Fig. 3.3). In all cases $L_2+L_3=-L_1$ was assumed, resulting in $K_{11}<K_{22}$ and yielding a homeotropic easy axis for intrinsic anchoring. The Landau parameters a, B, C, and the temperature were chosen such that $S_b\approx 0.3747$. The estimates for the "measured" effective extrapolation length

w_e	S_0	$S(\pm\frac{d}{2})$	l_i	l_e (nm)	l_{eff} (nm)
1	0	0.3720	58000 λ^*	—	400000
1	0.5	0.3756	500000 λ^*	374	375
5	0	0.3613	2350 λ^*	—	16700
5	0.5	0.3791	22000 λ^*	74	75
10	0	0.3484	610 λ^*	—	4300
10	0.5	0.3832	5800 λ^*	37	37
50	0	0.2606	33 λ^*	—	205
50	0.5	0.4072	400 λ^*	7	7
100	0	0.1861	12 λ^*	—	63
100	0.5	0.4255	160 λ^*	3	3

Table 3.1 Effective anchoring extrapolation lengths l_{eff} compared to the values l_i and l_e, predicted for intrinsic and external anchoring, respectively. All estimates for l_{eff} with $S_0 = 0$ refer to pure intrinsic anchoring, while the ones with $S_0 = 0.5$ refer to a superposition of intrinsic and external anchoring, where the latter prevails. Easy axes for both kinds of anchoring are homeotropic. The angle between the magnetic field direction and the surface normal is equal to $\alpha = 0.1(180^\circ/\pi) \approx 5.73^\circ$, the bulk value of the order parameter to $S_b \approx 0.3747$, and the sample thickness to $d = 1\mu$m.

l_{eff} are listed in Table 3.1. The results for $S_0 = 0$ show that if the coupling with the surface has a strength $w_e \leq 50$, the intrinsic anchoring is rather weak ($l_i > 100$ nm). Its strength increases with increasing w_e as $S_b - S(\pm\frac{d}{2})$ increases, which is in agreement with formula (3.19). However, if $S_0 \neq 0$, the external contribution to the anchoring is nonzero as well and is for, e.g., $S_0 = 0.5$ considerably stronger than the weak intrinsic part [compare Figs. 3.3 (a) and (c)]. Consequently, leaving other parameters unchanged, the effective extrapolation length decreases significantly in comparison to the $S_0 = 0$ case, and now only $w_e < 5$ yields extrapolation lengths of the order of those observed experimentally ($>$ 100 nm) [6]. Since the external contribution to the effective anchoring seems to completely overwhelm the intrinsic one, one cannot expect to observe any temperature-driven anchoring transitions due to their competition.

Comparing the predicted values for l_e in cases with $S_0 = 0.5$ [Eq. (3.20)] and the "measured" effective ones [Eq. (3.18)], a very good agreement is observed (see Table 3.1), which again shows that in these cases the intrinsic anchoring is negligible with respect to the external one. Further, setting $S_0 = 0$ and considering intrinsic anchoring alone, the agreement of predicted [Eq. (3.19)] and "measured" values of l_i can be achieved by setting $\lambda^* \approx 6 - 7$ nm, which is comparable to the thickness of the layer in which the S and ϕ variations occur. Note also that in all cases the deformation strength of the subsurface deformation is rather small. For instance, for $w_e = 5$ and $S_0 = 0.5$, yielding a still reasonable extrapolation length, and close to

$\phi_0 = \pi/4$ one finds $d\phi/dz \approx 3\times 10^{-4}/\rho_0 \ll 1/\rho_0$ ($\rho_0 \approx 1$ nm being the characteristic molecular dimension), as required by the elastic continuum theory. In this case also the variation of the order parameter is rather weak, i.e., $[S(\pm\frac{d}{2}) - S_b]/S_b \sim 0.01$. Cases with lower w_e yield a deformation strength that is even smaller.

3.2 Twisted cell: Landau-de Gennes analysis

In Sect. 3.1 (as well as in Refs. [50,51,68,69]) exclusively planar deformations were treated to analyze the coupling between S and director variations. Thereby the twist distortion was neglected and the subsurface deformation was present in the tilt angle profile $\phi(z)$. The aim of this Section is to extend the above analysis for the strong anchoring limit to non-planar distortions. In particular, here we would like to examine whether a localized subsurface twist deformation similar to that reported in Sect. 3.1 for the tilt angle can be observed, and, further, explore also the global (delocalized) coupling between the tilt and the twist angle in a twisted nematic slab. Analyses allowing also non-planar distortions have been performed in Refs. [150,151], but were used to investigate substrate-induced orientational phase transitions.

Consider again a nematic slab of thickness d where the z-axis is oriented along the surface normal and the surfaces are lying at $z = \pm\frac{d}{2}$, being parallel to the xy-plane. Dropping the in-plane restriction for the director $\mathbf{n}$, $\mathbf{n}$ can be parametrized as $\mathbf{n}(z) = (\sin\phi(z)\cos\omega(z), \sin\phi(z)\sin\omega(z), \cos\phi(z))$, $\phi(z)$ being the angle between $\mathbf{n}$ and the z-axis (the tilt angle) and $\omega(z)$ the azimuthal angle defined with respect to the x-axis (the twist angle). Now the free energy density (2.13) is given (neglecting biaxiality) by

$$f = f_0(S,T) + f_1(\phi, S') + f_2(\phi, \phi', \omega', S) + f_3(\phi, \phi', S, S'), \qquad (3.22)$$

where the prime still denotes the z-derivative. Like in the planar case, in (3.22) there are four free energy terms. The homogeneous term $f_0(S)$, the "polar" intrinsic anchoring term $f_1(\phi, S')$, and the quasi splay-bend term $f_3(\phi, \phi', S, S')$ are identical as in the planar case (Sect. 3.1). The Frank elastic term is now, however, different, i.e.,

$$f_2(\phi, \phi', \omega', S) = \frac{9}{4} L_1 S^2 \left\{ \left(1 + \frac{L_2'}{2L_1}\right)\phi'^2 + \sin^2\phi \left(1 + \frac{L_2'}{2L_1}\cos^2\phi\right)\omega'^2 \right\}, \quad (3.23)$$

where $L_2' = L_2 + L_3$. Note that the free energy density depends on ω', appearing in the Frank term (f_2), but not on ω itself. If one considered chiral nematics that form a structure twisted spontaneously already in the unperturbed ground state, the only changes in the free energy density appear in the Frank term (3.23). Then, apart from an ω-independent term, a term linear in ω' has to be added, and the f_2-contribution to the free energy density is still ω-independent. Considering chiral nematics would not substantially change the analysis, therefore it will be restricted only to nonchiral nematics where the twist is imposed by confining surfaces. Further, note that although the elastic deformations are non-planar now, the K_{24}-contribution still vanishes because **n** still depends on a single Cartesian coordinate, i.e., **n**=**n**(z).

In the strong anchoring case the total free energy per unit surface is given by

$$F = \int_{-d/2}^{d/2} f[\phi(z), \phi'(z), \omega'(z), S(z), S'(z)]\ dz. \tag{3.24}$$

Minimizing (3.24) with respect to $S(z)$, $\phi(z)$, and $\omega(z)$ yields the following Euler-Lagrange equations (ELE)

$$\frac{\partial f}{\partial S} - \frac{d}{dz}\frac{\partial f}{\partial S'} = 0, \qquad \frac{\partial f}{\partial \phi} - \frac{d}{dz}\frac{\partial f}{\partial \phi'} = 0, \qquad \text{and} \qquad \frac{\partial f}{\partial \omega} - \frac{d}{dz}\frac{\partial f}{\partial \omega'} = 0. \tag{3.25}$$

Since in f there is no explicit dependence on ω (also for chiral nematics), the last of the above ELE can be rewritten as

$$\frac{\partial f}{\partial \omega'} = \frac{\partial f_2}{\partial \omega'} = \alpha = \text{const.} \tag{3.26}$$

Taking into account Eq. (3.23), one can find that

$$\alpha = \frac{9}{2} S^2 \sin^2\phi \Big\{ L_1 + \frac{L_2'}{2}\cos^2\phi \Big\}\ \omega', \tag{3.27}$$

which, once integrated with respect to z over the whole slab, results in

$$\omega(\tfrac{d}{2}) - \omega(-\tfrac{d}{2}) = \alpha \int_{-d/2}^{d/2} \frac{dz}{\frac{9}{2}S^2(L_1 + \frac{L_2'}{2}\cos^2\phi)\sin^2\phi}. \tag{3.28}$$

If $\omega(\frac{d}{2}) = \omega(-\frac{d}{2})$ is chosen, it follows that $\alpha = 0$ must hold and from (3.27) also that $\omega' = 0$ everywhere in the sample. Hence in this case the twist deformation is absent and the director is lying in a plane — the problem is degenerate with respect to ω; see previous Section). If, however, $\omega(\frac{d}{2}) \neq \omega(-\frac{d}{2})$, $\alpha = 0$ no longer holds and the twist deformation is present. For such a twisted nematic slab the ELE (3.26) must be solved numerically. As weak anchoring would only reduce the deformation, here we will concentrate on strong anchoring boundary conditions, where the actual surface values of S, ϕ, and ω cannot deviate from those imposed by the substrate.

First consider S-profiles in a twisted nematic sample. The scalar order parameter always relaxes monotonously from the surface value S_0 to the bulk value S_b given by Eq. (2.9). Like in the planar case, the variation here occurs over a distance characterized by the nematic correlation length ξ (2.11) (see Fig. 3.4, bottom) and is hence again localized to a thin subsurface layer. For the present choice of a, L_1, and $T - T_*$, its thickness is about 20 nm. S-profiles in presence of the twist deformation are very similar to those reported in the previous Section. In general, any variation of ϕ or ω affects S-profiles only very weakly since the free energy contributions associated with the elastic deformation (f_1, f_2, and f_3) are considerably smaller than the homogeneous one (f_0).

On the other hand, in a twisted nematic slab there is quite a significant change in tilt angle profiles $\phi(z)$ in comparison to the non-twisted case. These profiles show a

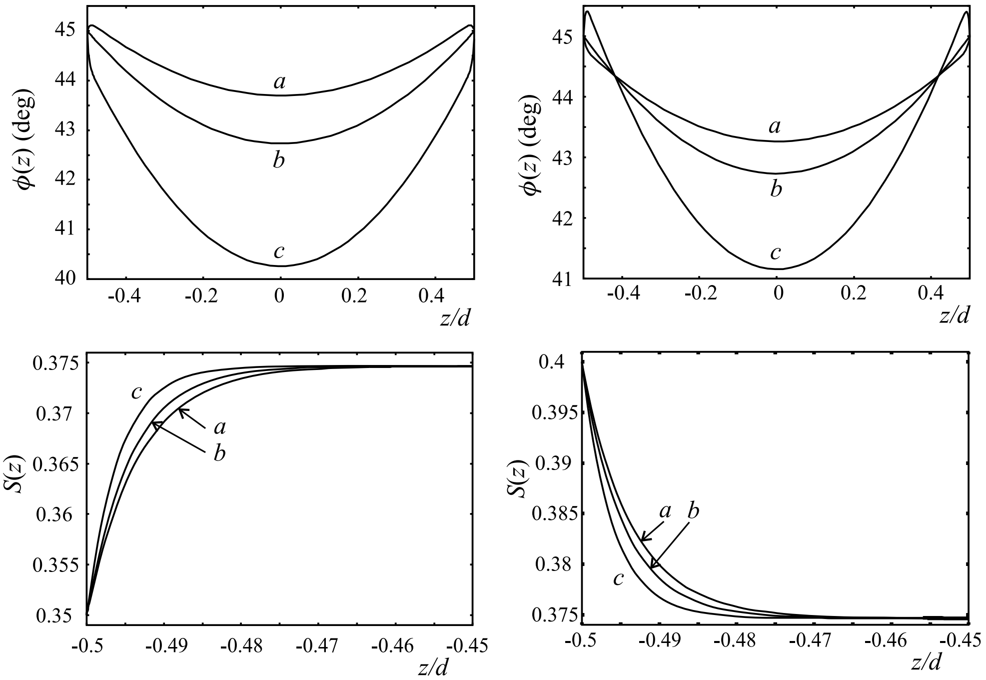

Figure 3.4 $\phi(z)$ and $S(z)$-profiles in a twisted nematic slab with strong anchoring. $\phi(\pm\frac{d}{2}) = 45^\circ$, $\omega(-\frac{d}{2}) = 0^\circ$, $\omega(\frac{d}{2}) = 45^\circ$, $S_b \approx 0.375$, $S_0 = 0.35$ (*left*) or $S_0 = 0.4$ (*right*), and $L_2' = L_1,\ 0,\ -L_1$ [curves (a), (b), and (c), respectively]. The sample thickness is equal to $d = 1\ \mu$m, $a = 0.13 \times 10^6$ J/m^{3}K, $B = 1.6 \times 10^6$ J/m^3, $C = 3.9 \times 10^6$ J/m^3, $T - T_* = 0.4$ K, and $L_1 = 10^{-11}$ N.

considerable variation of ϕ that spreads over the whole slab (Fig. 3.4, top) — even in the symmetric anchoring case in which $\phi(-\frac{d}{2}) = \phi(\frac{d}{2})$. The source of this delocalized deformation is the coupling between ω' and ϕ in the Frank elastic term f_2 (3.23). Namely, since the ω'^2-term — nonzero whenever the twist deformation is present — always gives a positive free energy contribution, the proportionality factor appearing in front of ω'^2 must be as low as possible, i.e., for $L_2' = 0, \pm L_1$ (as chosen for profiles plotted in Fig. 3.4) $|\phi|$ must decrease. However, this decrease is compensated by the ϕ'^2 term which is also present in f_2 and gives a positive free energy contribution as soon as ϕ varies. Note that because the ratio of the proportionality constants belonging to ω'^2 and ϕ'^2, respectively, is larger when $L_2' < 0$, in that case the decrease in $|\phi|$ can be larger than for $L_2' = 0$ (just the opposite holds for $L_2' > 0$). Further, it should be noticed that for $L_2' \neq 0$ the coupling between ϕ' and S' described by the f_3-term yields a localized S-variation-induced subsurface deformation in $\phi(z)$, behaving similarly as in the non-twisted case.

Consider, finally, also $\omega(z)$-profiles. These can be calculated by integrating Eq. (3.27) with respect to z. For simplicity, suppose first S and ϕ to be constant throughout the sample. The resulting profile is then a linear function of z, i.e.,

$$\omega(z) = \omega(-\tfrac{d}{2}) + \Delta\omega \left(\frac{z}{d} + \frac{1}{2}\right), \tag{3.29}$$

where $\Delta\omega = \omega(\frac{d}{2}) - \omega(-\frac{d}{2})$ is proportional to the constant α introduced in (3.26).

If, however, either ϕ (with S=const.; Frank solution) or both ϕ and S are allowed to vary with z, deviations $\delta\omega(z)$ from the linear profile given by (3.29) may occur. For example, global variations of ϕ appearing, e.g., when $\phi(-\frac{d}{2}) \neq \phi(\frac{d}{2})$, or even in a symmetric case where ϕ varies due to the twist deformation, give rise to deviations $\delta\omega(z)$ that are global as well [see Fig. 3.5 (a)].

On the contrary, a localized variation of $S(z)$ induces a variation of ω that is localized as well. Explore now this "subsurface deformation" in ω in more detail and compare it to the one appearing in the $\phi(z)$-profile. Let, for sake of clarity, the $\phi(z)$-dependence be omitted by setting $\phi(\frac{d}{2}) = \phi(-\frac{d}{2}) = 90^\circ$. In this case there is no source of the subsurface deformation in ϕ since the f_3-term (3.5) vanishes. Numerical solutions of the ELE (3.25) confirm indeed that then $\phi(z) = 90^\circ = \text{const.}$ holds throughout the whole sample. Putting now $\phi(z) = 90^\circ$ into (3.27) yields

$$\omega' = \frac{2\alpha}{9L_1 S^2(z)}. \tag{3.30}$$

Assume for the moment that the $S(z)$-profile is modeled by

$$S(z) = S_b - \Delta S \frac{\cosh(z/\lambda^*)}{\cosh(d/2\lambda^*)}, \tag{3.31}$$

representing the localized variation of S close to the confining walls with an amplitude $\Delta S = S_b - S_0$ and a characteristic length λ^* that is to be characterized by the nematic correlation length ξ. The integration of (3.30) is particularly simplified if $|\Delta S| \ll S_b, S_0$ is assumed in addition. The resulting $\omega(z)$-profile is then given approximately by

$$\omega(z) \approx \omega(-\tfrac{d}{2}) + \tfrac{\Delta\omega}{2} + \Delta\omega \left(z + 2\lambda^* \tfrac{\Delta S}{S_b} \tfrac{\sinh(z/\lambda^*)}{\cosh(d/2\lambda^*)}\right) \left(d + 4\lambda^* \tfrac{\Delta S}{S_b} \tanh(d/2\lambda^*)\right)^{-1}. \tag{3.32}$$

The ratio $\sinh(z/\lambda^*)/\cosh(d/2\lambda^*)$ appearing in (3.32) is nonzero only in the boundary layers and hence represents a localized subsurface variation of the twist angle, whose amplitude equals

$$\delta\omega_0 = \frac{2\lambda^* \frac{\Delta S}{S_b}}{d + 4\lambda^* \frac{\Delta S}{S_b} \tanh(\frac{d}{2\lambda^*})} \Delta\omega \approx 2 \frac{\lambda^*}{d} \frac{\Delta S}{S_b} \Delta\omega, \tag{3.33}$$

taking into account $\lambda^* \ll d$ in the end. The approximate $\omega(z)$-profile can be close to the substrates ($z \to \pm\frac{d}{2}$) simplified to $\omega(z) \approx \omega(-\frac{d}{2}) + \Delta\omega(\frac{z}{d} + \frac{1}{2}) \mp \delta\omega_0\{1 - \exp[(\pm z - \frac{d}{2})/\lambda^*]\}$.

This simple calculation proves the existence of a localized variation also in the ω-profile. Its amplitude is rather small, if compared to the overall variation of ω: for $\Delta\omega = 45^\circ$, $\lambda^* \approx 0.01d$ ($d = 1\mu$m), $\Delta S \approx 0.025$, and $S_b \approx 0.375$ it is $\delta\omega_0 \approx 0.06^\circ$. For comparison, the actual ω-profile in slab geometry can be derived also from solving the ELE (3.25) for $\phi(\pm\frac{d}{2}) = 90^\circ$ and the above parameters [see Fig. 3.5 (b)]. The $\omega(z)$-dependence shows a localized deformation $\delta\omega(z)$ that is added to the linear solution (3.29) with $\Delta S = 0$, exhibiting a functional dependence similar to that predicted analytically by Eq. (3.32). The amplitude of $\delta\omega(z)$, $\delta\omega_0$, is of the same order of magnitude as estimated above. However, the $\delta\omega$ effect could become easily measurable considering a very thin highly twisted nematic cell ($d \sim 100$ nm, $\Delta\omega \sim 2\pi$), using strongly ordering substrates ($|\Delta S| \sim 0.1$), and adjusting the temperature close to the NI transition, where $\lambda^* \sim 10$ nm.

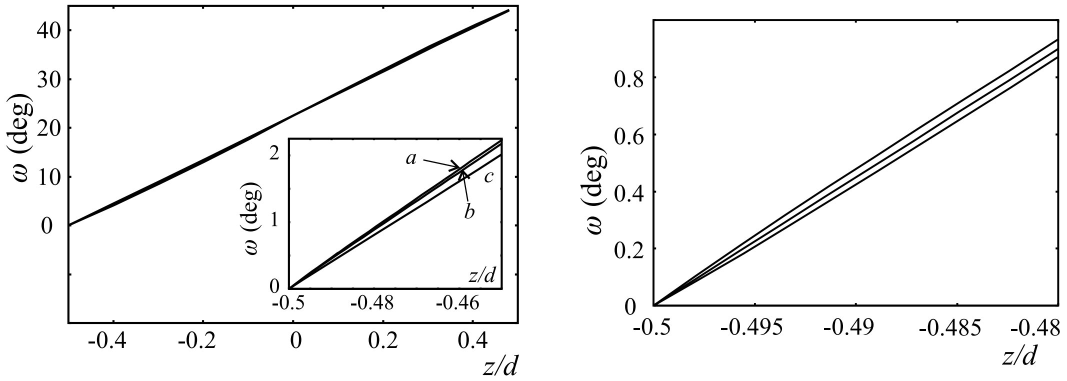

Figure 3.5 *Left:* $\omega(z)$-profiles in a twisted and strongly anchored nematic slab with a delocalized variation of ϕ. $S_0 = 0.4$, while all other parameters and labels are same as in Fig. 3.4. In the inset, $\omega(z)$ in the subsurface region is shown. The deviation $\delta\omega$ from the linear solution (3.29) spreads through the whole sample. Profiles for $S_0 = 0.35$ differ only negligibly from those plotted here. *Right:* $\omega(z)$-profiles in the subsurface region of a twisted nematic slab with a localized variation of S; $\phi(\pm\frac{d}{2}) = 90°$, $S_b \approx 0.375$, $\Delta S \approx 0.025,\ 0,\ -0.025$ (top, center, and the bottom curve, respectively), $\omega(-\frac{d}{2}) = 0°$, $\omega(\frac{d}{2}) = 45°$; $L_2' = 0$ [for $\phi(\pm\frac{d}{2}) = 90°$ the problem is degenerate with respect to the value of L_2']. The profiles cross in the middle of the sample and exhibit a similar behavior at the opposite side, the top curve, e.g., now corresponding to the negative value of ΔS. The values for a, B, C, $T - T_*$, and L_1 are same as in Fig. 3.4.

Note again that the source of the subsurface variation of the twist angle $\delta\omega(z)$ is the Frank elastic term (f_2) and that the origin of this ω-variation is different from that responsible for the in-plane variation of ϕ examined in the previous Section — in that case the source was the f_3 term. Both subsurface ϕ and ω-variations follow from a localized variation of S, but the latter can exist only if a global distortion in ω is already present (since $\delta\omega \propto \Delta\omega$), while for the former no deformation in ϕ is necessary to assure its existence.

Finally, note that in the Frank term (f_2) there is also a coupling between S and ϕ' that is mathematically equivalent to that between S and ω'. In samples where a delocalized deformation in ϕ is already present, e.g., in non-symmetric samples with $\phi(-\frac{d}{2}) \neq \phi(\frac{d}{2})$, this can, in principle, induce an additional localized variation in ϕ. Then the additional variation has to be added to the one already analyzed in Sect. 3.1, where this kind of deformation was not discussed since only symmetric planar samples were considered.

3.3 Planar cell: molecular approach

In this Section the properties of intrinsic anchoring (analyzed to some extent already earlier in the Chapter) will be addressed from the molecular point of view, especially its temperature dependence. The analysis will be based on the hexagonal lattice model [17], along with the spatially anisotropic modified induced dipole-induced dipole pairwise potential (2.34) — see Sect. 2.2.2. Before proceeding to anchoring studies, however, the nematic-isotropic transition in this model system will be briefly investigated. A similar molecular study of intrinsic anchoring was already given in Ref. [17], however, in the zero-temperature approximation. More recently, a finite-temperature Monte Carlo analysis of external anchoring was performed in Ref. [152] for the LL model, attempting to present a full temperature dependence of the external anchoring strength (expressed through the extrapolation length K/W).

Phenomenologically, the anchoring energy W decreases with increasing temperature, being roughly proportional to S^2 if modeled by (2.17), and is unable to yield any significant temperature dependence in K/W (recall that $K \propto S^2$ as well). To get rid of such behavior — in contrast also to most experiments — the anchoring energy can be modeled directly by (2.16) with $\mu \neq 0$. In fact, experimental analyses typically show a decrease of W — or an accompanying increase of the extrapolation length K/W — when the NI transition is approached [46,112,143,153,154]. In addition, thermal director fluctuations can substantially renormalize W [155,156].

While it is well known that $K \propto S^2$, there seems to be no general rule for the functional form of the $W(S)$-dependence [and, consequently, the temperature dependence of W]. In fact, W seems to be strongly related to specific properties of a given confining surface. For example, theoretical considerations in a system of hard rods confined between parallel hard walls show that $W \propto S$ [157], while in experiments measuring anchoring at rough pore surfaces even $W \propto S^4$ could be observed [46]. Given $K \propto S^2$, in the former case K/W decreases when the NI transition is approached (agreeing with simulation results in athermic systems of hard elongated particles [158]), but increases in the latter (as found experimentally for most thermotropics). Motivated by these developments, here the analysis performed in Ref. [17] will be upgraded to nonzero temperatures and K/W for intrinsic anchoring will be reestimated, attempting to extract its temperature dependence from the data. However, first a set of bulk sample simulations will be presented to determine the NI transition temperature.

Consider again a nematic sandwiched between two flat and parallel substrates, as shown in Fig. 2.8, the z-axis being the sample normal and d its thickness. To avoid bulk easy axes, nematic particles are allowed to rotate only in parallel xz-planes (coinciding with hexagon planes). Following Eq. (2.34), for nearest-neighbor particles i and j with orientations given by unit vectors $\mathbf{u}_i$ and $\mathbf{u}_j$, the interaction energy is given by

$$U_{ij} = -\epsilon' \left[\mathbf{u}_i \cdot \mathbf{u}_j - 3\nu(\mathbf{u}_i \cdot \mathbf{r}^*)(\mathbf{u}_j \cdot \mathbf{r}^*)\right]^2 , \tag{3.34}$$

where $\epsilon' > 0$ and $\mathbf{r}^*$ is the interparticle unit vector. Although the range of the van der Waals potential (2.34) is proportional to r^{-6}, for computational reasons in the present simulation only interactions between nearest neighbors were taken into account. Thereby the error in the estimation of the intrinsic anchoring energy is expected not to exceed 15%. There are eight nearest neighbors (in contrast to the LL model with six neighbors only): six in the xz hexagon plane, plus two out-of-plane ones (along the y-axis). It must be stressed again that while the lattice itself is three-dimensional, the particles $\mathbf{u}_i$ are two-dimensional objects. As already suggested in Sect. 2.2.2, the analysis must be restricted to low values of the anisotropy parameter ν to avoid solid-like periodic director solutions [17].

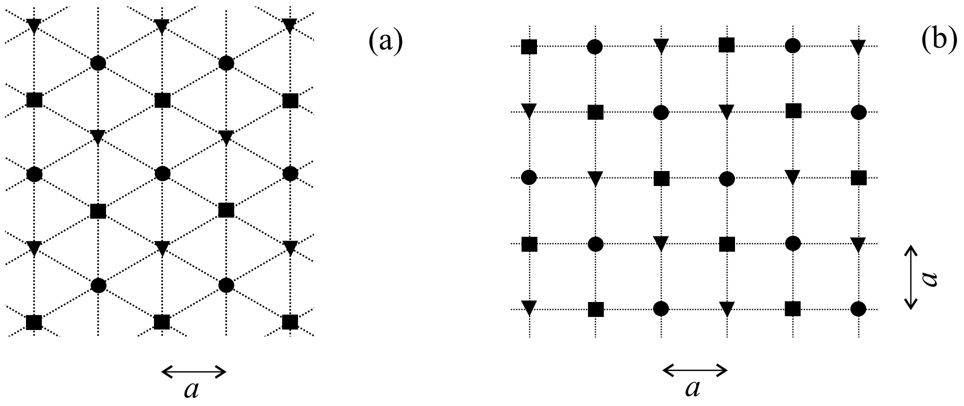

Figure 3.6 Tripartite hexagonal lattice and the three sublattices: squares, circles, and triangles. (a) xz-plane, (b) xy-plane.

Then Monte Carlo (MC) simulations were performed as follows. For the measurement of the extrapolation length the simulation box size was chosen to be $48 \times 48 \times 48$ particles, which amounts to 105984 particles taking part in the simulation (the boundary layers at $z = 0$ and $z = d$ being already excluded in this figure), while for the bulk simulation a smaller $30 \times 30 \times 30$ lattice with 27000 particles was considered. The hexagonal lattice was divided into three sublattices, as shown in Fig. 3.6. Thereby the bonds between neighboring particles on the lattice never connect two particles from the same sublattice. Considering the simple hexagonal lattice as tripartite made it possible to vectorize the simulation algorithm, which provided a significant speed-up in calculations. Moreover, in the bulk calculation in all directions periodic boundary conditions were assumed, while for the K/W measurement this was the case only along the x and y-axes. Then the simulation was started either from a random configuration in two dimensions (recall that $\mathbf{u}_i$ are restricted to hexagonal planes), or from an equilibrated configuration at a temperature slightly higher than the simulated one, if this was available. Then the standard Metropolis algorithm was applied [37]. For the vectorized algorithm to work correctly, in each MC cycle trial moves (in-plane rotations) involving particles in the first sublattice were attempted (and accepted/rejected) first, only then proceeding to the second one, and after this to the third one. In generating a new trial configuration for acceptance/rejection, each time only a single particle was involved. Typically 2×10^5 MC cycles for equilibration and after that another 10^5 production cycles (to accumulate averages of interest) were performed.

In a bulk sample, temperature scans were carried out to determine the NI transition temperature, calculating the average internal energy U by summing up pairwise contributions (3.34). The second relevant quantity for the problem is the order parameter, which, however, for two-dimensional in-plane ordering differs from the standard S introduced in the usual three-dimensional space (2.2). Further, attempting to measure the extrapolation length, the third important average is the director profile $\mathbf{n}(z)$. Both the order parameter and $\mathbf{n}$ can be extracted from the ordering matrix, which in two dimensions can be defined by

$$\underline{q} = 2\langle \mathbf{u}_i \otimes \mathbf{u}_i \rangle - \mathsf{I} \qquad (3.35)$$

differing from its three-dimensional counterpart $\underline{Q}$ given by Eq. (2.5). Further, the $\langle ... \rangle$ average goes both over particles $\mathbf{u}_i$ and over MC production cycles. Diagonalization of $\underline{q}$ leads to two eigenvalues, $\pm s$. The positive eigenvalue s can be identified as the two-dimensional nematic order parameter, while its eigenvector corresponds to the director $\mathbf{n}$. The order parameter is now given by $s = \langle 2(\mathbf{u}_i \cdot \mathbf{n})^2 - 1 \rangle$, giving $s = 1$ for a nematic aligned perfectly along $\mathbf{n}$ and $s = 0$ in the two-dimensional isotropic phase. Note that in the two-dimensional case there is no biaxiality. Finally, to deduce the z coordinate-resolved order parameter and the director profiles $s(z)$ and $\mathbf{n}(z)$, the ordering matrix $\underline{q}(z)$ was averaged separately for each layer with fixed z and then diagonalized. Alternatively, the director profile can also be expressed in terms of the tilt angle profile $\phi(z)$, with ϕ again measured from the sample normal. In this case $\phi = 0$ corresponds to homeotropic, while $\phi = \pi/2$ to planar alignment. Note that in Ref. [152] a different and less reliable method was used to obtain $\phi(z)$.

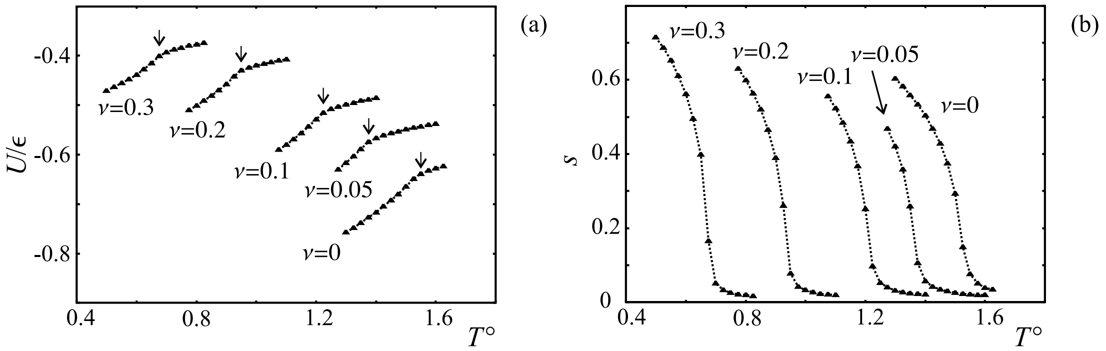

Figure 3.7 Temperature dependence of the reduced internal energy U/ϵ (a) and the order parameter s (b) in a bulk hexagonal lattice sample. The NI transition positions (indicated by the arrows) depend strongly on the ν parameter.

Turning now to a bulk sample, the NI transition temperatures T_{NI} can be approximately determined from the kinks observed in temperature scans of the internal energy $U(T)$ and of the order parameter $s(T)$, shown in Fig. 3.7. More reliably T_{NI} can be found by monitoring the variance of internal energy fluctuations, i.e., by determining the maximum of the heat capacity [123]. Here all temperatures are reported in a reduced scale defined by $T^\circ = k_B T/\epsilon'$. Note that even for $\nu = 0$ —

ν	T°_{NI}	T°	ℓ (a)
0.05	1.375 ± 0.025	1.3	15.5 ± 1
		1.2	13 ± 1
		1.1	13 ± 1
0.1	1.225 ± 0.025	1.175	4 ± 2
		1.1	5 ± 1
		1.0	5 ± 1
0.2	0.950 ± 0.025	0.9	-1 ± 0.5
		0.8	$+1 \pm 0.5$
		0.7	$+1 \pm 0.5$
0.3	0.675 ± 0.025	0.6	-4 ± 1
		0.5	-4 ± 1
		0.4	-4 ± 1

Table 3.2 Temperature dependence of the intrinsic anchoring extrapolation length ℓ (measured in units of lattice spacing a) for different ν, and the corresponding reduced bulk NI phase transition temperatures T°_{NI}.

corresponding to the spatially isotropic Maier-Saupe interaction — the transition temperature is higher than in the LL model (having already taken into account the difference in energy and temperature scale definitions in both models). This difference can be attributed to a different coordination number (8 vs. 6 nearest neighbors) and nematic particle dimensionality (two vs. three). Both distinctions lead to a different balance between the decrease of internal energy and loss of orientational entropy when going from the isotropic into the nematic phase. Further, from Fig. 3.7 it is evident that the position of the NI transition strongly depends on the anisotropy parameter ν. In particular, in the range $0 \leq \nu \leq 0.3$ T°_{NI} decreases with increasing ν, which indicates that the parallel aligning tendency giving rise to the nematic phase weakens with increasing ν. This seems to be in agreement with a decrease of the Frank elastic constant and an increasing softness of the nematic if ν is increased [129]. A full summary of reduced transition temperatures T°_{NI} can be found in Table 3.2.

A standard method to measure the strength of any anchoring is to impose an elastic distortion so that the average surface molecular orientation $\phi(0)$ deviates from the easy axis ϕ_0 defined by the anchoring. The magnitude of this deviation can then be used to estimate the anchoring strength and the corresponding extrapolation length [4] (see also Sect. 2.1.4). Note, however, that the length ℓ obtained by simple geometrical extrapolation (as in Fig. 2.3) can be straightforwardly interpreted as K/W only when anchoring is sufficiently weak, so that $\ell \gtrsim \xi$. Here ξ is the correlation length associated with interface-induced S-variations (2.11), matching also with the length scale over which subsurface ϕ-variations can occur, as shown in the first part of this Chapter. The elastic distortion in a nematic slab can now be imposed either by applying a magnetic field whose orientation must not coincide with the direction of the easy axis [17], or by antagonistic anchoring conditions at the opposing surfaces [152]. In the zero-temperature analysis of Ref. [17] the magnetic field method was used. On the other hand, for nonzero temperatures a strong enough magnetic field can enhance the degree of nematic order and even shift the NI phase transition, which can present additional difficulties in interpreting the results. Therefore, it is more appropriate to avoid any external field and consider a hybrid cell-like sample with antagonistic boundary conditions instead.

In the present simulation, the left ($z = 0$) surface was chosen to represent the free nematic surface (where the intrinsic anchoring is to act), while the right ($z = d$) surface corresponds to a solid wall represented by a layer of fixed particles with planar alignment. Since intrinsic anchoring was seen to promote homeotropic alignment for $\nu \leq 0.3$ [17], a bend deformation is expected to appear in the sample. The deformation should be present as long as the sample thickness d exceeds $d_c = |(K/W)_0 - (K/W)_d|$, where $(K/W)_0$ and $(K/W)_d$ refer to anchoring at the left and the right interface, respectively [114].

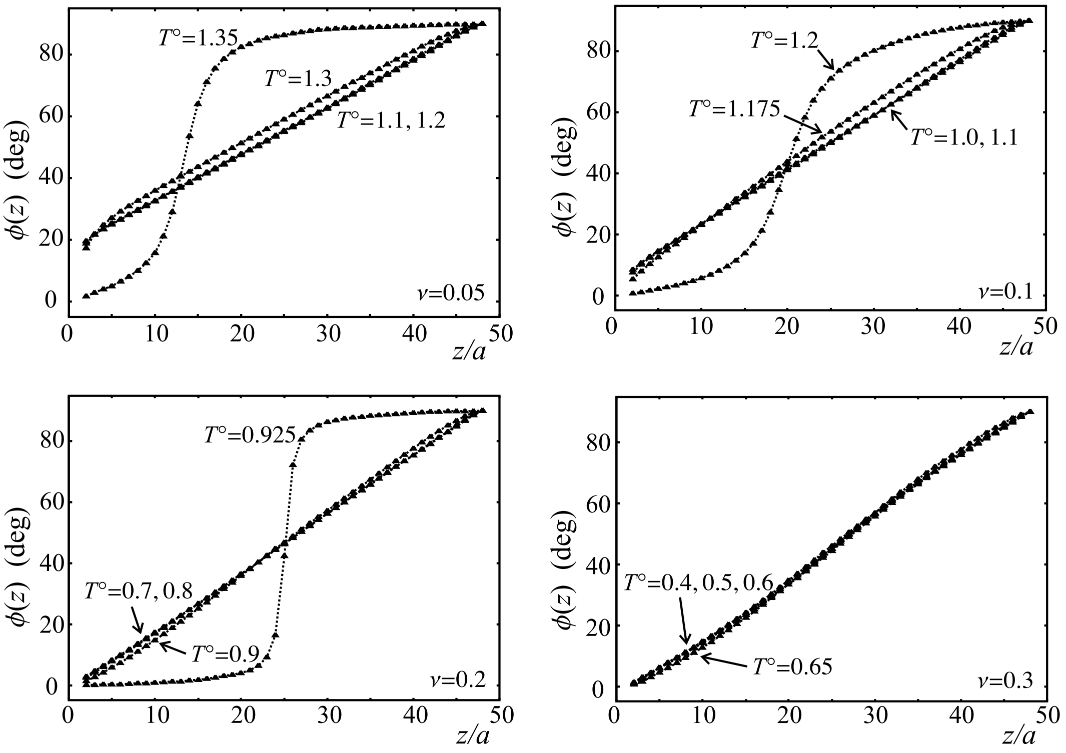

Figure 3.8 Temperature dependence of director profiles $\phi(z)$ for different ν. An extrapolation from the bulk to the left provides an estimate for ℓ at the free surface. At temperatures closest to the NI transition (for bulk T°_{NI} see Table 3.2) in the bulk the nematic melts down to avoid elastic distortions [compare with $s(z)$ profiles given in Fig. 3.9].

Figs. (3.8) and (3.9) show the order parameter and the director profiles for $\nu = 0.05$, 0.1, 0.2, and 0.3. To reliably treat cases with even lower ν (or cases with extremely weak anchoring), a thicker nematic slab should have been considered, ensuring $d > d_c$, so that the bent director structure becomes stable. In all cases displayed in Figs. (3.8) and (3.9), at the right surface the nematic was strongly

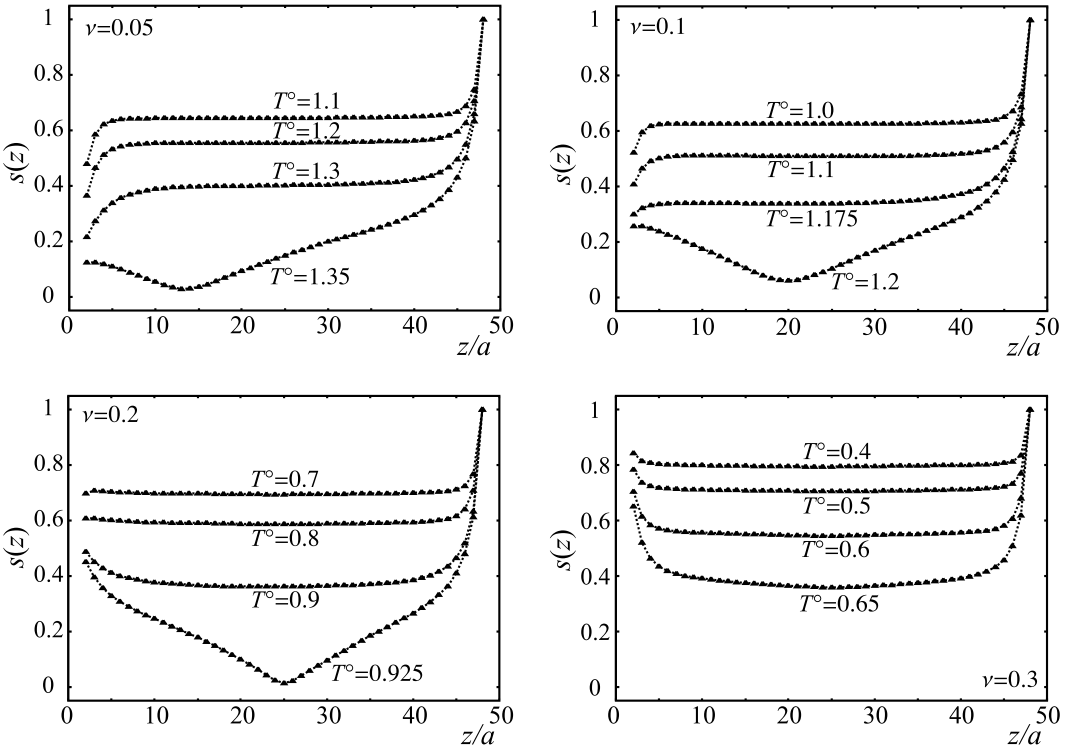

Figure 3.9 Temperature dependence of order parameter profiles $s(z)$ for different ν (see also the caption of Fig. 3.8).

anchored at $\phi = \pi/2 = 90°$ (planar orientation), while the intrinsic anchoring at the left surface tends to impose homeotropic alignment with $\phi = 0°$. Wherever there is no significant variation in $s(z)$ — like deep enough in the bulk — the $\phi(z)$-profiles roughly exhibit the linear behavior predicted by the Frank theory. On the other hand, if close to the sample surface the degree of order exceeds its bulk value, the nematic will reduce the deformation in this region because it is (free)energetically more expensive due to a larger elastic constant (and vice versa). As it is evident from order parameter plots, in the vicinity of the right solid wall with strong anchoring there is always an increase in $s(z)$, accompanied by a reduction in slope $(d\phi/dz)$ in the director profile $\phi(z)$. The same effect can be observed also close to the left wall when intrinsic anchoring is sufficiently strong (as for $\nu = 0.3$). For weaker intrinsic anchoring (e.g., with $\nu = 0.05$) the opposite is observed: a decrease in s induces an increase in the slope $d\phi/dz$. As also seen in the first part of this Chapter, all inhomogeneities in $s(z)$ and, consequently, in $\phi(z)$ occur on a length scale of the correlation length ξ that increases upon approaching the NI transition. As already stressed, the extrapolation procedure has to be performed from far enough in the bulk to ignore the subsurface region of thickness ξ. Then, in the $\ell \gtrsim \xi$ regime, $\ell = K/W$ is found as $K/W = \tilde{\phi}(0)/(d\phi/dz)_b$, where $(d\phi/dz)_b$ stands for the bulk slope of the $\phi(z)$ profile and $\tilde{\phi}(0)$ for the surface tilt angle, as extrapolated from the bulk.

The corresponding extrapolation lengths ℓ are summarized in Table 3.2 and mainly do not exceed a few molecular dimensions a, except for the weakly anisotropic

$\nu = 0.05$ case. Moreover, all ℓ seem to be fairly temperature-independent — except, again, for the $\nu = 0.05$ case showing a moderate increase of ℓ if the NI transition is approached — in contrast to both experiments in thermotropics and the findings of Ref. [152]. Therefore, the current results suggest that in the present model system one might have $W \propto S^\delta$ with δ close to 2, explaining the insensitivity of the extrapolation length to changing temperature. Note also that for, e.g., $\nu = 0.3$ the extrapolation procedure gives a negative ℓ. This is a consequence of having ignored subsurface variations of the order parameter $s(z)$ in the extrapolation procedure [143]. This happens whenever at the surface the nematic is more ordered than in the bulk and the above $\ell \gtrsim \xi$ condition is not met.

Exploring the behavior of director profiles when ν is varied, one can see that the actual surface value of the tilt angle $\phi(0)$ decreases with increasing ν. In other words, the corresponding intrinsic anchoring strength is nonzero for $\nu \neq 0$ and increases with ν, as already seen in Ref. [17], along with the decrease of the elastic constant K [129]. Microscopic values of the extrapolation length disagree with the typical experimental ones, that is 100 nm and above [6]. To reach a quantitative agreement of present results and experiments, a significant decrease of the ν parameter seems to be inevitable, as also suggested in Ref. [17]. A small ν in Eq. (3.34) promotes parallel molecular alignment, as it is also favored, e.g., by steric repulsions in a system of hard rods. A decrease in ν might therefore be regarded as an effective inclusion of steric repulsions excluded in the present model.

At the same time it should be borne in mind that at this stage looking for a strict quantitative agreement with experimental results is somewhat far-fetched. In fact, a number of other phenomena may also affect nematic ordering in the vicinity of an interface [159], such as dipolar and quadrupolar interactions, electrostatic interactions due to selective ion adsorption [160], presence of impurities [161], density variations [66,67], or roughness of a solid surface. All these phenomena can alter the local elastic properties of the liquid crystal, which affects the elastic torque transmitted from the surface to the sample bulk, and can thereby affect the determination of ℓ.

Further note that close to the NI transition the nematic can melt in the center of the sample if a strong enough elastic deformation is imposed (see Figs. 3.8 and 3.9). Then molecular alignment becomes homeotropic in the vicinity of the left surface, followed by a region of (nearly) isotropic liquid in the slab center, and by a region of planar alignment close to the right surface (see the snapshots shown in Fig. 3.10), as predicted also phenomenologically [162]. Thereby the elastic distortion vanishes, which — in a sample of current thickness — makes it difficult to measure K/W in the vicinity of T_{NI}.

Moreover, the variations in the $\phi(z)$-profile additional to the linear profile predicted by Frank elasticity seem to be a purely elastic effect driven by subsurface variations of the elastic constants. In this sense they are similar to the localized variations of the twist angle ω explored in Sect. 3.2. In the strongly bent nematic studied here, localized quasi-splay-bend-like subsurface deformations could not be identified, although — in principle — they might exist since for $\nu \neq 0$ one has $L_2 + L_3 \neq 0$.

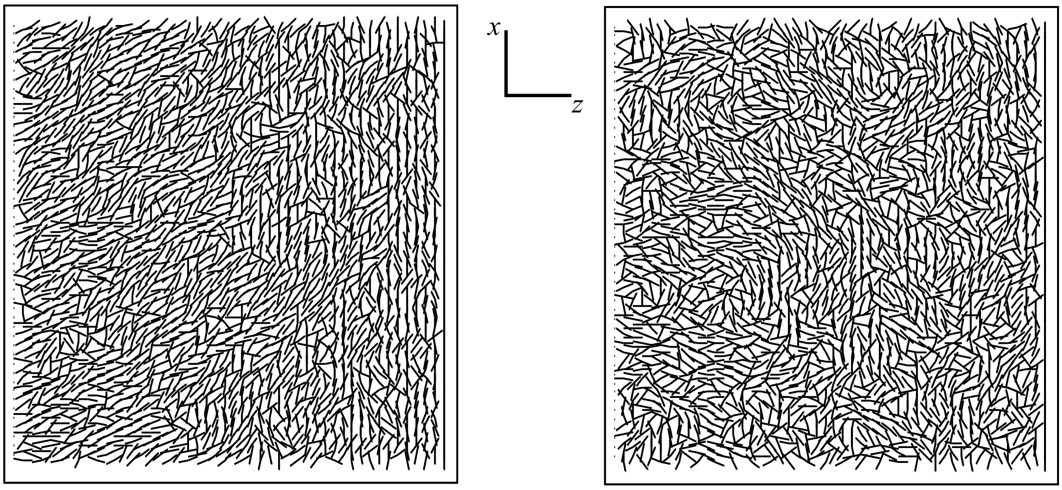

Figure 3.10 Snapshots of molecular configurations for $\nu = 0.05$ in a hybrid cell: right surface with strong planar anchoring, left surface is free (homeotropically anchored through intrinsic anchoring). *Left:* $T^{\circ} = 1.1$ (bent profile), *right:* $T^{\circ} = 1.35$; just below bulk T_{NI}° (homeotropic against planar alignment: the nematic melts in the middle of the cell).

The final note in this Section goes to possible residual bulk easy axes connected with the use of the spatially anisotropic pair potential (2.34) in a lattice model. Strictly speaking, in the present model there is no bulk easy axis for in-plane alignment only provided that the nearest-neighbor particles are all aligned strictly along the same direction. At any finite temperature, however, this never is the case, and therefore some lattice-induced orientational correlations may be expected for molecular ordering on short length scales comparable to the lattice spacing. However, for the applicability of any lattice model it is important that it appropriately reproduce large-scale elastic deformations and that the corresponding $\phi(z)$ director profiles be smooth and follow qualitatively the phenomenological picture. By all means, this is the case for the model presented here.

4

Polymer-dispersed liquid crystals

The following Chapter will be devoted to nematic ordering in microscopic spherical cavities, as encountered in polymer-dispersed liquid crystal (PDLC) systems. Spherical nematic droplets can be obtained by dispersing the liquid crystal in a polymer binder through either phase separation [28] or emulsification [163,164]. Reviewing PDLC samples, one encounters a rather broad distribution of droplet sizes, the lower bound for their diameter being several tens of nanometers (e.g., 20 nm [132]), and the upper well above 1 μm. In the past, nematic ordering in PDLCs has been subject to extensive studies (phenomenological, experimental, and simulation) and is well understood by now [5,91]. For this reason, here another question will be addressed, namely, of how to establish a correspondence between the information on nematic ordering obtained from Monte Carlo (MC) simulations and one of the possible experimental observables, deuterium (^{2}H) NMR spectra. A novel methodology for the calculation of ^{2}H NMR line shapes will be presented that is — in contrast to the existing MC approaches — applicable in presence of significant molecular motion. In particular, radial and bipolar droplets will be considered (see Fig. 1.4).

The MC simulations reported in this Chapter were performed in the framework of the Lebwohl-Lasher (LL) lattice model (Sect. 2.2.1). To model a PDLC droplet, a jagged sphere was carved from the cubic lattice, considering all the molecules lying closer than $R = 12a$ (the droplet radius, a denoting the lattice spacing) to the droplet center. The interaction with the polymer matrix was mimicked by assuming an additional layer of ghost particles, with orientations chosen in accordance with desired boundary conditions. The radial boundary conditions were obtained by orienting the ghost particles normal to the local droplet surface. Similarly, in case of bipolar droplets the ghosts were fixed tangentially to the local surface and in planes containing the symmetry axis of the droplet (see Fig. 4.1). Further, the nematic-nematic and nematic-ghost interaction strengths were assumed equal, which corresponds to a rather strong anchoring with a microscopic extrapolation length of the order of a, the lattice spacing. The number of particles inside the droplet was set to $N = 5832$, whereas in the additional surface layer fixing the boundary conditions to $N_g = 1352$. For radial and bipolar boundary conditions the calculations at the lowest temperature were started from perfectly ordered (zero-temperature) configurations. These are, in accordance with the given boundary conditions, a perfect hedgehog and a perfect bipolar structure in the radial and bipolar cases, respectively. At higher temperatures the simulations started from an already equilibrated configuration at the nearest lower temperature, when this was available. The standard Metropolis algorithm (Sect. 2.2.3) was then applied to update nematic particle configurations. Typically, 5×10^4 MC cycles (sets of N attempted trial moves) were performed for equilibration, followed by a set of further 1024 production cycles used to calculate averages of interest. Within one MC cycle, each of the nematic particles was selected at random for a trial move, using a random shuffling algorithm [123]. Then a new trial orientation for the chosen particle was generated by a controlled variation from the previous one, applying the Barker-Watts technique [131] (Sect. 2.2.3). The trial move amplitude was adjusted dynamically so as to ensure a rejection ratio not too far from 50%. The reduced temperature scale used in this Chapter is defined as $T^* = k_B T/\epsilon$, with ϵ introduced just below Eq. (2.29). The simulation runs corresponding to the nematic phase were all performed at $T^* = 0.8$. Similarly, cases in the isotropic phase were run at $T^* = 1.2$. Note again that in this temperature scale the bulk nematic-isotropic (NI) transition takes place at $T^*_{NI} = 1.1232$ [123] and is reduced to around 1, e.g., for a bipolar droplet in absence of external fields [100]).

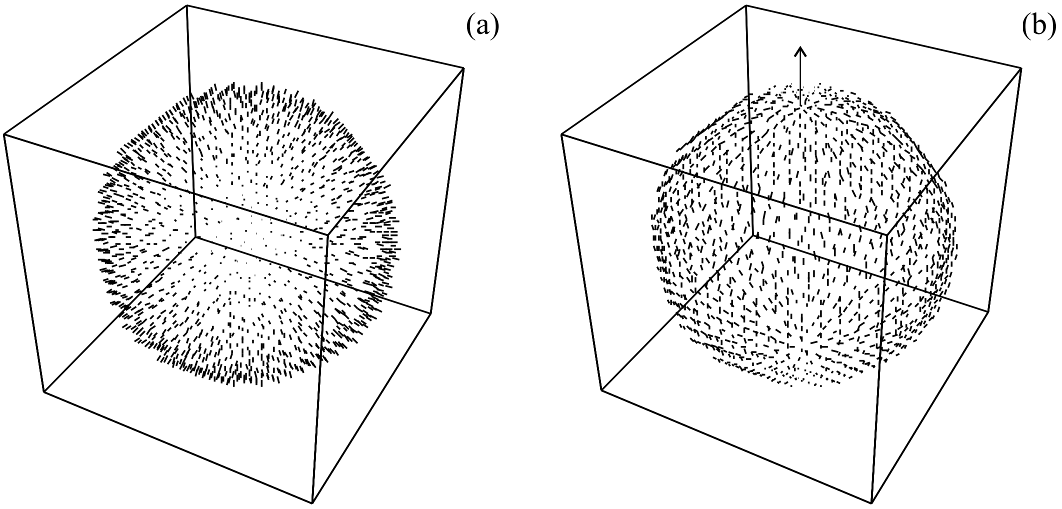

Figure 4.1 Surface layer of ghost particles defining the boundary conditions. (a) radial, (b) bipolar droplet (the arrow indicates the bipolar axis).

Recall that the dynamics of MC simulations is determined by the "non-natural" molecular evolution process driven by the Metropolis procedure (in contrast to molecular dynamics simulations following the equations of motion), and hence the time scale assigned to fluctuations generated by this technique does not necessarily have to match with the natural time scale indicated in Sect. 2.3.1. However, the update process adopted here rotates one molecule (particle) at a time for a certain angular step, which is a plausible physical evolution process. In this sense, one can map the MC dynamics onto a plausible real one, apart from an arbitrary time unit.

For the calculation of ^{2}H NMR line shapes the approach with the time-dependent nuclear spin Hamiltonian (Sect. 2.3.1) was used, allowing for a full treatment of dynamical effects in calculating the line shapes. Combining this approach with MC simulations, in this Chapter it will be possible to link ^{2}H NMR line shapes to fluctuations of molecular long axes, translational self-diffusion of molecules (homogeneous and inhomogeneous), as well as to aligning effects of external electric/magnetic fields. In the analysis of the spectra we will proceed from the static limit to the limit of completely motionally averaged spectra, in order to find out to which extent diffusive processes smear the spectra and thus make the identification of director configurations impossible.

4.1 Dynamical effects and ^{2}H NMR line shapes

To begin with, droplets in absence of external fields will be considered, assuming also that there is no coupling between the spectrometer magnetic field $\mathbf{B}$ and the molecular orientation. Indeed, in microconfined liquid crystals the aligning effects of a magnetic field can be ignored if the magnetic coherence length $\xi_m \propto 1/B$ (2.23) is much larger than the characteristic dimension of the confined system, i.e., if the magnetic field is weak enough not to overwhelm the aligning effect of the confining walls. In the droplet case, the condition $\xi_m \gg R$ must be fulfilled to justify omitting the molecular coupling with the spectrometer field.

4.1.1 Molecular fluctuations

First consider spectra in absence of translational diffusion, or, equivalently, spectra of large enough nematic droplets in which this kind of molecular motion can be considered as rather unimportant. The droplet size R in this case must satisfy $R \gg \sqrt{6Dt_0}$, where D is the diffusion constant, t_0 the characteristic NMR time scale, and $\sqrt{6Dt_0}$ the root-mean-square diffusive displacement covered by a molecule during t_0. Now the only relevant molecular dynamics is caused by fluctuations of long molecular axes $\mathbf{u}_i$. In order to obtain a spectrum with a sufficient resolution, it is necessary to simulate a relaxation signal $G(t)$ that is long enough, i.e., lasting for several NMR cycles of duration t_0 each. Comparing the time scales of molecular fluctuations t_F and the characteristic NMR "time-window" t_0 (see Sect. 2.3.1), it is evident that there should be approximately 10^3 molecular fluctuations per each NMR cycle, t_0. This relation between t_0 and t_F did not allow for generating a sufficiently long $G(t)$, as, for technical reasons, at this point only data for 1024 MC particle configurations were available. Therefore, generating $G(t)$, the nematic particle configuration was updated from the MC data less frequently than required by the natural time scale t_F so as to cover a long enough period in time. This approximation is not of essential importance, given the already mentioned arbitrariness in the Monte Carlo time scale.

In the case without diffusion, particle configurations inside the droplet were updated 8 times per NMR cycle, this being much less than the natural scale t_F. However, this made it possible to generate a $G(t)$ signal whose length is $128\,t_0$, yielding spectra with a resolution of 256 points in the relevant (nonzero) part of the spectrum. By comparing the order parameter S deduced from NMR spectra with that calculated directly from MC data, it is possible to check whether the chosen frequency of configuration sampling is sufficient or not. Further, the resulting spectra show some "noise" because the number of particles inside the droplet is still relatively small. To smoothen these spectra, a convolution with a Gaussian kernel of width $0.04\delta\omega_Q$ was performed. For $\delta\omega_Q \sim 2\pi \times 40$ kHz this width equals $\sim 2\pi \times 1600$ Hz, which is well above the natural line width, typically given by $\sim 2\pi \times 100$ Hz. Note that neither the width of the kernel nor its shape (Gaussian instead of Lorentzian) match with the features of natural single-spin NMR lines and that the purpose of performing such a convolution is merely to smoothen the spectra and not to simulate the natural linewidth.

According to Eq. (2.41), the maximum width of a doublet in the spectrum equals $2\delta\omega_Q S$. In the perfectly aligned nematic phase with $S = 1$ the spectral width amounts to $2\delta\omega_Q$, but as soon as dynamic effects are taken into account, the spectrum is narrowed, and molecular fluctuations effectively yield $S < 1$. The line shape obtained, for example, from the radial droplet, is somewhat more complex because now one also has $\mathbf{n} = \mathbf{n}(\mathbf{r})$. In the radial droplet most molecules are directed radially from the droplet center, while in the center there is a fairly small defect core [165] (the core structure will be discussed in more detail later). Consequently, molecular orientations are distributed almost isotropically over the whole solid angle Ω, which is equivalent to considering a polycrystalline sample with $dN/d\Omega = \text{const.}$, where dN is the fraction of molecules whose orientations fall into $d\Omega$. Then, taking into account (2.41), the spectrum is given by $I(\omega) = dN/d\omega \propto [\omega - (\omega_Z \pm \frac{1}{2}\delta\omega_Q S)]^{-1/2}$ (ω_Z denoting the Zeeman frequency) and is called *Pake-type powder pattern* [135]. It consists of two sharp asymmetric peaks positioned at $\omega_Z \pm \frac{1}{2}\delta\omega_Q S$, with two "shoulders" reaching up to $\omega_Z \pm \delta\omega_Q S$. In fact, similar features can be found also in the spectrum calculated from the MC simulation data for the radial droplet at $T^* = 0.8$ — see the top curve in Fig. 4.2, left. Now it is possible to deduce the value of S from the actual position of the peaks (or shoulders): $S \approx 0.72 \pm 0.02$. To check this result, one can calculate S also directly from the MC data by diagonalizing the MC time-averaged ordering matrix $\underline{Q}$ (2.5) for each particle and then averaging the largest eigenvalues obtained in this way over the whole droplet. Such a calculation then gives $S \approx 0.73 \pm 0.10$. Here the variance comes from the ensemble average over particles. This rather good agreement also indicates that even sampling MC structures rather infrequently (i.e., only 8 times per NMR cycle) still reproduces the effect of molecular fluctuations sufficiently well.

In the bipolar case, surface anchoring is planar and in the droplet core most particles are aligned along a given direction, determined by the bipolar symmetry axis [Fig. 4.1 (b)]. Where the axis intersects the droplet surface, there are two topological defects at the "poles" of the droplet. The spectrum of the bipolar droplet in the no-diffusion limit differs considerably from that of the radial droplet. If the NMR magnetic field $\mathbf{B}$ is applied along the bipolar axis, it still has two asymmetric peaks, which, however, are now located approximately at $\omega_Z \pm \delta\omega_Q S$. This reveals that indeed most of the molecules are aligned parallel to $\mathbf{B}$ — see the top curve in Fig. 4.2, right, calculated for $T^* = 0.8$. Evaluating S from the peak positions, $S \approx 0.73 \pm 0.01$ is obtained, while calculating S directly from the MC data yields $S \approx 0.76 \pm 0.04$. Again the agreement of the two estimates is good. In general, bipolar symmetry axes in droplets of a real PDLC sample can have arbitrary spatial orientations. Summing up contributions originating from droplets all over the sample then yields a spectrum similar to the Pake-type powder spectrum even for bipolar droplets [132] (this topic will be discussed later in this Chapter). If, however, the process of bipolar droplet formation in a polymer matrix is occurring in a sufficiently strong external magnetic field, the bipolar axes align along the field direction. This frozen-in alignment ("memory-effect") can be retained also after the field is switched off [40], which then corresponds to the case considered here. In the following it will be assumed that the NMR spectrometer magnetic field is directed along the droplet symmetry axes.

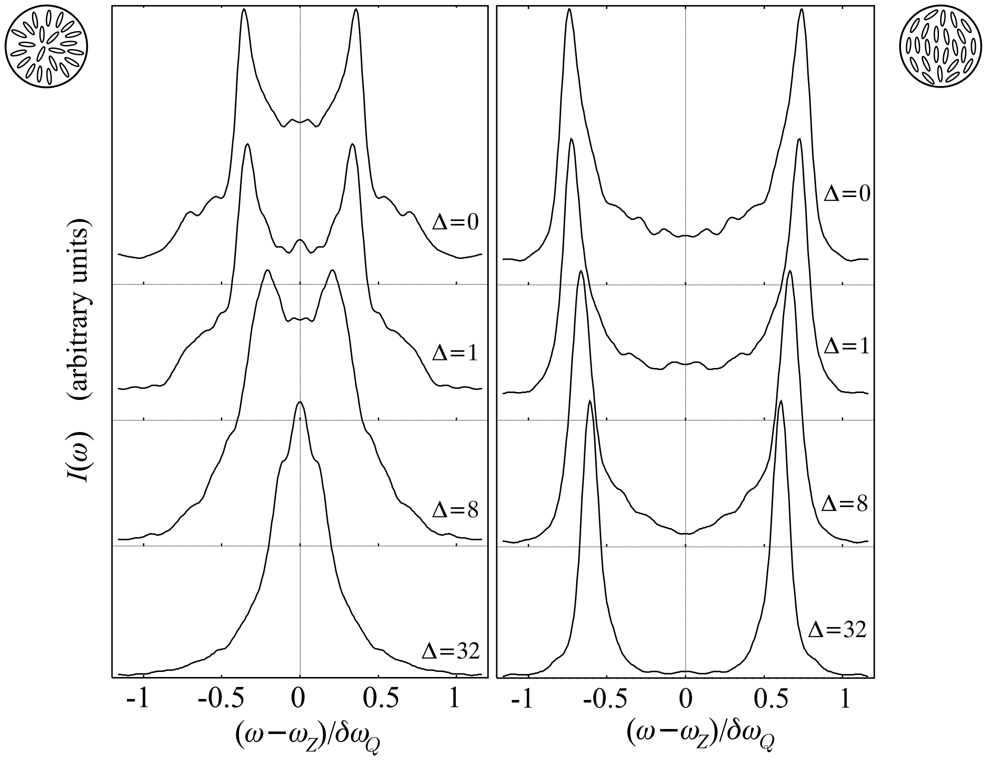

Figure 4.2 *Left:* ^{2}H NMR spectra of the radial droplet for different values of the diffusion parameter Δ: $\Delta = 0$ corresponds to the no-diffusion limit, while $\Delta = 32$ corresponds to the fast diffusion limit. The Pake-type powder spectrum obtained for $\Delta = 0$ collapses into a single line centered at zero quadrupolar splitting for $\Delta = 32$. *Right:* Same as *left*, however, for the bipolar droplet. The spectrometer magnetic field was aligned along the bipolar symmetry axis, which results in a spectrum consisting of two lines both in absence of diffusion and in the fast diffusion limit. In all cases $T^* = 0.8$, ensuring the existence of the nematic phase. Here and elsewhere in the thesis all spectra were normalized so as to obtain the same peak height.

4.1.2 Homogeneous translational diffusion

In addition to fluctuations of the molecular long axes, now also translational molecular diffusion will be included into the analysis. Note that since nematics are anisotropic liquids, the process of translational diffusion is anisotropic, characterized by a tensor $\underline{D}$. In a bulk unconstrained nematic phase the ratio of its eigenvalues — the diffusion constants $D_{||}$ and $D_{\perp}$ measured along the director $\mathbf{n}$ and perpendicular to it, respectively — can typically range around ~ 2 [4,40]. However, since here we are primarily interested in qualitative features of spectra, in the following analysis the diffusive process will be assumed isotropic and characterized by a single motional constant $D = D_{||} = D_{\perp}$. Some preliminary tests with anisotropic diffusion indeed showed that qualitatively current results do not change.

Translational diffusion was simulated by a simple random-walk process in which the particles representing one or several nematic molecules jump between lattice sites. In every simulation step each of the particles is allowed to move to its nearest neighbor site with equal probability in the present isotropic case, while in the anisotropic case this probability should be biased so as to increase the diffusion probability along the director [40]. After the diffusion jump has been performed, the particle acquires a new orientation, whose average (i.e., the local $\mathbf{n}$) in a distorted sample is different from the average calculated at the old coordinates. Calculating $G(t)$, like in the diffusionless case nematic particle configurations were updated from the MC data 8 times per NMR cycle. Now additional diffusion steps were added in between these structural updates, with their number Δ ranging from 1 to 32. In this last case the spectra are completely motionally averaged due to diffusion effects since for $\Delta = 32$ each of the particles exhibits a total of 256 jumps within the duration of one NMR cycle, this already corresponding to the fast diffusion limit with $\sqrt{6Dt_0} \approx 16a \gtrsim R$. It should be stressed that the diffusive random walk does not interfere with the MC evolution process; in fact, it only uses the particle configurations generated by the Metropolis algorithm, forwarding this information to the line shape calculation.

Starting by considering the radial droplet at $T^* = 0.8$, Fig. 4.2 (left) shows a sequence of spectra for this type of boundary conditions, ranging from the no-diffusion limit ($\Delta = 0$) to the limit of fast diffusion ($\Delta = 32$). In general, for any type of boundary conditions the fast diffusion spectrum consists of two lines centered at $\omega_Z \pm \langle\omega_Q\rangle$, where the average frequency is given by $\langle\omega_Q\rangle = \delta\omega_Q \,\langle S(\mathbf{r}_i)\,\frac{1}{2}[3\cos^2\theta(\mathbf{r}_i) - 1]\rangle_i$ and the average $\langle ... \rangle_i$ goes over the whole droplet. If the diffusion is fast enough so that molecules diffuse through a large enough portion of the droplet, in the radial configuration for which $\langle\omega_Q\rangle = 0$ the two lines should coalesce into a central line (zero quadrupolar splitting). Inspecting the simulated spectra (the sequence in Fig. 4.2, left), it is evident that this indeed happens. It is possible to deduce the value of $\langle\omega_Q\rangle$ also directly from the MC data, yielding $\langle\omega_Q\rangle \approx 0.03\,\delta\omega_Q$.

Repeating the same analysis for the bipolar droplet ($T^* = 0.8$), one can observe that the two lines in the spectrum do not merge into a single line, as just observed for the radial droplet when moving from the slow into the fast diffusion regime (Fig. 4.2, right). This happens because now one is dealing with an ensemble of molecules whose orientational distribution is spatially anisotropic. Hence, $\langle\omega_Q\rangle \neq 0$ should be expected, unless (by coincidence) the relative orientation of the NMR spectrometer magnetic field and the majority of molecules within the droplet yields $\omega_Q \approx 0$ already in itself. This is, however, not the case for the spectra shown in Fig. 4.2, right: here $\langle\omega_Q\rangle = (0.61 \pm 0.02)\,\delta\omega_Q$ from the peak positions and $0.59\,\delta\omega_Q$ from the MC data. Note also that the two lines in the spectrum move towards a lower splitting $\langle\omega_Q\rangle$, which is because not all particles are exactly parallel to the spectrometer field and thus yield smaller $|\omega_Q|$ contributions when the average $\langle ... \rangle$ is performed.

As indicated before, diffusive processes are expected to be more important in small droplets than in large ones. Therefore, it can be convenient to express the limit between the slow and fast diffusion regimes in terms of the droplet size, keeping the value of the diffusion constant (a temperature-dependent material constant) fixed. Then the degree of diffusional averaging can be quantified by introducing the dimensionless parameter $e = |\omega_Q| R^2/12\pi D$ [40], where D is the effective diffusion constant and ω_Q is given by Eq. (2.41). The parameter e is constructed by comparing the droplet radius R (i.e., the typical dimension over which $\mathbf{n}$ changes significantly) with the root-mean-square distance traveled by a molecule during the characteristic NMR time scale t_0. In cases without diffusion (or in very large droplets) one has $e \to \infty$ ($\sqrt{6Dt_0} \ll R$), while in the fast diffusion regime (or for small droplets) $e \to 0$ holds ($\sqrt{6Dt_0} \gg R$). The cross-over between the two regimes occurs for $e \approx 1$. The actual value of e can be deduced from simulation parameters and is, in cases claimed to correspond already to the fast diffusion regime ($\Delta \geq 32$), equal to $e \lesssim 0.45$. Here it was assumed that most molecules are aligned along the NMR field direction and that the nematic order is homogeneous with $S = 0.8$ throughout the droplet. Note that although $e \ll 1$ is still not fulfilled, the translational diffusion is already significant and the resulting spectra show features of diffusive motional averaging. Increasing the diffusion rate (decreasing e) even further would have resulted merely in an additional decrease of the spectral line width, maintaining the spectral shape. On the other hand, translational diffusion is seen to affect the line shapes spectra only negligibly for $\Delta \leq 1$, i.e., $e \gtrsim 14$ [95]. Choosing specific values for $\delta\omega_Q$ and D, it is possible to rewrite both bounds for e in terms of the droplet radius R. Hence, putting $\delta\omega_Q \approx 2\pi \times 40$ kHz, $D \approx 4 \times 10^{-11}$ m^2/s (e.g., for bulk 5CB at room temperature) [5], and again $S \approx 0.8$, one finds that the spectra of droplets smaller than $R \approx 60$ nm are already averaged by diffusion, while diffusive motions can be ignored in droplets larger than $R \approx 330$ nm. However, here it is again necessary to stress that a single particle in the LL model can represent a cluster of up to 10^2 nematic molecules [94] and that because the number of particles in the simulation is limited, only droplet radii below ~ 60 nm can be accessed. In this range of R the simulation is meaningful and, for the above values of $\delta\omega_Q$ and D, one is actually always in the fast diffusion regime. Therefore, the no-diffusion spectra are only given for a better comprehension.

Lining up spectra for radial and bipolar droplets (as in Fig. 4.2), one can readily identify each of the two boundary condition types just by inspecting the calculated line shapes. Indeed, in the slow diffusion limit it is always possible to identify the radial structure because of its characteristic Pake-type pattern not depending on the direction of the spectrometer magnetic field. The spectrum of the bipolar droplet, on the other hand, is two-peaked and the peak-to-peak distance depends on the magnetic field direction. This conclusion holds also in the fast diffusion regime, except that the Pake-type spectrum of the radial droplet now collapses into a single line at zero splitting, again regardless of the NMR magnetic field direction.

4.1.3 Inhomogeneous translational diffusion

The analysis of the diffusive motion presented so far has assumed the diffusive process to be both isotropic (with $D_\perp = D_{||} = D$) and homogeneous (D position-independent). However, as suggested by experimental results, in a thin subsurface layer molecular diffusive motion is hindered, which results in a significant reduction of the effective diffusion constant D. Consequently, in strongly confined systems this effect can play an important role, especially if the molecular surface dwell time is long, reducing D even by a factor of 3×10^3 [96,166]. It becomes even more pronounced if the molecular exchange between the bulk and the surface layer is accompanied by a significant change in either the degree of nematic order or in molecular orientation (or both). Therefore, in this Section surface inhomogeneities in the diffusive process will be examined.

In the simulation, the thickness of the surface layer was set to roughly one particle dimension (up to $a \sim 5$ nm), thereby leaving 1608 particles (out of 5832)

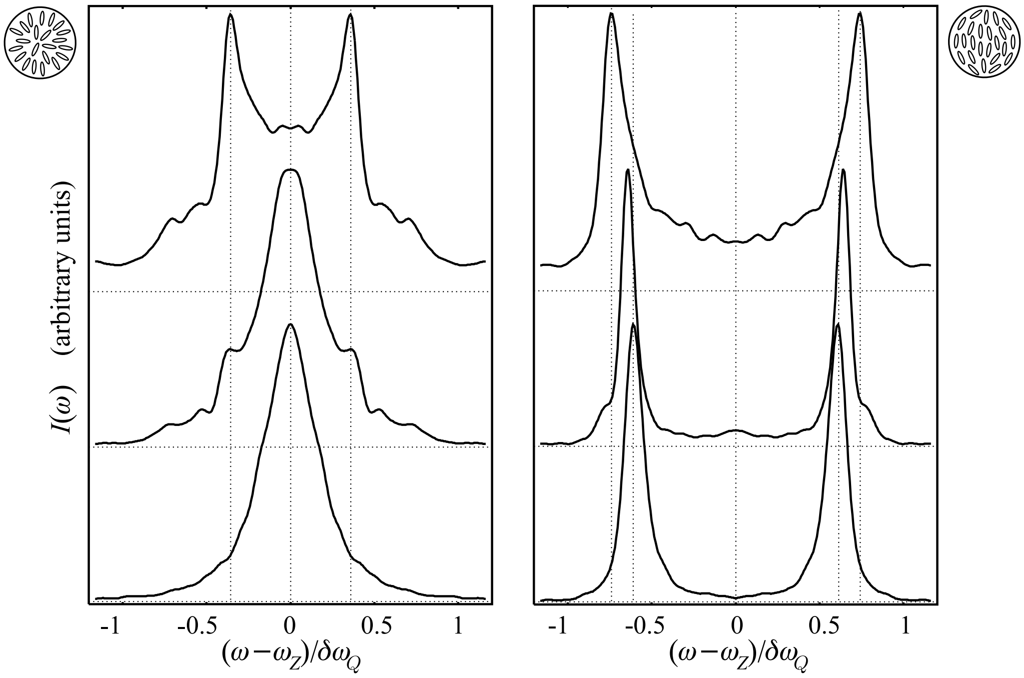

Figure 4.3 *Left:* Spectra of the radial droplet at $T^* = 0.8$: no diffusion (top), fast diffusion: inhomogeneous (center) and homogeneous (bottom). *Right:* Same as left, but for the bipolar droplet.

in the subsurface region. Then the rate of diffusive moves within this region was reduced and the same reduction factor was assumed also for moves entering or leaving the surface layer. Due to a significant portion ($\approx 28\%$) of particles lying in the surface layer, a substrate-induced slowdown in translational diffusion is expected to be clearly visible.

First consider the droplet with radial boundary conditions at $T^* = 0.8$. The top and bottom curves shown in Fig. 4.3, left, correspond to the no-diffusion and fast diffusion cases, respectively. If now surface inhomogeneities in translational diffusion are taken into account, in the spectra — apart from the diffusion-averaged central peak — there are now two well-pronounced peaks at $\omega_Z \pm 0.36\,\delta\omega_Q$, plus some additional signal at frequencies $0.4\,\delta\omega_Q < |\omega_Q| < 0.8\,\delta\omega_Q$. The spectrum displayed in Fig. 4.3 (center, left) was calculated for $D_b/D_s = 3 \times 10^3$, where D_b and D_s are the effective diffusion constants in the bulk and in the surface layer [96]. Since the ratio D_b/D_s is rather large, in the surface layer containing 28% of molecules there is almost no diffusive motion in comparison to the droplet core. Therefore, it is possible to understand the spectrum depicted in Fig. 4.3 as a weighted superimposition of a diffusion-averaged contribution originating from the droplet core — the central peak — and of an underlying Pake-type pattern originating from the surface layer, affected only negligibly by the slow diffusion. Then from peak positions $\omega_Z \pm 0.36\,\delta\omega_Q$ one can roughly estimate the value of the order parameter in the surface layer, which yields $S \approx 0.72$. For that layer the S-profiles calculated from MC data give $S \approx 0.80$ and the agreement is sufficiently good.

Turning now to bipolar droplets, again the bipolar axis was chosen parallel to the spectrometer magnetic field. Consequently, both without diffusion and for rapid (but homogeneous) diffusion the spectrum consists of two lines (Fig. 4.3, right), the splitting in the latter case being somewhat smaller than in the former one, as discussed above. If, however, diffusion is inhomogeneous (again with $D_b/D_s = 3 \times 10^3$), the two main peaks in the spectrum move slightly apart, but do not exceed the initial splitting obtained in the diffusionless case. The diffusive paths of particles now mostly avoid the surface region where the curvature of the director field is strongest and, consequently, the deviations from the maximum $|\omega_Q|$ are largest, which explains the re-positioning of the main peaks. Further, there are two additional “shoulders” positioned at a splitting slightly larger than that corresponding to the main peaks. These “shoulders” originate from the diffusion-unaffected surface layer, especially from particles aligned almost along the spectrometer field. Note that the “shoulder” positions match with the positions of the two main peaks obtained in absence of diffusion quite well, as also suggested by the dotted guidelines in Fig. 4.3.

4.1.4 “Powder” sample: bipolar droplets

Experimentally, ^{2}H NMR has been applied to study mostly PDLC samples with planar anchoring, resulting in bipolar droplets [25,40,90,132,133]. The spectra available from these analyses either consist of two well distinguished peaks, or are equivalent to the Pake-type powder pattern. In the former case all bipolar droplet symmetry axes were aligned along a given direction prior to recording the NMR spectrum (e.g., by a strong field during the droplet formation), which corresponds to the case analyzed so far. In the latter case, however, bipolar axes are distributed over the whole solid angle. Such a sample is then macroscopically isotropic, although the constituent bipolar droplets are not.

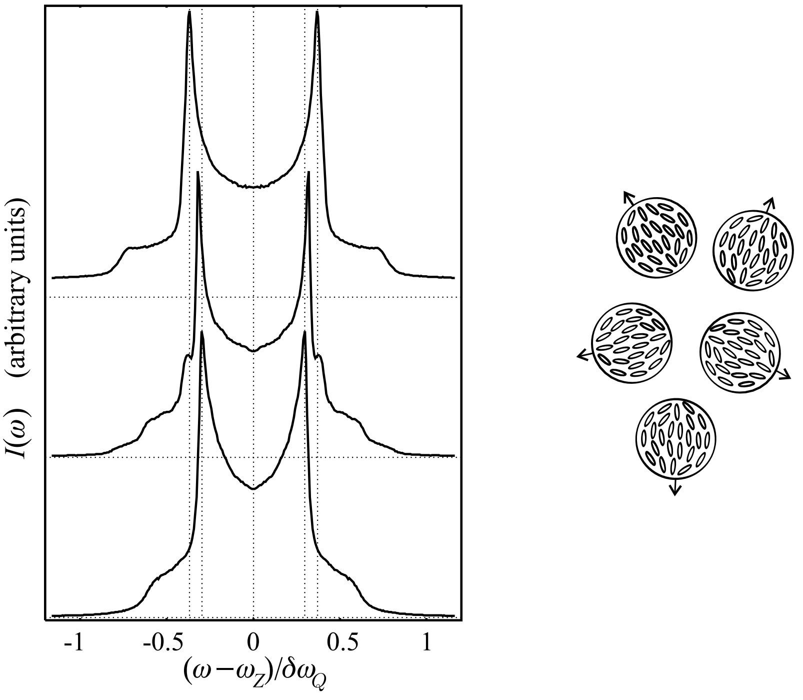

Figure 4.4 Spectra of 1000 bipolar droplets at $T^* = 0.8$, with symmetry axes oriented randomly: no diffusion (top), fast diffusion: inhomogeneous (center) and homogeneous (bottom).

Although in the present study only MC data for a single droplet were available, it was possible to simulate the effect of randomly oriented droplet symmetry axes by using the unaltered single-droplet data and by assuming to have a random distribution of spectrometer magnetic field directions. Since in this way one simply "clones" the data for a single droplet to model several droplets, this certainly results in unphysical correlations between particle orientations in different droplets, but at least in cases with diffusion this should not be of great importance since interdroplet correlations are smeared out by independent diffusion paths in each droplet. Note that now spectra show much less noise than for a single droplet and it is not necessary to perform smoothening convolutions.

The top curve in Fig. 4.4 is the spectrum of 1000 bipolar droplets without diffusion at $T^* = 0.8$ (nematic phase). It presents a Pake-type pattern, as expected, with peaks positioned at $\omega_Z \pm 0.37\,\delta\omega_Q$. This suggests that $S \approx 0.74$, which is close to $S \approx 0.73$, a value deduced from peak positions for a single bipolar droplet — see Fig. 4.2. In the spectrum, fast and homogeneous diffusion again results in a Pake-type pattern, albeit somewhat narrowed (Fig. 4.4, bottom). The ratio of line widths measured peak-to-peak in cases with and without fast diffusion should be equal to that calculated for a single bipolar droplet. For a single droplet this ratio is estimated by 0.83, while for an array of 1000 droplets one finds 0.80, indicating that the agreement is good.

Finally, if diffusion is inhomogeneous (Fig. 4.4, center), the spectrum is still similar to the Pake-type pattern, however, with less width reduction than in the homogeneous diffusion case. In addition, at splittings slightly larger than those corresponding to the main peaks, two "shoulders" appear again. Note that all these features agree with those observed for a single bipolar droplet; compare with Fig. 4.3, right. The central spectrum shown in Fig. 4.4 actually consists of two superimposed Pake-type patterns. The first one — comprising the two main peaks — is well-pronounced and originates from central droplet regions where diffusion is effective. The two "shoulders", on the other hand, are the main peaks of the less pronounced, but not diffusion-narrowed second Pake-type pattern representing the response from droplet surface layers. Note that the "shoulder" and no-diffusion peak positions (Fig. 4.4, top) match again.

4.2 External field effects

Applying an external field in a PDLC droplet system leads to a competition between the (usually) conflicting effects of the polymer matrix and the applied field. In case of bipolar droplets, at lower field strengths the effect is less dramatic, resulting in a mere reorientation of bipolar axes (provided that one is working with a non-aligned powder sample, Sect. 4.1.4) [25,90]. Then, only at field strengths extremely high the bipolar director structure itself is affected, too. These field-induced effects (especially the low-field reorientation) turn out to be of great importance for technical applications — mainly for the design of optical devices, such as switchable windows, displays, or fast light shutters [5]. In the radial droplet case, however, already a relatively weak external field can break the spherical symmetry of the molecular distribution, leading to significant changes in the corresponding director structure. This Section will present an upgrade of the analyses in Refs. [99,100]: it will reexamine the nematic ordering in radial and bipolar droplets in an external field, both in the nematic and isotropic phase, and establish a connection with the resulting dynamical ^{2}H NMR line shapes.

In the simulation, the coupling with the external field was modeled via (2.30), as described in detail in Sect. 2. The strength of the field will be characterized by the dimensionless parameter η introduced in (2.30) (just recall that the field strength is proportional to $\sqrt{\eta}$). In order to influence the molecular alignment inside the droplet significantly, the external (say, magnetic) field has to be strong enough so that the characteristic length of the field-induced distortion [i.e., the magnetic coherence length ξ_m (2.23)] becomes comparable to or smaller than the characteristic dimension of the confined system, here the droplet radius R. In an experiment with an aligning magnetic field it is usually the NMR spectrometer field itself taking the role of the external field introduced in the Hamiltonian (2.30). Here, however, a distinction will be made between the "weak" NMR spectrometer field and the "strong" external field of variable strength, responsible for the additional

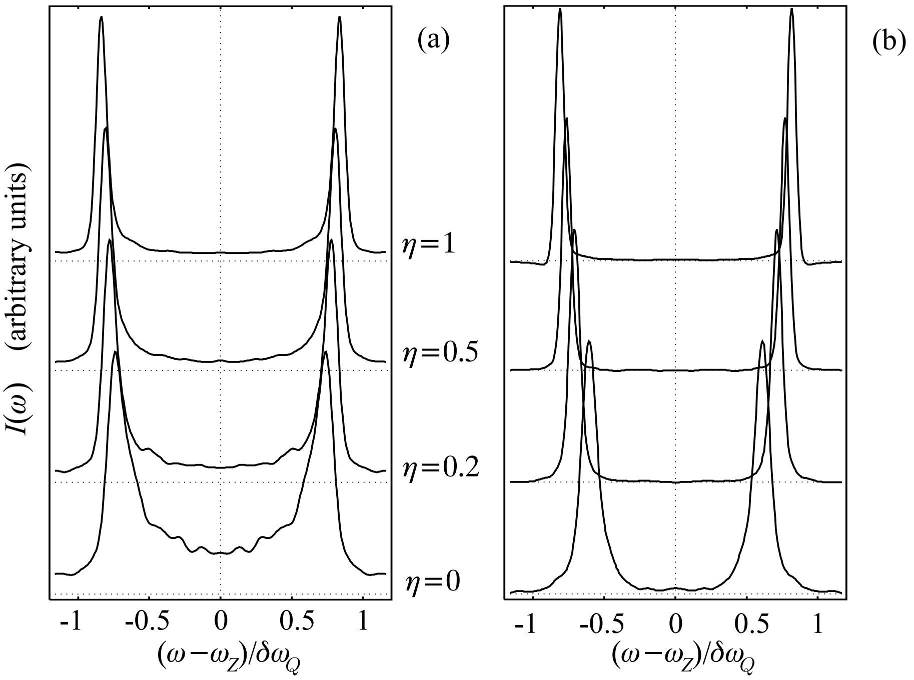

Figure 4.5 ^{2}H NMR spectra of a single bipolar droplet in the nematic phase at $T^* = 0.8$ for different values of the external field strength ($\propto \sqrt{\eta}$); no-diffusion limit (a), fast diffusion limit (b). The quadrupolar splitting increases with increasing η.

molecular alignment. Note that although referring to magnetic field effects, in a real experiment one can easier achieve the high field strengths required to align nematic molecules by applying an electric field [25,90].

4.2.1 Nematic phase

Consider the bipolar case at $T^* = 0.8$ without diffusion first, again supposing that the direction of the NMR spectrometer field and of the external field **f** match with the bipolar axis of the droplet, here denoted by z. Assume for the moment that there is no external field applied ($\eta = 0$), except for the weak spectrometer field that anyway does not disturb the nematic configuration. As already discussed, already in this case a considerable portion of nematic molecules — especially those in the droplet core — is directed approximately along the spectrometer field, which results in a spectrum consisting of two well-defined peaks (Fig. 4.5, left) situated almost at maximum quadrupolar splitting $\delta\omega_Q$, reduced by a factor of S. Increasing now the external field strength to yield $\eta = 0.2$, the two peaks in the spectrum move towards larger $|\omega_Q|$ and get narrower. Accordingly, the MC data also yield an increase in S — see Table 4.1. As it is evident from Fig. 4.5, this trend continues also in even stronger fields, followed by an agreement also in the MC-calculated S. Note, however, that already for $\eta = 0.2$ the external field is extremely strong: considering the magnetic case and taking $\epsilon = k_B T_{NI}/1.1232 \approx 0.023$ eV (with

$T_{NI} \approx 300$ K and $T^*_{NI} = 1.1232$), the macroscopic anisotropy of the magnetic susceptibility $\chi_a S \approx 10^{-6}$, and assuming a single particle to represent a cluster of up to 100 nematic molecules of volume 1 nm^3 each, one obtains as much as $B \approx 150$ T. If an electric field was used to align the nematic, the corresponding field strength for a typical liquid crystal with $\epsilon_a S \approx 1$ and for same η would be ≈ 45 V/μm, which is — like in the magnetic case — rather difficult to be implemented experimentally (here one encounters short-circuit problems in the dielectric nematic material). It must be stressed, however, that strong external fields are required to induce a detectable distortion because the simulated droplets are still rather small and because surface anchoring was chosen strong, as already noted.

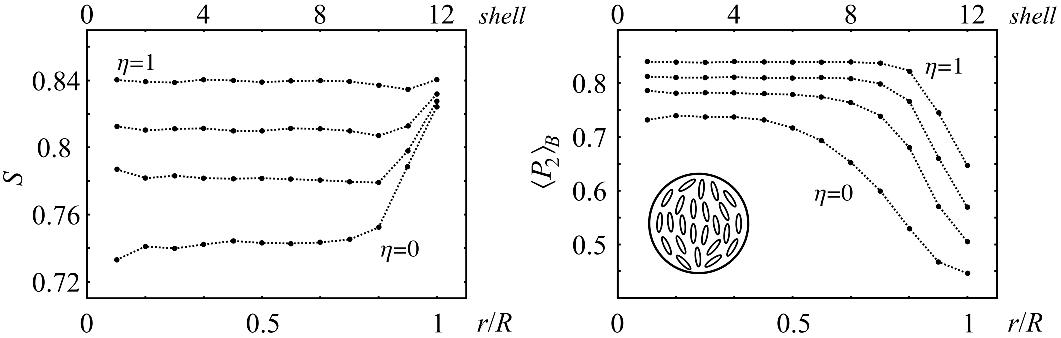

Figure 4.6 Order parameters calculated for the bipolar droplet at $T^* = 0.8$ (nematic phase): (a) standard nematic (S) and (b) external field ($\langle P_2 \rangle_B$) order parameter as a function of the distance from the droplet center r. Curves are plotted for (top to bottom): $\eta = 1$, $\eta = 0.5$, $\eta = 0.2$, and $\eta = 0$, respectively. External field enhances the degree of nematic ordering (a) and increases the size of the aligned core (b). The molecular alignment for $\eta = 0$ is depicted schematically as inset.

To gain more insight into field-induced changes of NMR spectra, it is convenient to divide the PDLC droplet into onion-like spherical layers (shells) of equal thickness and investigate nematic ordering layer by layer [126,127]. For this purpose the standard nematic order parameter S and the external field order parameter $\langle P_2 \rangle_B$ were calculated in each layer of radius r ($a \le r \le R$) separately, leading to $S(r)$ and $\langle P_2 \rangle_B(r)$ profiles, respectively. The parameter S was again obtained by diagonalizing the local ordering matrices, as described above, and gives information on the degree of nematic ordering with respect to the corresponding director. The parameter $\langle P_2 \rangle_B$, however, is defined as $\langle P_2 \rangle_B = \langle \frac{1}{2}[3(\mathbf{f} \cdot \mathbf{u}_i)^2 - 1] \rangle_i$, $\mathbf{f}$ being the unit vector directed along the external field and the brackets $\langle ... \rangle_i$ representing the time and ensemble average over orientations of molecules (particles) within a given spherical layer. Contrary to S, $\langle P_2 \rangle_B$ contains information on molecular ordering along a fixed direction — determined by $\mathbf{f}$ — and thereby reflects also spatial variations of the nematic director. Note also that the number of particles within a certain shell increases rapidly when moving from the droplet center towards the surface (from 8 particles in the 1st shell to 1392 in the 11th). Despite this, the variance of S (now calculated from the ensemble average over particles within a given shell) is not

	η	S_{peak}	S_{MC}	$(\langle\omega_Q\rangle/\delta\omega_Q)_{peak}$	$(\langle\omega_Q\rangle/\delta\omega_Q)_{MC}$
bipolar	0.0	0.73 ± 0.01	0.76 ± 0.04	0.61	0.59
	0.2	0.78 ± 0.01	0.79 ± 0.03	0.71	0.70
	0.5	0.81 ± 0.01	0.81 ± 0.02	0.76	0.77
	1.0	0.84 ± 0.01	0.84 ± 0.015	0.82	0.82
radial	0.0	0.72 ± 0.02	0.73 ± 0.10	0	0.03
	0.02	0.70 ± 0.02	0.73 ± 0.08	0	0.02
	0.03	0.70 ± 0.02	0.74 ± 0.08	0.31	0.28
	0.05	0.70 ± 0.01	0.74 ± 0.08	0.40	0.36
	0.2	0.77 ± 0.01	0.76 ± 0.065	0.59	0.57
	0.5	0.80 ± 0.01	0.79 ± 0.06	0.70	0.70
	1.0	0.84 ± 0.01	0.82 ± 0.05	0.78	0.78

Table 4.1 Bipolar and radial droplet at $T^* = 0.8$: comparison of S and $\langle\omega_Q\rangle$ deduced from NMR spectra ("peak") with those calculated directly from Monte Carlo data ("MC").

highest for the innermost shells. In the nematic phase, for example, it never exceeds 3% in the central shell containing 8 molecules only. The maximum variance (up to 6% in the bipolar and up to 30% in the radial case) usually occurs in intermediate shells or even close to the substrate. In these regions aligning effects of the substrate conflict either with the aligning effect of the external field or with the parallel aligning tendency of the nematic-nematic interaction. The competition of these effects may result also in a slight decrease of S.

The $S(r)$ profiles for the bipolar droplet in the nematic phase for $T^* = 0.8$ are displayed in Fig. 4.6 (a). They indicate that the degree of nematic order is almost constant throughout the droplet core with $S \approx 0.74$ when the external field is absent, while it increases to $S \approx 0.82$ in the surface layer due to ordering effects of the polymer substrate. Applying the field, the degree of molecular order inside the core increases, if compared to the case without field; e.g., for $\eta = 1$ even to $S \approx 0.84$. The profiles of the field order parameter $\langle P_2\rangle_B$ are plotted in Fig. 4.6 (b). The corresponding curve for $\eta = 0$ shows that already in absence of the field there is net molecular alignment along the z axis, which agrees with the imposed bipolar

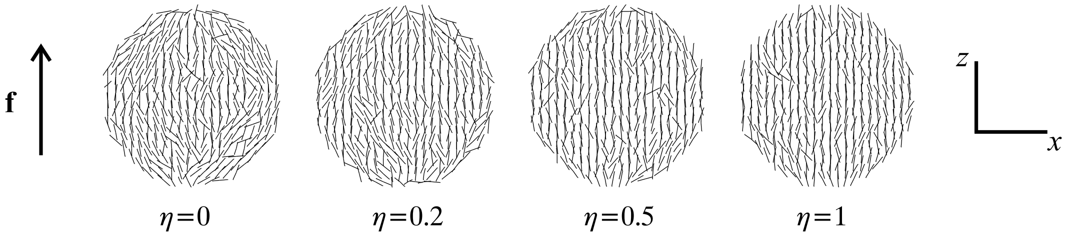

η=0 η=0.2 η=0.5 η=1

Figure 4.7 Bipolar droplet at $T^* = 0.8$ (nematic phase): snapshots of molecular configurations for different η; xz-cross sections.

boundary conditions whose symmetry axis matches with z (compare with snapshots of molecular configurations, Fig. 4.7). The curves for $\eta > 0$ show that with the increasing field strength more and more molecules orient along z (i.e., along $\mathbf{f}$), thereby increasing the size of the droplet core where the nematic liquid crystal is almost undistorted and $\mathbf{n}||z$. The thickness of the distorted region is related to the external field coherence length ξ_m and is obviously microscopic because the applied field is extremely strong.

According to the above observations and to snapshots shown in Fig. 4.7, the increase of the quadrupolar splitting ω_Q in strong fields can be attributed both to the overall increase in the local degree of ordering, i.e., to an increase of S — as observed also experimentally [117] — and to the additional molecular alignment along $\mathbf{f}$ resulting in an increase of $\langle P_2\rangle_B = \langle P_2(\cos\theta)\rangle$; see formula (2.41). Also the narrowing of the spectral lines is related to the increase of $\langle P_2\rangle_B$ since in the droplet

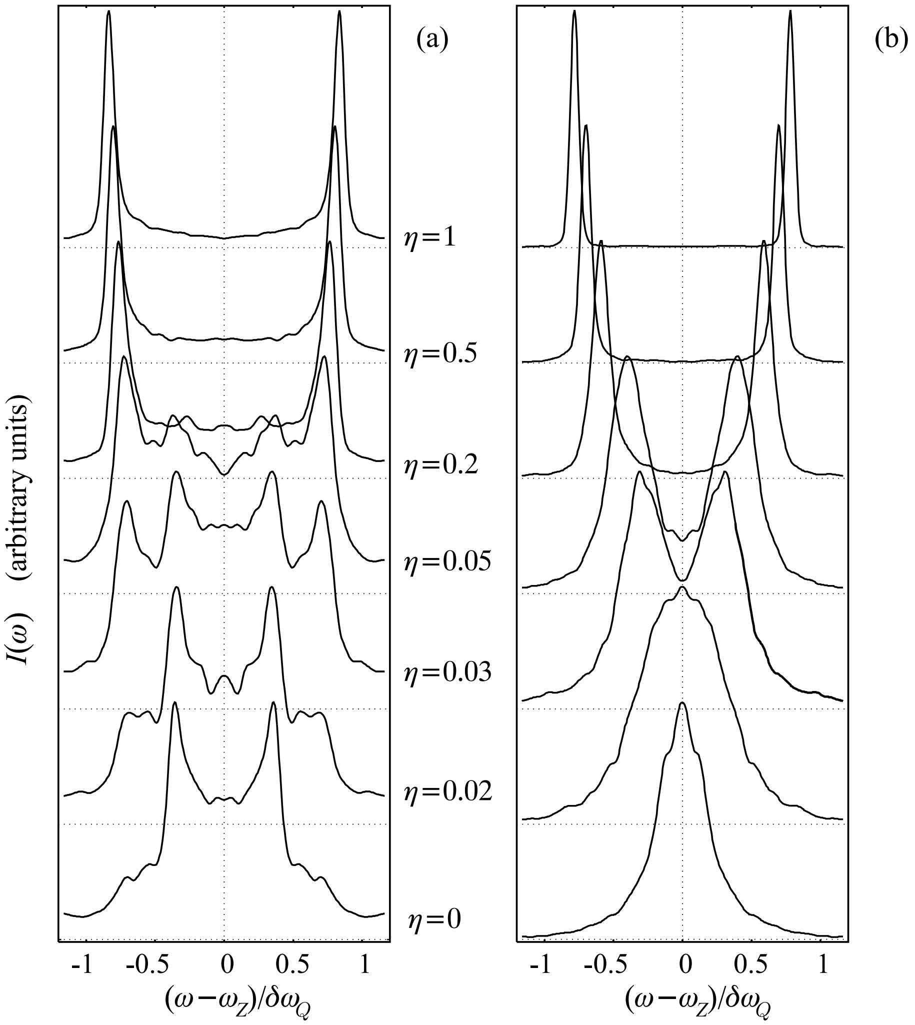

Figure 4.8 ^{2}H NMR spectra of a single radial droplet in the nematic phase at $T^* = 0.8$ for different values of η; no-diffusion limit (a), fast diffusion limit (b). A hedgehog-to-aligned structural transition occurs with increasing η.

core the bipolar configuration is replaced by the "aligned" one. The spectral line narrowing further follows from changes in the distribution of local $S(\mathbf{r})$. In fact, in strong fields the field-enhanced "bulk" value of S approaches the surface-induced value and thus the distribution of S becomes narrower.

Considering now Fig. 4.5 (b) and the spectra of bipolar droplets in the fast translational diffusion limit (or, equivalently, in small enough nematic droplets), the spectra for all η still consist of two well-defined lines now positioned, however, at an average quadrupolar frequency $\pm\langle\omega_Q\rangle$, where ω_Q is spatially-dependent and given by Eq. (2.41), and the averaging is to be performed over diffusive motions of all molecules inside the droplet [40,136]. The quantity $\langle\omega_Q\rangle$ can be calculated also directly from MC data and, according to values presented in Table 4.1, the agreement with actual peak positions is very good.

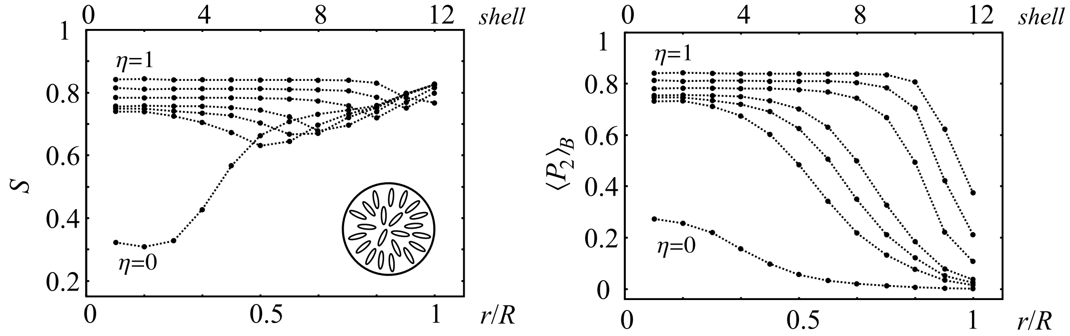

Figure 4.9 Order parameters calculated for the radial droplet at $T^* = 0.8$ (nematic phase): (a) standard nematic (S) and (b) external field ($\langle P_2\rangle_B$) order parameter as a function of the distance from the droplet center. Curves are plotted for (top to bottom): $\eta = 1$, $\eta = 0.5$, $\eta = 0.2$, $\eta = 0.05$, $\eta = 0.03$, $\eta = 0.02$, and $\eta = 0$, respectively. The defect core transforms into an aligned structure. The molecular alignment for $\eta = 0$ is depicted schematically as inset.

We now turn to radial droplets. In absence of external fields the nematic director is directed radially from the droplet center, giving rise to a "hedgehog"-like structure. Then in the very vicinity of the center the elastic deformation (splay) becomes rather strong and therefore it is convenient in this tiny region for the nematic to melt, i.e., to decrease the degree of nematic order (S) so as to reduce the elastic deformation free energy. In the rest of the droplet the radial alignment still exists and therefore in each of the intermediate and outer shells particle orientations are distributed evenly through the whole solid angle. As far as NMR is concerned, this situation is equivalent to having a polycrystalline powder sample and, indeed, as already discussed, the spectrum of the radial droplet for $\eta = 0$ is the Pake-type powder pattern shown in Fig. 4.8 (a) for the diffusionless case. A calculation of the nematic order parameter S [Fig. 4.9 (a)] for $\eta = 0$ shows that the value of S in the center of the droplet is nonzero, yet considerably smaller (≈ 0.32) than the value obtained in the intermediate and surface layers ($\gtrsim 0.75$). This confirms the existence of a small ($\sim 4a$ in diameter) and fairly disordered defect core. Looking at snapshots

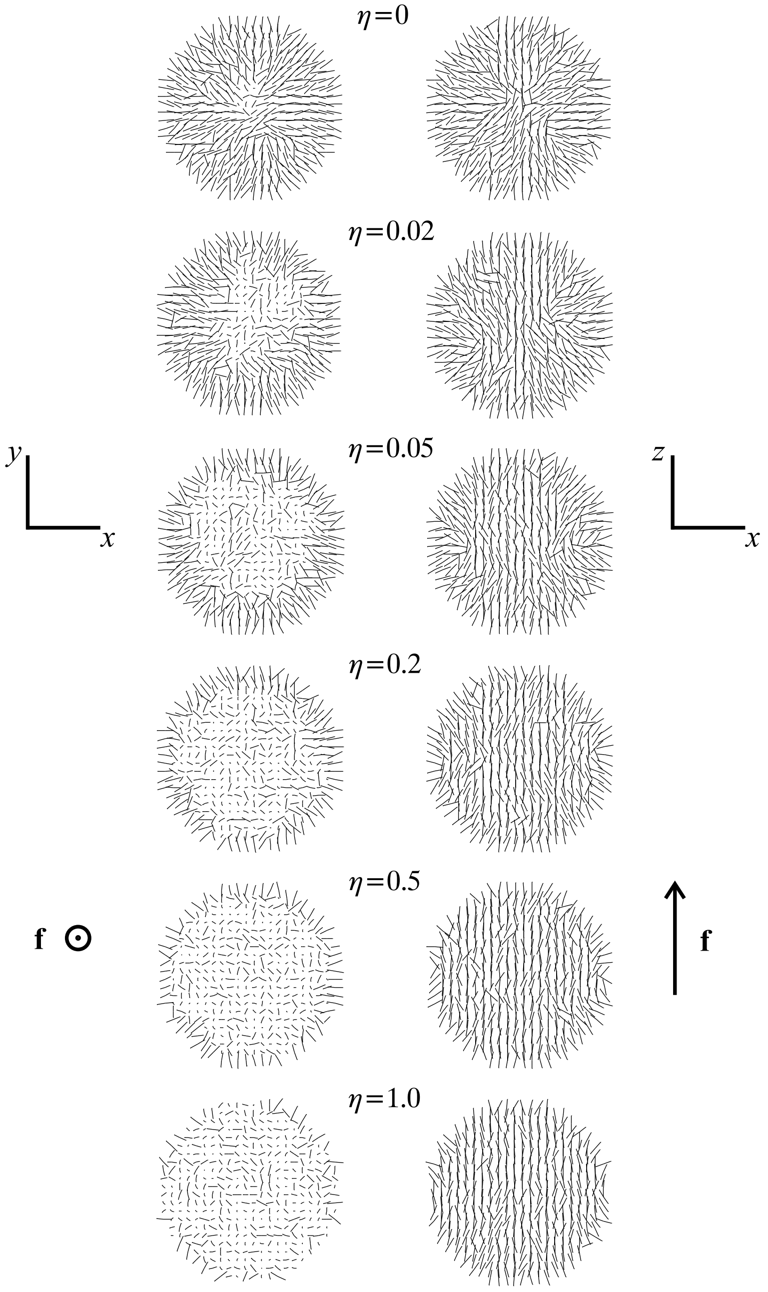

Figure 4.10 Radial droplet at $T^* = 0.8$ (nematic phase): snapshots of molecular configurations for different η; xy-cross sections (left column), xz-cross sections (right column). The external field **f** is applied along **z**.

of molecular configurations (Fig. 4.10), it can be readily observed that here one is not dealing with a point defect: the defect core actually consists of a weakly aligned nematic, encircled by a ring disclination line of strength $+\frac{1}{2}$. The plane of the ring takes an arbitrary orientation and can even rotate during the MC evolution. The characteristic time scale associated with reorientations of the ring is expected to be much larger than the time span covered by the 1024 MC cycles employed in the line shape calculation.

Applying an external field, with increasing η the disclination ring first orients normal to **f**, the field direction, and after that increases also in size (see Fig. 4.10). Thereby the radial "hedgehog" structure is transformed into an axially symmetric structure with a well-pronounced ring defect. The degree of ordering in the center therefore increases significantly and the molecules of the core align along the field direction (compare with order parameters S and $\langle P_2 \rangle_B$ plotted in Fig. 4.9). There is no critical field characterizing the transition between the "hedgehog" and the aligned structure: the size of the aligned core increases gradually with the increasing field strength [99]. This can be confirmed also by inspecting the resulting NMR spectra shown in Fig. 4.8 (a). For strong external fields with $\eta \geq 0.2$ the Pake-type pattern transforms into a spectrum with two narrow peaks, similar to those observed for bipolar boundary conditions. Again, this indicates that for $\eta \geq 0.2$ most of the molecules are aligned along **f**, except for those lying close enough to the polymer substrate (compare with Fig. 4.10). In fact, surface-induced radial order persists in the outermost molecular layers, which results in a strong decrease of the order parameter $\langle P_2 \rangle_B$ [Fig. 4.9 (b)] in the surface region. The thickness of this region is again roughly equal to the field coherence length ξ_m. In the intermediate regime with $0 < \eta < 0.2$ the spectra are composed both of the Pake type contribution originating from the surface layers and of two narrow peaks being a signature of the field-ordered core. With increasing η the latter contribution prevails, as it is clearly evident from Fig. 4.8 (a). Again it is possible to check the agreement of values for S deduced from peak positions and from MC data (Table 4.1).

As seen in previous Sections, in the fast diffusion regime the spectrum of the radial droplet for $\eta = 0$ consists of a single line located at $\langle \omega_Q \rangle = 0$ [40,136]. As soon as there is a preferred direction (like in the bipolar case with all droplets aligned or in a strong enough field), $\langle \omega_Q \rangle = 0$ no longer holds and the spectrum splits into two narrow and symmetric peaks. Fig. 4.8 (b) shows the fast diffusion spectra for radial boundary conditions. As expected, one observes a single line in the spectrum only if the external field is off or relatively weak with $\eta \leq 0.02$. Increasing the field strength, the spectrum gradually transforms into the two-peak pattern described above. For a comparison of peak positions and $\langle \omega_Q \rangle$ calculated from MC data see Table 4.1; the agreement of the two estimates is fairly good.

4.2.2 Isotropic and field-induced nematic phase

In the following we will consider both types of boundary conditions at $T^* = 1.2$, a higher temperature already above the nematic-isotropic transition. In absence of external fields molecular motion in the bulk isotropic phase is spatially isotropic (i.e., there is no long-range orientational order), hence one has $S = 0$. Consequently, the quadrupolar perturbative contribution to the deuteron energy levels is averaged out and the frequency splitting $\omega_Q \propto S$ vanishes [see Eq. (2.41)]. In this case a single line positioned at $\omega_Q = 0$ appears in the NMR spectrum.

Consider the bipolar droplet for $\eta = 0$ first: the corresponding spectrum consists of a single line at zero-splitting, as expected [Fig. 4.11 (a)]. A calculation of the nematic scalar order parameter S [Fig. 4.12 (a)] reveals some residual bipolar ordering with $S > 0$ in the outer molecular layers that is responsible for a rather large line width. Applying the external field, the two peaks characteristic for ordered nematic phases reappear. Also the nonzero values of both order parameters

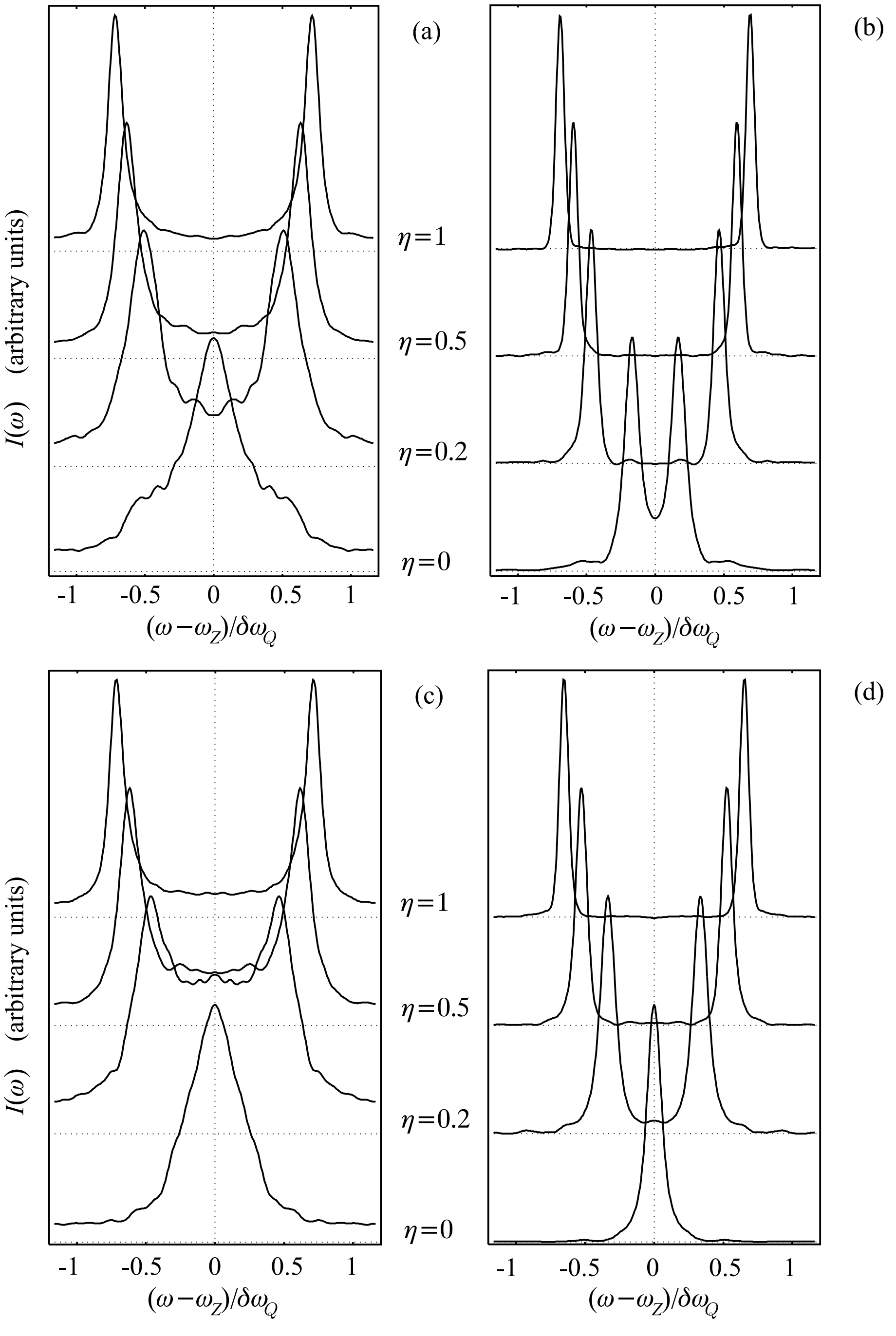

Figure 4.11 ^{2}H NMR line shapes of droplets at $T^* = 1.2$ (above T^*_{NI}). *Top:* bipolar droplet in the static (a) and fast diffision limit (b). *Bottom:* same as *top*, but for the radial droplet: static (c) and fast diffision limit (d). For strong enough fields a nonzero quadrupolar splitting is restored.

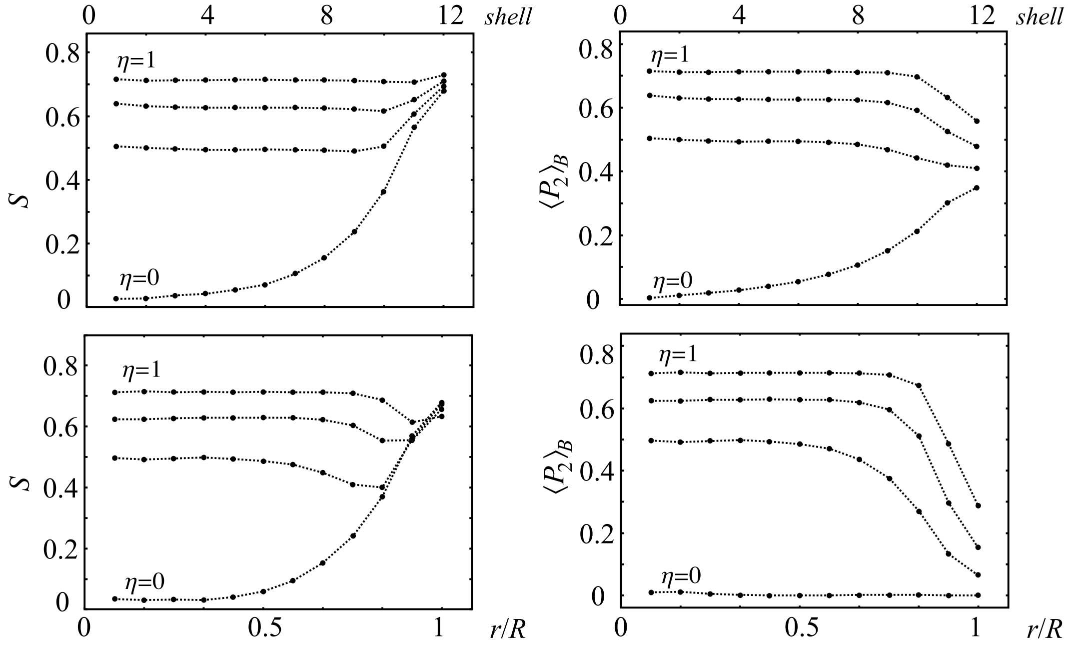

Figure 4.12 Bipolar (*top*) and radial droplet (*bottom*); same as Figs. 4.6 and 4.9, but at $T^* = 1.2$ (above T^*_{NI}). Even for $\eta = 0$ there is some residual surface-induced nematic order in the outer layers of the droplet, while in a strong enough external field nematic order is restored throughout the droplet.

(S and $\langle P_2\rangle_B$) given in Fig. 4.12 are restored again despite the fact that the at $T^* = 1.2$ one is already quite far from the NI transition. All these observations show that a strong enough external field can overwhelm temperature effects and induce nematic-like molecular ordering also above the nematic-isotropic transition temperature [99,100,167], which has been observed also experimentally [118], however, not that far from the NI transition in the absolute temperature scale. Like in the nematic phase, the quadrupolar splitting increases with increasing η. Again, peak positions and MC-data values for S match (Table 4.2). One can also compare the peak positions (and, simultaneously, the estimates for S) with those obtained for the lower temperature $T^* = 0.8$. As expected, for $T^* = 1.2$ the estimated values for S are lower than those for $T^* = 0.8$ (see above). This suggests that although unrealistically strong, the external field is still not the only important element in determining the structure inside the droplet and that disordering temperature-induced effects are still well-pronounced. In the fast diffusion limit all spectra, including that for $\eta = 0$, consist of two peaks since $\langle \omega_Q\rangle \neq 0$ [Fig. 4.11 (b)]. This result is expected for $\eta \neq 0$ and also for $\eta = 0$, where the ordering effect of the external field is absent, but there is residual surface-induced ordering [for the behavior of S see Fig. 4.12 (a)]. Checking the matching of peak positions and the MC-deduced values of $\langle \omega_Q\rangle$, the agreement is still very good (Table 4.2).

Repeating the analysis for radial boundary conditions and $T^* = 1.2$ gives similar results: in the no-diffusion limit the single broad peak centered at $\omega_Q = 0$ for $\eta = 0$ splits into a doublet for $\eta \neq 0$ and the splitting increases with η [Fig. 4.11 (c)].

	η	S_{peak}	S_{MC}	$(\langle\omega_Q\rangle/\delta\omega_Q)_{peak}$	$(\langle\omega_Q\rangle/\delta\omega_Q)_{MC}$
bipolar	0.0	0	—	0.17	0.18
	0.2	0.51 ± 0.01	0.53 ± 0.08	0.46	0.46
	0.5	0.63 ± 0.01	0.63 ± 0.05	0.59	0.60
	1.0	0.72 ± 0.01	0.71 ± 0.03	0.69	0.69
radial	0.0	0	—	0	0.001
	0.2	0.46 ± 0.01	0.48 ± 0.11	0.33	0.34
	0.5	0.62 ± 0.01	0.59 ± 0.08	0.52	0.52
	1.0	0.71 ± 0.01	0.68 ± 0.08	0.65	0.65

Table 4.2 Bipolar and radial droplet at $T^* = 1.2$: comparison of S and $\langle\omega_Q\rangle$ deduced from NMR spectra with those calculated directly from Monte Carlo data. S_{MC} for $\eta = 0$ is not given since in the isotropic phase the method employed to calculate S results in an overestimate because in a disordered phase the nematic director is not well-defined [124].

If the field is absent, the order parameters S and $\langle P_2\rangle_B$ plotted in Fig. 4.12 show the existence of residual radial order in the surface layers of the droplet, while in the core the liquid crystal is isotropic. For nonzero η both order parameters acquire a nonzero value and hence again confirm field-induced nematic ordering above T_{NI}. A comparison of peak position-determined S and MC-calculated S given in Table 4.2 again shows that the agreement of the two values is fairly good. Like for the bipolar droplet one can compare these values with those obtained at $T^* = 0.8$ in the nematic phase and again find that the degree of nematic ordering is lower at higher temperature. Finally, Fig. 4.11 (d) shows the corresponding fast diffusion limit spectra. For $\eta = 0$ the line is single-peaked in spite of residual order with nonzero S close to the surface (Fig. 4.12). Note, however, that in this layer one is dealing with radial order yielding $\langle\omega_Q\rangle = 0$ already in itself. In other cases with external field two peaks reappear and the corresponding splitting increases with η. The agreement of $\langle\omega_Q\rangle$ evaluated from peak positions and from MC data is very good again; see Table 4.2.

For a more serious quantitative comparison of all calculated spectra with the experimental ones, usually recorded for larger droplets than the ones studied here, it would be necessary to simulate droplets containing a significantly larger number of particles, so as to access radii of the order of $\sim 1\ \mu$m. Moreover, it turns out that the distribution in orientations of droplet symmetry axes is closely related to the shape of the droplets, which is not necessarily spherical — as assumed so far — but rather somewhat ellipsoidal, which may reflect in NMR spectra [25], as well as in other observables. Some simulation work with ellipsoidal droplets has also been performed in the past, presenting, however, no experimental observables [92].

5

Nematics with dispersed polymer networks

In this Chapter the complex-most of all confinement types in this thesis will be treated — low-concentration polymer networks dispersed in a nematogenic liquid. The networks typically consist of thin fibers — few nanometers thick — or of somewhat thicker bundles of such fibers. As already mentioned in the introductory Chapter, polymer fibers can play an important role in aligning the surrounding liquid crystal even at low polymer concentrations [5,26,39]. As such, they are important for the construction of electrooptical devices based on the external field-induced switching process. The detailed characteristics of this process are closely linked to the anchoring and ordering conditions at the fiber surface, as well as to the shape and regularity of the network. Experimentally, these network properties can be regulated during the network formation (photopolymerization from the monomer-liquid crystal mixture) through various parameters: monomer solubility, curing temperature, ultra-violet (UV) light curing intensity, and the degree of orientational ordering in the liquid-crystalline component [5]. In particular, poorly soluble monomers result in polymer fibers with a grainy and coarse surface morphology, while highly soluble monomers can form smooth fiber surfaces [15]. Further, high curing temperatures, as well as high UV light intensities, result in larger voids between polymer fibers [101]. If the liquid-crystalline component of the mixture is isotropic during the polymerization process, polymer fibers form directionless strands. On the other hand, performing the polymerization in the nematic phase, or applying an external aligning magnetic field, fibers can form bundles with a well-defined average direction [5]. Similar types of network-like confinement can be achieved also in silica aerogel systems, where irregular chains of silica particles play the aligning role of polymer fibers [5]. While thin (nanometric) polymer fibers typically promote planar surface anchoring along the fiber direction, thicker fibers or fiber bundles (several 10 nm in diameter) can be treated with surfactants to yield homeotropic anchoring conditions.

Like for PDLC droplets (Chapter 4), Monte Carlo simulations have been performed in the Lebwohl-Lasher lattice model system. In this Chapter following phenomena will be investigated in more detail: (i) a relation between the polymer fiber surface roughness and the long-range orienting ability of the network [102], (ii) the switching behavior in network systems with regular and irregular surface topography, (iii) pretransitional paranematic ordering, and (iv) topological defect lines (disclinations) [103]. The first two phenomena are of great interest for applicative purposes. Issues (i), (ii), and (iv) will be explored in a system of parallel and straight fibers. Such a regular fiber array is similar also to colloidal crystal systems. In addition, the analysis of issue (ii), the switching behavior, will be extended also to irregular fiber networks, dropping the initial requirement that the fibers be straight and regular in position. Pretransitional ordering, issue (iii), will also be addressed in an irregular sample. The simulation output will be expressed in form of ^{2}H NMR spectra (all issues), electric capacitance (the switching behavior), and transmitted polarized light intensity (the switching behavior and pretransitional ordering).

5.1 Aligning ability of the network

In this Section a thorough microscopic simulation study of the orientational coupling between polymer fibers and the surrounding liquid crystal will be presented, focusing on polymer networks with a well-defined net fiber direction (as shown in Fig. 1.3), and on effects of roughness at the fiber surface. In simulations the same model as for studying nematic droplets was used (see Chapter 4 and the references therein), however, only after appropriately adapting the simulation box and the boundary conditions to mimic the geometry of the current network sample.

As a first step towards modeling the complex topology of the polymer network, a single straight cylindrical fiber (oriented along the z-axis) was considered. The shape of the fiber was defined by carving a jagged cylinder from the cubic lattice and taking all particles that are lying closer than R — the fiber radius — from the center of the xy-plane (Fig. 5.1). The particle orientations in the surface layer of the fiber (ghost particles) were chosen in agreement with the desired boundary conditions and were kept fixed during the simulation. The strengths of nematic-nematic and nematic-ghost interactions were set equal, which corresponds to the strong anchoring limit. Further, periodic boundary conditions at the simulation box boundaries were assumed. Such a set-up in fact corresponds to a regular array of straight and parallel fibers. It is believed that such simplified topography of the fiber network does not qualitatively affect the effect of surface roughness studied here, at least for low-density polymer networks. More realistic network models will be presented later, including curved fibers positioned randomly inside the simulation box, allowing for cross-linking between them at somewhat higher polymer concentrations.

In the case of "perfect" anchoring ghost particle orientations were chosen either along $\mathbf{z}$ (a unit vector along the z-axis) for planar anchoring, or along the local radial unit vector for homeotropic anchoring. For cases with partially disordered anchoring — simulating the still cylindrical but rough fiber surface — the perfect planar or homeotropic ghost orientations were perturbed by performing an additional rotation for each of the ghost particles, characterized by a set of polar (θ) and azimuthal (ϕ) angles. While the ϕ angle was sampled from a uniform distribution within $[0, 2\pi]$, the sampling of θ (or, alternatively, $\cos\theta$) was biased so as to regulate the degree of randomness in ghost particle orientations. The biasing distribution was chosen to

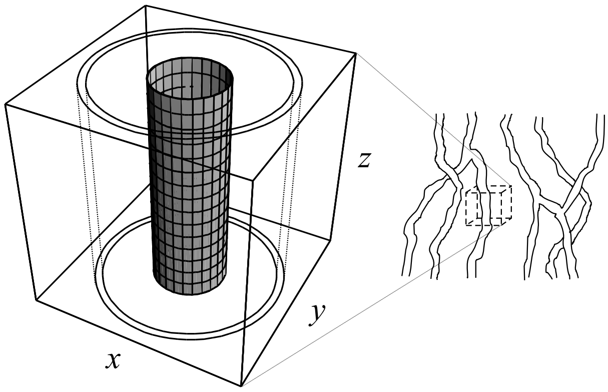

Figure 5.1 Schematic depiction of the polymer network (*right*) and the simulation box with the cylindrical fiber and one of the cylindrical shells (*left*).

be $dp/d\cos\theta \propto \exp(\mathcal{P}\cos^2\theta)$ (with p denoting the probability and $\cos\theta \in [-1,1]$), where for small $\mathcal{P}$ the resulting orientational distribution of ghosts becomes almost isotropic, while for large values of $\mathcal{P}$ it becomes strongly peaked at $\cos\theta = \pm 1$ (i.e., $\theta = 0, \pi$) and therefore approaches that of the perfect anchoring cases. In the case with completely disordering anchoring ghost orientations were sampled from a fully random orientational distribution. The degree of randomness can be given quantitatively by diagonalizing the ordering matrix $\underline{Q} = \frac{1}{2}(3\langle \mathbf{u}_i \otimes \mathbf{u}_i \rangle_g - \mathsf{I})$ (the average $\langle ... \rangle_g$ taken over ghosts), which gives the ghost director and the corresponding order parameter $\langle P_2 \rangle_g$. In all cases the $\langle P_2 \rangle_g$ order parameter is referred to the z-axis, the fiber direction. Therefore, cases with $\langle P_2 \rangle_g = 1$ and $\langle P_2 \rangle_g = -0.5$ stand for perfect planar and homeotropic alignment, respectively, and $\langle P_2 \rangle_g \approx 0$ for a random orientational distribution. Intermediate values of $\langle P_2 \rangle_g$ then correspond to partial planar ($\langle P_2 \rangle_g > 0$) or partial homeotropic order ($\langle P_2 \rangle_g < 0$) in ghost orientations. In principle, the phenomenological analogue to such partially disordered interfaces (characterized by a surface-imposed degree of order, $\langle P_2 \rangle_g$, and by a given easy axis, as here $\mathbf{z}$) can be found in modeling the surface free energy by (2.17), also used in Chapter 3.

To study the radial dependence of order parameters, it is convenient to split the cubic simulation box into cylindrical layers surrounding the fiber (see Fig 5.1). The observables accumulated during the production run were $\langle P_2^z \rangle$, quantifying the degree of ordering with respect to the z-axis, $\langle P_2^c \rangle$, indicating how the order deviates from perfect radial ordering in the xy-plane, and the standard nematic order parameter S. Then, for example, $\langle P_2^z \rangle$-profiles were calculated as $\langle P_2^z \rangle(r) = \frac{1}{2}\left[3\langle (\mathbf{u}_i \cdot \mathbf{z})^2 \rangle_r - 1\right]$. The average $\langle ... \rangle_r$ has to be performed over all nematic particles $\mathbf{u}_i$ belonging to the cylindrical layer with radius r, and over MC cycles. Analogously, $\langle P_2^c \rangle$ profiles were calculated with respect to the local unit vector $\mathbf{e}_r$, where $\mathbf{e}_r$ defines the local radial direction in the xy-plane at the ith lattice site. Finally, the nematic order parameter profile $S(r)$ was obtained from the diagonalization of the ordering matrix $\underline{Q}(r) = \frac{1}{2}(3\langle \mathbf{u}_i \otimes \mathbf{u}_i \rangle_r - \mathsf{I})$ averaged over sites in the nematic layer with radius r, and over MC cycles. The eigenvalue with the largest absolute value can then be identified as S and the difference between the remaining two eigenvalues corresponds to biaxiality.

In absence of significant collective molecular reorientation during the MC evolution, it is instructive to calculate also spatially-resolved director and order parameter maps $\mathbf{n}(\mathbf{r}_i)$ and $S(\mathbf{r}_i)$, respectively, where $\mathbf{r}_i$ denotes the position of the ith lattice site. For this purpose the local ordering matrix $\underline{Q}(\mathbf{r}_i) = \frac{1}{2}(3\langle \mathbf{u}_i \otimes \mathbf{u}_i \rangle_{\mathbf{r}_i} - \mathsf{I})$ was averaged over MC cycles and then diagonalized, yielding the local value of the order parameter $S(\mathbf{r}_i)$, as discussed above, and the corresponding eigenvector, i.e., the local director $\mathbf{n}(\mathbf{r}_i)$. Similarly, the biaxiality map can also be deduced from the data.

In simulations presented in this Section, the simulation box size was set to $30a \times 30a \times 30a$, which for the chosen fiber radius ($R = 5a$, a denoting the lattice spacing) amounts to 24600 nematic and 840 ghost particles in total. Simulation runs were started from a completely random (disordered or isotropic) orientational configuration not to impose any preferred orientation in the system. In general, simulation results were rather insensitive to changing the initial particle configuration. Then the standard Metropolis scheme [37] was employed to perform updates in particle orientations [91,131]. Once the system was equilibrated (after at least 6×10^4 MC cycles), a sequence of 6.6×10^4 (or more) successive particle configurations was used to calculate relevant observables. Results from MC simulations were expressed using selected order parameters and ^{2}H NMR spectra following the methodology presented in Chapter 4.

The following were obtained at two different reduced temperatures $T^* = kT/\epsilon$, $T^* = 1.0$ and $T^* = 1.2$, deep enough in the nematic and isotropic phases, respectively (recall again that the nematic-isotropic transition in the bulk takes place at $T^*_{NI} = 1.1232$ [123]). Other calculations, not reported here for reasons of space, were performed at $T^* = 1.1$ with results qualitatively similar to those obtained for $T^* = 1.0$. The correlation length for orientational ordering at these temperatures was found not to exceed $\approx 5a$, which with the present choice for the simulation box size is expected to be enough to avoid spurious correlations originating from periodic boundary conditions. In this study the fiber radius was fixed to $R = 5a$. Another set of runs for a thinner fiber with $R = 3a$ has also been performed, but has shown no major difference in comparison with the $R = 5$ case and is therefore not reported here.

5.1.1 Planar anchoring

First consider a nematic sample at $T^* = 1.0$, with planar anchoring along the $\mathbf{z}$ direction and with possible deviations from this perfect alignment, as described above. This situation corresponds to a series of polymer fibers whose surface morphology varies from smooth to rough and disordered. Fig. 5.2 (a) shows how the $\langle P_2^z \rangle$ order parameter changes across the simulation box from the fiber surface to the outer sample boundaries. Different curves shown in the plot correspond to different degrees of order in the ghost particle system, $\langle P_2 \rangle_g$. For perfect planar anchoring $||\mathbf{z}$ with $\langle P_2 \rangle_g = 1$ the nematic director $\mathbf{n}$ is parallel to $\mathbf{z}$. In this case $\langle P_2^z \rangle$ becomes a direct measure for S because $\mathbf{n}$ and $\mathbf{z}$ coincide. Far enough from the fiber the value of $\langle P_2^z \rangle$

approaches ≈ 0.6, matching with that of S in a bulk sample at $T^* = 1.0$ [123], while close to the fiber there is an increase in $\langle P_2^z \rangle$, reflecting the fiber-induced enhancement of nematic order. The same effect is further confirmed by the behavior of the $S(r)$ profile depicted in Fig. 5.3 (a), as well as by the $S(x, y)$ local order parameter map shown in Fig. 5.3 (b). For all three profiles the characteristic length of the nematic order variation ξ (2.11) roughly amounts to $\approx 3a$.

Studying cases with reduced (imperfect) planar anchoring $||\mathbf{z}$ [Figs. 5.2 (a) and 5.3 (a)], one can see that at least down to $\langle P_2 \rangle_g \approx 0.25$ the bulk value of both order parameters remains essentially unchanged if compared to the perfect $\langle P_2 \rangle_g = 1$ case. Note that now for, e.g., $\langle P_2 \rangle_g \approx 0.75$ the increase of order close to the fiber is smaller than for $\langle P_2 \rangle_g = 1$, and that already for $\langle P_2 \rangle_g \approx 0.50$ (as well as for $\langle P_2 \rangle_g \approx 0.25$) the surface degree of order is somewhat lower than its bulk value. From these observations one can conclude that the first effect of the partial disorder in surface anchoring is merely a slight decrease in the degree of nematic order in the vicinity of the fiber, but that at this point the long-range orienting ability of the polymer network is not lost. This ability, however, weakens upon further decreasing $\langle P_2 \rangle_g$, but is present at least down to $\langle P_2 \rangle_g \approx 0.09$ (the corresponding profiles not plotted here). Then only in a sample with a completely disordering fiber — for $\langle P_2 \rangle_g \approx 0$ — the net orientation of the nematic for the intermolecular potential (2.29) is completely detached from the fiber direction. This follows from the behavior of the $\langle P_2^z \rangle$ order parameter (calculated with respect to the fixed fiber direction) which now — in principle — can take any arbitrary value, and from the fact that the liquid crystal is still nematic, as suggested by a nonzero value of the S order parameter throughout the sample. Note that the bulk value of S remains almost unaltered in comparison to, e.g., the $\langle P_2 \rangle_g = 1$ case. The fact that it is actually slightly lower

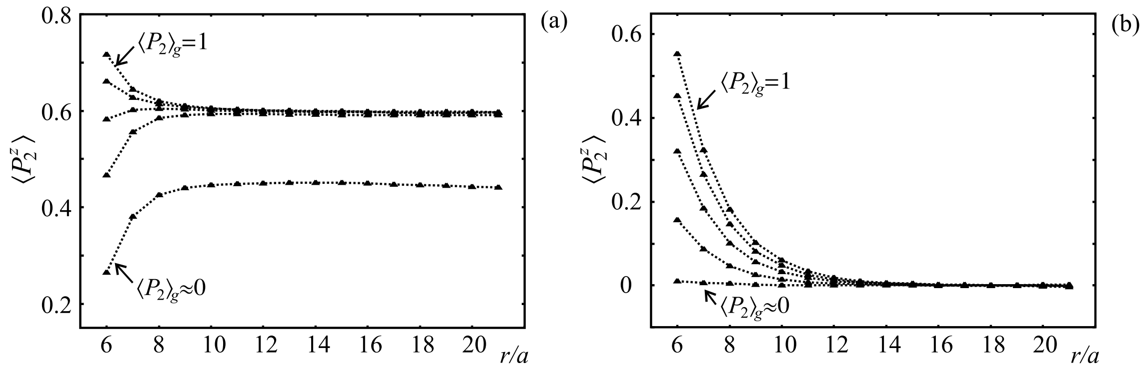

Figure 5.2 Order parameter $\langle P_2^z \rangle$ versus r (the distance from the simulation box center, measured in lattice units a) in a sample containing a single cylindrical fiber with $R = 5a$. Planar anchoring along the z-axis; (a) nematic ($T^* = 1.0$) and (b) isotropic phase ($T^* = 1.2$). In the plots each of the curves corresponds to a different degree of ordering in the ghost particle system: $\langle P_2 \rangle_g \approx 1.0$, 0.75, 0.50, 0.25, and 0 (top to bottom). The dotted lines serve as a guide to the eye (also in following Figures).

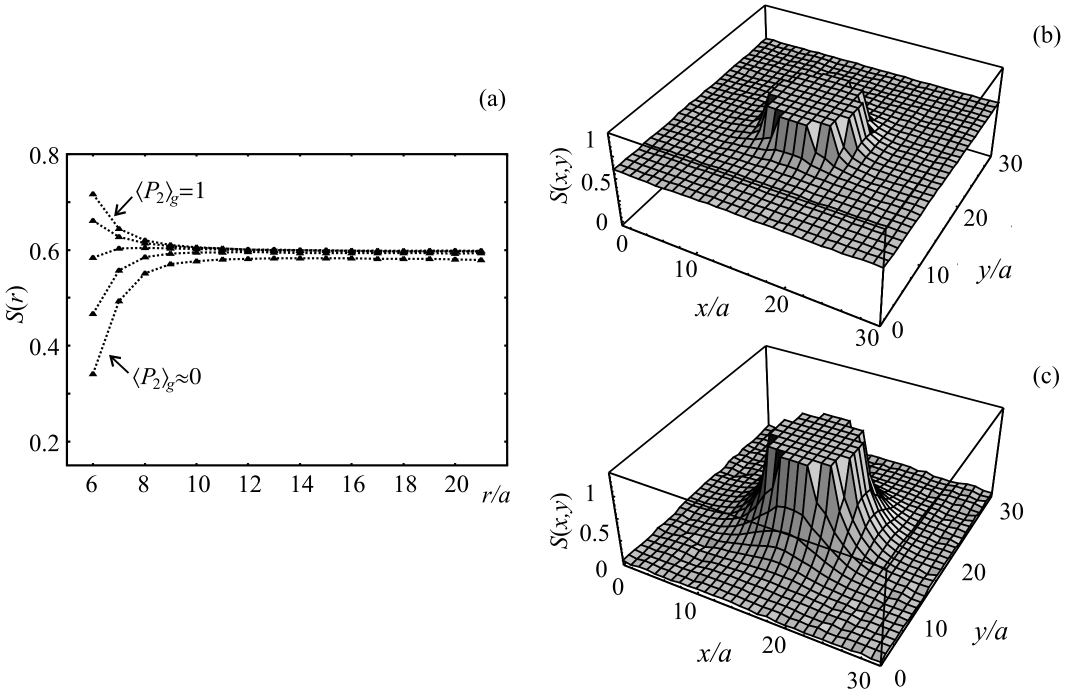

Figure 5.3 Planar anchoring $||\mathbf{z}$. (a) Order parameter radial profiles $S(r)$ for different values of $\langle P_2 \rangle_g$ in the nematic phase ($T^* = 1.0$); curves are labeled as in Fig. 5.2. (b) Perfect planar anchoring ($\langle P_2 \rangle_g = 1$); xy-cross section of the local $S(\mathbf{r}_i)$ order parameter map in the nematic phase ($T^* = 1.0$). (c) Same as (b), but in the isotropic phase ($T^* = 1.2$). The distances along x and y are plotted in lattice units.

than the value obtained for $\langle P_2 \rangle_g = 1$ (≈ 0.6) can be attributed to slow collective molecular motion during the production run.

If temperature in the LL model is increased to $T^* = 1.2$, in a bulk sample the isotropic phase is stable. However, like in PDLC droplets, also in a nematic with a dispersed polymer network one should expect surface-induced paranematic ordering. For the case of planar anchoring $||\mathbf{z}$ Figs. 5.2 (b) and 5.3 (c) show the $\langle P_2^z \rangle$ and the local $S(x, y)$ profiles and in fact confirm the existence of surface-induced planar ordering. Note that the layer-averaged nematic order parameter profile $S(r)$ would have looked exactly like the $\langle P_2^z \rangle$-profile and is therefore not shown here. The net molecular orientation is still along $\mathbf{z}$, as imposed by the fiber, and the corresponding degree of order (given either by $\langle P_2^z \rangle$ or S) decays to zero over a characteristic length of the order of $\xi \approx 5a$ (2.11).

5.1.2 Homeotropic anchoring: topological defects

Proceeding now to cases with $\langle P_2 \rangle_g < 0$, i.e., to perturbed homeotropic ordering, already for $\langle P_2 \rangle_g \approx -0.08$ the polymer fiber is able to align the liquid crystal. Molecules are now aligned perpendicular to $\mathbf{z}$, the fiber direction, i.e., mainly within

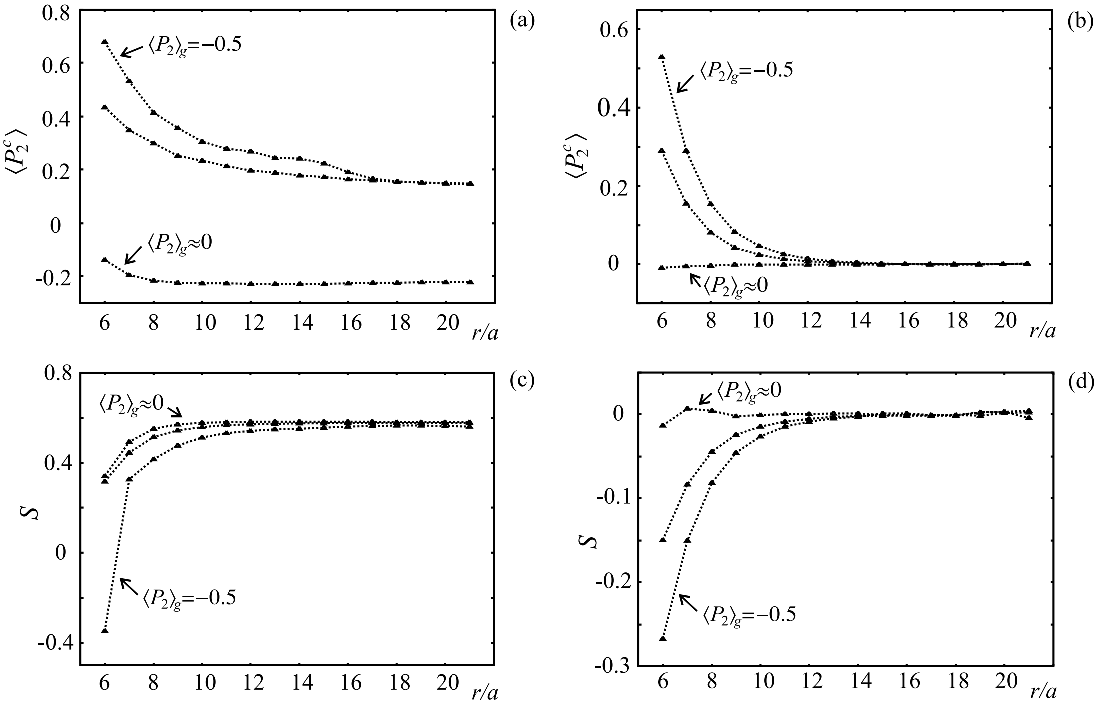

Figure 5.4 Order parameter profiles $\langle P_2^c\rangle(r)$ and $S(r)$ for homeotropic anchoring with $\langle P_2\rangle_g \approx$ -0.50, -0.25, and 0 (top to bottom). (a) and (c): nematic phase ($T^* = 1.0$), (b) and (d): isotropic phase ($T^* = 1.2$).

the xy-plane. This can be deduced from $\langle P_2^z\rangle$ profiles, the $\langle P_2^z\rangle$ values being now negative for all r (not plotted here). Similarly as for planar anchoring there is a decrease in the degree of nematic ordering close to the fiber, e.g., for $\langle P_2\rangle_g \approx -0.25$ (partial disorder) and an enhancement for $\langle P_2\rangle_g = -0.50$ (perfect homeotropic order). Studying cases with homeotropic surface alignment, it is more convenient to plot the $\langle P_2^c\rangle$ order parameter profiles. Note now that for $\langle P_2\rangle_g = -0.5$ the $\langle P_2^c\rangle$-profile — shown in Fig. 5.4 (a) — is always positive and that $\langle P_2^c\rangle$ values are rather high close to the fiber. This is a signature of strong radial ordering, along with the negative values of S in the first layer next to the fiber surface; see Fig. 5.4 (c). Going away from the fiber, $\langle P_2^c\rangle$ exhibits a plateau-like behavior, before relaxing to the bulk value close to $\approx \frac{1}{4}S$, which is characteristic for homogeneous (undeformed) nematic ordering. Such alignment far from the fiber is compatible with strong radial ordering in the fiber vicinity only if topological defects are to form. In fact, as shown in the director map $\mathbf{n}(\mathbf{r}_i)$ (Fig. 5.5, left), a pair of $-\frac{1}{2}$ strength defect lines forms along the fiber and close to the simulation box diagonal. The plateau in $\langle P_2^c\rangle$-profiles then corresponds to the distortion of the director field imposed by the defect lines.

As concluded from topological considerations, either a -1 strength disclination line or a pair of $-\frac{1}{2}$ lines can form in the neighborhood of the particle. This can be inferred from the fact that the insertion of a homeotropic fiber into a uniform nematic (the uniformity provided by periodic boundary conditions) is equivalent to an insertion of a $+1$ strength defect line. Then, in order to meet the conservation rule for topological charge (the total defect strength $\sum_i m_i$), defects of opposite sign have to form in the nematic, which is exactly what is seen also in the present simulation. The -1 line, however, does not seem to be stable and splits into a pair of $-\frac{1}{2}$ lines during the MC evolution, even if it is taken as initial configuration in the simulation run. This behavior agrees with simple estimates of defect line free energies where the defect line free energy scales as m^2 (where m is the defect strength; see Sect. 2.1.6) [4,24]. Moreover, a stable "escaped" structure (bent in the $\mathbf{z}$-direction) could also not be observed in present simulations. Here it should be stressed that the defects are able to form because the anchoring strength w is rather high. Decreasing w or considering a rough fiber surface, both defects vanish, which is because for small w (or for a rough surface) the anchoring penalty for homogeneous alignment also in fiber vicinity is lower. Note also that the following analysis of the defects is relevant not only for fiber network systems, but also for elongated colloidal particles embedded in a liquid crystal host [103].

The pair of defect lines always forms close to one of the simulation box diagonals although the cross section of the fiber is axially symmetric (ignoring its jagged shape); see the director fields shown in Fig. 5.5 and 5.6. This symmetry breaking may be attributed to two effects of different origin. The first one (and, according to preliminary tests, the more important one for the $30 \times 30 \times 30$ system size) is the repulsion between defects maximizing the defect-to-defect distance (recall the periodic boundary conditions), while the second one is a finite-size effect originating from collective fluctuations, resulting in a tendency to align the nematic along the simulation box diagonal [168]. These phenomena, as well as the presence of the polymer fiber, are believed not to affect any of the qualitative features characterizing the defect line inner structure studied in the following. Moreover, the presence of the fiber is reflected only in an enhancement of nematic ordering in its immediate surroundings.

The inner structure of a defect line is characterized by variations in the three eigenvalues of the ordering matrix $\underline{Q}$, Q_1, Q_2, and Q_3. The eigenvalues, along with the corresponding eigenvectors, were obtained by diagonalizing $\underline{Q}$ (2.5) for each of the lattice sites. The scalar order parameter S, biaxiality P, and director $\mathbf{n}$ maps can then be derived from these data, as discussed earlier. Fig. 5.5 (left) shows the director field and the order parameter map in the plane perpendicular to the long axis of the fiber. Fig. 5.5 (right) shows the Q_1, Q_2, and Q_3-profiles plotted along the y-axis through the left of the two disclinations. Note that the left-right asymmetry of the profiles with respect to the defect position is caused solely by the presence of the polymer fiber. After passing through the disclination, the Q_1-component changes from its positive bulk value (≈ 0.6), coinciding with the value of the order parameter S, to some negative value (≈ -0.3). At the same time, the Q_2-component increases from a negative value (≈ -0.3) to a large positive value (≈ 0.6) that roughly equals twice the absolute value of the negative one. This behavior is attributed to the director rotation by approximately $\pi/2$ when one crosses the defect along the y axis (just recall that the orientation of the eigensystem changes continuously on passing through the defect). On the other hand, the value of the Q_3-component does not change too much, indicating that the variation in the nematic ordering mostly occurs in the xy-plane perpendicular to the fiber direction, $\mathbf{z}$.

Alternatively, Q_1, Q_2, and Q_3-profiles can be interpreted also in terms of order parameters S and P (see Fig. 5.5, right). When the defect line is approached, the uniaxial order parameter S decreases from its temperature-defined bulk value and drops even below zero in the defect center. Note that there the nematic director, i.e., the eigenvector corresponding to the negative eigenvalue, is directed along the fiber. On the other hand, the biaxiality — close to zero far enough from the defect — increases when the defect line is approached, reaches a maximum and, finally, in the very center of the defect, again drops to a value that is close to zero. The characteristic length scales for these variations are of the order of a few (≈ 5) lattice spacings a and agree with the estimates for the corresponding correlation lengths in the nematic phase.

Qualitatively, molecular ordering close to a disclination line can be summarized as follows. In the very center of the defect molecular ordering is uniaxial with $S < 0$ and $P \to 0$. Far enough from the defect line the nematic liquid crystal is uniaxial again, however, with $S > 0$ and $P = 0$, as expected in a homogeneous or in a weakly distorted bulk sample. In the intermediate ring-like region, nematic

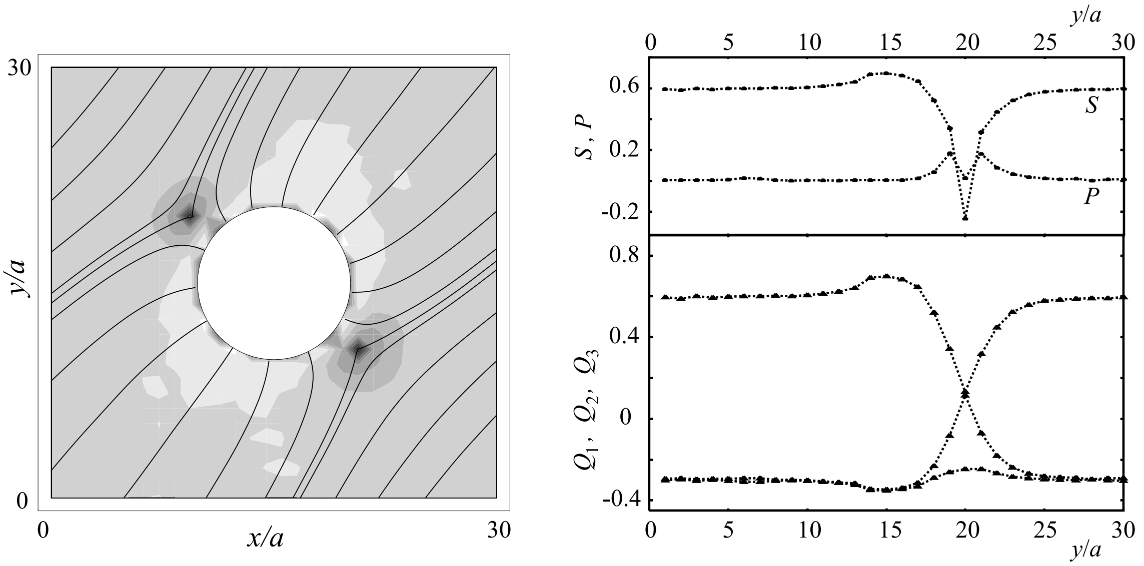

Figure 5.5 *Left:* cross section of the director field $\mathbf{n}(x, y)$ represented by "streamlines". The shading represents the value of the order parameter $S(x, y)$ (dark values correspond to a low S). A pair of $-\frac{1}{2}$ defects has formed on the diagonal. In the defect core molecules are (on the average) aligned in the xy-plane; ordering is uniaxial with $S < 0$ and the corresponding eigenvector, $\mathbf{n}$, is directed out-of-plane (along the z-axis). *Right:* eigenvalues of the ordering matrix Q_1, Q_2, and Q_3 plotted across the left defect along the y axis. In the upper panel the order parameter S and biaxiality P are plotted. The left-right asymmetry with respect to the defect core positioned at $y/a = 20$ is due to the presence of the fiber. While S exhibits a simple decrease if the defect is approached from any direction, P shows a more complex crater-like profile.

ordering is biaxial with $P \neq 0$. These conclusions agree also with results from alignment tensor-based phenomenological analyses of topological defects both of half-integer [104] and integer strength [105].

To conclude the discussion about defects, here are some final remarks related to their position. There are two parameters characterizing the position of each defect line: its distance from the fiber surface and the corresponding polar angle in the xy-plane. Increasing the system temperature from $T^* = 1.0$ to $T^* = 1.1$, the pair of defect lines moves away from the fiber, which increases the thickness of the deformed region where radial ordering is well-pronounced, as imposed by strong surface anchoring; see Figs. 5.6 (a) and (b). The increase of T^* results in an overall decrease of S and, consequently, in a decrease of the corresponding elastic constants (proportional to S^2). Moreover, when approaching the fiber surface, at higher T^* the increase in S is larger and occurs over a somewhat larger characteristic length ξ (2.11), which makes the defect formation and the accompanying elastic deformation in the immediate fiber vicinity rather unfavorable. Therefore, the defects are pushed away from the fiber surface when T^* is increased. On the other hand, at fixed T^* the defects move away from the fiber also as the fiber radius R is increased. In addition, for a given R the defect-to-fiber distance seems to be rather insensitive to changing the simulation box size. Indeed, for large R (i.e., for a low curvature of the fiber surface) the elastic deformation imposed by the defect is more compatible with the radial aligning tendency of the fiber if the defect is located far enough from the fiber surface. Finally, for the current system size the main mechanism for the formation of the defects close to the simulation box diagonal seems to be the repulsion between defects corresponding to adjacent fibers, as discussed above. Also this repulsion is mediated by curvature elasticity and weakens upon increasing temperature. The actual locus of defects is then determined by the subtle interplay between all the effects listed above. Note that for $T^* \lesssim 1$ the defect position becomes almost temperature-independent. Note also that the defect size increases with temperature, which qualitatively agrees with the increase of the characteristic length ξ on approaching the nematic-isotropic transition.

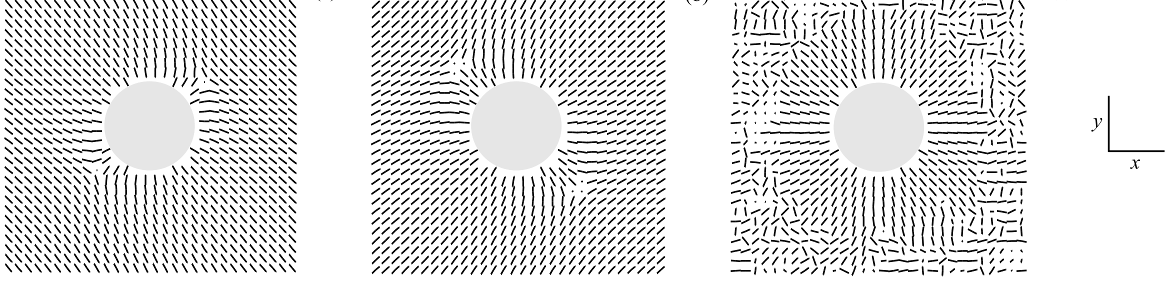

Figure 5.6 Director field for perfect homeotropic anchoring, xy-cross section. (a) $T^* = 1.0$, (b) $T^* = 1.1$ (both nematic), and (c) $T^* = 1.2$ (isotropic phase). In the nematic phase a pair of $-\frac{1}{2}$ defects has formed close to the diagonal.

Analogous conclusions as for planar anchoring can be drawn in the isotropic phase ($T^* = 1.2$) also for the homeotropic case, now inspecting the decays in $\langle P_2^c \rangle$ and S order parameters shown in Figs. 5.4 (b) and (d). Note that the two defect lines observed in the nematic phase for $T^* = 1.0$ and $T^* = 1.1$ have now vanished and that the residual surface-induced ordering is simply radial [Fig. 5.6 (c)]. This is because the current fiber-to-fiber distance exceeds 2ξ and hence the degree of ordering at the simulation box boundaries is already negligibly small. Consequently, no relevance should be attributed to the "randomly" distributed directors plotted in the outer cylindrical layers of the sample, Fig. 5.6 (c).

5.1.3 ^{2}H NMR spectra

The observations listed so far can be confirmed also by calculating ^{2}H NMR spectra using the numerical output from MC simulations. Fig. 5.7 shows the NMR spectra calculated for the $30 \times 30 \times 30$ particle sample and a single fiber ($R = 5a$) in the nematic (left, $T^* = 1.0$) and in the isotropic phase (right, $T^* = 1.2$), with the NMR spectrometer field applied along the fiber direction $\mathbf{z}$. The calculation was based on generating the relaxation function $G(t)$ (2.42) from the MC data and calculating its Fourier transform representing the spectrum, as described in detail in Sect. 2.3.1. Generating $G(t)$, effects of homogeneous translational diffusion were included. Following the methodology applied in Chapter 4 to PDLC droplets, the diffusive molecular motion was simulated by a random walk on the cubic lattice, performing 1024 diffusion steps per NMR cycle. The effective diffusion constant for such a random-walk process can be measured to be $D = 256a^2\delta\omega_Q/3\pi$, yielding a root-mean-square molecular displacement of $\sqrt{6Dt_0} = 32a$ in each NMR cycle. Here a stands for the particle-to-particle spacing on the cubic lattice, while $t_0 = 2\pi/\delta\omega_Q$ denotes the NMR cycle duration. Since this displacement is comparable to the sample size, the calculated NMR spectra are expected to be highly diffusion-averaged. Note that here a sufficient amount of MC data was available to update nematic particle configurations 1024 times per NMR cycle — thereby matching with the natural time scale t_F for fluctuations of molecular long axes — and not less frequently as in the PDLC case. For smoothening, a convolution of the spectra with a Lorentzian kernel of width $\approx 0.07\delta\omega_Q$ was performed. Finally, note that the NMR spectrometer magnetic field is assumed to be weak enough not to align nematic molecules, which, again, is the case only for strongly confined systems.

The calculated spectra are shown in Fig. 5.7, left. In the nematic phase with $T^* = 1.0$, for perfect planar anchoring ($\langle P_2 \rangle_g = 1$) in the spectrum one has two peaks positioned at $\omega_Q/\delta\omega_Q \approx \pm 0.6$. In the chosen geometry, $|\omega_Q/\delta\omega_Q|$ is supposed to be roughly equal to the value of S, the nematic order parameter, since the director and the direction of the NMR spectrometer magnetic field coincide. Indeed, for $T^* = 1.0$ one finds $S \approx 0.6$, as already seen above from various order parameter profiles. Translational diffusion in this case affects the spectra only negligibly: the nematic director is homogeneous throughout the sample and the degree of order is enhanced only slightly in the vicinity of the fiber. Therefore, the effect of diffusion should be merely a slight increase in quadrupolar splitting, but the resolution of the spectra is not high enough to clearly see this surface ordering-induced shift.

Proceeding now to fibers with partially disordered anchoring, in the spectra there is no noticeable change at least down to $\langle P_2\rangle_g \approx 0.25$, reflecting the ability of the polymer network to align the surrounding liquid crystal along $\mathbf{z}$. In the case when anchoring is completely disordered with $\langle P_2\rangle_g \approx 0$, the spectrum typically still consists of two peaks, however, the corresponding splitting can be arbitrary because there is no preferred direction in the system — note that only one example of the possible spectra is plotted. Note also that sometimes during the acquisition of the $G(t)$ signal slow collective molecular motion can occur, which results in an increase of the spectral line width. On the other hand, in homeotropic cases with $\langle P_2\rangle_g \lesssim 0$, molecular ordering is confined to the xy-plane. The quadrupolar splitting now decreases by 50% with respect to perfect planar anchoring because the director is perpendicular to the spectrometer field direction (see the two spectra in the bottom of Fig. 5.7, left).

In the bulk isotropic phase, however, quadrupolar interactions giving rise to the ω_Q splitting are averaged out by the rapid molecular motion. Therefore, ignoring translational diffusion, in a confined system for $S \approx 0$ one should expect a single-peaked spectrum at $\omega_Q \approx 0$, as already suggested above, and somewhat broadened

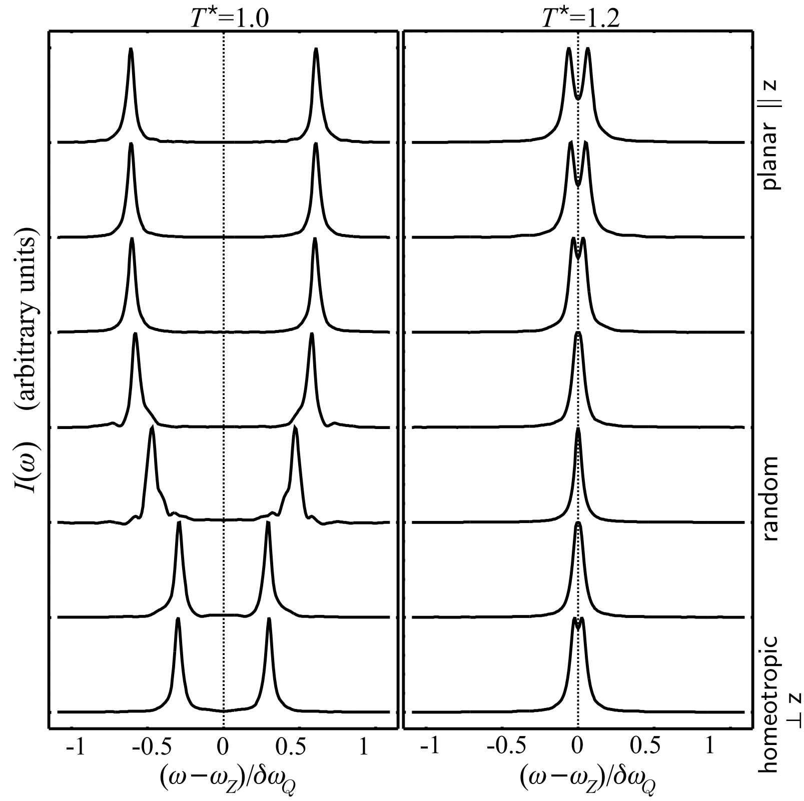

Figure 5.7 ^{2}H NMR spectra; $T^* = 1.0$ (*left*) and $T^* = 1.2$ (*right*). Top to bottom: spectra for $\langle P_2\rangle_g$=1.0 (planar), 0.75, 0.5, 0.25, 0 (random), -0.25, and -0.5 (homeotropic). The aligning capability of the network is lost only for $\langle P_2\rangle_g \approx 0$.

by the surface-induced order. The spectra shown in Fig. 5.7, right, were calculated with fast translational diffusion, and it is evident that some of them are actually double-peaked. This is a clear signature of surface-induced paranematic order. In fact, the peak-to-peak distance decreases with decreasing degree of surface order; compare with Figs. 5.2 (b) and 5.4 (d). For $\langle P_2 \rangle_g \approx 0$ exhibiting no surface order, the spectrum is again single-peaked. Finally, note that the splitting observed for perfect planar anchoring ($\langle P_2 \rangle_g = 1$) roughly amounts to twice the splitting seen in the perfectly homeotropic case ($\langle P_2 \rangle_g = -0.5$). This is again because the nematic director close to the fiber is parallel to the NMR spectrometer magnetic field in the first case and perpendicular to it in the second.

5.2 External field-induced switching

This Section is going to address the external field-induced switching of the molecular orientation in a nematic with dispersed polymer networks. First a regular array of straight and parallel polymer fibers will be treated, as in the preceding Section, here, however, exclusively with perfect planar anchoring. In this simple model system the stability of different director configurations in field presence will be analyzed in detail. Then we will proceed to more complex network topographies, first simulating irregularities in fiber positions (the fibers still taken as straight and parallel). After this, a sample with a full topographical complexity — a system of curved and potentially cross-linked fibers — will be treated. Also in these latter cases the fiber surface will be assumed smooth, with planar anchoring along the local (tangential) fiber direction. In the end, the switching process will be monitored by inspecting selected experimental observables predicted from the simulation output.

5.2.1 Regular fiber array

Now a regular array of parallel fibers (Figs. 5.1 and 5.8) will be considered. Again the fiber direction was taken along the z-axis and an external field was applied perpendicular to the fibers along the y-axis. Note that switching experiments are

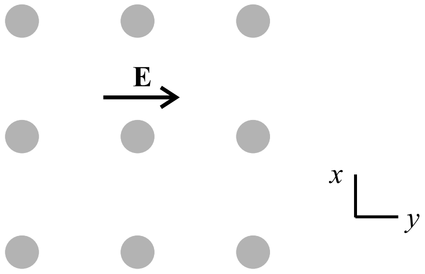

Figure 5.8 Regular fiber array: the switching geometry depicted schematically. Anchoring at fiber surfaces is planar along the fiber direction, $\mathbf{z}$, while the external field $\mathbf{E}$ is applied along $\mathbf{y} \perp \mathbf{z}$.

usually performed in an external electric field and that in an inhomogeneous dielectric (as encountered here) the electric field is not constant and homogeneous throughout the sample. In such situations, Maxwell equations are to be solved in order to obtain the local electric field strength vector $\mathbf{E}$. For simplicity, however, in the following $\mathbf{E}$ will be assumed homogeneous. Alternatively, one could perform a switching experiment also in an external magnetic field where the inhomogeneities of the corresponding susceptibility are weaker and the above homogeneity assumption for the external field is more plausible. As discussed in Sect. 2.1.5, the switching threshold is sensitive to changes in the surface anchoring strength. Therefore, here cases with different anchoring strengths will be examined, with a dimensionless anchoring strength defined as $w = \epsilon_g/\epsilon$. Here ϵ_g denotes the nematic-ghost coupling strength and ϵ the nematic-nematic one; see Eq. (2.29).

Before investigating external field-driven orientational transitions in the fiber array model system, it is instructive to draw a rough analogy with a nematic slab (compare also with Sect. 2.1.5). Let the slab of thickness d be confined between two parallel plates imposing strong planar anchoring along the z-axis, and let there be an external field $\mathbf{E}$ applied along the slab normal (y-axis). In a weak external field the equilibrium director profile ($\mathbf{n}$) is homogeneous with $\mathbf{n} \perp \mathbf{E}$ ("h-structure"). Increasing the field strength, at first the director profile does not change, but once the Fréedericksz threshold $E_F^0 = \sqrt{K/\epsilon_0\epsilon_a S}(\pi/d)$ is reached, a transition to a deformed structure is observed ("d-structure"). Here K denotes the effective Frank elastic constant and $\epsilon_a S$ the macroscopic anisotropy of the dielectric constant. For finite anchoring strengths W the Fréedericksz threshold E_F is reduced, satisfying the relation $\pi(K/Wd)(E_F/E_F^0) = \cot[(\pi/2)(E_F/E_F^0)]$ [115]. Increasing the field strength E even further, for finite W the orienting effect of the field overwhelms the anchoring and a second, saturation transition takes place. Above this second threshold E_s nematic molecules are aligned uniformly along the field, with $\mathbf{n}||\mathbf{E}$ ("s-structure"). Here E_s can be found from $\pi(K/Wd)(E_s/E_F^0) = \coth[(\pi/2)(E_s/E_F^0)]$ [115]. Note that in case of weak anchoring or in a very thin nematic slab with $K/W \gg d$, the thresholds E_F and E_s attain similar values, indicating that the region of stability for the deformed d-structure becomes extremely narrow. This can be inferred also from the phase diagram derived numerically for the h, d, and s structures in Ref. [115].

A similar switching behavior can be observed also in a regular array of polymer fibers favoring planar anchoring along $\mathbf{z}$, the fiber direction, if the field $\mathbf{E}$ is applied, e.g., along $\mathbf{y}$, as shown in Fig. 5.8. For comparison, yz-cross sections of director profiles calculated for each of the three structure types are shown in Fig. 5.9. It is interesting to notice that for the d-structure the nematic is bent in the yz-plane, while it is twisted in the xz-plane, as opposed to the slab case where the twist deformation is absent. Consequently, the transition threshold values may differ from those estimated for the slab geometry. Qualitatively, the switching behavior is also expected not to change if the field is applied in some direction other than $\mathbf{y}$, but still within the xy-plane so that $\mathbf{E} \perp \mathbf{z}$ is fulfilled. The specific in-plane orientation of $\mathbf{E}$ may, however, still affect the switching threshold position.

In the MC simulation, the sample size was again set to $30a \times 30a \times 30a$ and the fiber radius to $R = 5a$. All simulations were be performed at $T^* = 1.0$, deep in the

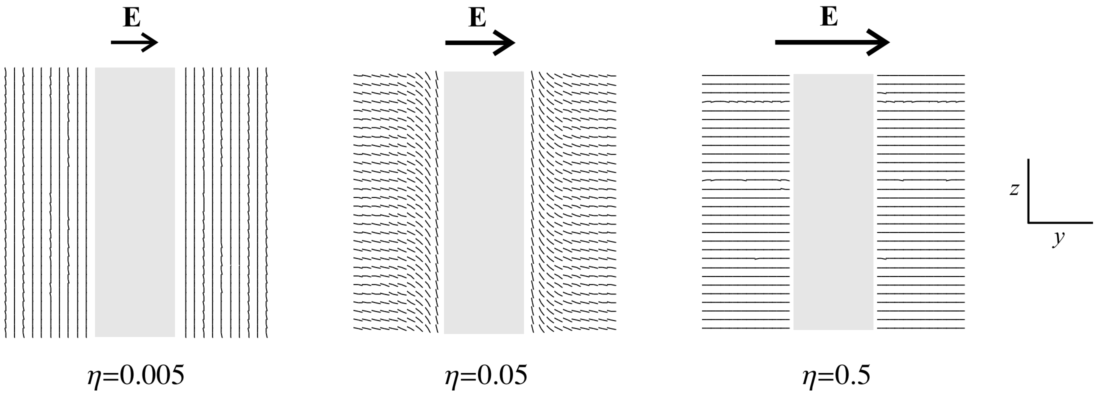

Figure 5.9 Switching in a regular fiber array: examples of director fields for different $\eta \propto E^2$; $T^* = 1.0$, $R = 5a$, and $w = 1$ (yz-cross sections through the fiber center). From left to right: homogeneous (h), deformed (d), and saturated (s) structure. Anchoring easy axis is planar and $||\mathbf{z}$, while the external field $\mathbf{E}$ is directed along $\mathbf{y}$.

nematic phase. To reliably estimate the field thresholds for the Fréedericksz and saturation transitions from the MC simulation, for a given anchoring strength w external field strength scans were performed as follows. The first run was performed at $\eta = 0$ in absence of an external field. Then the external field strength $\sqrt{\eta}$ was increased stepwise: at each stage, the last molecular configuration from the previous simulation run was used as input for the next run performed at somewhat higher η, and so on until the maximum field strength was reached. Then the field strength was decreased stepwise (following the same strategy as upon increase) so as to detect a possible hysteresis in the simulated switching process. In the vicinity of structural transitions, orientational fluctuations in the system can increase significantly. Therefore, equilibration runs somewhat longer than in preceding simulations were needed to produce reliable results: approximately 1.2×10^5 cycles for equilibration and further 1.2×10^5 cycles for average production.

Transitions between the three director structure types can conveniently be monitored by plotting the radial dependence of a suitable order parameter defined as $P_2^y(r) = \langle \frac{1}{2}[3(\mathbf{u}_i \cdot \mathbf{y})^2 - 1] \rangle_r$, where the brackets $\langle ... \rangle_r$ represent an average over MC cycles and over nematic particles lying within a cylindrical layer centered at radius r. Moreover, $\mathbf{y}$ is a unit vector along the external field direction. In case of perfect nematic alignment along $\mathbf{y}$ one has $P_2^y = 1$, while for perfect alignment perpendicular to $\mathbf{y}$ (e.g., along $\mathbf{z}$) $P_2^y = -\frac{1}{2}$ is obtained. For non-perfect alignment at finite temperature with $S < 1$ the above values reduce to $P_2^y \to S$ and $P_2^y \to -\frac{1}{2}S$ for alignment along $\mathbf{y}$ and $\mathbf{z}$, respectively.

The $P_2^y(r)$-profiles for strong ($w = 1$) and weak ($w = 0.1$) anchoring and different field strengths ($\propto \sqrt{\eta}$) are reported in Fig. 5.10. The corresponding anchoring extrapolation lengths can be estimated to be the order of $\approx a$ for $w = 1$ and $\approx 10\,a$ for $w = 0.1$, which is still below the fiber-to-fiber distance $d_{eff} \approx 20\,a$. For strong anchoring ($w = 1$, Fig. 5.10, left) at low η the homogeneous h-structure with $\mathbf{n} \perp \mathbf{y}$ is found and, consequently, $P_2^y(r)$ is negative and almost constant. The slight variation in $P_2^y(r)$ close to the fiber originates from an enhancement in the degree of ordering (S) close to the fiber, as discussed in Sect. 5.1.1. Above the first (Fréedericksz) threshold at $\eta_F = 0.0085 \pm 0.0015$, P_2^y is negative close to the fiber, while it is positive far enough from it. Such behavior is a signature of the deformed d-structure where close to the fiber the alignment is governed by anchoring, while far enough in the bulk it is governed by the external field. The characteristic distortion length — closely related to the external field coherence length ξ_e — can be deduced directly from the $P_2^y(r)$ dependences. After a further increase of η beyond $\eta_s = 0.30 \pm 0.015$ the second threshold is reached and P_2^y becomes positive for all r, which indicates that now the homogeneous saturated s-structure is stable. The variation of P_2^y in the vicinity of the fiber can be ascribed to a reduction of S with respect to its bulk value, occurring due to the conflicting alignment tendencies of the fiber and of the external field.

Decreasing the anchoring strength ($w = 0.1$, Fig. 5.10, right), one can readily identify homogeneous h and s-structures, while the deformed d-structure seems to be missing. This is in agreement with the narrowness of the stability region for the d-structure predicted in the nematic slab [115]. The Fréedericksz and the saturation threshold can be estimated to lie within the interval $\eta = 0.0034 \pm 0.008$. Note that now the variations of P_2^y close to the fiber for all η indicate a decrease of S in this region, which is a consequence of having weaker nematic-fiber than nematic-nematic interactions.

Having found three possible director structures (h, d, and s) for $w = 0.1$ and $w = 1$, it is interesting to explore their stability in an external field also at intermediate anchoring strengths and summarize the results in a structural phase diagram. However, the determination of threshold fields (both for the Fréedericksz and the saturation transition) is a rather delicate task. In fact, the recognition of different

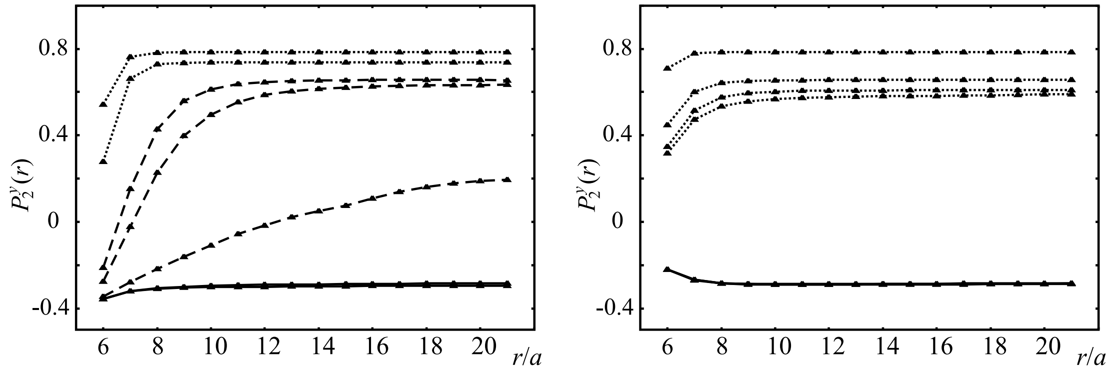

Figure 5.10 Regular fiber array: $P_2^y(r)$-profiles calculated for $T^* = 1.0$, $R/a = 5$, planar anchoring $||\mathbf{z}$, and an external field $||\mathbf{y}$. *Left:* $w = 1$; top to bottom: $\eta = 1$, 0.5, 0.1, 0.05, 0.01, 0.005, and 0.001. *Right:* $w = 0.1$; top to bottom: $\eta = 1$, 0.1, 0.01, 0.005, 0.001, 0.0005, and 0.0001. Solid, dashed, and dotted lines represent h, d, and s-structures, respectively. For $w = 0.1$ it is almost impossible to find the d-structure.

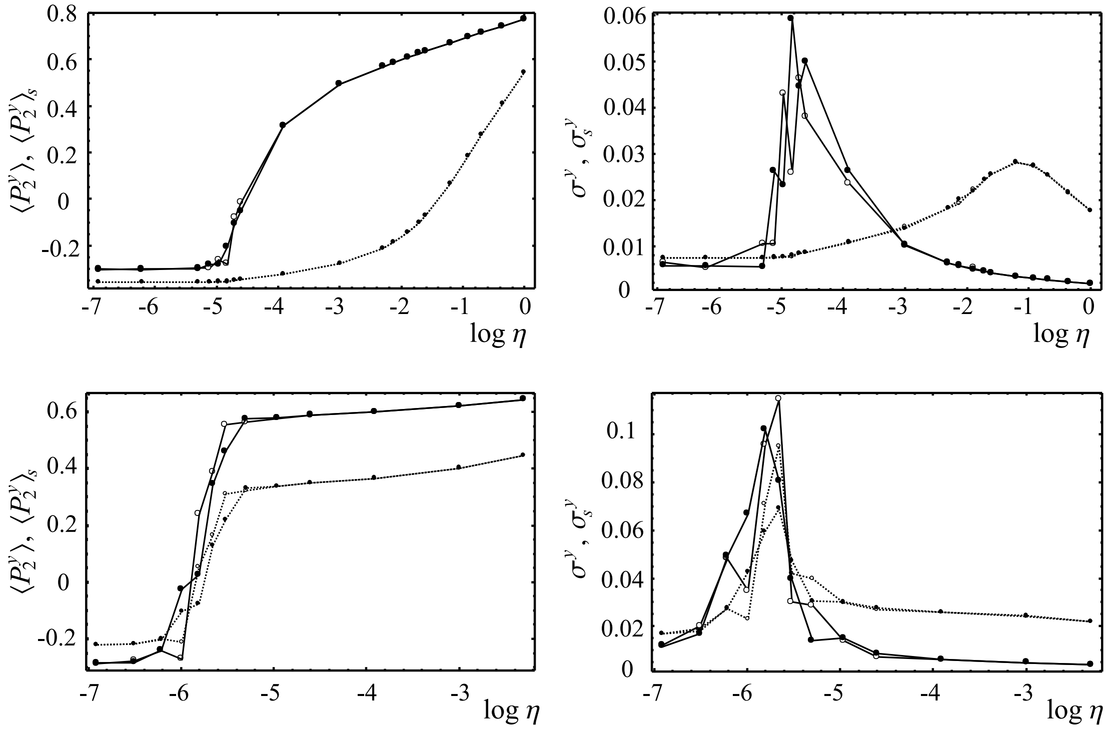

Figure 5.11 Order parameters $\langle P_2^y \rangle$ (solid line) and $\langle P_2^y \rangle_s$ (dotted line), plus the corresponding variances σ^y and σ_s^y. *Top:* $w = 1$, *bottom:* $w = 0.1$. Closed circles correspond to scans upon increasing η, the open ones to scans upon decreasing. Fréedericksz and saturation thresholds can be deduced from the positions of the σ^y and σ_s^y peaks, respectively. For $w = 0.1$ both transitions virtually overlap.

structure types from snapshots or director fields turns out to be highly unreliable and subject to human eye-generated bias. Therefore, one can tackle this problem exclusively by finding a more quantitative criterion for structure identification. Having applied an external field along the y-axis, an appropriate order parameter for monitoring is the overall $\langle P_2^y \rangle$, where the averaging $\langle ... \rangle$ must be performed over all particles and MC cycles. This order parameter is suitable for the detection of the Fréedericksz transition involving a significant portion of nematic particles. The saturation transition, however, is expected not to reflect that well in the overall $\langle P_2^y \rangle$ because it only affects a thin surface layer of particles. At this point one can conveniently define $\langle P_2^y \rangle_s$, calculated exclusively for particles in the surface layer of thickness a. This "surface" order parameter is sufficiently sensitive to particle reorientations that actually contribute to the saturation transition. Furthermore, the sudden rise either of $\langle P_2^y \rangle$ or $\langle P_2^y \rangle_s$ is accompanied by a significant increase of fluctuations of these order parameters. Then the corresponding variances of $\langle P_2^y \rangle$ and $\langle P_2^y \rangle_s$, σ^y and σ_s^y, can also be used to spot the field strength threshold for both transitions. This is equivalent to studying the NI transition by monitoring fluctuations of the internal energy where the corresponding variance is proportional to the heat capacity [123].

For $w = 0.1$ and $w = 1$ the behavior of $\langle P_2^y \rangle$ and $\langle P_2^y \rangle_s$ upon increasing field strength, along with their variances, is shown in Fig. 5.11. Note that the reproducibility of the data points is good (comparing scans up and down in field strength), yet it is somewhat poorer in the $w = 0.1$ case where the surface anchoring is much weaker than for $w = 1$. The fact that there is no obvious hysteresis suggests that both the Fréedericksz and the saturation structural transitions are second-order (hence continuous), in agreement with phenomenological studies.

After identifying both thresholds also for anchoring strength values other than $w = 1$ and $w = 0.1$, a stability phase diagram can be plotted. For $T^* = 1.0$ and $R = 5a$ it is shown in Fig. 5.12, together with the equivalent phase diagram for a nematic slab, derived in Ref. [115]. In weak enough fields one can always find the h-structure, while in strong enough fields the s-structure is always seen. The d-structure appears at intermediate field strengths, but its stability region gets narrower with decreasing w. As shown in Ref. [115] for the case of a nematic slab, the h-d and d-s coexistence lines do not merge upon decreasing the anchoring strength and there is no triple point where all three structures would coexist. Due to a finite accuracy in field threshold estimates, in the present stability analysis the Fréedericksz and saturation transitions below a certain anchoring strength ($w \approx 0.1$) coalesce and cannot be distinguished any more. This, however, should not be regarded as an indication for the existence of the triple point. Note that the qualitative agreement with results presented in Ref. [115] is rather good. Further note that here only results for a single temperature value, $T^* = 1.0$, are presented. The position of the coexistence lines in Fig. 5.12 may shift with changing T^*, the temperature dependence entering the field threshold values via the elastic constant K and the anchoring extrapolation length K/W.

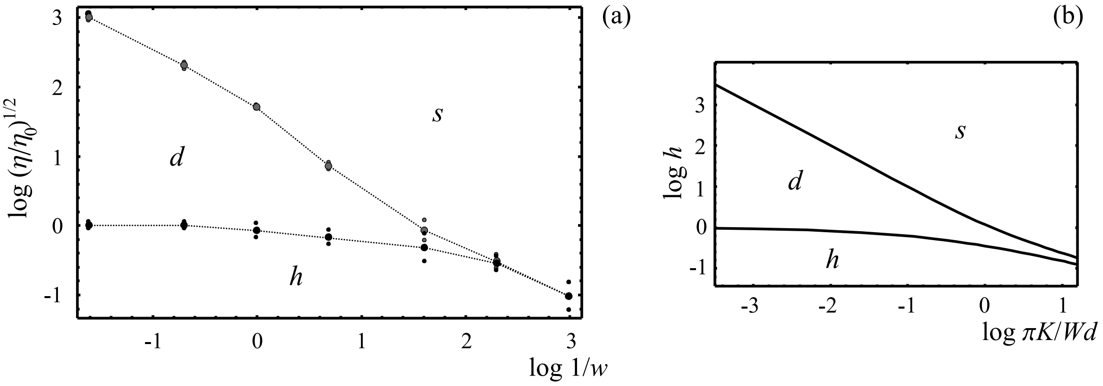

Figure 5.12 (a) Structural phase diagram $\log \sqrt{\eta/\eta_0}$ vs. $\log 1/w$ calculated for $T^* = 1.0$ and $R/a = 5$; η_0 corresponds to the Fréedericksz threshold at the strongest anchoring considered, $w = 5$. (b) Phase diagram for a nematic slab (from Ref. [115]) plotted in scales and ranges allowing for a comparison with (a). h denotes field strength values normalized with respect to the Fréedericksz threshold found for infinite anchoring.

Moreover, the position of the h-d coexistence line corresponding to the Fréedericksz transition is expected to depend on the effective fiber-to-fiber distance d_{eff}

(determined also by the polymer concentration in the sample): with decreasing d_{eff} at fixed w and T^* the line is expected to move towards higher critical field strengths. In other words, the nematic in fiber-rich samples is more difficult to switch. On the other hand, the d-s saturation transition line is expected not to shift significantly. To check these statements, one can explore transitions in a network consisting of, e.g., somewhat thinner fibers. Setting $R/a = 3$ (instead of $R/a = 5$ above) and considering a $18 \times 18 \times 18$ sample with a single fiber (instead of the $30 \times 30 \times 30$ one) roughly maintains the polymer concentration, but decreases the fiber-to-fiber distance. For the thresholds at $w = 1$ one now finds $\eta_F^{18} = 0.027 \pm 0.003$ and $\eta_s^{18} = 0.30 \pm 0.03$, which for both lines is in agreement with the behavior predicted above (just recall the corresponding thresholds for the larger $30 \times 30 \times 30$ sample: $\eta_F^{30} = 0.0085 \pm 0.0015$ and $\eta_s^{30} = 0.30 \pm 0.015$). Note that like in slab geometry (and for strong enough anchoring) the Fréedericksz threshold field strength scales approximately as $1/d_{eff}$, if d_{eff} is taken to be the shortest fiber-to-fiber distance. In fact, comparing d_{eff} for the $18\times18\times18$ and $30\times30\times30$ sample gives $d_{eff}^{18}/d_{eff}^{30} = 0.6$, while the ratio of threshold field strengths yields $(\eta_F^{30}/\eta_F^{18})^{1/2} = 0.56$. On the other hand, the saturation transition threshold remains almost unaltered.

All in all, the switching behavior in a regular fiber array system seems to be very close to that of a simple nematic slab although in the fiber array system the elastic deformation is somewhat different (twist and bend deformation combined). The latter, however, poses no problems because the LL model anyway is equivalent to the one-constant approximation. The difference in the type of geometrical confinement reflects at most in different quantitative behavior.

5.2.2 Irregular fiber array

The actual topology of a polymer network shown in typical SEM pictures [26,39] (Fig. 1.3) is much more complex than the regular array of straight and parallel fibers considered so far. In particular, the effective interfiber distance distribution is expected to play an important role in switching studies. Therefore, as a first step towards a more complex network topography an irregular array of straight fibers will be studied, increasing the lattice size to $50 \times 50 \times 50$ particles and including 8 fibers of equal thickness, with $R = 3a$. The fibers were modeled as straight and parallel (oriented along the z-axis), but distributed randomly within the xy-plane. The polymer concentration and the fiber radii were kept unchanged in comparison to the previous $18 \times 18 \times 18$ case. This should provide the same average fiber-to-fiber distance and thus facilitate the comparison of results. Again, the external field was applied along the y-axis and the surface anchoring was assumed planar (with $w = 1$) along the z-axis. The concentration of the polymer can be estimated by dividing the number of frozen (ghost) particles by the number of all particles, yielding approximately 9% polymer. In the following, the regular array sample (previous Section) will be referred to as "sample A", while the sample with the fiber position irregularity as "sample B". Moreover, "sample C" containing curved fibers will be considered later in this Section. Simulation runs involving samples of B and C-type consisted of 8×10^4 equilibration and 6.6×10^4 production cycles, while for

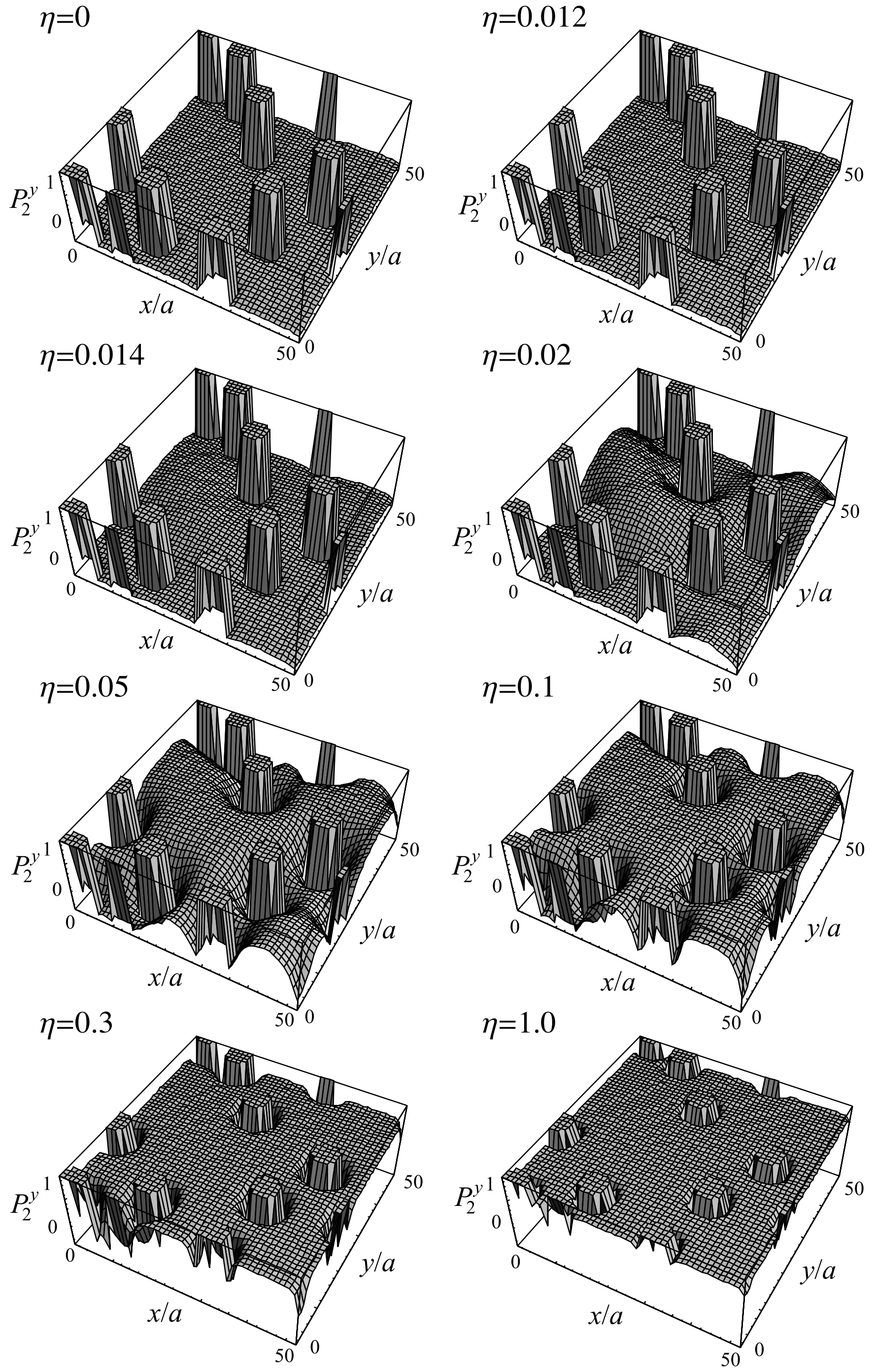

Figure 5.13 Array of several (8) straight fibers (sample B): $P_2^y(\mathbf{r}_i)$ order parameter map (xy cross section) for different η. The switching process starts approximately at $\eta_B = 0.013$. The "columns" represent parallel straight polymer fibers. Calculated for $T^* = 1.0$, $w = 1$, and $R/a = 3$.

the smaller A-type sample the equilibration was shortened to 6×10^4 cycles.

Fig. 5.13 shows the evolution of P_2^y averaged over MC cycles for every particle within a given xy-cross section for sample B. For $\eta \lesssim 0.012$ one has $P_2^y(\mathbf{r}_i) \approx -0.3$

constant and negative, showing that particles are still aligned along $\mathbf{z}$ (recall that at $T^* = 1.0$ one has $S \approx 0.6$) and that the Fréedericksz threshold has not been reached yet. Reaching, however, $\eta = 0.014$, in regions where the fiber density is below average (the interfiber distance above average), the particles start to reorient along the field direction and P_2^y increases, becoming even positive in some areas upon a further increase in η. It is important to notice that now the Fréedericksz threshold is significantly lower than in the regular array case with the same polymer concentration — sample A. This can be attributed to the fact that the external field always destabilizes the longest-wavelength distortion first. Then, unlike in sample A, in the irregular sample B there is a distribution of effective fiber-to-fiber distances, allowing also for deformations whose wavelength is larger than the average interfiber distance. As the field strength is increased even further, the parallel-to-fiber alignment persists only in the very vicinity of fibers and P_2^y becomes positive almost everywhere. Finally, for extremely strong fields the saturation threshold is reached as well, and then all molecules are aligned along the external field direction. In addition, the strong field enhances the degree of nematic order [117]. Note also that in extremely strong fields close to each fiber there is a decrease of P_2^y that can be attributed to a decrease in S. Indeed, in the vicinity of each fiber there is a conflict between the strong aligning tendencies of anchoring and of the external field.

Note that the switching of the molecular orientation has not occurred in all parts of the sample simultaneously. Indeed, very strong fields are required to switch the particle orientation, e.g., between two (or more) fibers positioned close to each other (see Fig. 5.13, for $\eta \lesssim 0.3$, in the left corner). Consequently, the Fréedericksz transition is not as sudden as in a regular array-system. The saturation transition, on the other hand, is driven merely by a competition between surface anchoring and the external field. Therefore, wherever the fiber density is not too high, the positional irregularity of the network is expected not to affect the saturation transition very significantly.

The last step in modeling the polymer network topography consisted of dropping the assumption that the fibers be straight and parallel and considering a system of curved fibers instead. Again, the general (average) fiber direction was taken along the z-axis. Then each of the fibers (whose thickness was assumed constant along z) was generated by performing a biased random walk: while progressing along the z-direction, random deviations from this direction within the xy-plane were performed with a given probability regulating the curvedness of the fiber. Doing this, care was taken to meet the periodic boundary conditions along the z-axis. Following such a procedure, at high enough polymer concentrations the neighboring fibers can meet and cross-link, thereby providing a complexity in the network topography that is already close to that present in a real sample (Fig. 1.3). The surface anchoring was assumed planar, here, however, along the local fiber direction (yet not necessarily matching with the z-direction) with $w = 1$. The fiber network used in switching simulations presented here — also referred to as "sample C" — is shown in Fig. 5.14. Because the orientations of ghost particles everywhere agree with the local fiber directions, the ghost order parameter $\langle P_2 \rangle_g$ introduced in Sect. 5.1 can be used also

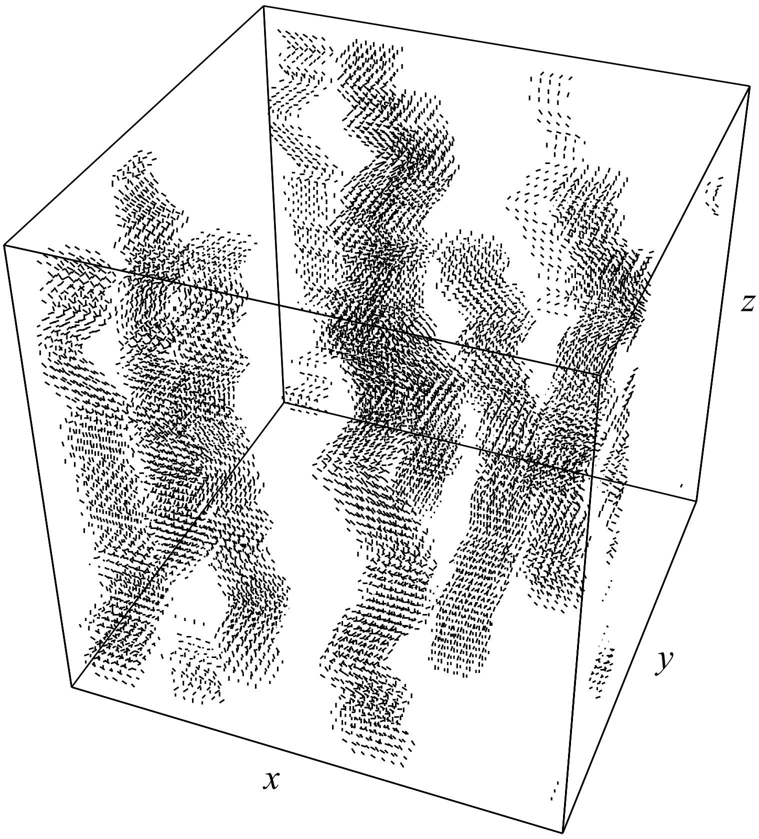

Figure 5.14 Array of several curved fibers (sample C): ghost particles representing the fixed polymer fiber network; $\langle P_2 \rangle_g \approx 0.28$.

to characterize the curvedness of the fiber system. For sample C shown in Fig. 5.14 $\langle P_2 \rangle_g \approx 0.28$.

The switching process was simulated also for the sample C. Fig. 5.15 shows director field yz-cross sections for different η. Despite fiber curvature, in absence of external fields ($\eta = 0$) the net molecular orientation seems to be still well-defined (along the average fiber direction, z-axis), except for the fiber vicinity where it is affected by the local anchoring easy axis. In Fréedericksz geometry where the magnetic field is strictly perpendicular to the easy axis (samples A and B), the orientational transition happens abruptly at a well-defined threshold. Here, however, due to network irregularity, the magnetic field and the anchoring easy axis are never perpendicular to each other, therefore — unlike in Fréedericksz geometry — a magnetic torque acts on nematic particles already at arbitrarily low field strengths. As we shall see later, this results in a decrease of the field threshold value in comparison to more regular samples A and B, while the switching itself is still relatively sudden.

At the same time it should be borne in mind that the sample C studied here covers length scales still far below the macroscopic ones. The linear dimension of the sample box $50a$ ranges from 50 nm to 250 nm, depending on which value of a is taken into account (1 nm $\lesssim a \lesssim$ 5 nm). As a consequence, the detailed switching behavior depends sensitively on the specific irregularities of the network generated

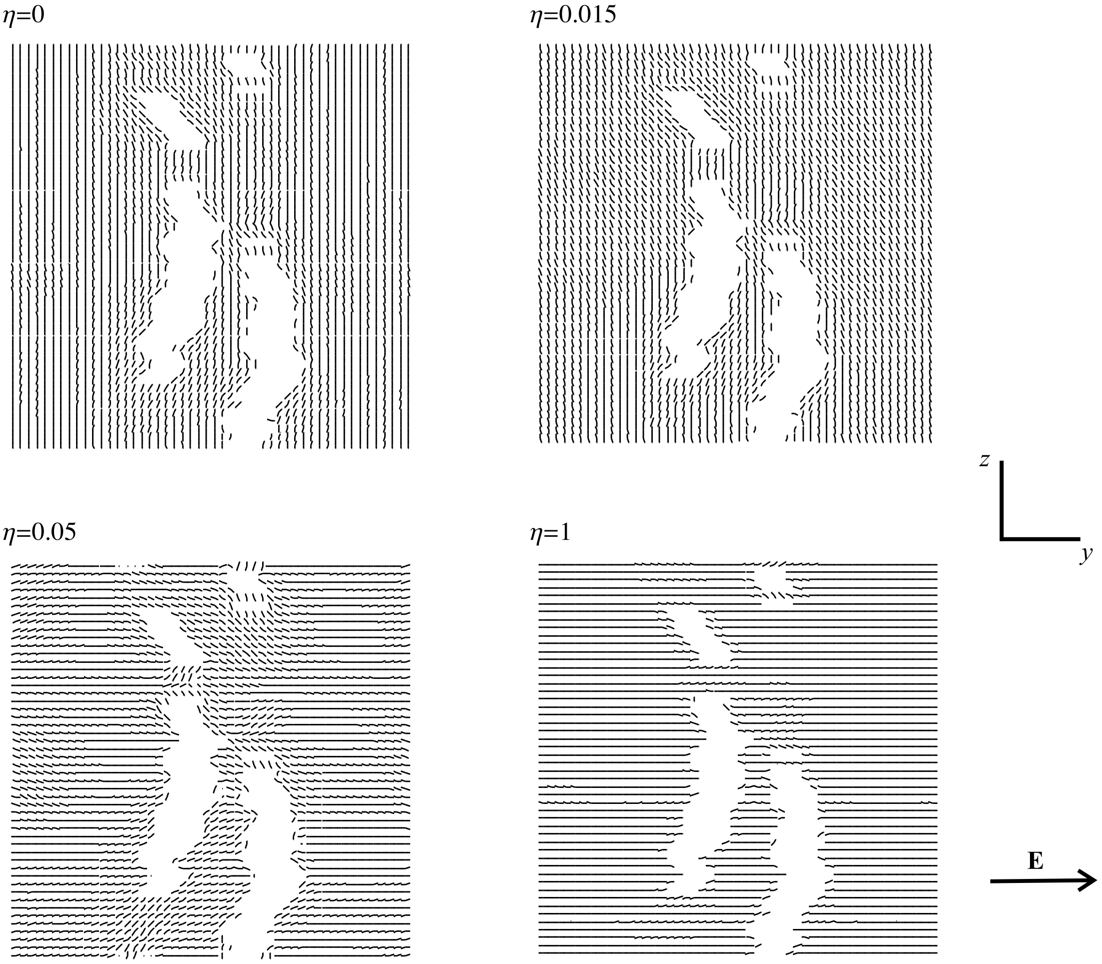

Figure 5.15 Sample C: yz-cross sections of the director field map at $x/a = 39$ for different η. Note that in absence of the field $\eta = 0$ most molecules are aligned along z (the average fiber orientation), except for those close enough to fibers where they align along local fiber orientations. Applying an external field ($\eta \neq 0$), the major particle reorientation is initiated at $\eta_C \approx 0.010$.

for sample C. To provide more general results, either a much larger sample should be considered, or a set of smaller samples, yet with different network topographies. Finally, in any symmetry-lacking sample it is less instructive to show order parameter or director map cross sections because they may not provide the information on the general behavior such complex systems. On the contrary, it is much more relevant to explore simulation-predicted experimental observables, which will be done in the next Section. A detailed comparison of samples A, B, and C will be given as well.

5.2.3 Experimental observables and network irregularity

This Section will be devoted to the analysis of experimental observables (electric capacitance, intensity of transmitted polarized light, and ^{2}H NMR spectra). As these methods all monitor the bulk response of the system, they are suitable for monitoring the Fréedericksz transition. For the same reason, they are rather insensitive to the saturation transition, affecting a relatively small number of molecules in a thin subsurface layer.

The Fréedericksz transition can be spotted most easily by performing an electric capacitance measurement, as described in Sect. 2.3.2. In the simulation, the experiment was set up as follows. The net fiber direction was chosen along z and, as above, the external field was applied along y. Then, following Eq. (2.45), normalized capacitance C_y was measured along the y direction to monitor the switching process. Below the Fréedericksz threshold, in a nematic aligned perfectly along z ($S = 1$) one would expect to have $C_y/\epsilon_0 = \epsilon'_\perp$, while for a perfect alignment along the external field (far beyond the saturation threshold) one should expect $C_y/\epsilon_0 = \epsilon'_{||}$ ($\epsilon'_\perp$ and $\epsilon'_{||}$ standing for the eigenvalues of the molecular dielectric tensor). On the other hand, for imperfect (but homogeneous) nematic alignment at finite temperatures with $S < 1$, one has $C_y/\epsilon_0 = \frac{1}{3}(1-S)\epsilon'_{||} + \frac{1}{3}(2+S)\epsilon'_\perp > \epsilon'_\perp$ for alignment along z and $C_y/\epsilon_0 = \frac{1}{3}(1+2S)\epsilon'_{||} + \frac{2}{3}(1-S)\epsilon'_\perp < \epsilon'_{||}$ for alignment along y, as it follows from (2.7). Here $\epsilon'_{||} > \epsilon'_\perp$ has been assumed. Therefore, the measured capacitance depends both on the orientation of the nematic director and on the degree of nematic ordering given by S. Consequently, in sample geometry chosen here, the capacitance C_y is expected to exhibit a more or less sudden increase whenever a major reorientation of nematic molecules takes place in the sample.

Fig. 5.16 shows the capacitance versus η (the field strength squared) for samples A, B, and C in a semi-logarithmic scale. Recall that all three samples are characterized by different network topographies, yet having roughly the same polymer concentration. Like in experiments with a dielectrically highly anisotropic nematic reported in Ref. [39], $\epsilon'_{||} = 29.8$ and $\epsilon'_\perp = 6.1$ were chosen in the simulation. Following Ref. [39], for simplicity same values of $\epsilon'_{||}$ and $\epsilon'_\perp$ were assumed also for the polymer network. Inspecting now Fig. 5.16, one can observe that the switching threshold is lowest in the irregular sample C and highest in the regular sample A: $\eta_A = 0.022 \pm 0.01$, $\eta_B = 0.013 \pm 0.01$, and $\eta_C = 0.010 \pm 0.01$. Again, η_B is lower than η_A because in sample B there is a distribution of interfiber distances. Moreover, η_C is lower than η_B because the absence of perpendicularity between fibers and the external field direction allows for a field torque to act on molecules already at arbitrarily low field strengths.

The second feature of curves depicted in Fig. 5.16 is their slope after exceeding the switching threshold. The curve corresponding to sample A is steeper than that of sample B because — as already seen — in the latter case the switching is a gradual process and in the high-fiber-density areas molecules refuse to switch unless the field is very strong. On the other hand, the curve pertaining to sample C is steeper than the curve B (and approximately as steep as that of the regular sample A), which is because now even molecules in the polymer-rich areas are not able to resist switching since the corresponding fibers are not perpendicular to the external field. Note also that in curve C there are jumps that may be attributed to the irregularities in the fiber network. In a macroscopic sample these would have been averaged out, yielding smooth capacitance curves comparable to those measured in

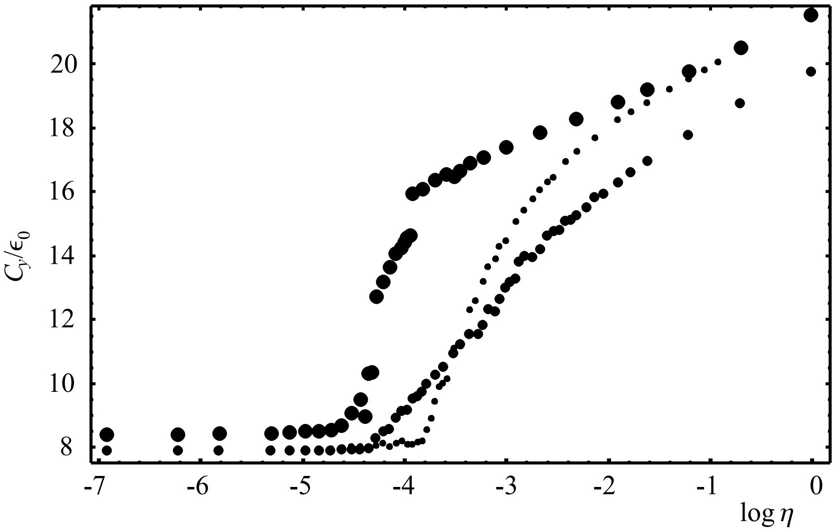

Figure 5.16 External field-induced switching as monitored by capacitance (C_y) measurements: sample A (small dots), sample B (medium dots), and sample C (large dots). For explanations regarding the sample topographies see text.

Ref. [39] experimentally.

The third feature of capacitance curves is the pre-threshold value of C_y. In fact, curves A and B in this region almost overlap, which is mainly because of the well-defined molecular alignment along z. For $\eta = 0$ in sample C the overall molecular alignment still matches with z, especially far enough from the fibers, but this is not quite true in the fiber vicinity (see the snapshots in Fig. 5.15). This is also why already below the threshold there are significant local deviations from z, resulting in an enhancement of C_y, if compared to the A and B cases.

Finally, note that for all samples at extremely high field strengths (above the saturation transition) the increase of C_y is attributed to an increase in the degree of nematic order (S) rather than to molecular reorientation. Further, as discussed in Sect. 4.2.1, the external fields applied in simulations to the rather small samples are typically unrealistically strong.

Another convenient method for the determination of the Fréedericksz threshold are the measurements of the intensity of polarized light transmitted through the sample (Sect. 2.3.3). The experimental set-up considered here is identical to that described at the end of Sect. 2.3.3. Let again the average fiber direction coincide with the z-axis and let the external field be applied along the y-axis, with the light beam also propagating in this direction. In a nematic slab with planar anchoring along z (and with no polymer networks) there is no x or z-dependence in the director field. The intensity of light transmitted through such a sample (if put between two polarizers crossed at a right angle) is given by the formula (2.48). As already mentioned in Sect. 2.3.3, the output signal is maximized when the angle between the projection of the director onto the xz-plane and the incident light polarization plane is equal to $\varphi_0 = \pi/4$. Having fixed φ_0, the output signal I depends only on the birefringence $\Delta\Phi = (2\pi/\lambda)\int_0^d [n_e(z) - n_o]dz$, i.e., $I \propto \sin^2(\Delta\Phi/2)$. This implies that below the Fréedericksz threshold I will be a constant depending on the sample thickness d and on the effective refractive indices of the nematic. Exceeding the threshold, the director reorients, which is accompanied by a change in the extraordinary index n_e [see Eq. (2.46)]. Consequently, $\Delta\Phi$ changes continuously as the director field deforms and, accordingly, the output signal $I \propto \sin^2(\Delta\Phi/2)$ oscillates. The total number of oscillations seen upon increasing the field strength ($\propto \sqrt{\eta}$) can be estimated by comparing $\Delta\Phi$ for the homogeneous alignment along z ($\Delta\Phi_z$) with that for the alignment along the external field ($\Delta\Phi_y$). In the latter case, $n_o \approx n_e$ because the optical axis ($\mathbf{n}$) matches with the light beam direction, yielding $\Delta\Phi_y \approx 0$. In the former case, however, the refractive index difference is nonzero and is, for nematics with weak optical anisotropy, proportional to the degree of order S [4]. Then, $\Delta\Phi_z/2\pi \approx \Delta n^0 Sd/\lambda$ is the approximate number of oscillations observed in the $I(\eta)$ graph, where Δn^0 stands for the maximum difference $n_e^0 - n_o^0$ in a perfectly ordered nematic (the superscript "0" referring to perfect nematic ordering with $S = 1$). From such a graph, the Fréedericksz threshold can be estimated by identifying the point where the $I(\eta)$ curve begins to oscillate (as, e.g., in Ref. [116]).

Turning now to a sample with dispersed polymer networks, the switching behavior is similar to that of a nematic slab, as seen in Sect. 5.2.1. In the simulation, the net fiber direction was chosen along z, while all other geometrical parameters were chosen as described in the previous paragraph, including the incoming light polarization plane fixed at $\varphi_0 = \pi/4$. The sample thickness in this optical part of the simulation was set to 10μm. This can be done although the linear sample size in samples B and C is just $50a$ — where $a \sim 1$ nm is the lattice spacing (or one

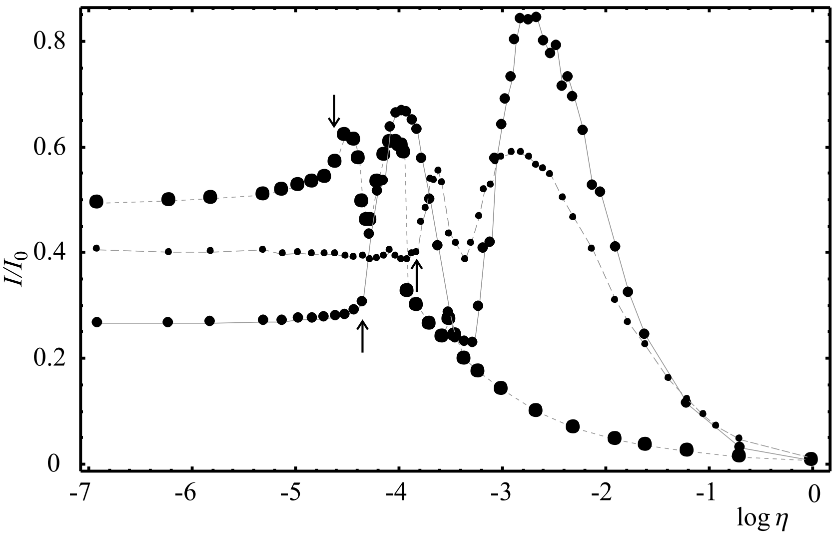

Figure 5.17 External field-induced switching as monitored by transmitted polarized light intensity I measurements: sample A (small dots), sample B (medium dots), and sample C (large dots). The arrows indicate the switching threshold as determined from the capacitance measurement (Fig. 5.16). I_0 denotes the intensity of the incoming light.

molecular dimension) — by letting the polarized light pass several (~ 200) times through the sample so as to accumulate a sufficient birefringence $\Delta\Phi$. In the smaller sample A 550 light passes were necessary to yield the same optical thickness. On each pass (i.e., MC cycle), the molecular configuration was refreshed from the MC data. However, unlike in the nematic slab discussed above, now the local director depends also on the x and z coordinates, and so does the outcoming light intensity $I = I(x, z)$. Because $I = I(x, z)$ is modulated on length scales much shorter than the light wavelength λ, $I(x, z)$ is to be averaged across the light beam cross section in the xz-plane to yield an average light intensity observable in a real experiment.

In the following it will be assumed that the polymer network is optically isotropic, with a refractive index $n_p = 1.499$. It will be further assumed that for the perfectly ordered nematic $n_e^0 = 1.7445$ (maximum value) and $n_o^0 = 1.520$, yielding $\Delta n^0 = n_e^0 - n_o^0 \approx 0.2175$. Probing such a sample with He-Ne laser light with $\lambda = 632$ nm, at $T^* = 1.0$ with $S \approx 0.6$ $\Delta\Phi_z$ can be estimated close to $\Delta\Phi_z \approx 2\pi\times 2.1$. Consequently, two oscillations can be anticipated in the $I(\eta)$-dependence. Inspecting the simulated $I(\eta)$ curves shown in Fig. 5.17, one immediately recognizes the oscillatory behavior predicted above. Again, curves for the A, B, and C sample are characterized by different Fréedericksz thresholds, matching with those observed already in the capacitance measurement. Moreover, the oscillations of I upon increasing η are slowest for sample B, which is in agreement with the lowest slope of the $C_y(\eta)$ capacitance curve (Fig. 5.16). At extremely strong fields I drops to zero which is because now the effective birefringence approaches zero, as discussed above. Note also that the value of I below the threshold is different for each sample, originating in different $\Delta\Phi_z$, as also already discussed.

Finally, let us inspect ^{2}H NMR spectra calculated for each sample type to monitor the switching process. Fig. 5.18 comparatively shows the spectra calculated for the samples A, B, and C, with the spectrometer field applied along the (average) fiber direction, $\mathbf{z}$. Again, a smoothening convolution with a Lorentzian kernel of width $\approx 0.07\delta\omega_Q$ was performed. Like in Sect. 5.1.3, translational diffusion was simulated, taking the same rate of diffusion. Consider sample A first. In absence of the external field, as well as for low η, in the spectrum there are two well-defined lines positioned approximately at a maximum frequency splitting reduced by a factor of $S \approx 0.6$, as it follows from Eq. (2.41). This is a signature of fiber-imposed molecular ordering along z below the Fréedericksz threshold. Once the threshold at $\eta_A \approx 0.022$ is reached, molecular orientations start to switch along $\mathbf{y}$, the external field direction, and the splitting is reduced. At very high fields already above the saturation transition the quadrupolar splitting should equal half the splitting seen at zero field, provided that the degree of ordering remains unchanged. In a strong external field, however, this never is the case and therefore the splitting keeps on increasing as the field is getting stronger. Moving to sample B, one can observe that the low-field splitting starts to decrease already at $\eta_B \approx 0.013$. Moreover, the switching process is also more gradual, which is all in agreement the other two experiments. In sample C at low fields one also finds a double-peaked line shape, yet at a splitting slightly lower than in the previous two cases. This indicates that despite the network is highly irregular, the z-orientation of molecules is still maintained in most of the sample,

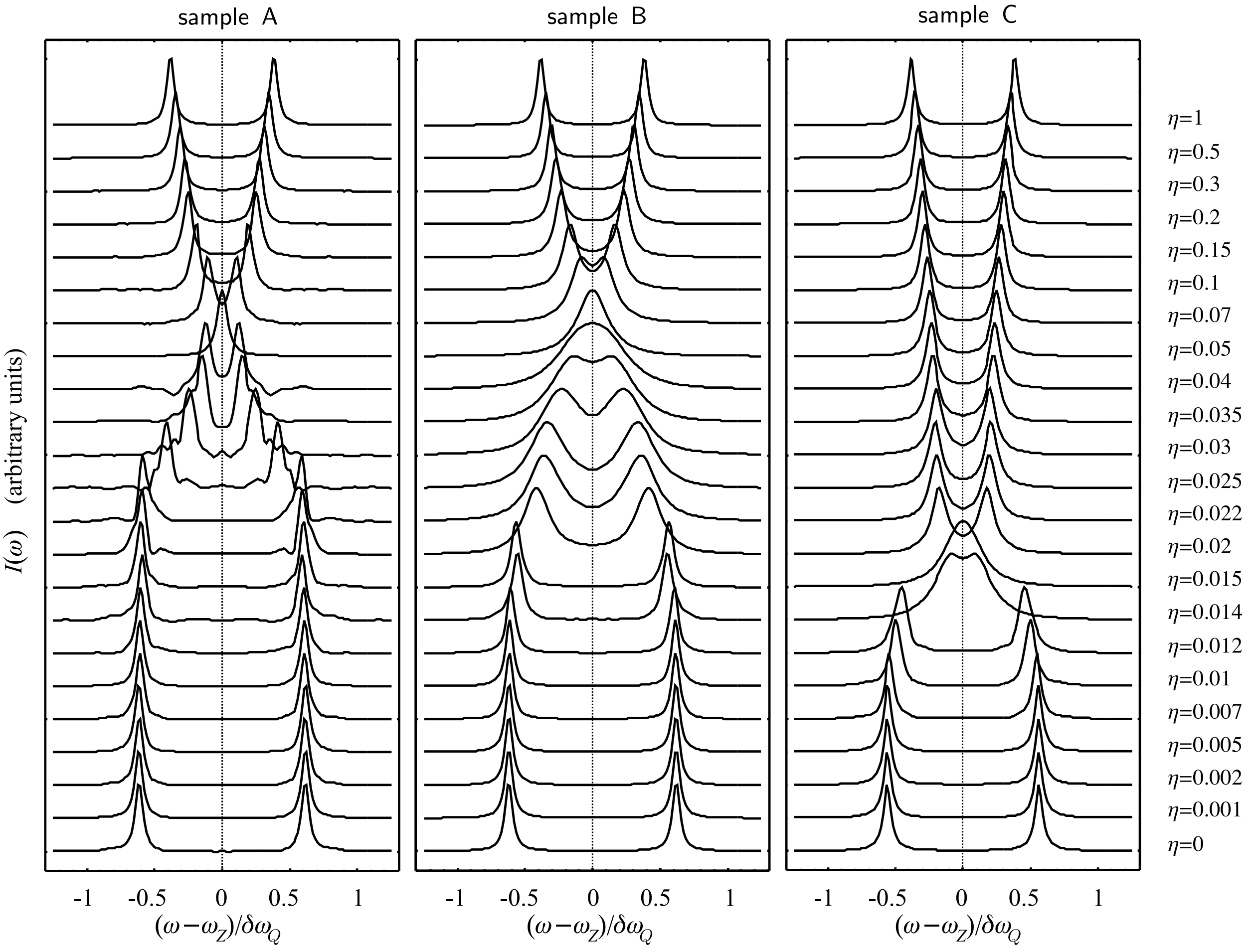

Figure 5.18 External field-induced switching as monitored by ^{2}H NMR spectra: sample A (*left*), sample B (*center*), and sample C (*right*). In all cases $T^* = 1$ and $w = 1$. The spectra of sample A show more noise because this sample contains 5256 particles only — as opposed to 112200 particles in samples B and C.

which agrees with snapshots plotted in Fig. 5.15. The fact that the splitting is somewhat lower than that observed for samples A and B, however, implies that in the vicinity of fibers nematic molecules do follow the local orientation of the network and thus deviate from the z-direction. Note also that the sample C switches already at $\eta_C \approx 0.010$, which, again, is the lowest threshold of all. In addition, the switching again occurs more suddenly than in sample B.

5.3 Pretransitional ordering in the isotropic phase

The last issue considered in this Chapter will be pretransitional ordering in a nematic sample with dispersed polymer networks above the NI transition ($T^*_{NI} = 1.1232$). As seen already in Sect. 5.1 studying a regular fiber array, some surface-induced

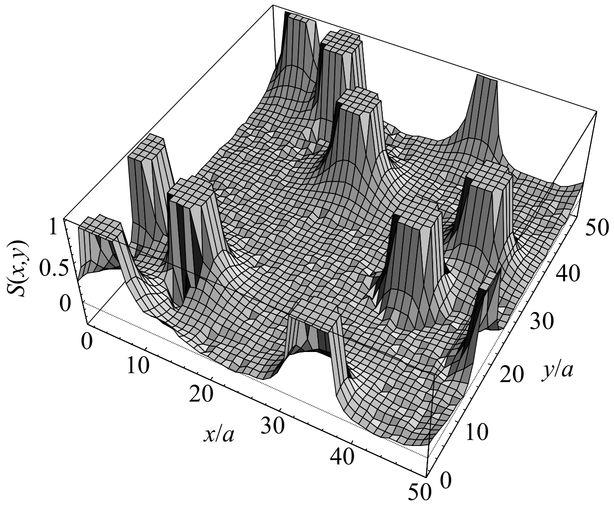

Figure 5.19 Pretransitional ordering in sample C at $T^* = 1.2$, for planar anchoring with $w = 1$: $S(x, y)$ order parameter map cross section at $z/a = 25$. The paranematic order decays to zero over the correlation length $\xi \approx 5a$, except in polymer-rich areas where nematic "bridges" can form in between fibers (as here in the left lower corner with $S \leq 0.2$). Note that while the "columns" denoting fiber positions are vertical, the fibers themselves can be tilted with respect to the xy-plane.

paranematic ordering may persist in the vicinity of fibers. This ordering can be detected by optical means [26], as described in Sects. 2.3.3 and 5.2.3. Alternatively, it can be detected also by ^{2}H NMR [132].

The simulations presented in this Section were performed with sample C presented in Sect. 5.2.3 (see Fig. 5.14). Again, planar anchoring along the local fiber direction was assumed and there was no external field applied. Paranematic ordering can then be characterized by a director parallel to the local fiber direction, and by a degree of order S decaying from a nonzero surface value to $S \approx 0$ over $\xi \approx 5a$ (at $T^* = 1.2$), the corresponding correlation length. Therefore, in a low-polymer-density sample areas with $S \neq 0$ are limited only to the very vicinity of fibers. In high-polymer-density samples, on the other hand, fibers can approach each other (or even cross-link) and thereby create "bridges" of nematic order with $S \neq 0$ wherever the lowest fiber-to-fiber distance becomes comparable to $\approx 2\xi$ — see Fig. 5.19. This effect is similar to the capillary condensation observed experimentally in thin nematic films by force spectroscopy [169], potentially allowing for a self-assembly of colloidal particles. The actual degree of paranematic order depends significantly also on temperature (T^*) and on the strength of the orientational coupling of the liquid crystal with the fiber surface (w). Therefore, in this Section simulation results for different T^* and w will be presented, focusing on the experimental output: transmitted light intensity and ^{2}H NMR line shapes. In the simulation, the sample was equilibrated during 8×10^4 MC cycles and, afterwards, 7×10^4 cycles were used to accumulate the relevant observables.

The set up of the optical experiment was identical to that used in Sect. 5.2.3:

net fiber direction along the z-axis, light beam along the y-axis, and the polarizer and analyzer crossed in the xz-plane, each of them at an angle of $\pi/4$ with respect to the z-axis. Further, same sample thickness of $d = 10$ μm and light wavelength $\lambda = 632$ nm were considered. Again, the polymer was assumed optically isotropic and the refractive indices of the liquid crystal equal to those used in Sect. 5.2.3. As already discussed, the intensity of outcoming light I is proportional to $I \propto \sin^2(\Delta\Phi/2)$ (2.48), where the effective birefringence $\Delta\Phi$ is proportional to Δn, the difference between the extraordinary (n_e) and ordinary (n_o) refraction index averaged along the path of the light beam. Assuming that the net direction of paranematic ordering — averaged over the whole sample — is still along the z-axis, as imposed by the polymer network, and that Δn is small in comparison to n_e and n_o, Δn is simply proportional to the overall degree of order, in this case given by $\langle P_2^z\rangle$. This relation can be obtained from the expression for the eigenvalues of the high-frequency dielectric tensor (2.7), assuming that $\langle P_2^z\rangle\Delta\epsilon/\epsilon_i \ll 1$. Herewith $\Delta\epsilon = \epsilon_{||}^{\infty} - \epsilon_{\perp}^{\infty}$ and $\epsilon_i = \frac{1}{3}(\epsilon_{||}^{\infty} + 2\epsilon_{\perp}^{\infty})$ were introduced, where $\epsilon_{||}^{\infty}$ and $\epsilon_{\perp}^{\infty}$ stand for the eigenvalues in a perfectly ordered nematic. In the weakly ordered paranematic phase the above assumption is expected to hold sufficiently well. Note that the averaging performed to calculate Δn has to be carried out both over local rapid fluctuations of molecular long axes (defining the local standard nematic order parameter S), and across the sample over changes in the local director and polymer fiber orientations (characterized by the $\langle P_2\rangle_g$ order parameter, as in Sect. 5.1). Furthermore, in the fiber vicinity S is strongly spatially-dependent; see Figs. 5.3 (c) and 5.19. Following the addition theorem for spherical harmonics, one can now write $\langle P_2^z\rangle = \langle S\rangle\langle P_2\rangle_g$, where $\langle S\rangle$ is the spatial average of S performed in the vicinity of the fiber (wherever $S \neq 0$).

In should be also noted that the above discussion is pertinent for low-density networks only where there are no nematic “bridges” (areas with enhanced ordering) between polymer fibers, and that sample C with approximately 9% polymer does not necessarily meet this requirement. Moreover, the form of the addition theorem for spherical harmonics that was applied above is valid only if there is no biaxiality either in ordering of nematic molecules, or in the polymer network shape. Neither of this is, however, strictly true for the sample C considered here. But, in any case, if $\langle P_2\rangle_g$ is fixed, the transmitted light intensity I should increase with increasing $\langle S\rangle$ (i.e., with decreasing T^*), and I can be taken as a measure for the degree of ordering in the system, as it was done in Ref. [26]. Note also that in an inhomogeneous sample refraction of light, as well as light scattering should in principle be included in studies of light propagation. Light scattering on refractive index inhomogeneities characterized by a length scale much smaller than light wavelength λ, as in sample C, can be neglected [26]. Refraction of light, however, may become important, resulting in slight deviations of the light beam from the incident y-axis. For simplicity, both effects were ignored in the present calculation.

Fig. 5.20 shows the simulated transmitted light intensity (I) curves versus reduced temperature (above $T_{NI}^* = 1.1232$) for different anchoring strengths w. As expected, the intensity I is nonzero due to paranematic surface-induced ordering, $\langle S\rangle \neq 0$, and decreases with increasing T^*. Curves in Fig. 5.20 are similar to the

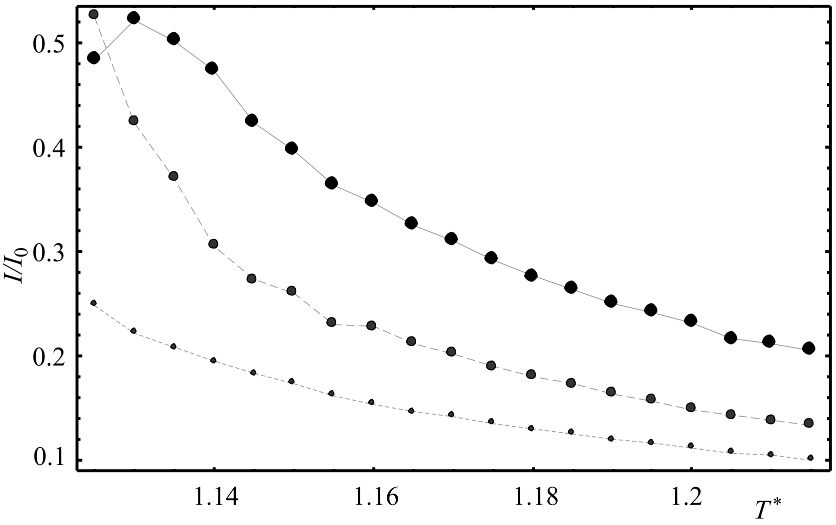

Figure 5.20 Pretransitional ordering: transmitted polarized light intensity I as a function of T^* for different anchoring strengths: $w = 1$ (large dots), $w = 0.5$ (medium dots), and $w = 0.1$ (small dots). I_0 denotes the intensity of the incoming light.

corresponding experimental ones plotted in Ref. [26]. Note, however, that the increase of I/I_0 on approaching T^*_{NI} from above is not as abrupt as in Ref. [26]. This may be because in the present simulation the NI transition was not approached as closely as in the experiment. Further, in the present study I/I_0 is well-behaved also because the effective birefringence is not necessarily small — the polymer network is rather dense and $\Delta\Phi \ll 1$ does not always hold (e.g., for $w = 1$) — and a possible significant variation of $\Delta\Phi$ is saturated in the $I \propto \sin^2(\Delta\Phi/2)$ dependence. For the same reason, the curve for $w = 1$ is not monotonous close to the NI transition. Moreover, with decreasing anchoring strength w the degree of ordering decreases, which then translates into a lower I/I_0 signal.

One can also try to estimate I/I_0 from the formula (2.48) and compare it with the simulated one. Taking $\Delta n^0 = 0.2175$ and $\langle P_2\rangle_g \approx 0.28$, as above, and estimating $\langle S\rangle$ from the simulation for a single fiber ($\langle S\rangle \approx 0.13$ at $T^* = 1.2$ and $w = 1$) yields $\Delta\Phi = \Delta n^0\langle S\rangle\langle P_2\rangle_g(2\pi d/\lambda) \approx 0.78$. This then gives $I/I_0 = \sin^2(\Delta\Phi/2) \approx 0.15$, while the simulated value for $T^* = 1.2$ and $w = 1$ is $I/I_0 \approx 0.23$. Recall now that in the simulation I/I_0 is deduced by averaging transmitted light intensities within the xz-plane — across the light beam cross section. In a real (macroscopic) sample, the outcoming light at each of the points in the xz-plane has accumulated roughly the same phase shift $\Delta\Phi$ when traveling through the sample, i.e., the intensity of the outcoming light is uniform within the probing light beam cross section. Therefore, in a real experiment the quantities $\langle\sin^2(\Delta\Phi/2)\rangle_{xz}$ (calculated in the simulation) and $\sin^2(\langle\Delta\Phi\rangle_{xz}/2)$ (estimated above and measured in Ref. [26]) are within reason equal. Here $\langle...\rangle_{xz}$ stands for a spatial average in the xz-plane. The degree of network irregularity in the simulated $50 \times 50 \times 50$ particle simulation box is, however, still rather far from that of irregularities in a macroscopic sample. As a consequence, one should not be surprised by the disagreement of the estimated and simulated I/I_0, and better focus on the qualitative behavior of I/I_0 instead.

Alternatively, pretransitional ordering can be detected also via ^{2}H NMR. As discussed in great detail in Sect. 2.3.1 and elsewhere, the quadrupolar line splitting $\omega_Q(\mathbf{r})$ (2.41) depends both on the local orientation of the nematic director (matching with the local orientation of the fiber network) and on the local degree of order. The spectra presented in Fig. 5.21 were calculated for sample C in the fast diffusion limit (the rate of diffusion being 1024 diffusive steps per NMR cycle, as earlier in this Section), with the spectrometer magnetic field directed along the z-axis. In this case the spectrum consists of one or two well-defined lines positioned at an average frequency $\omega_Z \pm \langle\omega_Q(\mathbf{r})\rangle$, where $\langle ...\rangle$ stands for the spatial average. As above, in case of predominantly uniaxial molecular ordering the spherical harmonics addition theorem can be applied to Eq. (2.41) when $\langle\omega_Q(\mathbf{r})\rangle$ is calculated, resulting in $\langle\omega_Q(\mathbf{r})\rangle = \delta\omega_Q\langle S\rangle\langle P_2\rangle_g$.

Fig. 5.21 shows the evolution of ^{2}H NMR spectra upon increasing T^* for different values of the anchoring strength w. A convolution of the spectra with a Lorentzian kernel of width $\approx 0.07\delta\omega_Q$ was performed in order to smoothen the spectra. The

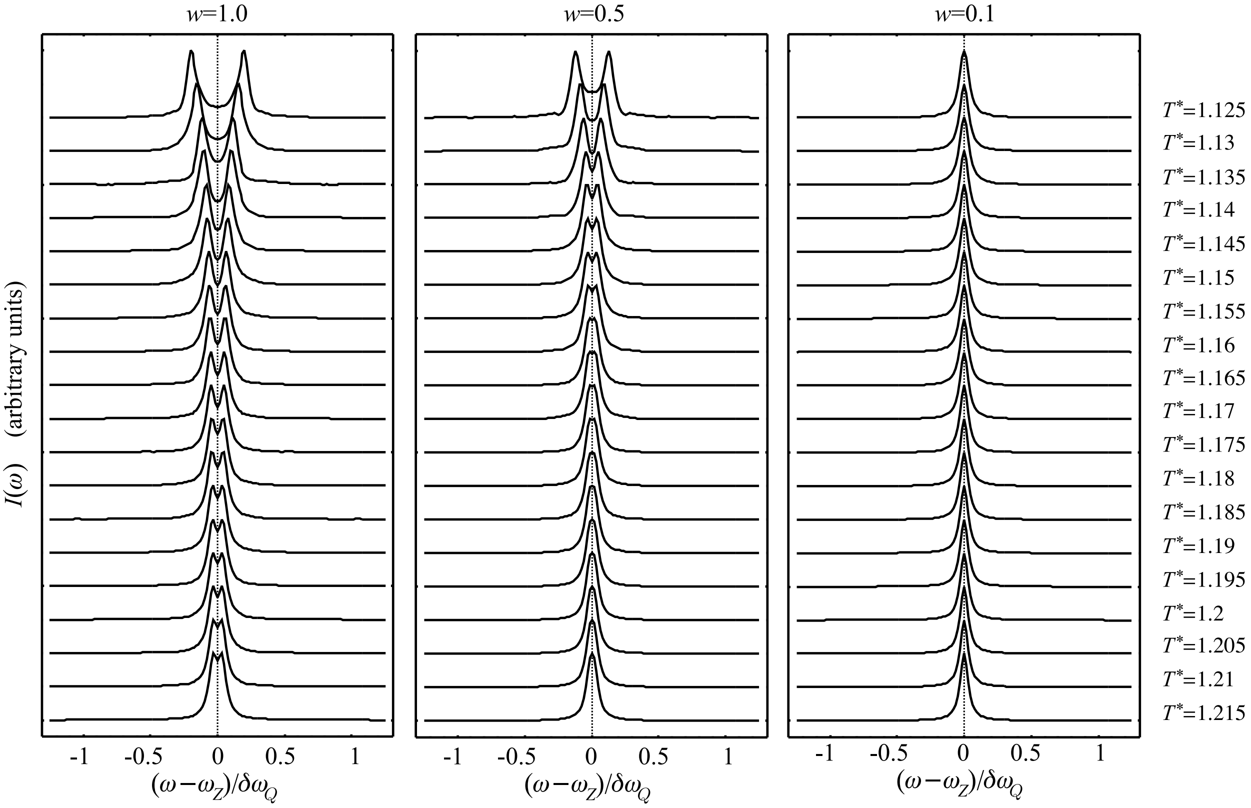

Figure 5.21 Pretransitional ordering: diffusion-averaged ^{2}H NMR spectra as a function of T^* for different anchoring strengths: $w = 0.1$ (*left*), $w = 0.5$ (*center*), and $w = 0.1$ (*right*). Double-peaked line shapes are a signature of surface-induced paranematic ordering.

left sequence of spectra in Fig. 5.21 is plotted for $w = 1$ where the surface degree of order is high enough to yield a double-peaked spectrum. For $T^* = 1.2$ the peak is estimated to be located at $|\omega_Q/\delta\omega_Q| \approx 0.04 \pm 0.01$. On the other hand, $\langle S\rangle\langle P_2\rangle_g$ gives ≈ 0.036, and hence the agreement of the two estimates is reasonably good. The agreement indicates that in case of paranematic molecular ordering in sample C biaxiality effects are not extremely important, supporting also the simple estimates in the above optical experiment. When decreasing the temperature towards T_{NI}^*, the effective quadrupolar splitting increases, which results from an increase of $\langle S\rangle$. For weaker anchoring ($w = 0.5$ and $w = 0.1$) the overall $\langle S\rangle$ is smaller and the calculated spectra are only single-peaked — except rather close to T_{NI}^* for $w = 0.5$ — because their resolution is not high enough to detect $\langle S\rangle$ that approaches zero.

In conclusion, the simulations presented in this Section clearly confirm the existence of paranematic ordering above T_{NI}^*. This ordering weakens with increasing temperature and with the decreasing strength of the orientational coupling with the polymer surface. These effects were both observed also through simulated ^{2}H NMR line shapes and transmitted light intensity measurements.

6

Conclusion

In this concluding Chapter we will review the new achievements presented in the thesis, along with the still open questions and possible future directions. The thesis was mainly concerned with modeling confined nematics, applying well-established phenomenological (Landau-de Gennes) and, more extensively, simulation (Monte Carlo-type) approaches to selected open problems in the field.

Motivated by experiments indicating significant subsurface elastic deformations in nematics, the first part (Chapter 3) focused on molecular ordering in a nematic slab, with a special emphasis to the vicinity of its interfaces. In the framework of the phenomenological Landau-de Gennes theory it was shown that unless the one-elastic constant approximation is applied, any variation of the degree of nematic order S — as occurring typically close to any interface — yields a subsurface elastic deformation whose characteristic length matches with that of the S-variation, the corresponding correlation length. This subsurface deformation exists only for planar distortions (in the tilt angle ϕ profile), while it is absent in case of pure twist distortions. Note that the free energy functional was expanded only up to first spatial derivatives of S and ϕ, and that the observed subsurface deformation stems exclusively from the S-variation, having thus an origin completely different from that of deformations predicted in connection with the controversial splay-bend elastic constant. In addition, the S-variation yields an intrinsic contribution to the surface anchoring energy, with an easy axis either parallel or perpendicular to the sample normal. If the effective (intrinsic plus external) anchoring strength is adjusted to yield an extrapolation length approaching those observable experimentally ($\ell \sim 100$ nm) — here estimated by matching external field and anchoring effects — the subsurface deformation and the S-variation are both small. This agrees with the use of a truncated first-order free energy functional. Nevertheless, it should be clearly stressed that the described phenomenological continuous approach cannot explain short-scale peculiarities in the orientation of molecules observed experimentally in the first molecular layer in direct contact with the substrate.

The phenomenological study of ordering in a nematic slab was complemented by a molecular Monte Carlo (MC) simulation analysis based on the novel simple hexagonal lattice model. This model allows for the use of spatially anisotropic pairwise potentials (like the induced dipole-induced dipole one considered here) without creating any artificial bulk easy axes. In a deformed hybrid cell-like slab with one free surface, intrinsic anchoring was explored in detail. Its microscopic origin comes from incomplete spatially anisotropic intermolecular interactions close to the free surface. For the induced dipole-induced dipole interaction the corresponding extrapolation length ℓ is microscopic, as estimated from simple profile extrapolation. It approaches experimental values only if the interaction anisotropy is significantly reduced. Moreover, ℓ exhibits almost no temperature dependence, even if the nematic-isotropic transition is approached. This obvious disagreement with experimental findings might be attributed to the great simplicity of the present model. Possible extensions of the model comprise simulations of density variations close to the surface (inserting vacancies into the lattice) and simulations of rough or modulated solid substrates (both expected to reduce the anchoring strength). Nonetheless, a full (and also computationally more demanding) description of nematic interfaces can be provided only by dropping the lattice restriction, allowing thereby directly for density variations and the formation smectic phases. This remains one of the goals of the future research.

In the following Chapters, a rather simplified picture of interfaces was adopted: anchoring (exclusively external) characterized with a well-defined easy axis and strength. Instead, more complex confining geometries were treated: spherical PDLC droplets (Chapter 4) and polymer networks (Chapter 5).

Chapter 4 was concerned with molecular ordering in radial and bipolar PDLC droplets. Recently, PDLCs have gained renewed interest with the advent of holographic PDLC materials. The ordering in spherical PDLC droplets was explored by performing MC simulations in the Lebwohl-Lasher model system. This model is also based on a lattice (however, simple cubic), with particles interacting via a spatially isotropic pair potential giving rise to no intrinsic anchoring. Following extensive simulation studies of nematic droplets in the past, the focal point of the present PDLC study was the development of a novel methodology for calculating ^{2}H NMR spectra — one of the important experimental observables for these systems — in presence of significant molecular motion, such as translational diffusion (both spatially homogeneous and inhomogeneous) and fluctuations of molecular long axes. The methodology was tested successfully for bipolar and radial droplets, allowing for an identification of both director structures by inspecting the calculated line shapes. The results indicate that molecular fluctuations lead to a narrowing of the NMR spectrum, while its shape remains similar to that obtained in the static case. From this narrowing it was possible to deduce the values of S, the order parameter, which turned out to be in an excellent agreement with values deduced directly from the MC data. Further, molecular diffusive motions result in an averaged spectrum, which in the fast diffusion limit consists of one or two rather narrow lines, depending on the type of boundary conditions. The positions of these lines can also be predicted from MC data, and again the agreement is fairly good. If the diffusive motion close to the confining substrate is significantly hindered, this results in perceptible changes in NMR spectra. These changes should be detectable also experimentally in droplets with a high enough surface-to-volume ratio. Moreover, “powder” spectra for an array of many bipolar droplets with randomly oriented symmetry axes were calculated as well. Finally, droplets in an external electric or magnetic field were studied, together with the evolution of the corresponding spectra upon increasing the field strength. The field-induced effects seen to reflect in the spectra are: molecular reorientation along the field direction, enhancement of the degree of nematic order, and the formation of the nematic phase at temperatures even higher than the nematic-isotropic transition. The two latter effects can be detected only in external fields that are unrealistically strong. In the radial droplet the external field induces a continuous structural transition from the radial "hedgehog" structure to an aligned one whose spectrum becomes similar to that of the bipolar droplet. Note that currently it is still impossible to fit experimental spectra with the simulated ones because of the smallness of the simulation box. To reduce the noise present in the spectra, smoothening convolutions must be applied, distorting the spectra to some degree. Qualitatively, however, the agreement of experimental and simulated spectra is very good.

Another type of confinement — polymer networks dispersed in a nematic — was investigated in Chapter 5. Like PDLCs, these systems are becoming important for applicative purposes, yet to date lacking molecular simulation studies. Here as a first step towards a realistic fiber network a regular array of straight and parallel fibers was studied, focusing on effects of surface roughness. Different types of anchoring conditions at the fiber surface were considered: planar along the fiber direction, homeotropic, and partially or completely random. In cases with perfect planar or homeotropic anchoring in the very vicinity of the fiber nematic order is enhanced. However, once the anchoring conditions are partially distorted, the surface degree of nematic order may drop below its bulk value, but the long-range orienting capability of the fiber network is still retained. This ability seems to be lost only for completely random anchoring imposing no well-defined direction in the system, as confirmed also by the ^{2}H NMR spectra calculated from the simulation output. Further, above the nematic-isotropic transition surface-induced paranematic ordering could be detected, reflecting clearly in the translational diffusion-averaged ^{2}H NMR spectra. In addition, in the nematic phase two $-\frac{1}{2}$ strength disclination lines parallel to the fiber were observed for perfect homeotropic anchoring, and were seen to move away from the fiber upon increasing temperature. Plotting order parameter S and biaxiality P maps made it possible to resolve the inner structure of the defect core: in the very center nematic ordering is uniaxial with $S < 0$, surrounded by a ring where ordering is strongly biaxial with $P \neq 0$ and $S > 0$. These findings agree very well also with those coming from phenomenological defect studies. Then, in the same model system, an external field was applied in the direction perpendicular to the fibers to investigate the switching behavior of nematic molecules. Monitoring fluctuations of relevant order parameters, both the Fréedericskz and the saturation transition were identified for different anchoring strengths. A stability phase diagram for possible nematic structures was plotted and was found to be in good qualitative agreement with the one calculated from the Frank elastic theory for the simple slab geometry. As a second step in increasing the complexity of the fiber network, a system of several straight and parallel, yet randomly positioned fibers was considered. At unchanged polymer concentration, the Fréedericskz switching threshold in such a sample shifts towards lower field strengths, and the switching process is more gradual than in a system of regular fibers. An even more realistic network model includes randomly positioned fibers that are curved and allows also for cross-linking between them. This model represented the most complex type of confinement considered in the thesis. The Fréedericskz threshold in such a sample is not well-defined any more, but the switching is still relatively sudden. These conclusions were all demonstrated also by the simulated experimental observables, namely ^{2}H NMR line shapes, electric capacitance, and transmitted polarized light intensity. Finally, paranematic ordering was inspected also in the irregular fiber system. Results obtained from diffusion-averaged ^{2}H NMR spectra and from the optical experiment measuring the intensity of transmitted light qualitatively agree with real experiments. It should be noted that some of the above findings can be relevant also for the behavior of other composite systems like nematic gels and colloids, including regular colloidal crystals formed by capillary condensation.

All in all, the simulation part of the thesis has presented a number of effects and phenomena in confined nematics qualitatively known either from phenomenology, experiments, or simply from pure intuition. For this reason, someone might argue that they are not that novel and striking. However, the great value of studies like the present ones is, first, to allow for a treatment of complex confinement whenever phenomenology fails (either for conceptual or merely for technical-computational reasons). Second, simulation studies presented here were able to establish a qualitative relation between rather subtle details in the microscopic material properties and the macroscopic behavior of the system. In addition, with the ongoing improvement of computing performance this qualitative relation — here established for the still simplified confining geometries — should definitely evolve into a more quantitative one, with the simulated experimental observables comparable directly to the real ones.

⋆ ⋆ ⋆

Bibliography

[1] F. Reinitzer, Monatsch. Chem. **9**, 421 (1888).

[2] O. Lehmann, Z. Physikal. Chem. **4**, 462 (1889).

[3] G. Friedel, Ann. Physique **18**, 273 (1922).

[4] P. G. de Gennes and J. Prost, *The Physics of Liquid Crystals* (Clarendon Press, Oxford, 1993).

[5] G. P. Crawford and S. Žumer, *Liquid Crystals in Complex Geometries Formed by Polymer and Porous Networks* (Taylor and Francis, London, 1996).

[6] L. M. Blinov, A. Yu. Kabayenkov, and A. A. Sonin, Liq. Cryst. **5**, 645 (1989).

[7] C. Mauguin, Bull. Soc. Fr. Minéral. Cristallogr. **34**, 71 (1911).

[8] G. Barbero, N. V. Madhusudana, J. F. Palierne, and G. Durand, Phys. Lett. A **103**, 385 (1984).

[9] Y. Sato, K. Sato, and T. Uchida, Jpn. J. Appl. Phys. II **31**, L579 (1992).

[10] J.-H. Kim and C. Rosenblatt, J. Appl. Phys. **84**, 6027 (1998).

[11] O. Lehmann, *Handbuch der biologischen Arbeitsmethoden* (Urban und Schwarzenberg, Berlin, 1922).

[12] S. Naemura, Appl. Phys. Lett. **33**, 1 (1978).

[13] R. Sun, J. Guo, X. Huang, and K. Ma, Appl. Phys. Lett. **66**, 1753 (1995).

[14] J. L. Janning, Appl. Phys. Lett. **21**, 173 (1972).

[15] I. Dierking, L. L. Kosbar, A. Afzali-Ardakani, A. C. Lowe, and G. A. Held, Appl. Phys. Lett. **71**, 2454 (1997).

[16] P. G. de Gennes, Mol. Cryst. Liq. Cryst. **12**, 193 (1971).

[17] G. Skačej, V. M. Pergamenshchik, A. L. Alexe-Ionescu, G. Barbero, and S. Žumer, Phys. Rev. E **56**, 571 (1997).

[18] F. C. Frank, Discuss. Faraday Soc. **25**, 19 (1958).

[19] C. W. Oseen, Trans. Faraday Soc. **29**, 883 (1933).

[20] H. Zöcher, Trans. Faraday Soc. **29**, 945 (1933).

[21] A. Rapini and M. Papoular, J. Phys. (Paris) Colloque **30**, C4-54 (1969).

[22] M. Nobili and G. Durand, Phys. Rev. A **46**, R6174 (1992).

[23] M. Kléman, *Points, Lines, and Walls: In Liquid Crystals, Magnetic Systems, and Various Ordered Media* (John Wiley & Sons, New York, 1983).

[24] P. M. Chaikin and T. C. Lubensky, *Principles of Condensed Matter Physics* (Cambridge University Press, Cambridge, 1997).

[25] M. Ambrožič, P. Formoso, A. Golemme, and S. Žumer, Phys. Rev. E **56**, 1825 (1997).

[26] Y. K. Fung, A. Borštnik, S. Žumer, D.-K. Yang, and J. W. Doane, Phys. Rev. E **55**, 1637 (1997).

[27] G. P. Crawford, L. M. Steele, R. J. Ondris-Crawford, G. S. Iannacchione, C. J. Yeager, J. W. Doane, and D. Finotello, J. Chem. Phys. **96**, 7788 (1992).

[28] J. W. Doane, N. S. Vaz, B. G. Wu, and S. Žumer, Appl. Phys. Lett. **48**, 269 (1986).

[29] C. C. Bowley, H. J. Yuan, and G. P. Crawford, Mol. Cryst. Liq. Cryst. (Sci. Tech. A) **331**, 2069 (1999).

[30] S. C. Jain and H.-S. Kitzerow, Appl. Phys. Lett. **64**, 2946 (1994).

[31] M. J. Escuti, C. C. Bowley, G. P. Crawford, and S. Žumer, Appl. Phys. Lett. **75**, 3264 (1999).

[32] L. D. Landau, *On the Theory of Phase Transitions*, in *Collected papers of L. D. Landau*, edited by D. ter Haar (Gordon and Breach, New York, 1967).

[33] R. Evans, Advances in Physics **28**, 143 (1979).

[34] M. M. Telo da Gama, Mol. Phys. **52**, 585 (1984) and Mol. Phys. **52**, 611 (1984).

[35] J. H. Thurtell, M. M. Telo da Gama, and K. E. Gubbins, Mol. Phys. **54**, 321 (1985).

[36] B. J. Alder and T. E. Wainwright, *Molecular Dynamics by Electronic Computers*, in *Proc. of the Int. Symp. on Statistical Mechanical Theory of Transport processes (Brussels, 1956)*, edited by I. Prigogine (Interscience, Wiley, New York, 1958).

[37] N. Metropolis, A. W. Rosenbluth, M. N. Rosenbluth, A. H. Teller, and E. Teller, J. Chem. Phys. **21**, 1087 (1953).

[38] R. Ondris-Crawford, E. P. Boyko, B. G. Wagner, and J. H. Erdmann, J. Appl. Phys. **69**, 6380 (1991).

[39] R.-Q. Ma and D.-K. Yang, Phys. Rev. E **61**, 1567 (2000).

[40] A. Golemme, S. Žumer, J. W. Doane, and M. E. Neubert, Phys. Rev. A **37**, 559 (1988).

[41] S. Žumer, P. Ziherl, and M. Vilfan, Mol. Cryst. Liq. Cryst. **292**, 39 (1997).

[42] Y. R. Shen, Nature **337**, 519 (1989).

[43] X. Zhuang, L. Marucci, and Y. R. Shen, Phys. Rev. Lett. **73**, 1513 (1994).

[44] C. Bahr and D. Fliegner, Phys. Rev. A **46**, 7657 (1992).

[45] M. Vilfan and M. Čopič, Mol. Cryst. Liq. Cryst. **351**, 419 (2000).

[46] A. Mertelj and M. Čopič, Phys. Rev. Lett. **81**, 5944 (1998).

[47] G. S. Iannacchione and D. Finotello, Phys. Rev. Lett. **69**, 2094 (1992).

[48] P. Guyot-Sionnest, H. Hsiung, and Y. R. Shen, Phys. Rev. Lett. **57**, 2963 (1986).

[49] Y. R. Shen, Liq. Cryst. **2**, 635 (1989).

[50] B. Jérôme, Mol. Cryst. Liq. Cryst. **251**, 219 (1994).

[51] B. Jérôme, J. Phys. Condens. Matter **6**, A269 (1994).

[52] J. Nehring and A. Saupe. J. Chem. Phys **54**, 337 (1971).

[53] J. Nehring and A. Saupe, J. Chem. Phys. **55**, 5527 (1972).

[54] C. Oldano and G. Barbero, Phys. Lett. A, **110**, 213 (1985).

[55] G. Barbero, A. Sparavigna, and A. Strigazzi, Nouvo Cimento D **12**, 1259 (1990).

[56] S. Faetti, Liq. Cryst. **15**, 807 (1993).

[57] S. Faetti, Phys. Rev. E **49**, 5332 (1994).

[58] I. Dahl and A. de Meyere, Liq. Cryst. **18**, 683 (1995).

[59] H. P. Hinov, Mol. Cryst. Liq. Cryst. **148**, 197 (1987).

[60] V. M. Pergamenshchik, Phys. Rev. E **48**, 1254 (1993).

[61] V. M. Pergamenshchik, P. I. C. Teixeira, and T. J. Sluckin, Phys. Rev. E **48**, 1265 (1993).

[62] S. Faetti and M. Riccardi, J. Phys. II **5**, 1165 (1995).

[63] S. Faetti and M. Riccardi, Nuovo Cimento **17D**, 1019 (1995).

[64] A. L. Alexe-Ionescu and G. Barbero, Liq. Cryst. **25**, 189 (1998).

[65] H. Yokoyama, Phys. Rev. E. **55**, 2938 (1997).

[66] V. M. Pergamenshchik, Phys. Lett. A **243**, 167 (1998).

[67] V. M. Pergamenshchik and S. Žumer, Phys. Rev. E **59**, R2531 (1999).

[68] G. Skačej, A. L. Alexe-Ionescu, G. Barbero, and S. Žumer, Phys. Rev. E **57**, 1780 (1998).

[69] M. C. J. M. Vissenberg, S. Stallinga, and G. Vertogen, Phys. Rev. E **55**, 4367 (1997).

[70] P. I. C. Teixeira, T. J. Sluckin, and D. E. Sullivan, Liq. Cryst. **14**, 1243 (1993).

[71] G. Barbero, C. Ferrero, T. Günzel, G. Skačej, and S. Žumer, Phys. Rev. E **58**, 8024 (1998).

[72] P. I. C. Teixeira, Phys. Rev. E **55**, 2876 (1997).

[73] L. R. Evangelista and S. Ponti, Phys. Lett. A **197**, 55 (1995).

[74] J. C. Gay and B. J. Berne, J. Chem. Phys. **74**, 3316 (1981).

[75] A. P. J. Emerson, S. Faetti, and C. Zannoni, Chem. Phys. Lett. **271**, 241 (1997).

[76] S. J. Mills, C. M. Care, M. P. Neal, and D. J. Cleaver, Phys. Rev. E **58**, 3284 (1998).

[77] M. A. Bates and C. Zannoni, Chem. Phys. Lett. **280**, 40 (1997).

[78] E. Martín del Río and E. de Miguel, Phys. Rev. E **55**, 2916 (1997).

[79] M. P. Allen, Mol. Phys. **96**, 1391 (1999).

[80] D. Andrienko, G. Germano, and M. P. Allen, Phys. Rev. E **62**, 6688 (2000).

[81] G. Barbero, L. R. Evangelista, and S. Ponti, Phys. Rev. E **53**, 1256 (1996).

[82] P. Galatola, C. Oldano, M. Rajteri, and G. Barbero, Phys. Lett. A, **210**, 101 (1996).

[83] M. Rajteri, G. Barbero, P. Galatola, C. Oldano, and S. Faetti, Phys. Rev. E **53**, 6093 (1996).

[84] J. Stelzer, L. Longa, and H.-R. Trebin, J. Chem. Phys. **103**, 3098 (1995).

[85] J. Stelzer, *Molekulardynamische Studien von Oberflächeneffekten nematischer Flüssigkristalle* (Verlag Shaker, Aachen, 1995).

[86] J. Stelzer, P. Galatola, G. Barbero, and L. Longa, in *Book of Abstracts, 25. Freiburger Arbeitstagung Flüssigkristalle* (Freiburg, 1996).

[87] Z. Zhang, A. Chakrabarti, O. G. Mouritsen, and M. J. Zuckermann, Phys. Rev. E **53**, 2461 (1996).

[88] C. Rosenblatt, Phys. Rev. Lett. **53**, 791 (1984).

[89] B. M. Ocko, Phys. Rev. Lett. **64**, 2160 (1990).

[90] R. Aloe, G. Chidichimo, and A. Golemme, Mol. Cryst. Liq. Cryst. **203**, 1155 (1991).

[91] P. Pasini and C. Zannoni, *Advances in the Computer Simulations of Liquid Crystals*, (Kluwer, Dordrecht, 2000).

[92] R. K. Bharadwaj, T. J. Bunning, and B. L. Farmer, Liq. Cryst. **27** 591, 2000.

[93] P. A. Lebwohl and G. Lasher, Phys. Rev. A **6**, 426 (1972).

[94] C. Chiccoli, P. Pasini, F. Semeria, E. Berggren, and C. Zannoni, Mol. Cryst. Liq. Cryst. **266**, 241 (1995).

[95] C. Chiccoli, P. Pasini, G. Skačej, C. Zannoni, and S. Žumer, Phys. Rev. E **60**, 4219 (1999).

[96] G. P. Crawford, D. K. Yang, S. Žumer, D. Finotello, and J. W. Doane, Phys. Rev. Lett. **66**, 723 (1991).

[97] C. Chiccoli, P. Pasini, G. Skačej, C. Zannoni, and S. Žumer, Mol. Cryst. Liq. Cryst. **367**, 2987 (2001).

[98] C. Chiccoli, P. Pasini, G. Skačej, C. Zannoni, and S. Žumer, Phys. Rev. E **62**, 3766 (2000).

[99] E. Berggren, C. Zannoni, C. Chiccoli, P. Pasini, and F. Semeria, Phys. Rev. E **49**, 614 (1994).

[100] E. Berggren, C. Zannoni, C. Chiccoli, P. Pasini, and F. Semeria, Phys. Rev. E **50**, 2929 (1994).

[101] I. Dierking, L. L. Kosbar, A. C. Lowe, and G. A. Held, Liq. Cryst. **24**, 397 (1998); Liq. Cryst. **24**, 387 (1998).

[102] C. Chiccoli, P. Pasini, G. Skačej, C. Zannoni, and S. Žumer, to appear in Phys. Rev. E.

[103] D. Andrienko, M. P. Allen, G. Skačej, and S. Žumer, to appear in Phys. Rev. E.

[104] N. Schopohl and T. J. Sluckin, Phys. Rev. Lett. **59**, 2582 (1987).

[105] A. Sonnet, A. Killian, and S. Hess, Phys. Rev. E **52**, 718 (1995).

[106] V. L. Ginzburg, Fiz. Tverd. Tela **2**, 2031 (1960) [Sov. Phys. Solid State **2**, 1824 (1961)].

[107] E. B. Priestley, P. J. Wojtowicz, and P. Sheng, *Introduction to Liquid Crystals* (Plenum Press, New York, 1974).

[108] V. Fréedericksz and V. Zolina, Trans. Faraday Soc. **29**, 919 (1933).

[109] V. Fréedericksz and V. Tsvetkov, V. Sov. Phys. **6**, 490 (1934).

[110] R. D. Polak, G. P. Crawford, B. C. Kostival, J. W. Doane, and S. Žumer, Phys. Rev. E **49**, R978 (1994).

[111] S. Faetti and M. Nobili, J. Phys. II (France) **4**, 1617 (1994).

[112] J. H. Erdmann, S. Žumer, and J. W. Doane, Phys. Rev. Lett. **64**, 1907 (1990).

[113] G. P. Crawford, R. Ondris-Crawford, S. Žumer, and J. W. Doane, Phys. Rev. Lett. **70**, 1838 (1993).

[114] G. Barbero and R. Barberi, J. Phys. (Paris) **44**, 609 (1983).

[115] J. Nehring, A. R. Kmetz, and T. J. Scheffer, J. Appl. Phys. **47**, 850 (1976).

[116] H. Gruler, T. J. Scheffer, and G. Meyer, Z. Naturforsch. A **27**, 966 (1972).

[117] I. Lelidis, M. Nobili, and G. Durand, Phys. Rev. E **48**, 3818 (1993).

[118] I. Lelidis and G. Durand, Phys. Rev. E **48**, 3822 (1993).

[119] L. Onsager, Ann. N. Y. Acad. Sci. **51**, 627 (1949).

[120] W. Maier and A. Saupe, Z. Naturforsch. A **14**, 882 (1959).

[121] W. Maier and A. Saupe, Z. Naturforsch. A **15**, 287 (1960).

[122] G. Lasher, Phys. Rev. A **5**, 1350 (1972).

[123] U. Fabbri and C. Zannoni, Mol. Phys. **58**, 763 (1986).

[124] C. Zannoni, J. Chem. Phys. **84**, 424 (1986).

[125] C. Chiccoli, P. Pasini, F. Semeria, and C. Zannoni, Mol. Cryst. Liq. Cryst. **221**, 19 (1992).

[126] C. Chiccoli, P. Pasini, F. Semeria, and C. Zannoni, Phys. Lett. A **150**, 311 (1990).

[127] C. Chiccoli, P. Pasini, F. Semeria, and C. Zannoni, Mol. Cryst. Liq. Cryst. **212**, 197 (1992).

[128] F. Biscarini, C. Chiccoli, P. Pasini, F. Semeria, and C. Zannoni, Phys. Rev. Lett. **75**, 1803 (1995).

[129] G. Barbero, Mol. Cryst. Liq. Cryst. **195**, 199 (1991).

[130] L. F. Rull, Physica A **220**, 113 (1995).

[131] J. A. Barker and R. O. Watts, Chem. Phys. Lett. **3**, 144 (1969).

[132] A. Golemme, S. Žumer, D. W. Allender, and J. W. Doane, Phys. Rev. Lett. **61**, 2937 (1988).

[133] J. Dolinšek, O. Jarh, M. Vilfan, S. Žumer, R. Blinc, J. W. Doane, G. Crawford, J. Chem. Phys. **95**, 2154 (1991).

[134] R. Y. Dong, *Nuclear Magnetic Resonance of Liquid Crystals* (Springer-Verlag, New York, 1994).

[135] A. Abragam, *The Principles of Nuclear Magnetism* (Clarendon Press, Oxford, 1961).

[136] S. Kralj, M. Vilfan, and S. Žumer, Liq. Cryst. **5**, 1489 (1989).

[137] L. D. Landau, E. M. Lifshitz, and L. P. Pitaevskiĭ, *Electrodynamics of Continuos Media, 2nd edition* (Butterworth-Heinennan, Oxford, 1998).

[138] P. J. Collings and J. S. Patel, *Handbook of Liquid Crystal Research* (Oxford University Press, New York, 1997).

[139] G. Barbero and G. Durand, J. Appl. Phys. **69**, 6968 (1991).

[140] R. Barberi, G. Barbero, and C. Ferrero, Mol. Mat. **3**, 77 (1993).

[141] A. di Garbo and M. Nobili, Liq. Cryst. **19**, 269 (1995).

[142] A. L. Alexe-Ionescu, R. Barberi, G. Barbero, and M. Giocondo, Phys. Rev. E **49**, 5378 (1994).

[143] H. Yokoyama, S. Kobayashi, and H. Kamei, J. Appl. Phys. **61**, 4501 (1987).

[144] G. Vertogen, S. D. P. Flapper, and C. Dullemond, J. Chem. Phys. **76**, 216 (1982).

[145] G. Vertogen, Physica (Amsterdam) **117A**, 227 (1983).

[146] G. Barbero and L. R. Evangelista, Phys. Rev. E. **56**, 6189 (1997).

[147] W. H. Press, B. P. Flannery, S. A. Teukolsky, and W. T. Vetterling, *Numerical Recipes: The Art of Scientific Computing*, (Cambridge University Press, Cambridge, 1987).

[148] H. J. Coles, Mol. Cryst. Liq. Cryst. **49**, 67 (1978).

[149] R. Barberi, G. Barbero, M. Giocondo, and R. Moldovan, Phys. Rev. E **50**, 2093 (1994).

[150] T. Z. Qian and P. Sheng, Phys. Rev. Lett. **77**, 4564 (1996).

[151] T. Z. Qian and P. Sheng, Phys. Rev. E **55**, 7111 (1997).

[152] N. Priezjev and R. A. Pelcovits, Phys. Rev. E **62**, 6734 (2000).

[153] S. Faetti, M. Gatti, V. Palleschi, and T. J. Sluckin, Phys. Rev. Lett. **55**, 1681 (1985).

[154] C. Rosenblatt, J. Phys. (France) **45**, 1087 (1984).

[155] J.-B. Fournier and P. Galatola, Phys. Rev. Lett. **82**, 4859 (1999).

[156] G. Barbero and A. K. Zvezdin, Phys. Rev. E **62**, 6711 (2000).

[157] K. Okano, Jpn. J. Appl. Phys. **22**, L343 (1983).

[158] D. Andrienko and M. P. Allen, Phys. Rev. E **65**, 021704 (2002).

[159] S. Ponti and L. R. Evangelista, Liq. Cryst. **20**, 105 (1996).

[160] A. L. Alexe-Ionescu, G. Barbero, and A. G. Petrov, Phys. Rev. E **48**, R1631 (1993).

[161] B. Jérôme, Rep. Progr. Phys. **54**, 391 (1991).

[162] A. Šarlah and S. Žumer, Phys. Rev. E **60**, 1821 (1999).

[163] J. L. Fergason, Soc. Inf. Dis. Dig. **XVI**, 68 (1985).

[164] P. S. Drzaic, J. Appl. Phys. **60**, 2142 (1986).

[165] C. Chiccoli, P. Pasini, F. Semeria, T. J. Sluckin, and C. Zannoni, J. Phys. II **5**, 427 (1995).

[166] M. Vilfan, G. Lahajnar, I. Zupančič, S. Žumer, R. Blinc, G. P. Crawford, and J. W. Doane, J. Chem. Phys. **103**, 8726 (1995).

[167] G. R. Luckhurst and P. Simpson, Chem. Phys. Lett. **95**, 149, (1983).

[168] F. N. Braun and C. Viney, Phys. Rev. E **63**, 031708 (2001).

[169] K. Kočevar, A. Borštnik, I. Muševič, and S. Žumer, Phys. Rev. Lett. **86**, 5914 (2001).

Izjava

Izjavljam, da sem v doktorskem delu predstavil rezultate lastnega znanstvenoraziskovalnega dela.

V Ljubljani, 13. 3. 2002. Gregor Skačej